*Author:*
**Alston, Jonathan**

*Title:*
**Detection of kissing bonds with non-collinear nonlinear ultrasound**

# Detection of kissing bonds with non-collinear nonlinear ultrasound


Jonathan Alston

A dissertation submitted to the University of Bristol in accordance with the requirements for award of the degree of Doctor of Philosophy in the Faculty of Engineering

06/01/2019

Word Count:

70121

# Abstract

The development of cost effective and reliable bonded structures ideally requires an NDT method to detect the presence of poor quality, weak, or kissing bonds. If these bonds are more compliant in tension than in compression stress-strain nonlinearities provide a possible route to detection with the use of nonlinear ultrasonic techniques. This work focuses on the kissing bond case and the resulting contact acoustic nonlinearity of the interface. The technique developed in this research is a non-collinear ultrasonic method; this involves the interaction of two beams, and it allows the removal of virtually all signal related to system nonlinearity except for that produced in the region where the two beams overlap. Mixing of two shear waves producing a sum frequency longitudinal wave is the selected mode of interaction in this research. The frequencies of the two beams and the angle between them are varied during the experiment. By measuring the nonlinear mixing response as these two parameters are swept through a 'fingerprint' of the nonlinear properties in the interaction region can be obtained. This fingerprint is shown to contain information about the bulk material and the interface status.

To interpret the fingerprints an understanding of the bulk mixing response is first required. This was gained through modelling and experimental testing of solid metal samples. The characteristic pattern of bulk mixing could then be distinguished from that of kissing bonds which were also investigated with models and experimentally. Kissing bonds were created by compressive loading of two aluminium blocks. It was found that the bulk mixing and interface mixing occurred in overlapping regions of the parameter space and thus could not be measured independently in the compressively loaded samples. Isotropic materials are primarily used for this research because improved understanding of the fundamentals of non-collinear mixing were required before results from more complex scenarios could be interpreted in a meaningful way.

The experimental contacting interfaces are tested with varied interfacial loading, and surface roughness. The rougher surfaces result in an increase in scattering amplitude as load is increased, but the polished interface has a more complicated response. Secondary peaks in the parameter space become more pronounced in both cases as loading is increased. Many other changes in the fingerprint patterns are observed suggesting that non-collinear mixing does not evenly sample the area of interaction. In the process of the above investigation a new mixing phenomenon is discovered which occurs at the interface between water and the solid samples. A finite element model is developed that can replicate this mixing behaviour.

# Author's Declaration

I declare that the work in this dissertation was carried out in accordance with the requirements of the University's Regulations and Code of Practice for Research Degree Programmes and that it has not been submitted for any other academic award. Except where indicated by specific reference in the text, the work is the candidate's own work. Work done in collaboration with, or with the assistance of, others, is indicated as such. Any views expressed in the dissertation are those of the author.

Jonathan Alston
Date of submission

# Acknowledgments

I would like to thank: Anthony Croxford for his sustained support for this research. His input into the project was vital to its success. Jack Potter for his help at various stages of the research, particularly for the use of his bulk mixing model. And, Philippe Blanloeuil for his collaboration on the modelling of contacting interface.

I am very grateful for the opportunity that the Bristol Composites Institute (ACCIS) gave me to learn about engineering and to be part of such a diverse research group. Of which, Dmitry Ivanov provided insightful guidance for the work reported here. Thanks must go to the Ultrasonics and NDT group for accepting me as one of their own and providing me with the many pieces of equipment necessary for my research. This work would also not be possible without the funding provided by the Engineering and Physical Sciences Research Council (EPSRC).

And finally, I would like to thank my parents for providing me the possibility to do the many things that ultimately lead to this research.

# List of publications

**Journals:**

Alston, J., Croxford, A., Potter, J., & Blanloeuil, P. (2018). Nonlinear non-collinear ultrasonic detection and characterisation of kissing bonds. NDT & E International.

**Conference proceedings:**

Alston, J., Croxford, A., Potter, J., & Blanloeuil, P. (2017, April). Development of a nonlinear ultrasonic NDE technique for detection of kissing bonds in composites. In Nondestructive Characterization and Monitoring of Advanced Materials, Aerospace, and Civil Infrastructure 2017 (Vol. 10169, p. 101691J). International Society for Optics and Photonics.

# Contents

# List of Figures

# List of Tables

# Chapter 1

# Introduction

Adhesive bonding has numerous advantages over fastener based attachment; in many situations an adhesive solution is lighter because only a small amount of adhesive is required in comparison to the weight of bolts or rivets, it also does not require holes to be made in the structure. The lack of these holes improves the strength of the parts that are being attached by removing areas of stress concentration which in turn allows further weight reductions to be achieved. Carbon fibre reinforced plastic structures particularly benefit from the use of adhesive bonding because they are not ductile like metals so the load is not as evenly distributed between multiple fasteners causing premature failure. Adhesive bonding can be cheaper because it does not require precise drilling of the parts, however great care should be taken to prepare the surfaces for bonding and the process must be well controlled to avoid the production of defects in the bond, this can increase the cost. A major reason why such great care must be taken in adhesive bonding is that poor quality bonds can be hard to detect with conventional NDT methods.

Another effect of the difficulty of inspection of adhesive bond lines is that they are less likely to be used in safety critical areas. This has limited their usage in aerospace, with one solution being the use of 'chicken rivets' to reinforce adhesive bonds, acting as a backup if the bond were to have an undetected weakness. Of course, this is not optimal. The best solution would be to develop methods to detect all possible defects related to adhesive bonding that could reduce the performance of the joint. This would allow designers to take full advantage of the benefits of adhesive bonding without the safety concerns. Therefore, the aim of the work presented in this thesis was to improve the detection of defects that are currently difficult or impossible to detect conventionally in bond lines.

Conventional testing methods can detect some of the defects that occur in the bond lines,

such as disbonds, large voids, and high porosity. Ultrasonic testing tends to be the most cost effective way of finding these faults but X-ray based methods are also sometimes used. Both of these methods usually require the defect to be volumetric in nature, with the volume having a contrasting response to the mechanical or electromagnetic waves from that of the surrounding adhesive. The difficulties in detection occur when the defect becomes vanishingly thin, such as in the case of the adhesive not bonding properly perhaps because of a surface contaminant. These 'zero-volume' defects are often referred to as kissing bonds.

It is worth noting at this point that kissing bonds do not only occur in adhesive bond lines, similar defects can be found in welds, and similar defects seen in solid materials, such as so called 'breathing cracks'. It is probable that a method for detection of one of these cases could be suitable for the others so would have widespread usage with both composites and metals. In the future it is likely that thermoplastic based composites will become more popular. They have the possibility to be welded together, so this research will presumably be relevant to structures based on this technology as well.

The various types of kissing bonds and potential ways to detect them are discussed in Chapter 2. It was found that the use of nonlinear ultrasonics offers a promising route to detection due to the way the nonlinear stiffness of them distorts the waves, creating harmonics. The nonlinear technique used in this work is non-collinear mixing. Compared with other nonlinear methods it has many benefits such as spatial sensitivity and effective removal of inspection system nonlinearities. The method was pioneered in the 1960s by Jones, Kobett, Taylor, and Rollins (18; 13). They developed an understanding of the mixing in nonlinear solids with nonlinear elasticity.

Chapter 5 builds upon their work by investigating this mixing over a wide range of input conditions for solid samples. This forms the baseline measurement of a sample with no kissing bond to which later tests are compared. Testing was conducted experimentally and also theoretically using a model developed by Jack Potter of the UNDT research group at Bristol University.

During the bulk material testing unexpected behaviour was observed when taking readings near the surface of the samples. Chapter 6 documents the exploration into this surface mixing. This research was important because many structures, particularly CFRP ones, are thin so it is likely that bond lines will be near the surface of the material. Finite element modelling was conducted to assist with the analysis of this mixing behaviour.

With a better understanding of the solid material mixing gained the research progressed onto kissing interfaces, Chapter 7. Two key interface features were tested, compressive

loading level, and surface roughness. This testing was also conducted over a wide range of input beam conditions, unlike the work of previous researchers in the field. Philippe Blanloeuil from the University of New South Wales Sydney, Australia, collaborated with us for this work by providing modelling results for comparison.

In Chapter 8 theory briefly discussed in the previous chapters is developed further for the case of mixing at an interface. A variety of predictions are made, to be tested in future work. The following chapter looks at the implications of the findings of the work as a whole in regards to composite bond line inspection. It highlights the difficulties associated with non-collinear measurements in composites and potential solutions. Finally, in Chapter 10 the thesis is concluded; key findings are detailed and future work is summarised.

# Chapter 2

# Literature review

## 2.1 Kissing bonds

The aim of this research, despite the title, is not to detect kissing bonds, for they are poorly defined and easily detectable by conventional means in some cases. Really, the goal is to improve the detection of defects in bond lines that are currently difficult to spot. It happens that the term kissing bond is often used to describe such bond defects, but the precise meaning of the term varies. In order to clarify this situation so that meaningful improvements in NDT can be made the usage of the term 'kissing bond' must first be understood. From that a more accurate definition of what defects are intended to be detected can be devised. Following that the common causes of kissing bonds will be discussed and how they might relate to the detectability of the defects. Next, a range of NDT methods are introduced and then further research into the promising avenues of investigation is presented, ending in detailed discussion of the non-collinear ultrasonic method.

### 2.1.1 Definitions

- One of the most popular definitions of a kissing bond is a 'zero-volume disbond', as used by Brotherhood, Solodov, Sui, et al. (2; 19; 20). The zero-volume concept is shared by the many other definitions that require that there be no voids between the surfaces of a kissing bond.
- 'Intimate contact with little or no bonding strength', as used by Nagy, Brotherhood, and Yan et al. for example (21; 2; 22), could be interpreted as being very similar in meaning, although there is some ambiguity in the word intimate that allows for small voids at the microscopic scale.
- 'Solid-solid contact' extends the idea of two unbonded surfaces to a case where there could be air/voids between the two surfaces (2). The term seems to be used to differentiate defects from the following definition.
- 'Liquid layer kissing bond'. Some definitions allow for the presence of a liquid in the interface, (2; 23).
- In other cases, such as Jiao et al.'s work, the mechanical behaviour of the interface is stated as the defining feature such an interface with 'no transmission of shear stress' (24; 25).
- The last definition of a kissing bond is one where there are many unbonded spots between the two surfaces but these are much smaller than the wavelength they

are being interrogated by so appear as a bond of reduced strength. This is the definition of a partial bond given by Nagy in (25), but in some ways all of the above types of kissing bond could occur on such small length scales such as to appear this way.

Nagy's work from 1992 (25) is likely the most comprehensive and rigorous analysis of the various different interface types, particularly in relation to ultrasonic inspection. This work suggests how one might determine the type from some simple linear tests, although he concludes that "...very tight kissing bonds are very difficult to detect, let alone classify, from conventional reflection measurements used in ultrasonic NDE". This paper makes it clear why some types of interface can be detected with linear ultrasonic methods but others cannot.

The usage of the term kissing bond appears to have fallen out of fashion recently, perhaps due to its ambiguity, with most relevant recent research instead referring to the defects in other ways such as 'imperfect interfaces' (14), or 'closed cracks' (6; 26), although both of these are also quite vague. It seems each research group has their own preferred way of referring to this kind of defect. The situation gets further clouded in modelling work when approximations to these interfaces become removed from reality such that idea of the practical differences in defect type (e.g. presence of voids or fluids) are no longer applicable, such as in Zhang et al.'s work where the interface is replaced by a system of nonlinear springs, (14).

### 2.1.2 Defect types

The above discussion of kissing bond types tends to be related to theoretical ideals. While understanding these can inform the fundamentals of an NDT method it is also important to know how real world defects relate to these ideals. After all, the range of definitions for kissing bonds is probably related to the fact that there are a range of defect types. In the case of an adhesively bonded interface some commonly used terms for defects are (1; 27; 28);

- Porosity; small bubbles of air occurring in regions or throughout a bond line, called voids when larger or more isolated in occurrence. These would generally not be considered a kissing bond but could perhaps meet the 'intimate contact with little or no bonding strength' definition.
- Poor adhesion; when the interface between the adhesive and adherend has reduced

strength. This defect type matches with many of the kissing bond definitions, depending upon the level of reduction of strength.

- Cracks (in the adhesive); they could meet some of the kissing bond definitions, the key factor in many cases is if the crack is open or closed.
- Disbonds; generally refers to case where more extensive voids are present. The presence of a void greatly increases the detectability of these defects and the lack of contact of the two surfaces generally excludes them from being kissing bonds.
- Unbonded regions (no voids); the extreme case of poor adhesion, they meet most definitions of kissing bonds.
- Foreign object (solid or liquid); these are highly dependent on the size and composition of the object. An object with similar properties to the adhesive (relating to those probed by the NDT method of choice) and one that forms strong bonds with the adhesive might meet very few of the definitions; creating no weakness, behaving very similarly to a good bond, and creating no voids. The opposite could also be true.

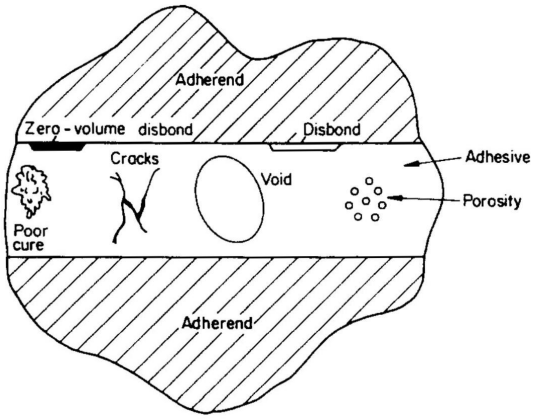


**Figure 2.1:** An example of possible adhesive defects from Adams and Cawley's work (1)

Despite kissing bonds in adhesives being the focus it is worth considering other ways that similar defects could be created in other bonding cases, such as friction welding in metals or thermoplastics (29). Some of these will be discussed in the section below about methods of experimentally simulating kissing bonds.

These defects can be catagorised into two types; volumetric and zero-volume. Porosity, voids, and open cracks are the former, and poor adhesion, closed cracks, and unbonded regions the latter. Foreign objects could be of either type depending upon the the exact nature of the object and how it interacts with the inspection method. For the rest of this work the term kissing bond will be used to refer to the zero-volume type defects.

### 2.1.3 Defect causes

The mechanisms behind the formation of the defects mentioned above may also be useful to the understanding of defect properties so some commonly occurring ones are discussed here.

Porosity may be due to bubbles being mixed into the adhesive or from volatiles released from the adhesive during curing, such as water vapour or air. Regions of high porosity may cause a coalescence of bubbles forming a void. Generally porosity is not referred to in regards to kissing bonds except for when it occurs with a high void ratio at the adhesive-adherend interface. In this case it can greatly reduce the bonding strength and lead to the creation of a disbond. As mentioned above the disbond should be detectable with conventional means but perhaps the earlier state with small voids at the adhesive-adherend interface might not be. Detection of this would therefore be a useful improvement in the early detection of potential failure.

Unbonded regions (no voids) can be created in many ways such as by loose oxide layers on the surface of metals, or from a skin forming on a resin before it is used (1). Foreign objects are most likely to cause a problem when they prohibit bonding, as such most items that bond with the adhesive are not an issue if they are small enough. Common items that do not bond are release agents/films, oils, unmixed resins, water (1).

The differences between these types of defect means that different detection methods may be more appropriate to one type than another and thus if commenting on the detectability of a defect the specific type of kissing bond should be mentioned.

## 2.2 Ways to simulate a kissing bond

In order to experimentally test an NDT method a controllable way of creating kissing bonds is required. A simple way to prevent the bonding is to introduce a contaminant such as grease into an adhesive interface, similar to how it could occur industrially. This creates a liquid layer kissing bond which should be detectable with conventional NDT methods due to the contrasting properties of the contaminant with the surroundings and its non-negligible thickness. This method has been used by many researchers but is probably not the best way of simulating difficult to detect kissing bonds (27; 23). In some ways the liquid layer kissing defects are also more complex than dry interfaces due to the fluid flow within them. This can make it more difficult to create models to compare against experimental results.

A thinner area of reduced bonding can be achieved by the use of release agent, coating the surface of the adherend in a thin film that prevents bonding with the adhesive (27; 21). Another benefit of this method is the ability to alter the concentration of the release agent to tune interface properties. The trial and error approach involved with this can take significant time to get right and often requires mechanical testing to failure of the parts in order to validate the reduction of bonding strength. This method also has good similarity with possible real world production defects.

PTFE inserts have been used by many to prevent adhesive bonding (30; 23; 31; 7). Generally they have significant thickness compared with the release agent method and quite different properties from host materials so can often be easily detected with conventional means.

Products such as ElectRelease allow a good adhesive bond to be formed that can then be later weakened by the application of electricity (32). They only require a small voltage and about half an hour, so it is fairly quick and safe when bonding between two metal components. It is more difficult to do with less conductive adherends though. The use of them is discussed in detail in Yan's doctoral thesis (33).

All the above adhesive interface methods result in a kissing bond surrounded by a three layer system; adherend-adhesive-adherend. In some cases this structure can cause interference with the inspection method, particularly ultrasonic methods operating in the megahertz due to the similar size of the wavelengths and bond thicknesses (33). Easier to interpret results may be achieved by the use of these techniques on systems without adhesives, as discussed below.

Diffusion welding is the process of bonding metals together by the application of pressure. Over time the atoms at the interface can rearrange to form continuous metallic structures if done correctly. This technique can produce a wide range of bonding qualities but it requires specialist equipment to do and is difficult to make repeatable defects (34; 35).

Friction welding is another process that allows for continuous metal bonding to be formed by the frictional melting of material at the interface (29). Again this method is limited by the machinery required to execute.

A much lower cost method is the compressive loading of two flat surfaces. The smoother these surfaces are the closer contact they will make for a given load. In some cases a universal testing machine is used to apply the load (15), and in others bolts are used to apply the force (36; 30; 22). In the bolted approach the torque on the bolts can be adjusted to alter the contact pressure however the accuracy of this is much lower than

that of a universal testing machine. The latter method can be restrictive in terms of access to the sample for inspection and the requirement for the testing to be performed around the loading machine. Bolts are less obstructive. The ability to control the level of interfacial contact is a great strength of this method as it allows the potential for different kissing bond regimes to be explored.

## 2.3 NDT techniques overview

The kissing bonds of interest in this work are those occurring in adhesively bonded interfaces. Therefore it is likely that the defect will be hidden below some depth of material on either side. It might be that some surface based NDT techniques could detect the defect if the structure is thin enough but it would be preferable to find a method that could work over a wider range of depths. Because of this preference there will not be much discussion of surface NDT methods here. Such surface methods include the use of eddy currents, magnetic penetrants, and guided ultrasonic waves (1; 37).

There are three main classes of NDT that could be applied to the detection of deep kissing bonds; acoustic, X-ray, and thermal. Acoustics, or more specifically ultrasonics, is probably the most widely used NDT method after visual inspection so the discussion of detectability of kissing bonds will begin there. Within the vibrational techniques there are a wide variety of options including conventional ultrasonics, and mechanical resonance methods. Often beams of ultrasound are used with many aspects of the propagation monitored such as reflection, attenuation, and time of flight to infer the state of a sample.

Conventional ultrasound is sensitive to changes in acoustic impedance (38). In the case of kissing bonds the lack of voids means that there is very little contrast between the impedance of a good bond and kissing bond. If the kissing bond is of the type that does not transmit shear stresses then this is a clear route to detection, but in the case of an interface with compressively loaded intimate faces the shear stresses can be transmitted in a similar way to a good bond. Another acoustic route to detection is the change in resonant behaviour of the structure; the reduced stiffness of a kissing bond could result in a change in resonance.

As well as the linear acoustic methods discussed above there are various nonlinear routes to detection available. Two common types of this are the exploitation of the sensitivity to input wave amplitude of a system with nonlinearities present (39; 40) or the mixing of multiple input frequencies that are possible by modulation at the kissing interface

(13; 41). There are a wide variety of techniques based on these principles that show great promise for kissing bond detection.

Thermal methods also have the possibility to detect kissing bonds due to the reduced flow of heat over an imperfect interface. Tighe et al. investigated the detectability of a PTFE insert or grease contaminant in CFRP bond lines using infrared thermography (23). The method is more advanced than simply detecting the flow of heat from one side of the sample to another, they used a pulsed heat source and analyse the phase of the detected heat relative to the applied. With this method they showed that the PTFE was detectable but the silicone grease was not. For reference they tested the adhesive joints with a 25 MHz ultrasonic c-scan, both defects could be detected by this method. It appears that currently thermographic methods are not as sensitive as conventional ultrasonic techniques and are limited to cases where the defect is near the surface.

X-ray has proven itself as a powerful inspection technique. However, Adams et al. say that even delaminations (which should be easier to detect than a kissing bond with intimate contact) are difficult to detect due to the defect often occurring normal to the inspection direction (1). The issue is that x-rays require a volume of material with different electromagnetic permeability in order to cause a change in the absorption/diffraction but tightly closed interfaces could potentially have very low void volume. This limitation demonstrates the strength of acoustics; the ability to probe the bonding between the interfaces even if the interface has no thickness. Also the adherends generally absorb a lot of the X-rays so the overall absorption is changed very little by a disbond/delamination.

Radiographic methods in general suffer from similar limitations to the visible, x-ray, and infrared methods discussed above: either too high or low penetration, meaning they do not interact or can barely get below the surface of samples, are a danger to humans, involve expensive equipment, and are not sensitive to zero-volume defects.

As can been seen from the above discussion, acoustics probably offers the most promising route for improving the detection of kissing interfaces at adhesive bond lines. It has the ability to probe the bonds themselves, not relying upon contrasting volumes, is generally safe to use around people, and can be cost effective. Therefore further investigation into different acoustic methods is presented below.

## 2.4 Linear acoustic methods

In this section many types of linear ultrasonic methods will be analysed in regards to their ability to detect different types of kissing bonds, commenting on the fundamental reasons why some inspection strategies are more likely to have improved sensitivity to certain defects. This analysis can be somewhat difficult for the experimental testing because most publications focus on what they were able to detect, and in cases where the method could not detect anything it is often unknown if kissing bonds were present.

Probably the most conceptually simple way to improve the detectability of kissing bonds is to increase the frequency of the probing wave. This allows smaller and smaller defects to be found. Vine et al. tested a 50 MHz focused transducer at normal incidence in their work (42), detecting corrosion-driven edge-disbonds between epoxy adhesive and aluminium adherends as well as micro defects in the adhesive. In work by Nagy the relationship between frequency and reflection coefficient of a kissing bond is clearly apparent in the experimental data (21). Nearly all types of kissing bonds in the real world will have regions of reduced transmission on some length scale (atomic bond lengths being the smallest) so if the wavelength can be reduced down to this then detection should be possible. Of course other factors can become prohibitive before this achieved; perhaps the material is too attenuative at high frequencies, or sampling at that frequency is too difficult/expensive.

The other benefit of higher frequencies is that they allow focusing of the beam to smaller spots according to diffraction limitations. This increases resolution which helps improve detection of small defects. It can also result in increased wave amplitudes, which can enable the wave to open the interface and results in enhanced reflection. This is a nonlinear mechanism and will be discussed later, the concept is noted here due to the possible impact it can have on conventional, ostensibly linear methods. The defects investigated in Vine et al.'s work (42) likely had larger volumes than could be expected in some other defect cases (e.g. release agent contamination), and included the ingress of water. It would be expected that the water would reduce the acoustic contrast of the interface because it has an impedance more similar to that of adhesive and adherend than air. However, it is also possible that it aided detection by working into the cracks that otherwise might have relaxed back to a closed state with good contact. These defects represent the limit of the longitudinal ultrasonic wave method. At 50 MHz the wavelength is around 0.1 mm in aluminium, much larger than the length scales at which defects might occur.

As was briefly discussed in the kissing bond definition section, one route to the detection

of some types of kissing bonds is the use of shear waves, or longitudinal waves at oblique angles to the interface (24; 25; 43). To some extent this concept is flawed by the fact that this definition of a kissing bond assumes a low coefficient of friction between the surfaces and is an idealisation, intended mainly for modelling purposes (24; 2). In reality it is likely that if stresses normal to the interface are transferred effectively then the level of contact between the two surfaces is so good that the interlocking asperities of the surface will transfer stresses quite effectively as well. Despite this experimental results show that some improvement can be achieved by applying these shear stresses to the interface and noting the difference in reflection/transmission compared to normal stress waves.

One drawback of this method was the difficulty in producing shear waves that propagate normal to the interface at high enough amplitude. An alternative is to use wedges to generate these waves via mode conversion but since they produce shear waves at an angle another transducer was required to be carefully positioned to detect the reflection from the interface. Brotherhood et al. solved this issue in their 2003 work by the use of an electromagnetic acoustic transducer (EMAT) (2), their experimental arrangement is shown in Figure 2.2. EMATs also have the benefit that they are non-contact, allowing for more consistent coupling with the sample, particularly when compared with piezoelectric shear transducers. EMATs are not suitable for use in CFRP however requiring induction in the material to function so might be useful for testing purposes but are not as generally applicable, or as powerful as other ultrasonic transducers.

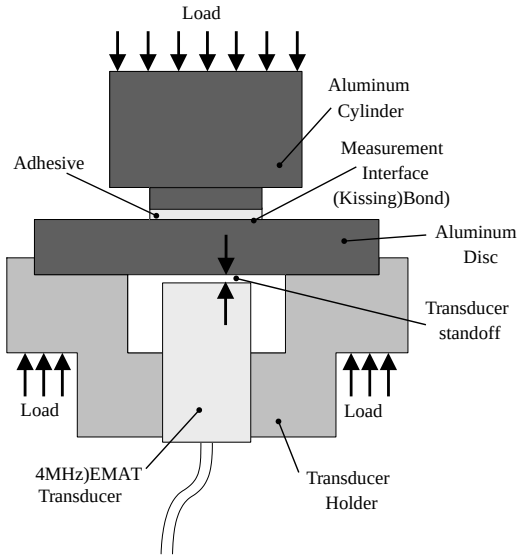


**Figure 2.2:** Brotherhood et al.'s EMAT shear wave experimental set-up. (2)

With all of these linear ultrasonic beam based methods there is the issue that the signal of interest being reflected from the defect is contending with other significant sources

at the same frequency resulting in a poor signal to noise ratio. For example, in some materials scattering occurs in the bulk material due to grain boundaries, and in the case of an adhesive interface the change in impedance between the adherend and adhesive causes reflection. This results in techniques with poor sensitivity to kissing bonds that do not have substantial voids or contaminants present. Nonlinear methods offer the ability for energy to move away from the noisy fundamental frequency to another when a defect is present, this concept is used in nearly all of the nonlinear methods described in the following section.

Before the discussion of nonlinear methods linear resonance techniques should be mentioned. They involve the stimulation of a sample with a range of frequencies, and a measurement of the resulting amplitude of oscillation from each of those frequencies. A structure will naturally have resonant modes at various frequencies and these modes can be altered by the presence of a bond of reduced stiffness (44; 45). In practice this technique can be difficult to apply in a robust way; for a change in resonance to be detected the defect must be located in a position and orientation that is sampled by the stresses of the existing resonant modes. Cracks in certain locations within the structure may be undetectable for this reason. The methods lack spatial sensitivity, but this can be a positive in some situations since it allows for checking of a large sample for any defects quickly. It also appears from the literature that the method is best suited to major cracks in a structure (46), with most of the recent work using nonlinear variants to improve the sensitivity to more subtle defects. These will be discussed below.

## 2.5 Nonlinear acoustic methods

Linear methods had some sensitivity to defects that could be classified as kissing bonds, but in general lacked sensitivity to zero-volume defects. As discussed above this is largely due to the fact that adhesive interfaces already interact with the acoustic waves and the differences due to a kissing bond can be small in comparison. In this section the fundamental mechanisms related to the nonlinearity of kissing interfaces are explored. Following that, the methods that utilise the mechanisms are detailed, including both single frequency and dual frequency techniques.

### 2.5.1 Contact acoustic nonlinearity

There are two main mechanisms involved in CAN; the opening and closing of the interface modulating the transmission and reflection coefficients, and the impact of the

faces when they collide (2; 47). In Brotherhood et al.'s work they refer to the latter specifically as clapping but the distinction does not appear to be universal. Both of the cases result in the transfer of energy from the input frequency but the specifics of which frequencies they are transferred to vary. The sudden impulse of clapping generates a broad frequency spectrum, exciting the natural modes of the structure. As such, these modes are not necessarily sub or superharmonics. This means that there is uncertainty in the frequencies that will be produced, this can make detection of them more difficult. On the other hand the frequencies that will be generated by the changing of interface transmission can be understood by looking at how the transmitted wave will be perturbed. The work by Van Den Abeele et al. includes useful plots of how a few different types of nonlinearity affect the waveform and the resulting spectral content (3), Figure 2.3. Broda et al. include further examples of particular relevance to kissing bonds in their 2014 review as a well as a vast amount of information relating to the nonlinear methods discussed in this section (48).

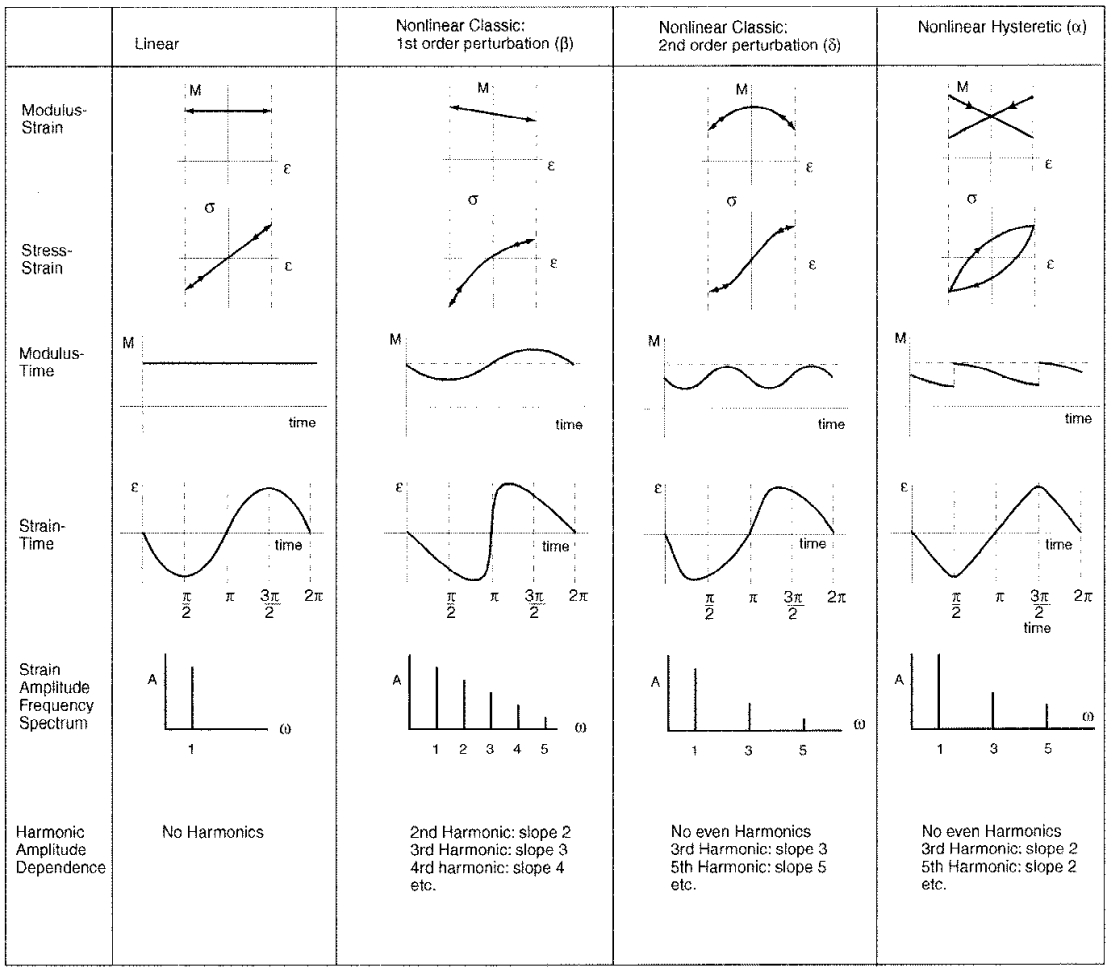


**Figure 2.3:** Overview of different types of wave perturbations and their impact on frequency components of the modified wave. From Van Den Abeele et al.'s work in 2000, (3).

If the surfaces of a kissing bond are perfectly flat and it is assumed that the interface is under a constant static compressive load then the stresses that can be transferred across the interface are as shown in Blanloeuil et al.'s work (4), Figure 2.4. It shows how normal and tangential displacements of the interface, $u_n$ and $u_t$, result in different stresses depending upon interface pre-stress. These relationships can then be used to understand the possible interface states. It is simple to understand the states for the stress component normal to the interface; if the wave is applying less stress than the pre-stress then the interface is closed and transmissive to normal stresses, otherwise it is open and reflective. For the shear component it is more complicated because the shear stress that can be transferred across the interface is dependent upon the coefficient of friction, the pre-stress, and the normal stress applied at that moment in time by the wave.

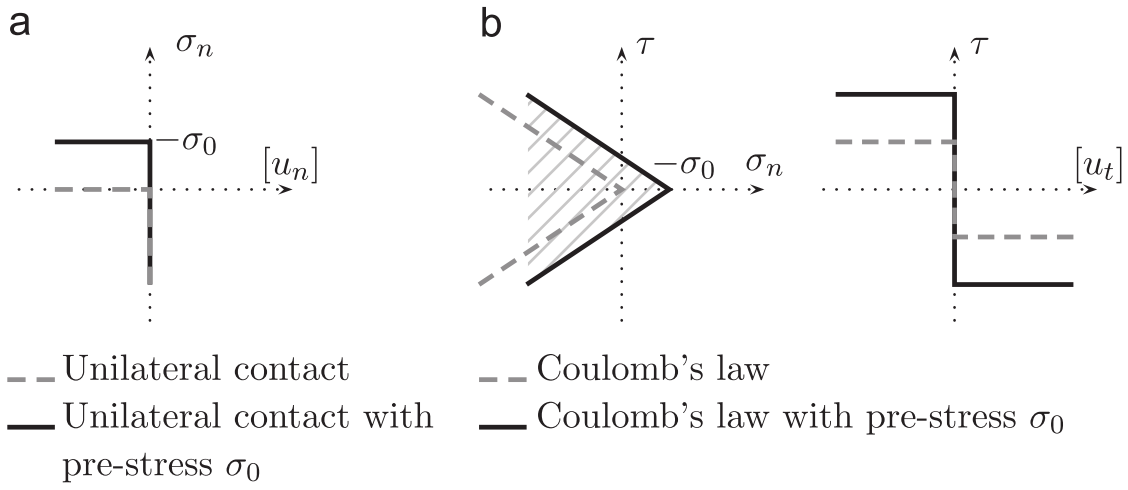


**Figure 2.4:** Representation of the contact laws with the pre-stress, $\sigma_0$. a) Unilateral contact, applicable to the normal stress components, b) Coulomb's law, related to the transverse stresses. (4)

The states discussed above result in the normal component of the wave experiencing clipping on the tensile side of the wave if the interface opens, and the shear component being clipped on both peaks and troughs if sliding occurs. These transitions between states are a different type of nonlinearity from that seen in Figure 2.3, however in practice behaviour similar to the 1st order perturbation case is likely to be observed for the normal stresses and the 2nd order perturbation for the tangential component. This is because the surface asperities of a real world interface are much smaller than the ultrasonic wavelengths that are likely to be used, creating a range of pre-stresses and thus smoothing out the abrupt transitions between states. It should be noted that although most of the discussion focuses on the wave that is transmitted through the interface the reflected wave will experience enhanced stresses when the interface opens or slides creating similar harmonics.

There appears to be one further variant of CAN, notable for its ability to produce subharmonics, a hysteretic interface. It is not as widely reported in the literature. One example is the work by Moussatov et al. which discusses the possibility that hysteresis is the cause of the behaviour they observe in a cracked sample, (49). It is unclear which types of defect would be expected to produce an interface with significant hysteretic behaviour but it seems to be largely ignored in most work relating to kissing bonds.

### 2.5.2 Single frequency methods

As has been discussed above, contacting interfaces can change the spectral content of waves that propagate through or reflect off them. Therefore by looking at the output frequencies when a single frequency input wave is used it is possible to infer the nonlinear properties of the medium (or media) that the wave passed through (50). The fact that the output is sensitive to nonlinear elasticity at all parts of the propagation results in unknowns in the location of this nonlinearity however. This would not be as much of a problem if there were not so many potential sources of nonlinearity in experimental systems; the signal generator, amplifier, transducer, coupling medium, and the bulk of the sample are all common examples (51; 52; 53). The methods described below are often limited by these factors and require great care to be taken to minimise them.

A parameter that is commonly measured in this type of technique is the beta parameter

$$\beta \propto \frac{A_2}{A_1^2} \tag{2.1}$$

where $A_1$ and $A_2$ are the amplitudes of the fundamental and second harmonic respectively. By factoring in the square of the input amplitude it is expected that a constant $\beta$ would be measured for a particular (quadratic) nonlinearity, independent of input amplitude (54; 55; 22). This quadratic approximation has been shown to be true experimentally for contacting interfaces in Biwa et al.'s later work (56).

In recent years Blanloeuil et al. have improved the understanding of single beams propagating through kissing interfaces by their comprehensive finite element (FE) work. In (5) the interaction between a crack and elastic waves at an oblique angle of incidence is simulated. A 2D FE model is used to investigate the interaction between elastic waves and cracks of different orientations. Very similar definitions of the crack appear to be used throughout all of Blanloeuil's work, the main difference is that some are of finite length and referred to as 'closed cracks' and others are effectively infinitely long cracks

and called 'contacting interfaces'. Common to both is the use of contact laws which define what state the interface is in. These states were described previously in the section above. A static pre-stress is applied to the interface before the waves are propagated across it in order to close the interface, creating a kissing bond by most definitions. The paper explores the effect of crack pre-loading and angle incidence for both longitudinal and in-plane polarised shear (SV) input waves in terms of the various harmonics that are produced, see Figure 2.5. It also looks at the directivity of the outputs.

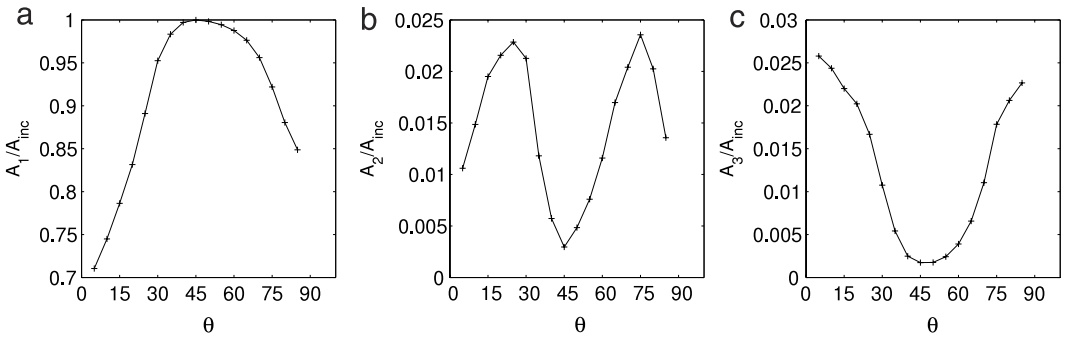


**Figure 2.5:** The first (a), second (b), and third (c) harmonics as a function of the angle of incidence, $\theta$, for a finite length crack. A shear wave polarised perpendicular to the interface was used as the input and was lower in stress than the applied pre-stress, never fully opening the interface. The amplitudes of the harmonics are normalised by the input wave amplitude. Work by Blanloeuil et al. (5).

In this work a key point about the direction of stresses induced in the interface by the input wave is made and clearly explained. It shows that the normal forces on the interface are maximal for a SV wave when it propagates at 45° to the interface. Therefore, if the interface is pre-stressed such that the input wave amplitude is only strong enough to cause sliding, not opening, then at 45° there will be no nonlinear effects because the wave exerts no shearing forces at this angle. This paper is generally very useful for visualising the nonlinear behaviour of single waves interacting with nonlinear interfaces, with a lot of this information transferable to the non-collinear cases that will be discussed later. There are further useful visualisations and concepts presented in some related works also involving Blanloeuil (57; 5).

In order to acquire better spatial information tomographical methods have been used for imaging biological tissues (58). They reported improved contrast between two types of tissue compared with linear measurements but found that attenuation of the second harmonic limited the sensitivity of the method. In engineering there is often limited access to the region of interest which restricts the ability to use tomographic methods, instead array imaging (also widely used in the medical world (59; 60)) appears to be more suitable. Blanloeuil et al. have extended their work to this imaging case (6).

They found that when using longitudinal waves the image formed from scattering at the fundamental frequency accurately indicated the crack length at all interface pre-stress levels that were investigated. The amplitude of the signal decreased as the load was increased. Meanwhile, the second harmonic appeared to be produced at the crack tips and centre with improving contrast as load was increased, see Figure 2.6. Even though this model did not produce a kissing bond that was invisible at the fundamental frequency it showed that increasing load on the interface had a trend of reduced conventional detectability while the second harmonic improved with load.

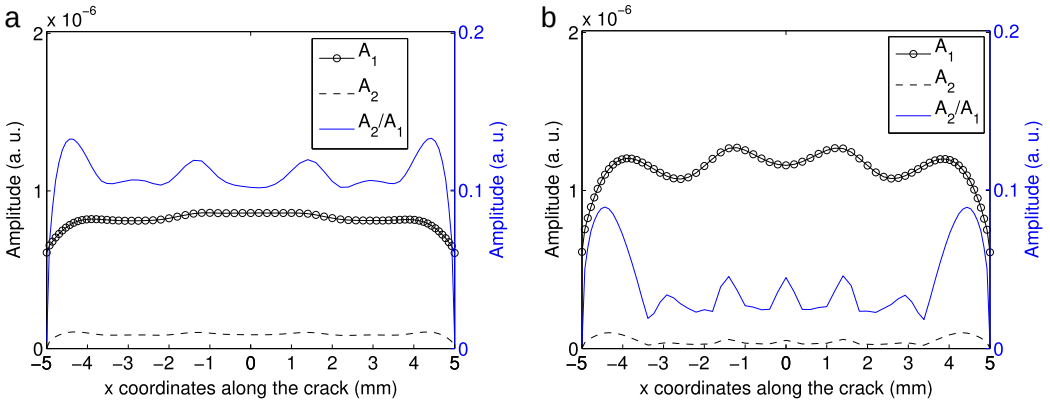


**Figure 2.6:** Evolution of the first and second harmonic as well as their ratio along the crack for a normal incidence and for a pre-stress of; a) $\sigma_0 = -0.3$ MPa and b) $\sigma_0 = 0$. Blanloeuil et al. (6).

Experimentally nonlinear array methods have been developed by Potter et al. (39; 61) and Haupert et al. (40). Both compared the second harmonic response of the sample at different input amplitudes and saw that features such as crack tips produced substantially increased signal at higher amplitudes. Potter et al.'s work differs from conventional array imaging in that it is the amplitude of the diffused field that is observed. It appeared to produce a greater contrast between linear features such as the back wall and side drilled holes, and the nonlinear fatigue crack than was observed in Haupert et al.'s study. This method is very promising but it relies upon high quality array controllers to supply consistent power levels to the array's elements independent of the number of elements that are being transmitted on. This can result in the requirement of expensive and bulky equipment.

The methods discussed above have all been beam based methods but there are also nonlinear spectroscopic techniques available. These techniques tend to be less applicable to goals of this research as they generally do not offer good spatial information.

An example of these methods is the use of nonlinear resonant ultrasound spectroscopy

(NRUS) by Johnson et al. in the late 90s for the detection of cracks and damage in plexiglass and sandstone samples (62; 63). The sample is excited with a range of frequencies (at different times) and various features of the spectral response can indicate damage. The appearance of new resonant modes when compared with a known good sample is one indicator, this of course requires a reference measurement to function so is not ideal. Another is the change in the resonances as the amplitude of oscillations is increased, nonlinear features like kissing bonds change their behaviour as amplitude is increased thus altering the resonant frequency. This method has been applied to composites by Meo et al. (64). As well as the lack of positional information there are difficulties relating to ensuring all areas of the sample are probed by this method and the lack of sensitivity to cracks oriented in ways that are not stressed by the applied waves.

Some of the above methods have show good potential for the detection of kissing bonds but all are sensitive to other nonlinearities in the testing system which can be a problem. The section below discusses a way to improve the rejection of signals from these unwanted sources.

### 2.5.3 Dual frequency methods

Dual frequency techniques offer a way to avoid the unwanted signals produced at the harmonics of the input signal due to the many other possible nonlinearities in the measurement system and thus can result in improved signal to noise ratios. By inputting two different frequencies it is possible for the waves to modulate each other if they both pass through a nonlinear medium at the same time. This can produce waves at the sum and difference frequencies of the input waves, which if intelligently selected will be different from the harmonics of the individual input waves, Figure 2.7. In the case of an interface that exhibits CAN this can provide the required nonlinearity for interaction of the two waves. This occurs because each wave modifies the state of the interface experienced by the other.

Following on from the end of the previous section is the development of spectroscopic methods involving the interaction of two different input frequencies, referred to as nonlinear wave modulation spectroscopy (NWMS). If the sample behaves in a linear manner then it will only oscillate at the input frequencies, but if nonlinearities are present then mixing may occur. It has been used by many people including Van Den Abeele et al., Sutin and Johnson, and Zumpano et al. (3; 65; 66). NWMS suffers from many of the same limitations as other spectroscopic methods; primarily a lack of spatial sensitivity

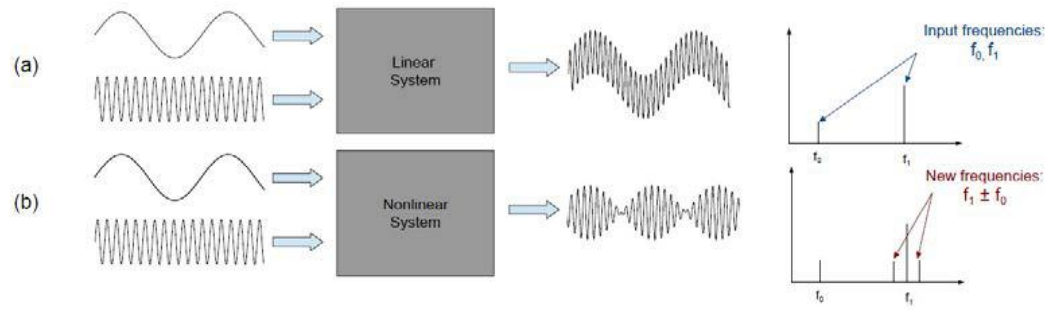


**Figure 2.7:** Comparison of output frequencies produced by a linear system, a), and a nonlinear system, b), in the dual input frequency case. Dunn et al. (7).

and is best used when a measurement can be taken of the sample before damage. These properties make it ideal for structural health monitoring and allow very fast testing of large structures.

The recent work by Dunn et al. uses this method in the detection of delamination in composite beams (7). For this work the low frequency wave, called a pumping wave, was tested over the range of 40 to 70 Hz, and the high frequency, probing, wave was kept at 380 kHz. Both were continuous sine waves. They found that the technique had a very high sensitivity to delamination when correct pumping frequencies were used; a pump frequency that causes minimal nonlinear behaviour in the system is ideal. Therefore it should be selected to not be a resonant frequency, as nonlinearities are largest there.

Mezil et al. use the wave modulation concept with lasers as the source of the vibrations to detect the properties of a crack (67). They note that the static heating caused by the lasers could cause complete local closure of the crack. This concept was explored by Ohara et al. although they use a more conventional phased array method to image the crack in open and closed states (26).

Mentioned earlier was the work of Gong et al. on tomographic methods of inspection (58). In some of their work they used co-propagating collinear input beams and detected at the difference frequency after transmission through the sample, achieving better results than the second harmonic detection method. This is partly due to the fact that the difference frequency is lower than the second harmonic so suffers less from attenuation. Consideration of this may be critical for composite structures that are generally highly attenuative. The paper by Cai et al. is another earlier example of this method (68). Just like NWMS this method is limited in the same way as its single frequency predecessor, requiring access to many observation angles to achieve good results.

The 2017 work of Blanloeuil et al. deals with the improvement in speed of numerical modelling of wave modulation by a close crack (69). They achieve this by instead

of modelling both the lower frequency and higher frequency input waves at once they instead simplify the lower frequency pump wave into an oscillating term in the closed crack state and then propagate the higher frequency wave through the system. The method is demonstrated for both a 1D finite difference model, then a 2D FE model. This work brings up the concept of using linear FE modelling to find the stresses that an interface would experience and then applying that information in an analytical way (modifying the contact conditions) potentially allowing for the simplification of wave modulated CAN modelling.

In contrast to the NWMS which uses lower frequencies that oscillate large parts of the sample is the non-collinear mixing method. It uses higher frequency beams (generally in the megahertz range) of ultrasound that can be directed to overlap at a specific location within a sample. In this case the creation of mixed frequencies is only caused by the nonlinear properties in the overlap region. This method has great potential due to its spatial sensitivity combined with the high sensitivity to nonlinearity of the two frequency methods. It will be discussed in detail in the section below.

## 2.6 Non-collinear mixing

Non-collinear mixing solves the spatial sensitivity and unwanted system nonlinearity problems of the previously discussed nonlinear methods. One limiting factor of it when trying to detect signals coming from nonlinear interfaces is likely to be the mixing of waves in the interaction volume due to the bulk material itself. There is a lot to understand about the bulk mixing behaviour, in some ways it is more complex than the mixing generated at interfaces due to the resonance criteria that will be described below. An example of one of the early non-collinear bulk mixing experiments is shown in Figure 2.8.

### 2.6.1 Bulk mixing

The seminal work in this field is that of Jones and Kobett, published in 1963 (18). It describes how the inclusion of cubic particle displacement terms in the elastic energy of an isotropic solid result in the possibility of mixing occurring due to the modified equations of motion. In it they state the scattered wave can either have a frequency that is the sum or difference of the two input waves and that it will travel in a direction determined by the sum or difference, respectively, of the input wave vectors, $k_1$ and $k_2$. The wave equations used mean that the results are only accurate for plane waves

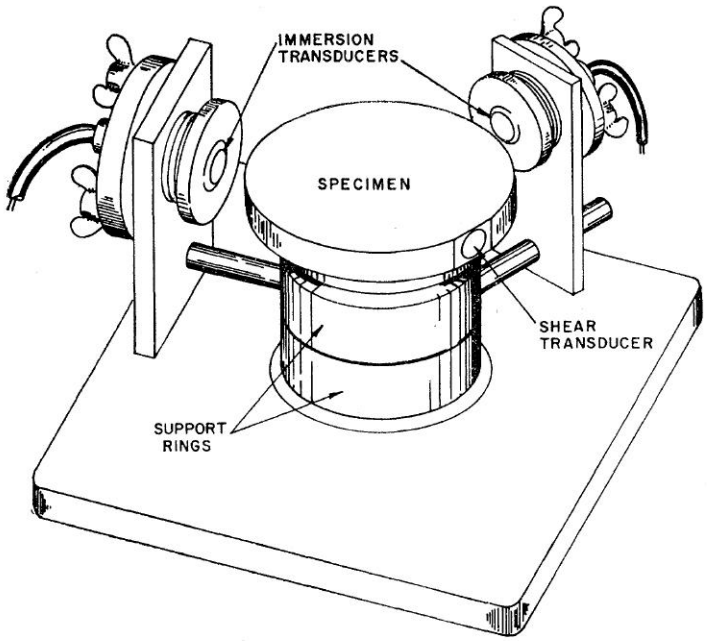


**Figure 2.8:** Experimental set-up for the testing of non-collinear mixing of shear and longitudinal waves, producing a longitudinal wave. Rollins et al. (8)

of uniform intensity. They show that in the direction of scattering the integration of all points within the interaction volume is constructive and thus the scattered amplitude is directly proportional to the volume. This statement only applies when the input waves are at the correct angle and frequency ratio as defined by the energy and momentum conservation rules, a state referred to as a resonant condition.

Jones and Kobett define the frequency ratio of the two input waves as $a = \omega_2/\omega_1$ and speed ratio as $c = C_t/C_l$. They presented five primary mixing modes; the combination of various transverse and longitudinal input waves forming transverse and longitudinal outputs, see Table 2.1. The polarisation of these waves is not mentioned in the main table of interaction cases but is discussed at various points in the paper, stating its impact on scattered wave amplitude. Also given in the table are the ranges of frequency ratio for which the resonant conditions can be satisfied. The specific case of two shear waves interacting has further examination presented; showing how the resonance condition is applied and met in the sum frequency case but not in the difference, and stating that if the polarisation of the two inputs are different then they cannot mix. It is left to the reader to calculate the mixing coefficients and decide if the polarisation and resonant conditions allow for mixing in the other cases.

The work of Taylor and Rollins, published the following year, took a different approach to the mixing theory by applying quantum mechanical methods to the problem (41). As such, the paper does not talk about the mixing of waves, like Jones and Kobett, but the

**Table 2.1:** Possible interaction cases and their associated properties by Jones and Kobett (18).

| Primary waves | Resonant wave type and frequency | Direction of scattered wave | $\cos\varphi$[a] | Frequency limits[b] |
|---|---|---|---|---|
| Two transverse | Longitudinal $(\omega_1+\omega_2)$ | $\mathbf{k}_1+\mathbf{k}_2$ | $c^2+[(c^2-1)(a^2+1)/2a]$ | $\frac{1-c}{1+c}<a<\frac{1+c}{1-c}$ |
| Two longitudinal | Transverse $(\omega_1-\omega_2)$ | $(\mathbf{k}_1-\mathbf{k}_2)/(\omega_1-\omega_2)$ | $1/c^2+[(c^2-1)(a^2+1)/2ac^2]$ | $\frac{1-c}{1+c}<a<\frac{1+c}{1-c}$ |
| One longitudinal and one transverse[c] | Longitudinal $(\omega_1+\omega_2)$ | $\mathbf{k}_1+\mathbf{k}_2$ | $c+[a(c^2-1)/2c]$ | $0<a<\frac{2c}{(1-c)}$ |
| One longitudinal and one transverse[c] | Longitudinal $(\omega_1-\omega_2)$ | $(\mathbf{k}_1-\mathbf{k}_2)/(\omega_1-\omega_2)$ | $c+[a(1-c^2)/2c]$ | $0<a<\frac{2c}{1+c}$ |
| One longitudinal and one transverse[c] | Transverse $(\omega_1-\omega_2)$ | $(\mathbf{k}_1-\mathbf{k}_2)/(\omega_1-\omega_2)$ | $1/c+[(c^2-1)/2ac]$ | $\frac{1-c}{2}<a<\frac{1+c}{2}$ |

[a] $\varphi$ is the angle between $\mathbf{k}_1$ and $\mathbf{k}_2$ at resonance; $a$ is the frequency ratio $\omega_2/\omega_1$; $c$ is the velocity ratio $C_t/C_l$.
[b] When $a$ is within the limits shown, it is possible to choose an angle $\varphi$ that will give a scattered wave.
[c] The frequency of the longitudinal primary wave is $\omega_1$.

combination of phonons. Despite the different methods the results are the same. In the key table of this work the choice is made to show the interaction cases such that the total wave frequency is balanced either side of the arrow. For example the mixing of two longitudinal waves to form a difference frequency shear wave is written as $\mathrm{L}(\omega_1) \rightarrow \mathrm{L}(\omega_2) + \mathrm{T}(\omega_1 - \omega_2)$. This makes sense when thinking in the quantum mechanical way in terms of phonons. The energy of these phonons is related to their frequency and thus to conserve energy it should be displayed this way. Viewing interactions in this way also lends itself to the better understanding of possible interaction modes; Taylor and Rollins make the point that fundamentally only two types of non-collinear mixing are possible, $\mathrm{L} \leftrightarrow \mathrm{T} + \mathrm{T}$ and $\mathrm{L} \leftrightarrow \mathrm{L} + \mathrm{T}$. This is due to the fact that transverse waves travel slower than longitudinal ones and that the momentum and energy of the input phonons must be conserved. All possible non-collinear interaction cases are just forms of these two fundamental interactions.

In this work, (41), the five interaction types as specified originally by Jones and Kobett are kept as the ones in the table, the main difference is the addition of a factor, $\Lambda$, which is used for the calculation of scattering amplitude. The equation for scattering amplitude is given as

$$X_3 = \frac{X_1 X_2 \Lambda \omega_1^3 a(1+a)}{8\pi r \rho c_t c_l} \tag{2.2}$$

where $X_1$ and $X_2$ are the amplitudes of the two input waves, $r$ is the distance from the centre of the interaction volume to the observer, $\rho$ is the density, and $c_t$ and $c_l$ are the shear and longitudinal wave speeds. In other literature the form of this equation varies,

moving velocity terms and a factor of two in and out of the mixing coefficient, and sometimes writing in terms of $\omega_1$ and $\omega_2$ instead of $\omega_1$ and $a$ so care must be taken when using the mixing coefficient from one to make sure the correct version of the rest of the amplitude equation is used.

Within the table cases numbered one and five include mixing coefficient terms for both vertically and horizontally polarised shear wave input cases. So you could say that the table shows seven different interaction cases (mixing only occurs with like polarised waves). The scattering angle shown in the table is written in terms of interaction angle, frequency ratio, and in some cases the velocity ratio of the input waves with four different variations in total.

It was also accompanied by an experimental paper (8). In this work a cylindrical sample is used to allow the interaction angle to be varied without altering the path lengths. For the production of longitudinal waves quartz immersion transducers were used that were attached to rotating arms. Shear waves were created by shear transducers fixed onto the sample. It appears that for some of the work presented towards the end of the paper it required the longitudinal transducers to be bonded to the sample because the immersion transducers could not produce a strong enough signal over a wide frequency range. This range was required when investigating the scattering amplitude at various different resonant points. It is impressive that they managed to get good enough results that matched with the theoretical predictions using a procedure that required the transducers to be bonded and removed from the sample nearly 20 times. They state that the large variation in amplitude is likely due to the variation in this adhesion, as might be expected. The interaction type specifically tested in this way was L + T $\rightarrow$ L. Input frequencies between 5 MHz and 50 MHz were used at various points in their experimentation and a polycrystalline magnesium sample was used.

Since the sixties Zarembo et al., Korneev, and Demčenko have given further attention to the theory of bulk non-collinear mixing (70; 71; 9). The most recent work (9) provides a more thorough explanation of nonlinear elasticity and how that leads to the mixing of non-collinear waves than was present in the works of the sixties. It covers the fundamental theory of nonlinear elasticity developed by Murnaghan (72), and Landau and Lifschitz (73). It makes very clear many concepts such as the impossibility of non-collinear mixing in a fluid due to the relationship of the k-vectors, and the reasons why a particular interaction case might not be possible. In this work the scattering angle is shown in a general form that allows it to be easily applied to any interaction mode; if it is a sum frequency case then the plus signs should be used, and if it is difference then negatives should be used.

$$\tan\theta = \frac{\pm\frac{v_1}{v_2}a\sin\phi}{1\pm\frac{v_1}{v_2}a\cos\phi} \tag{2.3}$$

Where $\theta$ is the scattering angle (defined relative to the reference input beam), $\phi$ is interaction angle, and $v_1$ and $v_2$ are the input wave velocities. Some of the notation has been changed in the equation to make it more similar to that of the rest of the work presented in this thesis. This work differs from the foundational work of Taylor, Rollins, Jones, and Kobett by the use of SV and SH terminology to differentiate shear waves that are polarised in the plane of interaction, SV, and those perpendicular to it SH.

The most useful part of this paper is probably this specification of polarisation types so that the reader does not have to calculate for each case based on the fundamental equations, they are all written out clearly in a table containing 54 variations; a combination of 9 different input wave cases, comprised of L, SV, and SH, and six different output waves for each, L, SV, and SH sum and difference frequency waves. For each it is specified if mixing will occur and if not one of three possible reasons is given, only collinear mixing possible, polarisation restriction, or not satisfying the resonance criteria. It also includes detail of if the interaction is possible with waves propagating in opposite directions a detail not mentioned in many other places. Two of the combinations have only the possibility of collinear mixing; these are the sum and difference forms of interactions with only longitudinal input and output waves. Another eight of the combinations allow for non-collinear mixing.

When inspecting this table in detail it can be seen that the row of mixing options for L + SV has different results from that of the SV + L row. This seems confusing and might not be what would be expected upon first reading. The author believes that the distinction between the two cases is largely due to which of the longitudinal or the shear input waves is of higher frequency. It suggests that only when the longitudinal wave is the higher frequency is difference frequency mixing possible. It is unclear why this would be the case but it seems as though the displaying of all 54 cases explicitly might have been partly intended to show details like this that are not immediately apparent. There are very few other published works that focus on the mixing of shear and longitudinal waves in the difference frequency case so it was not possible to confirm this behaviour.

The possible mixing modes are:

1. $\mathrm{L}(\omega_1) + \mathrm{L}(\omega_2) \rightarrow \mathrm{L}(\omega_1 + \omega_2)$, collinear only
2. $\mathrm{L}(\omega_1) + \mathrm{L}(\omega_2) \rightarrow \mathrm{L}(\omega_1 - \omega_2)$, collinear only
3. $\mathrm{L}(\omega_1) + \mathrm{L}(\omega_2) \rightarrow \mathrm{SV}(\omega_1 - \omega_2)$,

4. $L(\omega_1) + SV(\omega_2) \rightarrow L(\omega_1 + \omega_2)$,
5. $L(\omega_1) + SV(\omega_2) \rightarrow L(\omega_1 - \omega_2)$,
6. $L(\omega_1) + SV(\omega_2) \rightarrow SV(\omega_1 - \omega_2)$,
7. $SV(\omega_1) + L(\omega_2) \rightarrow L(\omega_1 + \omega_2)$
8. $SV(\omega_1) + SV(\omega_2) \rightarrow L(\omega_1 + \omega_2)$,
9. $SH(\omega_1) + SH(\omega_2) \rightarrow L(\omega_1 + \omega_2)$,
10. $L(\omega_1) + SH(\omega_2) \rightarrow SH(\omega_1 - \omega_2)$,

It is unclear why 4 and 7 are both included as they appear to be the same. This issue may be related to the previously discussed lack of similarity in the L + SV and SV + L rows of Table 1. Although in the discussion and conclusions section it states "Sum frequency interactions 4 for L + SV $\rightarrow$ L and 7 SV + L $\rightarrow$ L combinations are reciprocal." so perhaps they only include them for completeness of logic. In their work they say that Taylor and Rollins have presented five possible interactions, omitting the problem of separation of SV and SH polarization for shear waves, however, as was discussed above these polarisation options were included but more work was left to the reader to calculate the scattering coefficients for them. In fact, by including the polarisation terms given in a table in (41), which showed that further mixing variants occur with different polarisations, they had also accounted for all seven possible non-collinear mixing modes. The same number as are identified in Korneev and Demčenko's work.

The ten (seven non-collinear, two collinear, and one repeat) possible interactions have the scattering coefficients shown for them in the second table of Korneev and Demčenko's paper (9). In their work the interaction volume is a sphere for the purpose of calculating scattering coefficients as it results in an analytical form for the volume factor, the same as was done in older works. For this interaction volume an estimate of the beam width is made which for small angles reduces to the same equation as usually used for calculating the divergence of beam based upon width at the source and wavelength. Essentially this suggests that the spherical source acts in similar way to a 2D circular source. Also shown in the table are the possible frequency ratios that mixing can occur for, written as $d$ here instead of the usual $a$. They are slightly different from those shown in Jones and Kobett's work as they are rigorous in their usage of $\omega_1$ and $\omega_2$, and they do not allow difference frequency interactions if they would technically create a negative frequency. Ignoring the differences caused by this method their results are in agreement with those of the other publications.

Finally, this paper contains plots of the resonance conditions, the scattering angle, and the resulting scattering coefficients for all the interaction modes. These are very useful for quickly visualising the parametric behaviour of the various modes but they are only valid for the resonant conditions. There is no mention of expected behaviour away from resonance. It can be seen in Figure 2.9 that the maximal scattering is predicted to occur at $a = 1.5$ (but not at $a = 0.66$ as well), a surprising result considering the expected interchangeability of the two input beams in the SV + SV $\rightarrow$ L case. The author believes this is due to the choice of which terms to group into the 'scattering coefficient' and which to leave outside it in the rest of the amplitude of scattering function. It is somewhat a matter of preference but it might have been better to maintain the reciprocal nature of frequency ratio in this case by grouping the terms differently.

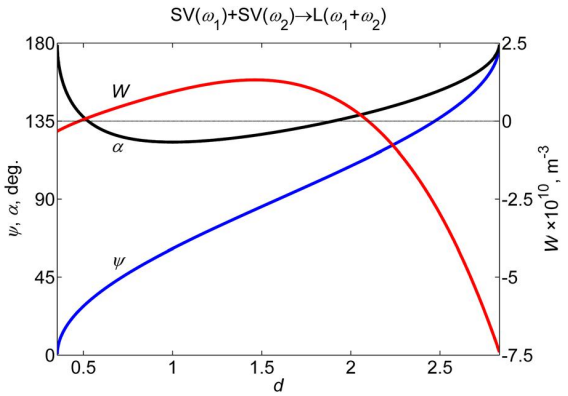


**Figure 2.9:** Scattering coefficient $W$, interaction angle $\psi$, and scattering angle $\alpha$ (defined relative to reference input beam, $\omega_1$, for the SV($\omega_1$) + SV($\omega_2$) $\rightarrow$ L($\omega_1 + \omega_2$) case at resonance. $d$ is frequency ratio. Korneev and Demčenko (9).

In all of the theoretical work relating to non-collinear mixing the waves are assumed to be well collimated within the interaction volume and of uniform intensity. Also, the output amplitude is quoted for the centre of the output beam. Experimentally a sum over a range of observation angles will always be taken, due to the finite size of transducers, or the use of an array. The output beam will also not have the same beam profile due to the spatial variation in the mixing source amplitudes. It is not thought that these simplifications will have very large impacts on the mixing behaviour but they may be significant in some situations. It should be noted that all of the above mentioned papers only discuss non-collinear mixing at resonant conditions, there is very little published work on bulk mixing away from resonance.

One example of bulk mixing at non-resonant conditions is presented in Zhang, Nagy, and Hassan's conference paper from 2015 (10). In this work they introduce the concept of the geometric mixing efficiency that can be applied to off-resonant cases. The way this is presented is very well explained, particularly by Figure 2.10, and is a key concept

not discussed explicitly in many other works. They also show, with an FE model, that the mixing of SV + SV $\rightarrow$ L is proportional in amplitude to the Murnaghan coefficient $m$, and independent of $l$ and $n$; confirming the expected behaviour from the analytic equations presented in the papers above, but that requires no further discussion here.

They state that the amplitude of the mixed longitudinal wave is proportional to both the material mixing efficiency and geometrical mixing efficiency. They found fairly good agreement between the prediction of this geometric factor and the FE model when testing interaction angles between 100° and 150° for a Ti-6Al-4V sample, although there is a slight disagreement in the peak of the two responses in terms of interaction angle. It appears that a fixed material mixing efficiency was used for the range of interaction angles, this could be the cause of the disagreement and is examined in detail in Chapter 5 of this work. An experimental version of this test was also conducted with five interaction angles measured, these results again appeared to agree with the geometric factor well although the five points were not enough to examine the finer features of the predicted trend.

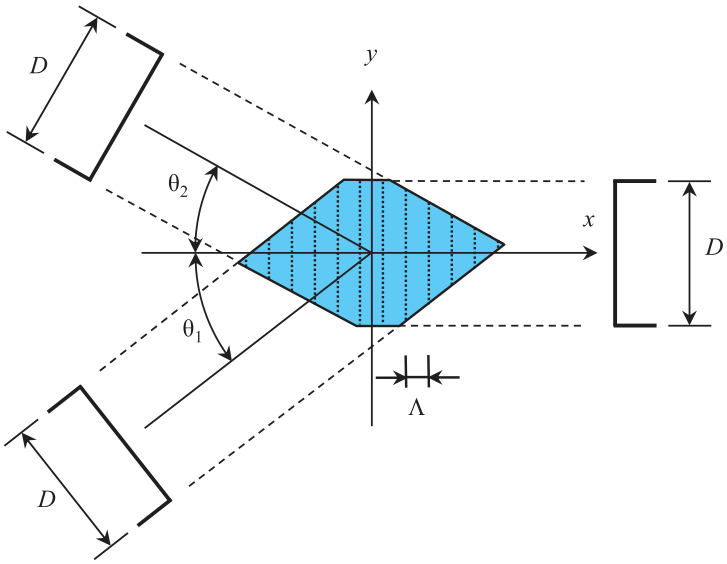


**Figure 2.10:** Schematic of a non-collinear interaction volume. $D$ is the beam width, $\theta_0$ and $\theta_1$ are the input angles relative to the classical scattering direction, and $\Lambda$ is the period of the mixing pattern in the scattering direction. (10)

This work also presented theory for what they call an 'imperfect interface' (an interface with nonlinear stiffness). These concepts were refined and added to in their work published the following year (14). This later paper has a greater focus on the mixing caused by various types of imperfect interfaces and much less detail about bulk mixing away from resonance. It largely refers to the bulk mixing for the purpose of avoiding it when only signals caused by the interface are desired; a very useful concept. However,

before discussion of mixing at interfaces some attention should be given to more of the experimental work conducted using the bulk mixing theory discussed above, focusing on the practicalities of the technique and its applications.

Croxford et al. published a paper on the detection of plasticity and fatigue using non-collinear mixing (11). Tests were made on two 2014-T4 aluminium samples, one subjected to plastic deformation and the other low-cycle fatigue. For this work the SV + SV $\rightarrow$ L interaction case was used, with perspex wedges on one side of the sample generating the shear waves by mode conversion from longitudinal waves at the perspex-aluminium interface. Hann-windowed 20-cycle tone bursts at 5.5 MHz were used, both at the same frequency to make the experiment more simple. Even without frequency filtering the spatial and temporal filtering combined with subtraction of sequential firings from parallel provided good results. The scattered signal was collected by a single transducer, on the same side of the sample as the input transducers, after being reflected off the back-wall of the sample. They found that the amplitude of the scattered wave, experimentally measured using a laser interferometer was only 38% less than the predicted value, a small disagreement given the approximations involved. The results of this work showed that as residual strain or number of fatigue cycles increased the scattered wave amplitude increased significantly (up to 30%).

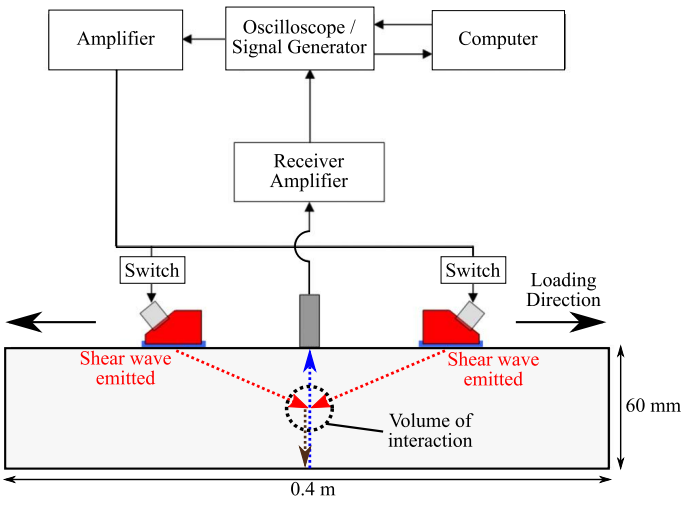


**Figure 2.11:** Experimental arrangement for the testing of a fatigued sample. Croxford et al. (11).

The work by McGovern et al. (74) talks about oxidative aging of asphalt concrete. The methods used are based upon those developed by Johnson et al. (75). McGovern et al. refer to asphalt as a material with nonlinear mesoscopic elasticity, a property shared by rocks, soil, and powdered aluminium. It is not clear how the behaviour of this type of nonlinearity might correlate with that of a kissing bond or solid CFRP but it is interesting

nonetheless. For longitudinal waves the asphalt is non-dispersive between 100 kHz and 350 kHz, but this is not the case for shear waves. Dispersion is not considered in the founding theory of non-collinear mixing and could lead to other interesting mixing behaviours. It is something that might need to be considered in relation to composites in terms of different waves speeds at different angles to the ply directions.

They chose to use the interaction of two longitudinal waves at 31° to each other, producing a difference frequency scattered shear wave. This was a very different interaction mode from most of the other experimental work. They varied the frequency ratio and kept the spatial size of the interaction volume the same by varying the number of cycles in each tone burst. One transducer was fixed at 200 kHz. An optimal frequency ratio of 0.68 was found that was fairly close to the predicted 0.71. As the material was aged the frequency ratio of maximal response generally increased, although the error bars were large reducing the significance of the result. The amplitude of the scattered signal had a smaller error relative to the trend, showing a reduction in scattering up to 24 hours of aging and then a sharp increase in production after that. They achieved reliable coupling by mounting the transducers in a fixed geometry 3D printed jig but said that they had to stop testing after 36 hours due to cratering in the surface of the sample limited the coupling quality. The consistency of coupling is a major problem for these measurements of amplitude, whereas the frequency ratio is less sensitive to errors in coupling. Other tests are present in their later works (76; 12).

As well as the theoretical work by Demčenko and Korneev, they have also published experimental bulk mixing work in collaboration with Koissin (77). In this they investigated the sensitivity of sum frequency mixing modes of SV + L $\rightarrow$ L and SV + SV $\rightarrow$ L to physical aging of polymethyl methacrylate and polyvinyl chloride, and epoxy resin cure state. They state that the SV + L $\rightarrow$ L mode was preferred experimentally due to the larger interaction angles required by the SV + SV mode. These large angles are difficult to produce in low ultrasonic wave velocity materials (PMMA and PVC) because a smaller amount of the input wave energy is transmitted inside the sample. This was not a problem for the epoxy testing. Both interaction cases are described as being sensitive to only one of the three Murnaghan coefficients, $m$.

An example of expected scattering coefficients for SV + L is presented for aluminium and PVC, showing that the scattering should be about two orders of magnitude greater in amplitude in the PVC case when testing at a similar frequency ratio and operating at resonance. They say that this is due to the higher nonlinearity of PVC and the more efficient transmission of the input signal from the water into the sample. As with their previous work there appears to be a lack of symmetry about $a = 1$, it is unclear

why this is the case. From the discussion it seems as though one of the input beam frequencies may be fixed in their methodology; they mention that higher frequency ratios will produce higher frequency output and suffer from greater attenuation. For the experimental testing they chose a frequency ratio of 1.5, using 6 MHz and 4 MHz input transducers as these were readily available and offered good frequency separation of the scattered wave.

Plates of plastics around 10 mm thick were investigated. The input transducers had a diameter of 10 mm so the interaction volume is of a similar size to the thickness of the material. The plastics were aged by being heating in boiling water for 10 minutes and then quenched in -27°C fluid. Various behaviours were observed, it appeared that the nonlinear mixing was much more sensitive to aging than a conventional linear ultrasonic measurement. The shear-shear mixing case was shown to detect many stages of the epoxy resin curing process. Finally, testing was conducted on epoxy bonded aluminium plates in a c-scanning method with both non-collinear and conventional techniques. The linear method had a better resolution, likely due to the focused probe compared with the large interaction volume of the nonlinear method. There is very little discussion of this final test, likely due to the complexity and difficulty in interpreting the results. The research presented in this thesis aims to understand this situation much better. Demčenko was also involved in another work on PVC aging in collaboration with Nagy and others (78). This paper will not be discussed in detail here as the results are somewhat superseded by the later work. It does however contain more information on the properties of PVC, including dispersion, that was not mentioned in the later work.

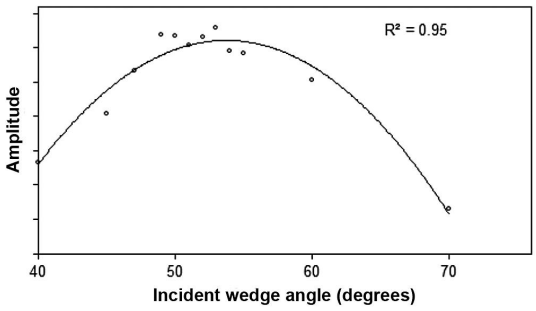


**Figure 2.12:** Amplitude of scattered wave from asphalt sample with a range of input wedge angles. A parabola is fitted to the data to find the maximum and has an $R^2$ of 0.95. McGovern et al. (12).

Nearly all of the above mentioned experimental tests have been focused on the absolute magnitude of the scattered beam at conditions near to the predicted resonance. In some cases such as Demčenko's work they talk of adjusting one of the interaction angles in order to get maximal output but the tests are not conducted with enough precision to

know if this adjustment is due to the experimental errors in the interaction angle or if the maximal output signal is not actually produced at the classical resonance conditions. The one example measuring at multiple frequency ratios was the work by McGovern et al. (74). They utilised a fixed interaction angle therefore the testing must have been non-resonant at some points. This fact is not discussed in their work, generally there is very little thought given to what happens to non-collinear bulk mixing away from resonance. In their later work (12) they also briefly mention the experimental variation of interaction angle, although it appears this was only done in the case where the linear elastic properties of the material were not known well enough to predict what the resonant conditions would be, with the goal simply to find resonance. Figure 2.12 taken from their paper shows that mixing occurred over a wide range of angles in this case. As will be seen in the contacting interface work below this could be a key issue due to interfering signals coming from the bulk and from interfaces.

### 2.6.2 Interface mixing

In recent years a range of modelling approaches have been applied to the simulation of contacting interfaces, an example used by Blanloeuil et al. was discussed previously in the CAN section. Here further methods will be introduced and applied to the case of non-collinear mixing. Following that is a discussion of experimental tests, many of which were conducted in relation to the modelling.

In terms of modelling Zhang et al. have applied a variety of methods to the problem of non-collinear mixing at contacting interfaces. The papers (10; 14) by Zhang et al. were discussed earlier with respect to their content on bulk non-collinear mixing, however they also contain investigation into ‘imperfect interfaces’. The later work (14) contains investigation of two analytical models and two FE models for these interfaces. One of the analytic models simulates the interface by a set of vanishingly thin springs between the two solids, these springs have nonlinear stiffnesses. The other model has a thin region around the interface that is given much larger bulk nonlinear elastic properties than typically found in the rest of the solid. The effective nonlinear interfacial stiffness was then calculated analytically for the thin nonlinear region. This showed that the thin nonlinear region was effectively the same as a special case of the first model where the effective compliance coefficients are equal to each other.

A COMSOL FE model was also conducted to compare the analytic models against. ‘Contact pairs’ between neighbouring nodes on the upper and lower surfaces of the interface were created. The nonlinear stiffness relations for these pairs could then be

specified. For this the bulk of the model was set to include only geometrical nonlinearity, and not nonlinearity related to the TOECs. The author believes that this means that the hyperelastic COMSOL package was not used for this section, although it is possible that it was but with Murnaghan coefficients set to zero. 4.5 MHz and 5.5 MHz input pulses of 6 and 7 cycles respectively were used. Pulse inversion was used to remove the fundamental input frequencies. This model confirmed that the reflected and transmitted scattered waves were of the same amplitude and opposite phase. The results of this model matched the analytic model quite well for a range of interaction angles. It is suggested that the differences between the behaviours are likely due to the finite beam widths of the FE model compared with the plane waves of the analytic model.

A further COMSOL FE model was made that included the thin nonlinear region and used the hyperelastic COMSOL module to capture the bulk mixing effect that would be classically caused by this solid. This produced a very similar result to the other FE model demonstrating that bulk nonlinear mixing in a thin region is effectively the same as mixing by a nonlinear interface at the centre of that region. A comparison of various scattering amplitudes, produced by the some of the interface models and some other bulk ones, over a range of interaction angles is shown in Figure 2.13.

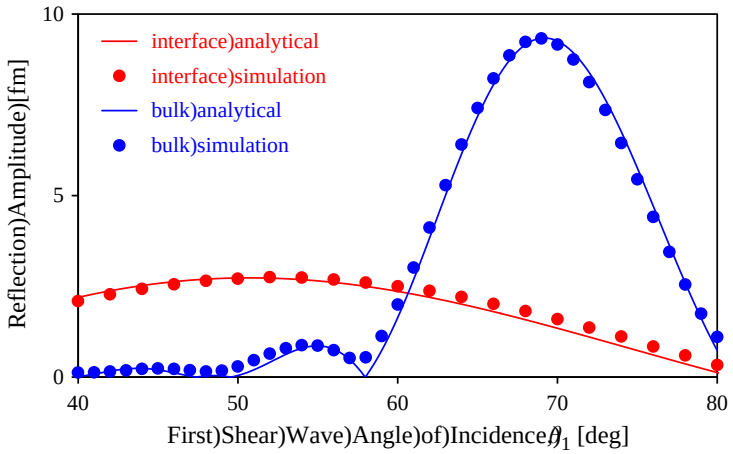


**Figure 2.13:** Comparison between different models showing the scattering amplitude at a range of interaction angles. The thin nonlinear interphase model was used for the interface cases, the classical equations derived by Taylor and Rollins were used for the analytic bulk (13), and COMSOL's hyperelastic FE tools for the bulk simulation. Zhang et al. (14).

Blanloeuil et al. take a different approach to the modelling, as described earlier in the single frequency section. Their model attempts to capture the interaction of the crack faces with fewer approximations than those of Zhang et al.'s work. In (15) the FE model is applied to the non-collinear case. The chosen interaction case is SV + SV $\rightarrow$ L, sum frequency. It also included experimental testing for comparison, this will be discussed

later. This model predicts that the non-collinear mixing produces scattered waves in both directions from the interface, in agreement with Zhang et al.'s.

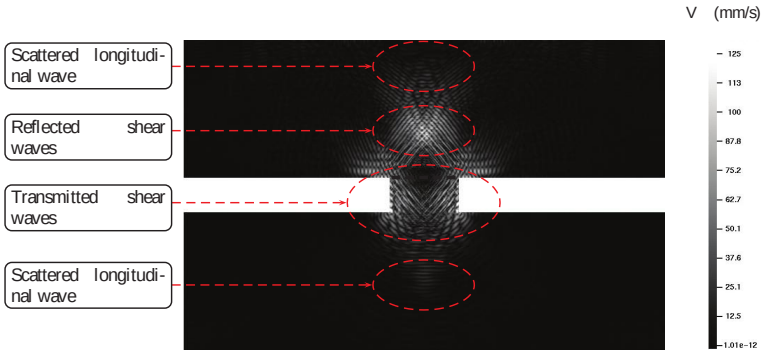


**Figure 2.14:** An example velocity field of the interaction of two shear waves at a kissing interface, indicated by the dark grey dashed line. Blanloeuil et al. (15).

The model was then extended to the case of finite length cracks in (4). Also investigated were different crack orientations. Far more FE results are shown for this work allowing for a clearer picture of the mixing behaviour to be formed. Also added are directivity plots for the mixing when the interface is perpendicular to the acoustic waves (as previously) and when rotated by 20°. It appears that when the interface is perpendicular the reflection and transmission scattered waves are of equal amplitude but when rotated the transmitted wave becomes stronger than the reflected. Many concepts explored in the previous paper are developed further here, also added is an investigation into input beam interaction angle. The scattering peaked at 80° within the tested range of 60° to 120°. The reason given for this is related to the single beam discussion in (5), that maximal normal stress is applied by SV waves when they are at 45°, which should give an interaction of 90°. The peak is less than this due to the way the model is constructed with larger interaction angles having sources further away from the interaction volume thus reducing the intensity in that volume because of beam divergence. It would be good to see this hypothesis tested with a circular model more like the original experiments of Rollins (13).

Blanloeuil et al.'s work from 2016 (16) builds upon the previously discussed models to calculate the scattered far-field more efficiently by measuring at a circle of nodes in the near-field of the FE model which is then analytically extended to the far-field. This allows the FE model to be smaller and reduces the computation time. This method is applied to both single longitudinal input beam and dual SV input beams cases. A lot of very useful figures are presented related to the various scattering cases. One example of interesting behaviour can be seen in Figure 2.15, it shows in what direction scattering would be expected for an interface inclined at 20°. It is particularly useful because the outputs are separated by frequency and wave mode (longitudinal or shear). A study with

similar plots after subtraction of the individual input beams would be useful for greater clarity, indicating which beams are produced by mixing and which are simply due to single beam clipping as they pass through the interface.

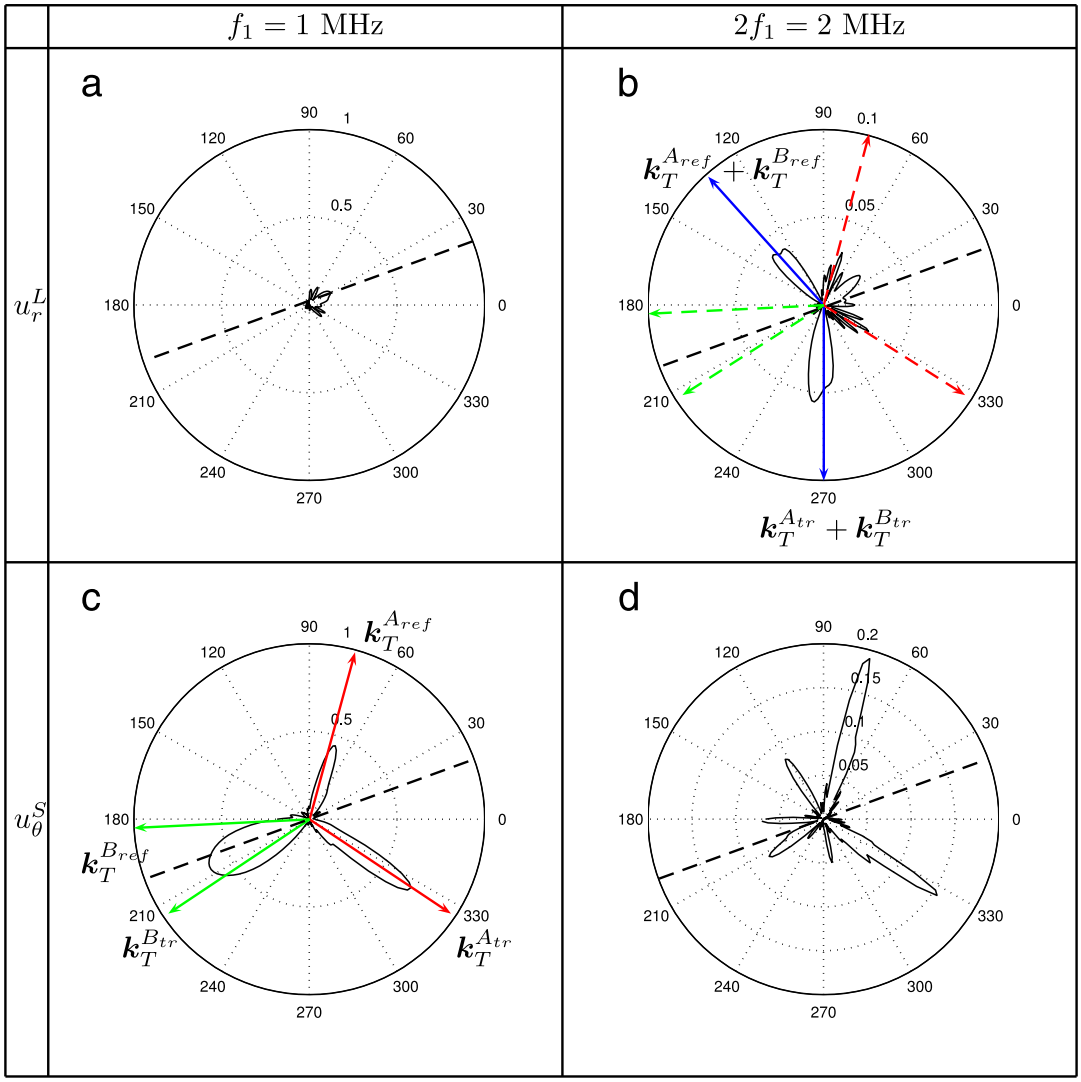


**Figure 2.15:** Directivity patterns as a result of the interaction of two 1 MHz SV waves input from the 35° and 145° directions ($\phi = 110°$). a) Longitudinal waves at the fundamental frequency, b) longitudinal waves at second harmonic/sum frequency, c) shear wave component at the fundamental, and d) shear waves at 2 MHz. See the original work for information on the $k_T^{ref}$ markings. (16)

The modelling results show promise in the method of non-collinear mixing at an interface, and are generally in agreement about the interaction angle related response. However, the models include many simplifications that might mean they do not accurately predict real world behaviour. The research discussed below attempts to experimentally test the behaviour for comparison.

Blanloeuil et al. included experimental testing in their work (15), producing qualitatively

similar results to the model. The contacting interface is created by the compressive loading of two aluminium blocks. Input waves are generated at 5 MHz in a similar way to the plasticity and fatigue testing conducted by Croxford et al. in (11). An interaction angle of 114° was used, as suggested by classical resonance equations, therefore bulk mixing would also be expected to occur in this case. The model showed that maximal scattering when the normal stress at the interface due to the acoustic waves was four times that of the compressional pre-loading. Experimentally the scattering was found to increase and then decrease as interface loading was increased, in agreement with the modelling. Measurements with the interaction volume above and below the interface were conducted to verify that this sensitivity was caused by the contacting interface.

Escobar et al. published a work focused on the experimental measurement of diffusion bonds in a titanium alloy using the non-collinear method (34). They were one of the first groups to explicitly test at multiple interaction angles in order to selectively receive either bulk or interface mixed waves. They define two configurations in which the experiment was run, one at a classically resonant case to maximise bulk mixing using an interaction angle of 119°, and another at 96°. It is unclear why this second angle was selected, the text simply states that it is a different angle from the resonance but does not mention if it was a peak in the scattering from the interface defects. An equation is given for a 'phase matching' condition but the relevance of this is unclear. The interaction of two SV waves producing a sum-frequency longitudinal wave was used in both configurations. The figures indicate that the reception transducer was positioned on the same side as the input transducers and that it collects signal that has been reflected from the back wall of the sample. This was probably done to allow both the bulk mixing and interface mixing to be detected for comparison, but a better signal from the interface could likely have been received by capturing at an earlier time in order to collect the directly reflected mixed wave from the interface. This method was used in the later work by Zhang et al. discussed below.

A range of samples with differing cross-boundary grain growth (CBGG) were tested; the largest signal in the interface configuration was produced with CBGG between 50% and 80%. Testing in the bulk configuration showed a reduced sensitivity to the interface condition, as would be expected, and had a similar trend overall. They state that the signal received from a strongly scattering interface in the interface configuration was two to three orders of magnitude stronger than the bulk mixing signal. It is unclear if they are referring to bulk mixing produced in the bulk or interface configurations at this point. Also tested in this work were conventional linear pulse-echo c-scan methods at 10 MHz and 25 MHz. Both reduced in amplitude as CBGG increased with the 25 MHz version performing better than the 10 MHz inspection. Neither offered good sensitivity

to the samples with greater than 70% CBGG, unlike the nonlinear method. They point out that the resolution of the non-collinear method could be improved by reducing the interaction volume and this would be favourable for the suppression of the bulk signal as it scales to a higher power with the radius of the interaction volume than the interface mixing.

A conference paper by Zhang et al. (35) tests the theory discussed in their previous work experimentally on diffusion bonded Ti-6Al-4V samples. Some of the samples were the same as used in (34) and another set of higher bond quality were also investigated. It focused on improving CAN detection by suppressing bulk mixing signal. This was achieved by receiving the signal in the reflected direction, although a considerable amount of the testing was conducted in transmission configuration for comparison with Escobar et al.'s previous results (34). The testing was conducted using a completely computer controlled system including input transducer angle and position through LabView. Another key improvement in their procedure was the use of 'four-way polarity flipping', a type of pulse inversion where all combinations of input pulse inversions are used. They show that this allows the fundamental and second harmonic components of the input beams to be removed from the signal which is an improvement on conventional pulse inversion. The final aspect analysed in their work is the effect of averaging coherently and incoherently, they believe that the coherent method produced better results when inspecting near perfect bonds because it suppressed the material noise better. However, the incoherent method gave greater sensitivity to interface quality when the lower quality bonds were tested. It seems that there is more research to be done on the phase related behaviour of the reflected signal so that the best averaging method can be selected with greater insight.

There is only one other experimental work that investigates the non-collinear method's interaction with a type of kissing bond, Demčenko et al.'s (30). In this paper they present the results of the SV + L $\rightarrow$ L sum frequency interaction with two PVC plates bolted together to simulate a kissing bond. Also studied is the sensitivity to subsurface micro-cracks in PMMA. An unusual orientation of interaction is used for the PVC testing where the two beams enter the sample from opposite sides of the crack. The interaction mode is also not as well documented in relation to interface mixing, the works of Zhang and Blanloeuil et al. investigate the SV + SV $\rightarrow$ L instead. Like the later work by Zhang et al. there is discussion of the mixing occurring at non-resonant conditions. In this work the focus appears to be on the prediction of the scattered beam's shape due to the interaction volume's shape rather than how the amplitude of the scattered beam is altered.

The testing was conducted in immersion with 10 mm diameter 2 MHz and 3 MHz input transducers on one side of the sample and a focused 3 mm transducer on the other side for detection. Pulses of 40 and 60 cycles were used to create a narrower bandwidth than many other experimenters, and should produce results closer to those predicted by single frequency models. Also it allows for a greater margin of error in the overlapping of the pulses. A conventional c-scan at 5 MHz was conducted for comparison and showed up to a 25% drop in amplitude in the kissing bond region. The back-wall reflection c-scan shows that the interface varies along its length; the centre region that is less compression loaded by the bolts produces much less signal than the outer regions. The difference between these two regions can be seen even more clearly in the non-collinear c-scans. In this case the kissing interface also produces less nonlinear signal than the bulk. This seems somewhat counter intuitive because the point of using non-collinear mixing generally is to exploit the nonlinearity of a kissing interface in order to produce more scattering. Perhaps in this case the vertical interface is simply reflecting the input beams stopping them from overlapping and thus preventing mixing. If this is the case then a linear method that tests the transmission of the interface would likely also have a good sensitivity to the kissing bond.

The results in this paper relate to the discussion earlier in this chapter about the importance of the type of kissing bond being investigated. Experimentally it can be difficult to produce the ideal case where it would be almost imperceptible to a linear method but still have a lack of strength. Thus it is often more convenient to investigate interfaces that could be detected conventionally but in this case it is key that the signal being produced can be proven to be due to CAN mixing. Demčenko et al.'s work here seems to suggest that less signal is being produced by the regions with kissing interfaces in and therefore struggles to prove that interface mixing is occurring. The lack of conclusive results suggests that there was something about the experiment that prohibited strong interface mixing; this may be the interaction case, the relative orientations of the input beams and interface, or maybe the mixing parameters (interaction angle and frequency ratio) were too far from ideal. The author believes the fact that this experiment failed to produce conclusive evidence of interface mixing despite the researchers being well established in both the theoretical (71; 9; 30) and experimental (78; 77) parts of the field demonstrates how much more there is to learn about the phenomenon.

There is clearly a lack of experimental work in this area and the theoretical work often relies upon a lot of simplifications that will likely limit their applicability to the prediction of real world kissing bond behaviour. For example, none of the models take into account the roughness that would be present at the interface, and many models

assume that the interacting waves are of uniform intensity, are perfectly collimated, and form a spherical interaction volume. The roughness of the interface could have a major impact on the scattering behaviour as it does not fit with the concept of the interface being in either a stick or slip state, it might be far more complex than that. This would likely be too difficult to model with current computing power without a more intelligent modelling strategy than simply creating an FE model with jagged edges.

Encouragingly, these initial modelling and experimental tests have shown that non-collinear mixing at an interface is possible, and have explored a few parameters related to it. But, neither bulk or interface mixing have been measured experimentally over a wide range of interaction angles, with only a few interaction cases investigated with models. Much more work is needed to test the predictions of those models, and the other interaction modes should not be forgotten about despite the lack of success in the SV + L $\rightarrow$ L sum frequency testing.

## 2.7 Conclusions

The many different types of possible defects in adhesive bond lines were discussed and how they relate to various kissing bond definitions. An overview of NDT methods showed why some of these defects are difficult to detect, and thus which should be the focus of the work; zero-volume disbonds. Acoustic methods appeared to be the most promising for detecting such defects due to the way they probe the bonds between the materials. The intention to develop a technique capable of working in the bulk of material was stated with the aim of making the method more generally applicable. Some success was seen in conventional ultrasonic methods by using high frequencies, amplitudes, or shear waves but the sensitivity was limited by the small difference between the interaction with a good bond, and poor bond.

Nonlinear methods were proposed as a solution to this, moving energy from the fundamental input frequency into other harmonics only when a material nonlinearity was present. The nonlinear dynamics of contacting interfaces were discussed. The difficulty with these methods is that there are many potential sources of nonlinearity in an experimental system which could also cause a change in the spectral content. The non-collinear method offers the ability to avoid this problem by selectively sampling only the volume where the beams interact. Harmonics generated in the input beams are spatially separated from the beam(s) produced from the interaction volume. It also has other features that allow for greater suppression of unwanted signals; if pulses are used then there can be a temporal difference between the signal from the interaction

volume and other scattering from the sample, and if two different input frequencies are chosen then there can be frequency separation between input beam harmonics and the frequencies produced by modulation.

One limiting factor of non-collinear mixing is the potential beam mixing in the interaction volume due to the bulk nonlinearities of the materials. In order to know whether the signal is coming from bulk mixing or from a kissing interface the bulk mixing must be well understood. The mixing of different interaction modes at resonant interaction angles and frequency ratios is well understood but there is a lack of investigation into the behaviour away from resonance. This is critical because it is likely that the mixing caused by the interface will occur optimally with different mixing parameters from the bulk, but it is uncertain how much bulk mixing will occur in those conditions. Ideally there would be minimal overlap in the two scattering behaviours, and the bulk could be used as an independent reference for the amplitude of the interface scattering.

Non-collinear mixing at contacting interfaces is poorly understood in comparison to bulk mixing. Few researchers have studied it and have tended to focus on only one of the seven possible modes; sum frequency shear wave mixing, producing a longitudinal wave. It has been shown experimentally that the mixing occurs and models have been developed to explore the phenomenon's behaviour. The interaction of SV + L $\rightarrow$ L, sum frequency was investigated for two contacting blocks of PVC but no scattering was observed. This may be due to the vertical orientation of the crack, or the materials chosen rather than the interaction case. Experimenters have used input frequencies ranging from 2 MHz to 5.5 MHz with pulse lengths from 6 to 60 cycles. These properties appear to be the ideal range for the production of narrow beams with interaction volumes contained within easily fabricated sample sizes and associated testing arrangements. Simple interface configurations, avoiding the use of adhesives, were preferred with either loading together of two flat surfaces, or diffusion bonding. This removes the possibility of thin film interference effects on the scattered signal.

From the above it is clear that non-collinear nonlinear mixing has great potential for the detection of zero-volume disbonds, but more research is required to understand the mixing behaviour. Particularly, how the method responds to changes in input parameters (interaction angle and frequency ratio) for both bulk and interface mixing needs further investigation and also a focus on experimental testing due to limitations in the accuracy of computer modelling.

# Chapter 3

# Experimental methods

## 3.1 Introduction

The method decided for investigation into improved kissing bond detection was non-collinear mixing. In the literature review it was noted that previous works have focused on behaviour at resonance, with little known about mixing in the rest of the parameter space. To improve the understanding of this technique an experimental arrangement was required that could accurately control interaction angle, $\phi$, and frequency ratio, $a$, of the input beams. The mixing in a solid sample will be measured for the $\phi - a$ parameter space. This information can then be compared with mixing behaviour from a 'kissing bond' sample. This chapter details how each of these was achieved. The measurements of scattering behaviour over the interaction angle and frequency ratio parameter space will be referred to as fingerprints and it is thought that the patterns contained within them could be useful for kissing bond detection and/or material property measurement.

This chapter details the apparatus, how the desired mixing signal was acquired and processed, and the samples that were investigated. It also includes discussion of factors that impact the fingerprint, experimental errors, such as interaction angle uncertainty and input amplitude variation, as well as information on the interface loading method and other linear ultrasonic methods used in this work.

## 3.2 Apparatus

An experimental rig from previous non-collinear testing, (79), was used as the starting point for the experimental design. It was comprised of two carriages on a leadscrew that when turned in one direction increased the separation of the carriages, and vice versa. The carriages each contained a motor and worm gear system that rotated a shaft on which an ultrasonic transducer could be mounted, this allowed for independent control of the angle of the input beams, Figure 3.1 is a picture of these carriages. A schematic of the experimental rig is shown in Figure 3.2 (b). The experiment is conducted in immersion to allow for consistent coupling between the input transducers and the sample while allowing them to be freely positioned. Originally, a potentiometer based feedback system was used to control the position of the carriages and angle of the transducers, however this suffered from limited ranges of rotation, inaccuracy, and instability. To improve this the motors were upgraded to those with built in encoders; Maxon RE 10 motors (part No. 256094), with GP 10 K 256:1 reduction gearing (part No. 110311), and MR 16 CPT encoders (part No. 201933). These motors are controlled by EPOS2 24/2 boards, connected to a standard PC by USB.

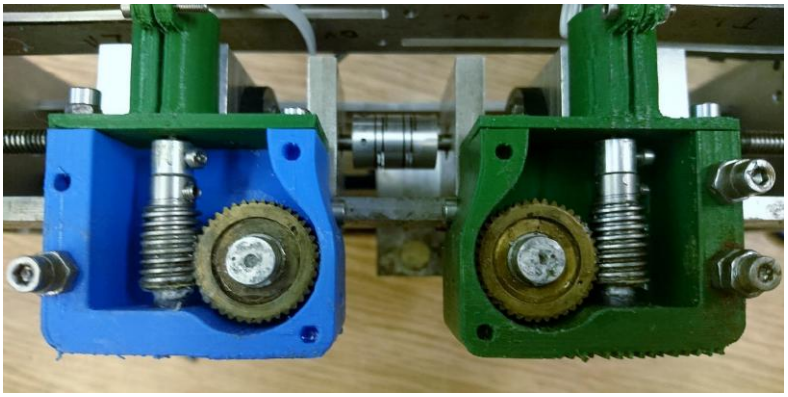

**Figure 3.1:** The carriages which hold the transducer rotation systems. Motors are attached to the vertical worm gears which turn the attached gears. The shafts of these gears extend out the back of the carriages and have the input transducers mounted to them. The carriage separation worm gear can be seen in the background.

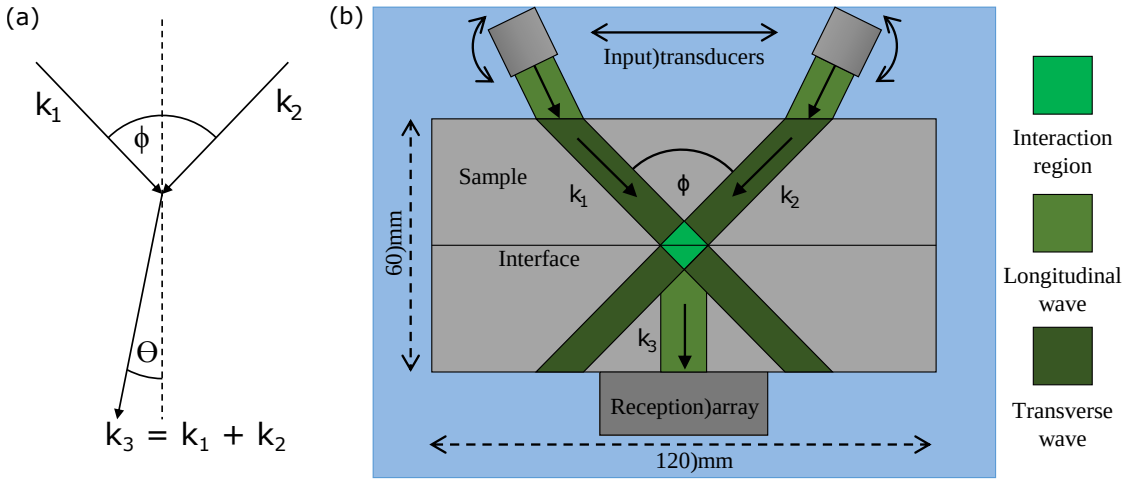


**Figure 3.2:** a) The interaction of input waves with k-vectors $k_1$ and $k_2$ producing the scattered beam, $k_3$. $\phi$ is the interaction angle, and $\theta$ the scattering angle. The input beams are symmetric about the vertical dashed line. b) Experimental geometry, indicating simplified beam paths and types for the SV + SV $\rightarrow$ L mode.

Key to the testing is the ability to alter interaction angle while keeping the interaction volume centred at the same point, a combination of carriage separation and transducer angle changing can achieve this. If separation is altered on its own then it can control the depth of interaction in the sample. An array is positioned below the sample to collect the scattered signal. As the frequency ratio is changed the scattering angle changes so an array allows for signals to be collected over a range of interaction angles. The scattering angle can be predicted by using the relevant equation from Table 1 of (18). The array is also useful for collecting information about the width of the scattered beam. Tests with thin samples (less than 30 mm) were conducted with a standoff between the array and sample to create better separation between the input beams and the scattered beam. The other tests had the sample in contact with the array.

Testing will be conducted using two different sets of input transducers, one with centre frequencies around 5 MHz, and another at 2.25 MHz. The higher frequency probes should produce less divergent beams and generate more bulk mixing due to the cubic frequency scaling, see Equation 2.2. The lower frequency transducers are useful for comparison with models that are not possible to run at higher frequencies, and for testing materials with greater attenuation such as CFRP. To accompany the input transducers are two different detection arrays with appropriate centre frequencies at the mixing frequencies.

The 5 MHZ transducers are Olympus V551, which have an active diameter of 10 mm and a centre frequency of 4.7 MHz. The pulse-receive -6 dB bandwidth is 74% of the centre frequency. They are paired with an Imasonic linear 128 element 10.4 MHZ centre frequency array, -6 dB bandwidth of 85%. The elements are 10 mm long, 0.30 mm in pitch. This array is most sensitive at a frequency ratio around one, but should provide good sensitivity over a wide range due to the large bandwidth. The 2.25 MHz transducers are Olympus V549, also 10 mm in diameter. The array used for these tests was also made by Imasonic and had 128 elements, 4.99 MHz centre frequency, 67% bandwidth, and elements with the same dimensions as above. The slightly reduced bandwidth will cause a faster drop off in signal as frequency ratios away from one are tested. A MicroPulseFMC array controller was used to detect, filter, and average the signals received by the array and send that information to a PC.

To generate the input pulses two separate arbitrary waveform generators were required. This allowed the frequency of each input to be controlled independently and also for the output to be switched on and off by the computer, the reason for this requirement is described in the signal processing section below. Agilent 33250A arbitrary waveform generators were used. To amplify the signals to levels required

for nonlinear experimentation Amplified Research 75A250A/100A400 amplifiers were used. These were also connected to the computer allowing the gain to be adjusted more precisely. A schematic of the experimental apparatus is shown in Figure 3.3.

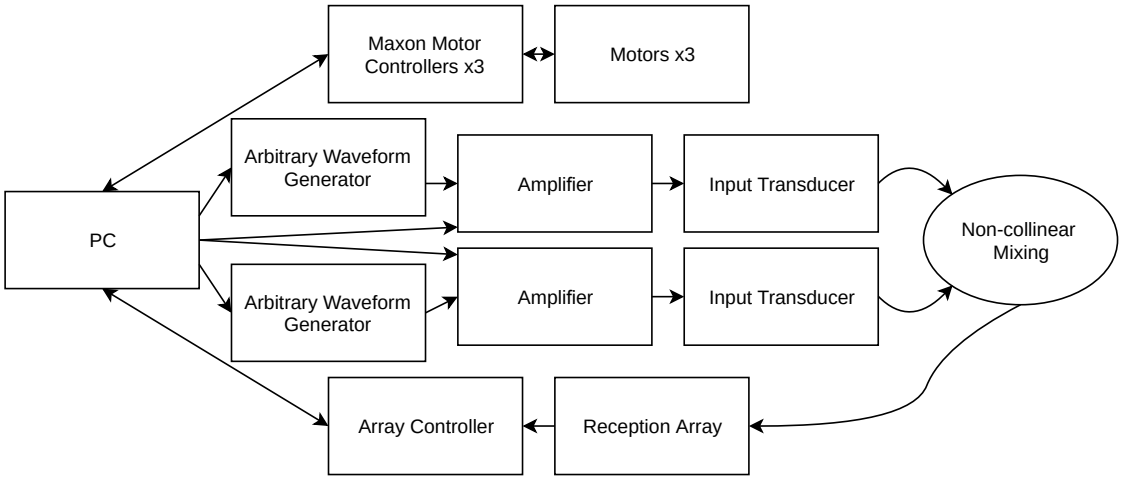


**Figure 3.3:** Schematic of hardware and connections in experimental set-up.

20-cycle Hann-windowed pulses were used for both input transducers. These long pulses create a narrow frequency bandwidth (around 0.2 MHz) which makes the experiment more sensitive to frequency ratio and improves the filtering of the output signal because the energy is within a smaller frequency window. The Hann window is used to reduce frequency sidebands. Longer pulses could be used to enhance the frequency sensitivity further but this would limit the temporal filtering potential of the method.

The experiment was operated in through transmission mode only since it was not possible to position the array above the sample. If it had been there it would have limited the minimum spacing between input transducers, and would not have been able to collect the bulk mixing signal as effectively. In the future, testing with a single transducer on the reflection side may be useful for observing the interface scattering in isolation.

## 3.3 Signal processing

One of the key strengths of the non-collinear method is that it allows for the removal of the signal relating to the individual propagation of the input beams. This includes both the fundamental and harmonic components that can sometimes obscure the signal of interest. To do this measurements must be collected with each input transducer on its own, these signals can then be subtracted from the signal received when both are fired simultaneously. This is complemented by frequency filtering, which was done at

the sum of the input frequencies with a 1.5 MHz bandwidth for the 5 MHz testing, and 0.8 MHz for the 2.25 MHz. The filter bandwidths are wider than that of the input pulses allowing all of the desired signal to pass through, and long enough to provide good temporal resolution which aids in later time windowing, described below. Figure 3.4 shows examples of the time data at various points of acquisition and processing. In plots (a), (b), and (c) of Figure 3.4 the side lobes of the input pulses dominate but after subtraction, shown in (d), the scattered pulse becomes visible. Note the different colour scales. Filtering at the sum frequency, Figure 3.4 (e), removes nearly all of the remaining unwanted signal allowing the pulse of interest and its echoes to be clearly seen.

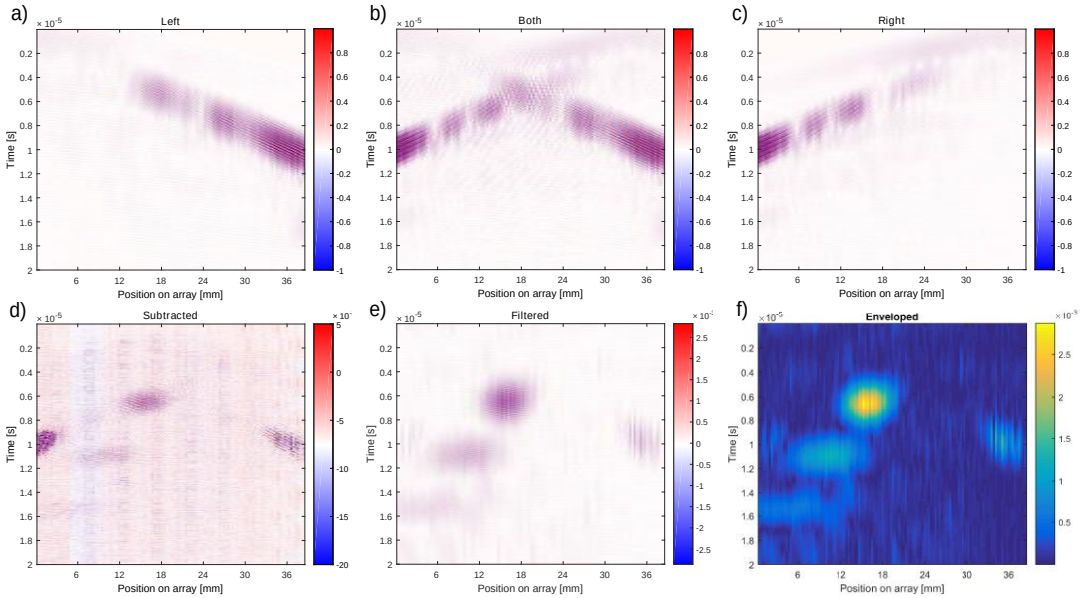


**Figure 3.4:** Time data captured by the array shown at various stages of processing. Array element position is on the x-axis and time in seconds on the y-axis. Note the differing colour scales. The data was collected for a frequency ratio of 0.8 and an interaction angle of 120° in solid aluminium. (a) The raw signal received when the left transducer is fired at $\omega_1$ (5 MHz), (c) is the right at $\omega_2$ (4 MHz) and (b) is both at their respective frequencies. The result of subtracting left and right from both is displayed in (d). (e) The subtracted signal after filtration at the mixing frequency $\omega_1 + \omega_2$ (9 MHz). The envelope of the signal is shown in (f).

An alternative to the subtraction method is pulse inversion. It is a commonly used technique in nonlinear ultrasonics (5; 80; 81) as it can be used to remove either the even or odd harmonics from the signal. However, it is less useful in sum-frequency non-collinear mixing since the signal of interest is at a similar frequency to the second harmonic of the input beams when the frequency ratio is close to one. In non-collinear mixing the second harmonic component of the input beams' side lobes is commonly the largest source of unwanted signal that remains after processing in the way detailed in the previous paragraph. Conventional pulse inversion is not able to remove these side lobes while enhancing the sum-frequency scattered wave. There is a more advanced form

of pulse inversion where all combinations of inversions of the input pulse are applied, requiring a total of four firings (35). This method was not used in the experimentation presented here but is promising for future work.

A window of the data in time and space was selected based upon the predicted time of arrival and angle of scattering, as stated in (18). This window removed most of the unwanted signal from the sidelobes of the input beams that normally arrived later than the signal of interest. Focusing on reception was then performed to enhance the measurement of the wave scattered by the interface. To do so a delay is applied to each element's response, depending on the position of the element within the array and its location with respect to the interaction volume. The remaining signal was then summed element-wise to complete the focusing operation. Finally, the Hilbert transform was used to acquire the envelope of the signal and the peak value of this was recorded. This value is used as the metric of scattering and referred to in later figures as 'peak scattering amplitude'. By recording this scattering value for the range of input parameters a 'fingerprint' can be made. These steps are shown as a flowchart in Figure 3.5.

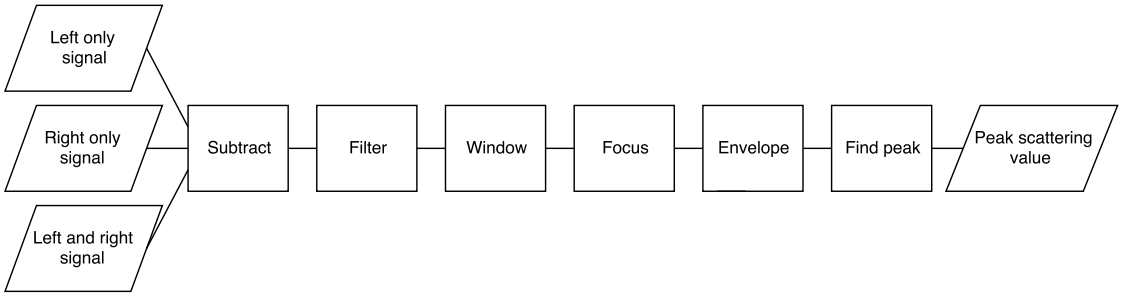


**Figure 3.5:** The steps involved in the processing the three captured time signals into the value used for one point in the fingerprint. The steps are described in detail in the main text.

## 3.4 Experimental fingerprint factors

This section explores how various aspects of the experimental design impact the fingerprints that are produced. Ideally the fingerprint would be independent of such factors so that it is just a product of the sample properties within the interaction volume.

### 3.4.1 Mode conversion

The experimental design, as shown in Figure 3.2, was selected for many reasons. One benefit of using transducers in immersion is that it allows for longitudinal and shear waves to be produced inside the sample via mode conversion at the water-solid interface.

This is useful because it allows many different interaction cases to be investigated without the need to change transducers. A negative is that at some angles both shear and longitudinal waves will be produced, this could cause multiple different interaction volumes and modes to occur, complicating the received signal. Also, the amplitude of the waves varies with incident angle so this should be factored in to a fingerprint if the intention is to produce standardised output. Figure 3.6 shows the expected acoustic amplitudes reflected and transmitted from an incident longitudinal wave.

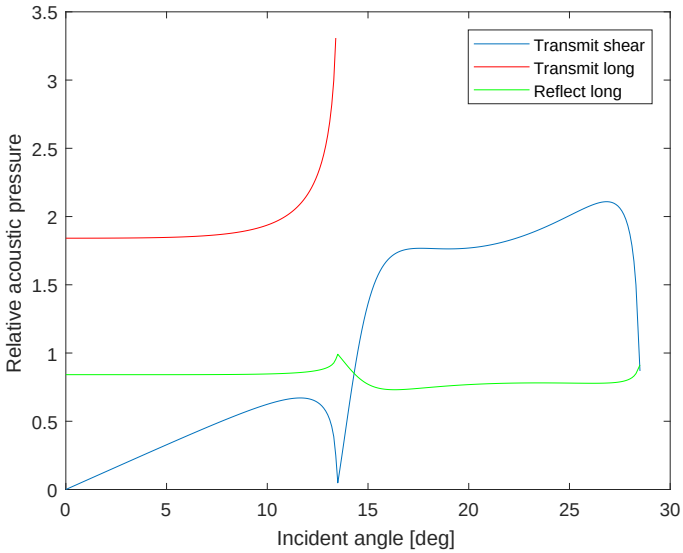


**Figure 3.6:** Mode conversion at a water-aluminium interface showing the transmitted shear wave pressure in blue, transmitted longitudinal wave pressure in red, and reflected longitudinal wave amplitude in green.

The equations used for mode conversion calculation are from the Krautkramer brothers' book (82). It can be seen in Figure 3.6 that there are two critical angles in aluminium at around 13° and 28°. These are the angles when the longitudinal and shear waves, respectively, are refracted such that they are parallel to the interface. The pressure values of the longitudinal beam above 13° are ignored for this reason. Therefore, with incident angles larger than 13° only shear waves are created in the bulk of the aluminium. The output beam angles can be calculated using Snell's law.

The selected experimental arrangement is particularly suited for testing the SV + SV $\rightarrow$ L mode as shear can be produced in isolation. This interaction mode was the only one shown to produce mixing at kissing interfaces in the literature, though it is unclear if much investigation into the other modes had been done. It would be interesting to test other modes but they have the difficulties of multiple interaction cases occurring at once as described above, and there is uncertainty that mixing will be achieved so exploration of the $\phi - a$ parameter space for a known working mode was prioritised.

### 3.4.2 Frequency ratio factors

One major factor in the frequency ratio response, as mentioned previously, is the limited bandwidth of the transducers. Quite broadband transducers were selected to achieve reasonable sensitivity between $a = 0.5$ and $a = 2$. It is not possible to predict the range over which scattering will be possible to observe without knowing the signal to noise limitations of the experiment. Use of broadband transducers reduces the sensitivity/output amplitude at the centre frequency so a balance between this and the range of $a$ sensitivity must be found. Narrower bandwidth transducers could be used in the future to test specific frequency ratios of interest. Frequency ratios further away from those described above would likely cause scattering at an angle that would not be detectable with the array unless it is repositioned. This is another reason why extreme ratios will not be tested.

It was decided that in the testing one transducer will be kept at a fixed frequency, with the other varying to change frequency ratio. In some ways this is not ideal but this method was selected early on in the experimental development and became the standard partly due to its simplicity. It has the side effect of altering the scattered wave frequency and breaking the symmetry; e.g. $a = 0.8$ does not use the same input frequencies as its inverse $a = 1.25$ with this method. Another viewpoint is that testing in this way provides more information as it could be assumed that $a = 0.8$ would give the same results as $a = 1.25$ and thus is not worth testing. Instead it is possible to observe the difference between the two by keeping one beam fixed, indicating the absolute frequency response of the mixing. This concept may be limited in practice by the bandwidth of the transducers.

When comparing modelling to experimental results the transducer bandwidths will be factored in to make the fingerprints more directly comparable. The angle of scattering, which is related to the frequency ratio, will also affect the amplitude of detection at the array since it will only detect the vertical component of the longitudinal wave, resulting in greatest sensitivity at normal incidence.

## 3.5 Samples

Several different samples were used in the testing reported here. A solid block of aluminium was used to acquire reference fingerprints of bulk mixing. The sample measured $120 \times 80 \times 60$ mm. These dimensions were selected to match those of the kissing bond sample which will be described later, and to provide a sample where the

interaction volume could fit completely inside. It was made from 2024 T351 aluminium.

Further tests on solid samples were conducted on fatigued metals. The aluminium samples were also 2024 T351 and had dimensions of $350 \times 100 \times 14$ mm. The 100 mm dimension was narrowed by 30 mm at the middle to form a 'dog bone' sample, see Figure 3.7. They were cycled in a four point bending mode to reach 40%, 60%, and 80% of their fatigue lives which was measured to be 17200 cycles of the loading defined by Ellwood (17). A reference unfatigued sample was also provided. Similar 347 stainless steel specimens were also tested, provided by Amec Foster Wheeler. Further details of these samples are provided in Chapter 5.

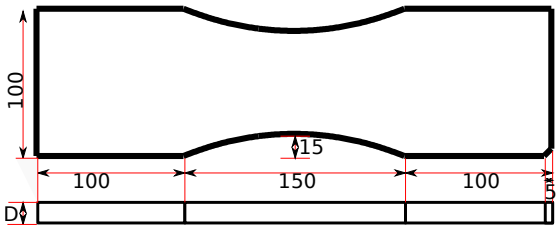


**Figure 3.7:** Diagram of the aluminium fatigue sample geometry from Ellwood's thesis (17). The sample is 14 mm thick.

A sample containing a kissing interface was made by bolting two blocks of aluminium together, Figure 3.8. This aluminium was cut from the same block as used for the reference solid block, ensuring it was nominally identical. The overall dimensions of this sample are the same as the solid one. Details of the design of this specimen are given in Section 3.8. The geometry was created based upon the loading requirements for the production of a suitable kissing interface, and dimensions that allowed for non-collinear inspection over a wide range of interaction angles.

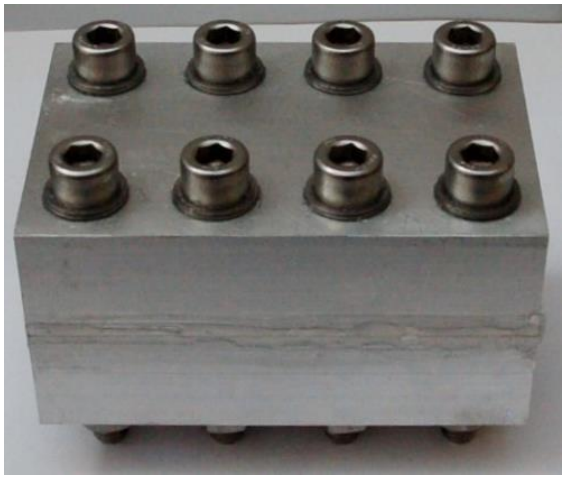

**Figure 3.8:** Photograph of bolted aluminium sample used to simulate a kissing bond. There is sealant around the loaded interface to prevent the ingress of water.

Testing was conducted with the contacting surfaces of this sample finished in two different ways. In one case the surfaces were finely ground using P1000 grit wet and dry paper (18 micron average particle size). This case is referred to as the 'rough interface'. The sample was also tested with the surfaces polished to a mirror finish using a one micron diamond suspension. Different results might be expected with different surface finishes due to changes in the fraction of the surfaces in contact and the range of angles at which they meet. The interface sample was sealed with silicone to prevent water ingress when immersed.

### 3.5.1 Material properties

In order to achieve the interaction of the desired wave modes, depth in the sample, and angle of interaction the linear material properties must be known. This is because the velocity of the input waves in the sample affects the angle of refraction at the surface. It also allows the scattering direction and time of arrival to be calculated which is necessary for post-processing of experimental data. For the modelling presented in this work the nonlinear properties were also required.

The properties of the 2024 T351 aluminium that are generally used in this work are $E = 73.1$ GPa, $\nu = 0.33$, $l = -324$ GPa, $m = -397$ GPa, $n = -403$ GPa, and $\rho = 2780$ kg.m$^{-3}$ (83). These values give a longitudinal wave velocity of 6242 ms$^{-1}$, and a shear velocity of 3144 ms$^{-1}$.

The properties of the 347 stainless steel are given as $E = 195$ GPa, $\nu = 0.27$, and $\rho = 8000$ kg.m$^{-3}$ (84). These values predict a longitudinal velocity of 5520 ms$^{-1}$ and shear velocity of 3100 ms$^{-1}$. However, the velocity of the longitudinal wave was measured at 5730 ms$^{-1}$ so this was used in the experiment and data processing. The shear wave velocity was not measured.

## 3.6 Angle and position control

There are many aspects of the experimental system that must be considered in order to achieve accurate interaction angle and position control. The motors with encoders provide good repeatability of motor rotations, and are very precise due to the high reduction ratios; 16 counts per rotation on the encoder, 1:256 gearbox on motor, and 1:40 worm gear reduction. The result is one encoder count is about $10^{-5}$ degrees of rotation of the transducer. The limitations of the system comes from the lack of absolute

reference, and friction, which is variable, in the mechanical system. In order to solve these problems a method of measuring the transducer angle for a given motor position was developed.

The angle measurement method is described in the section below but before that the backlash of the system should be mentioned. All axes of movement had significant backlash. Anti-backlash gears were used on the rotation axis but they did not appear to be strong enough to resist the friction of the system. To minimise the impact of backlash the fingerprints and testing procedures were conducted by moving the carriages out to a larger separation and the transducers were rotated further inwards than required in the following fingerprint measurement. The drives were then only moved in one direction; inwards for the carriages, and outwards pointing rotation for the transducers (i.e. towards smaller interaction angles) during the position and angle critical parts.

### 3.6.1 Angle calibration

In this procedure the transducers are fired without a sample present with the intention of hitting the array directly with the output beams. From the data collected by the array it is possible to calculate what relative angle the transducers are at by analysing the angle of the wavefronts. This results in an experimental system where the angles are relative to the rotational position of the array. This is good because the samples are positioned on top of the array, also aligning them with this reference. Care must be taken when doing these calculations to convert from the time dimension recorded by the array into a spatial dimension required for assessing the angle of the wavefronts.

It is critical for the measurement of transducer angle that the analysis is based upon the centre of the beam due to the curvature of the wavefronts. Analysis was conducted to ascertain the error caused by incorrect selection of the beam centre with the use of an FE model, Figure 3.9. It was found that under typical conditions (80 mm between transducers and array, using 5 MHz, measuring over a 16 array element window) that selecting a centre off by one array element (0.3 mm in pitch) that the beam angle will be altered by 0.02°. Experimentally the centre of the beam is found by finding the peak intensity, thus the error associated with it will be related to how noisy the time trace detected by the array is. This is just one of many factors that create uncertainty in the transducer angle, a study of the overall variation caused by them is presented below rather than attempting to assess each one individually.

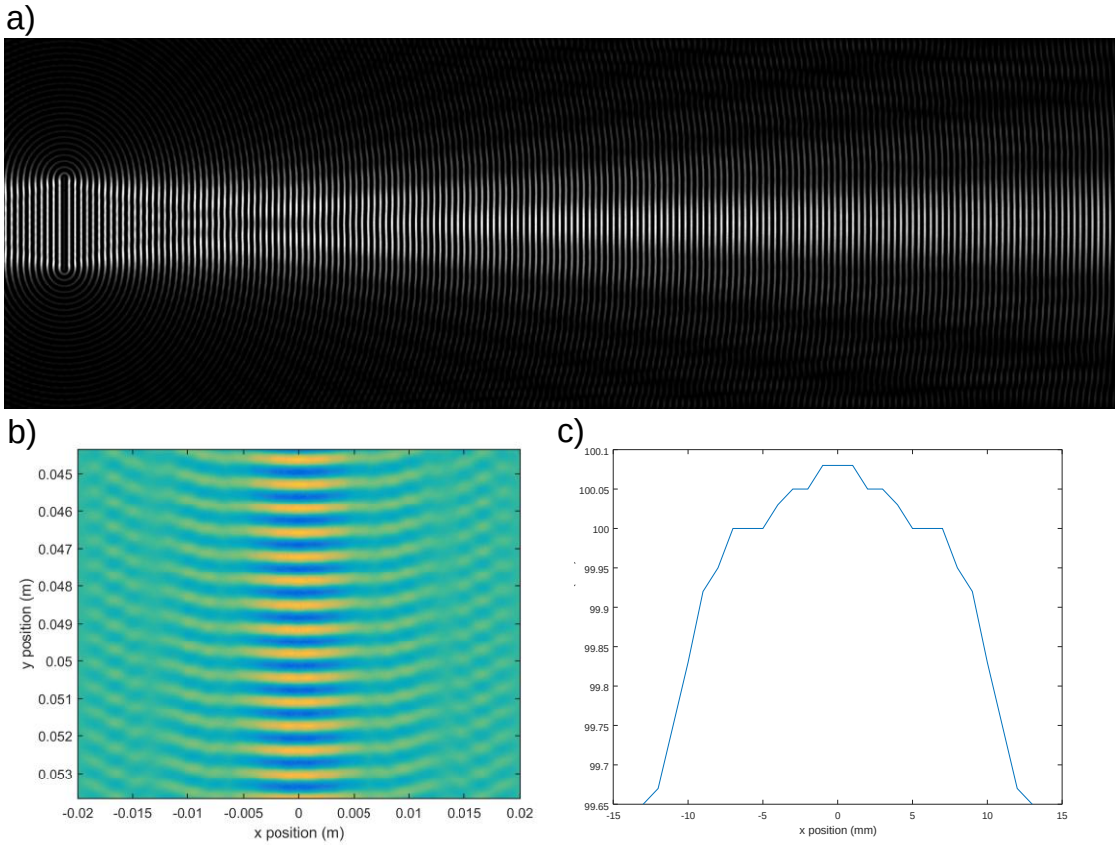


**Figure 3.9:** a) FE model of 2.25 MHz wave from 10 mm source in water, b) closer view of beam profile after 50 mm of propagation, c) analysis of wavefront position after 100 mm of propagation.

**Near field distance**

The far-field distance of the beams should be considered, in relation to peak finding, but also more generally to the way it affects the interaction volume, and scattering from it.

$$N = \frac{D^2}{4\lambda} \tag{3.1}$$

Where $N$ is the near field length, $D$ is the transducer diameter, and $\lambda$ is the wavelength. For water at 5 MHz with 10 mm transducers this length is 83 mm, and for shear waves in aluminium it is 40 mm. A combination of these lengths should be used if the beam travels through both media. For the angle calibration testing the beams only propagate through water to the array, so a distance of 83 mm or larger should be used to ensure that there are not multiple peaks in intensity in the beam profile as that could cause the measurement to be off-centre.

Some experimental tests presented in this thesis were conducted with the interaction volume closer to the input transducers than the near field length. This means that the interaction volume will have a different intensity profile from those taken at long distances. This will likely result in some minor effects such as; alteration of scattered beam profile, and changes to off-resonance bulk scattering amplitude. Comparison of fingerprints measured at different interaction depths will be presented to explore these effects.

### 3.6.2 Temperature control

The assembly was placed in a water tank, submerging the input transducers, sample, and array to minimise the coupling variation as positions were changed. The temperature of the water was controlled with 0.1°C precision to maintain a constant speed of sound in water, ensuring reliable refraction angles into the sample. To calculate the speed in water the Coppens equation was used (85). It is stated as being valid between 0°C and 35°C, 0 to 45 parts per thousand salinity, and depth between 0 and 4000 m. At a depth of zero the Coppens equation gives a velocity, $c$, of

$$c = 1449.05 + 45.7t - 5.21t^2 + 0.23t^3 + (1.333 - 0.126t + 0.009t^2)(S - 35) \tag{3.2}$$

where $t$ is temperature in degrees Celsius divided by 10, and $S$ is salinity in parts per

thousand. The salinity of the water provided in the area is limited to one part per thousand. The maximal variation in velocity caused by these levels of salinity is less than 0.01%. For 25°C degrees, 0 m depth the velocity of water is 1496.69 $ms^{-1}$.

### 3.6.3 Angle error measurements

#### Absolute error

The results presented here are from the calibration procedure performed before testing, as described above. It measures the actual transducer angles over a range of intended angles, corresponding to those required for the desired interaction angles to be used in the main non-collinear experiments. This test was conducted for interaction angles ranging from 60° to 125° in an aluminium sample, this required transducer angles from 16° to 25°. The error in these angles is shown in Figure 3.10 (a).

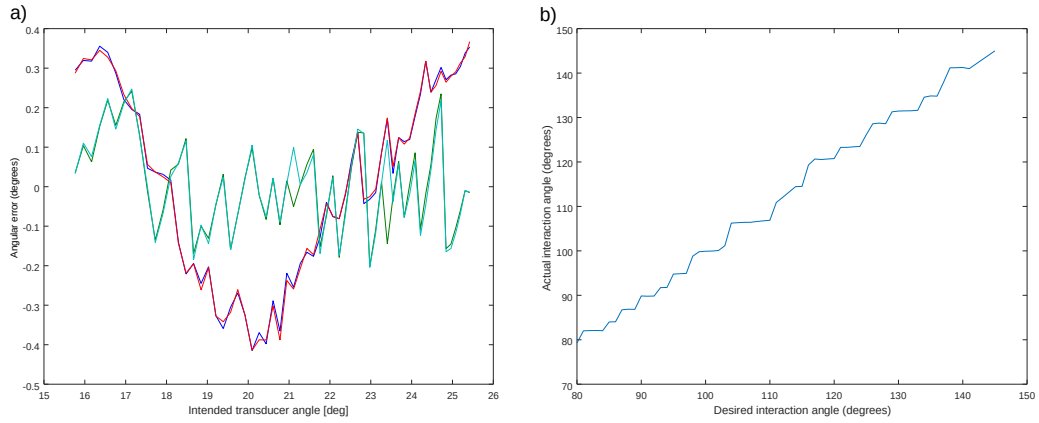


**Figure 3.10:** a) Transducer angle calibration measurements showing difference between desired angle and measured wavefront angle. Two sweeps of the angles were conducted to check for repeatability. The left transducer results are the red and blue lines, the right are the green and teal lines. b) Example from a different data set of the interaction angle that would result from the measured wavefront angles.

It can be seen in Figure 3.10 (a) that the left transducer had an overall trend of a shift towards smaller angles as the intended angle was moved closer to 20°. The right transducer did not have any significant trends except for a random variation of around $\pm$ 0.15°. This was larger than the random variations in the left transducer angle. These small errors are thought to be partly caused by stiction; static friction preventing rotation from occurring, followed by a larger amount of movement than intended once the load overcomes the friction. It is unclear what caused the large variation in the left transducer, it might also be due to friction variation as the output shaft turns.

The stiction is shown clearly by the steps in Figure 3.10 (b), it is an example of the interaction angles that would result from the errors in transducer angle (this was based on a different calibration measurement than that shown in (a) ). It can be seen in this plot that the combination of angle inaccuracies from both transducers, amplified by refraction, can result in considerable error in interaction angle, approximately $\pm 2^{\circ}$. This behaviour could result in difficulty in accurately finding peak mixing conditions unless smoothing is applied, although smoothing cannot address variations such as those seen in the left transducer of Figure 3.10 (a). As a result the fingerprint measurements are limited in absolute accuracy to around $\pm 2^{\circ}$.

### Relative error

To test the variation in interaction angle between fingerprint measurements 50 sweeps of the transducers from the $140^{\circ}$ to $80^{\circ}$ interaction angle positions were performed. The angle of the wavefronts was measured as described in the calibration section above. There was no sample in the rig, and the input transducers were spaced such that the beams from them could hit the array at all effective interaction angles. Figure 3.11 shows the resulting variation in transducer angle (note that this is not the same as interaction angle). Each coloured line in the plot represents one of the 61 interaction angles.

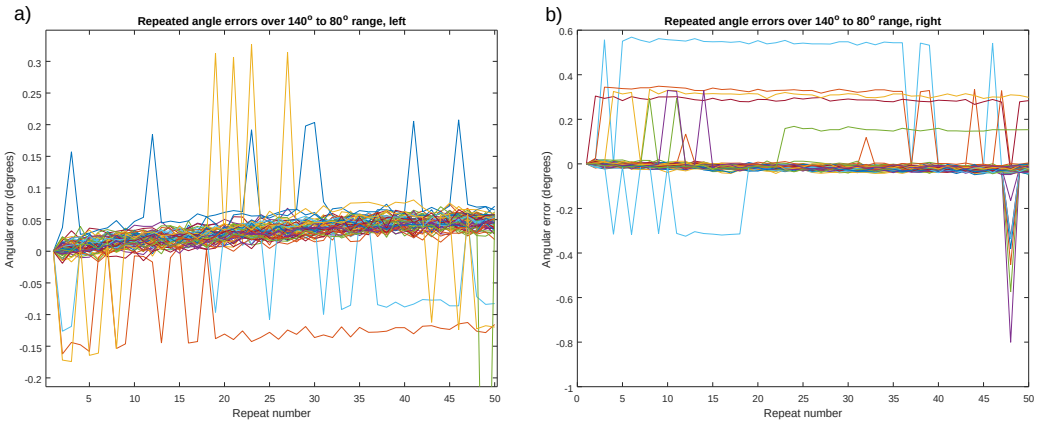


**Figure 3.11:** Difference in measured wavefront angle compared to first measurement sweep, for effective interaction angles between $140^{\circ}$ and $80^{\circ}$ with $1^{\circ}$ steps. Each angle is represented by one coloured line. a) Left transducer, b) right.

It can be seen that most of the interaction angles had a very small error, less than $0.05^{\circ}$, but other frequently jumped by $0.15^{\circ}$ or more. In some cases the starting measurement was an outlier resulting in an offset line for most of the later measurements, there is one example of this in the left results (the orange line) and many in the right. A gradual drift can be seen in the left transducer angles. It is thought that these errors are mainly due to

changes in the frictional behaviour of the transducer rotation system. Ideally, the anti-backlash sprung gears would keep themselves centered between the teeth of the worm gears, but due to friction on the output shaft there is resistance that perturbs it from this center position. Any change in the friction results in a different output angle. Changes in friction could occur due to the repeated rotation of the shaft in the bushing that alter the distribution of lubricants or other contaminants on the surfaces. The absorption of water by the plastic bushing and carriage structure, causing swelling, is also thought to contribute to the behavioral differences of the experiment due to the length of time the setup has been immersed. The transducers were cycled through multiple angle sweeps before experiments that required accurate angles, this reduced the probability of these transitions happening between the calibration measurement and the fingerprint acquisition.

A statistical analysis of this data is presented in Figure 3.12. The angular error for each interaction angle is analysed, with measurement point one being the 140° positions, and 61 the 80° positions. In the plots the boxes indicate the 25th to 75th percentiles, the whiskers are the limits of the results not considered outliers, and the crosses are outliers. These results show that the fingerprint to fingerprint variation at a particular interaction angle is generally very small, with the 50% box smaller than 0.05°. Cases where the first measurement point was an outlier were adjusted to account for this.

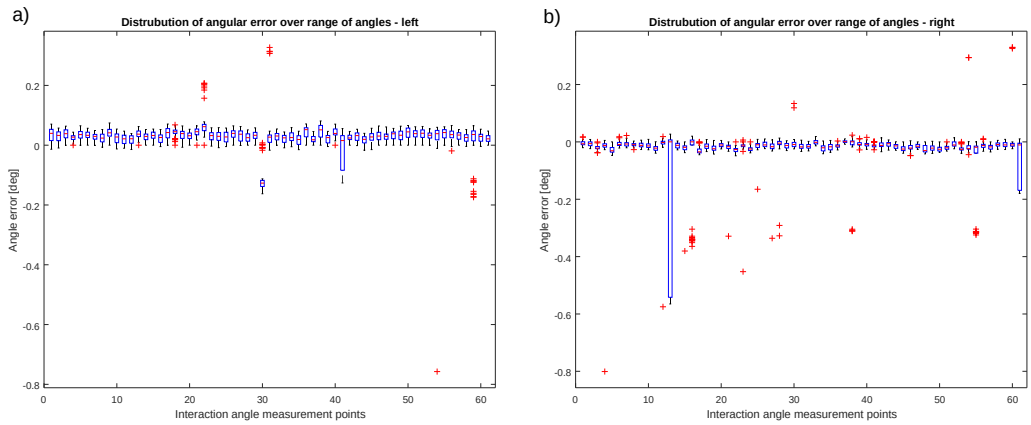


**Figure 3.12:** Variation in transducer angles for a range of interaction angle positions between 140° and 80°. Measurement point 1 is 140°, and 61 is 80°. a) left transducer, b) right transducer.

It can clearly be seen from these results that the repeatability of measurements is generally very good, there are only a few interaction angles that suffered from high variability. This should mean that the fingerprints overall are reliable but there may be points which vary significantly. Measurement point 13 of the right transducer fluctuated between two angles different by 0.5°. Accounting for the refraction of this angular error it would result in a shift of interaction angle of 2°. Therefore, the scattering amplitude

of measurements at single interaction angles should not be directly compared, instead multiple interaction angles should be measured and the response smoothed in order to remove these anomalies.

### Rotation error due to translation

The above tests were conducted with the transducer carriages at a fixed separation. As the carriages move they can rotate slightly, here the impact of that behaviour on the transducer angle is tested. A separation range of 68 mm to 42 mm to was used, tested from large to small, the same direction as the main experiment is conducted. It was limited to this range because the signal had to hit the array without rotating the input transducers. Figure 3.13 shows the resulting fluctuations in transducer angle. The angle error was tested 10 times, showing similar behaviour each time. The error appeared to gradually grow as the carriages moved before suddenly jumping back in the other direction. The left carriage error gradually moved to positive values, and jumped in the negative direction, the right carriage had the opposite behaviour. In the sign convention of the experiment positive angles correspond to rotation that would move the ultrasonic beams towards the centre of the rig. The two carriages did not jump at the same time. The maximum error was approximately 0.15°. Errors of around 0.1° were common and often occurred in the same direction on both sides resulting in a total error of 0.2°. This would cause an interaction angle error of around 1°.

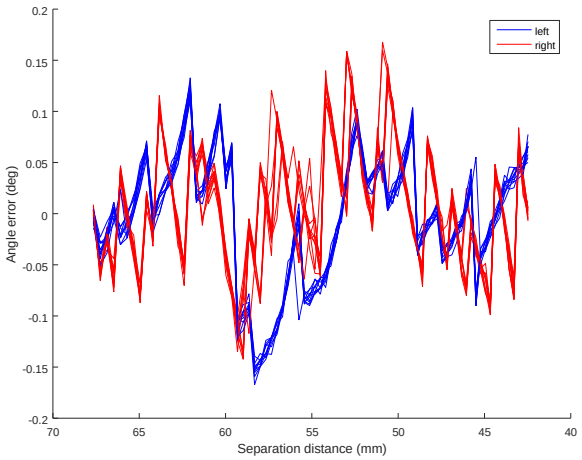


**Figure 3.13:** Change in input transducer angle due to changes in transducer separation via movement of carriages. Left transducer results shown in blue, right in red.

Overall, it can be seen that the motorised rig has significant absolute interaction angle error with a combination of the carriage wobble and the transducer rotation itself, totaling a variation of interaction angle of up to ±3°. However, it was also seen that the

relative error between tests was far smaller; the carriage movement contributed about 0.05° of variation to transducer angle, which was similar to that caused by the rotation of the transducers. Together these relative errors result in a variation in interaction angle of ±0.2°.

It might have been possible to calibrate the system to reduce the absolute angular errors, iteratively offsetting angle commands to account for the measured error, but it appeared that frictional and gear interactions would prevent significant improvements. It was decided that the limitation in absolute angle would not be a problem to the usefulness of the fingerprint testing to be conducted in this work. The focus here is more to generally understand the patterns caused by different samples, and to study the relative differences between them. The small relative error should allow this to be done with good accuracy.

An attempt was made to use the measured transducer angles to populate an irregular grid of the parameter space and then interpolate that onto a regular grid but this did not produce good results. This is likely because only the rotation measurements were included, not the error due to the separation changes. Measurement of carriage wobble over the entire range of movement is difficult due to the limited array size, but could possibly be done in the future. This correction method is not necessary to get good results because the relative error between measurements is low, but it could help to reduce the absolute error.

### Fingerprint angle analysis

Another possible way to measure the error in transducer angles is by analysis of the nonlinearly scattered beam position on the array at a frequency ratio of one. At this ratio the beam should always scatter in the direction of the bisector of the input beams. Therefore if one input beam angle varies it will shift the output by half of that change. This does not allow a direct measurement of interaction angle; if both input beams have an equal magnitude error in the same direction (inwards, or outwards) then no change in scattering direction will occur, but it does provide a rough indication of input angle error in general. In Figure 3.14 the peak position of the scattered beam on the array is plotted for a range of interaction angles. This is from testing done on mixing when the interaction volume is at the surface of the sample, discussed in Chapter 6.

It was seen in these tests that the scattered position repeatably followed the pattern seen in Figure 3.14, although different trends were seen for other periods of testing. In this case the position drifted by about 1 mm over the course of the fingerprint. The change occurred at a fairly constant rate as interaction angle was reduced from 130° until about

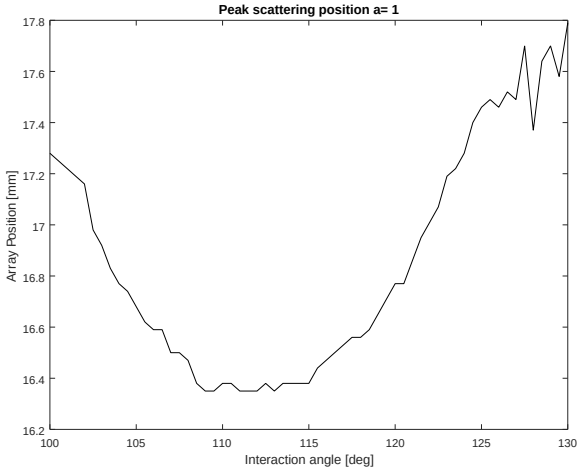


**Figure 3.14:** Position on array of peak signal from scattered pulse for a range of interaction angles at $a = 1$. Measured at 5 MHz at 0 mm deep on solid aluminium sample.

112° was reached, it then reversed direction and returned back to approximately where it started at $\phi = 100°$. The angular error of the transducers was the most likely cause of such a variation and the link becomes clear when studying the pattern in Figure 3.10. There is a drift in the left transducer of about 0.7°. At 20° incidence to the sample surface this would result in a change in the refracted angle from 47° to 49° for example. This 2° shift would result in the rotation of the interaction volume by half that, 1°. It also would cause a translation of the interaction volume. Both these effects cause a change in where the scattered pulse hits the array. For a depth of interaction of 0 mm (as in the near surface testing) the interaction volume would be shifted by about 0.5 mm, and the rotation of the volume would result in an additional shift of approximately 1 mm in the same direction. This is similar to what was observed in the peak scattering position.

The information collected above was useful in the processing of data at other frequency ratios because it provided a baseline scattering position, allowing more accurate prediction of where the scattered beam should hit the array. Knowledge and correction of this underlying error means that the spatial window can be made smaller while still capturing all the scattered signal, reducing noise.

### 3.6.4 Transducer separation error

The variation in the separation of the transducers was measured using calipers to be around $\pm 0.1$ mm. This error is mainly due to the measurement method. It is unlikely that an error of this size is significant in the testing conducted in this thesis, causing shifts in interaction volumes much smaller than the wavelengths used.

## 3.7 Amplitude variation

Another source of error in the fingerprints is the variation in the input transducers' ultrasonic amplitude. A test was devised where the transducers would be pointed at the array without the sample in place and the amplitude of the signal coming from them measured. The amplifiers required some time to achieve a stable output, shown in Figure 3.15. Before fingerprint testing at least a five minute monitoring period of the input signal amplitude was conducted to check that equilibrium had been reached. Once stable, variation was $\pm$ 0.1%.

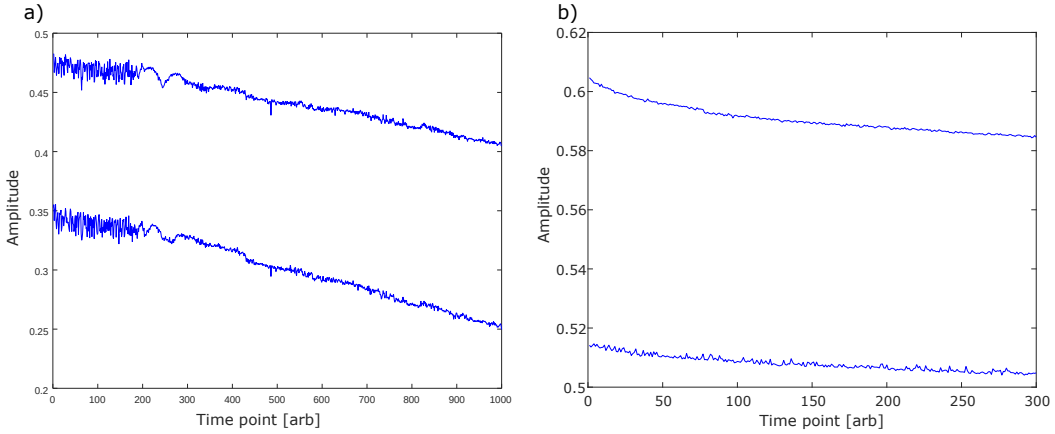


**Figure 3.15:** Signal amplitudes from left and right transducers during power stabilisation process. Each time point is roughly three seconds apart. a) 1000 measurement time points totaling 46 minutes, still not stabilised at end. b) An example of the level of stability achieved before testing commenced.

## 3.8 Interface loading

The previous sections looked at the errors involved in the ultrasonic inputs of the experiment. In contrast, this section is about the design of the contacting interface sample, including the variation in its key parameter, loading. The loading force of the kissing bond sample is controlled by the variation in torque of the bolts. The most simple and generally used equation for the relationship between torque and bolt loading is

$$T = KPD \tag{3.3}$$

where $T$ is torque, $K$ is the nut factor, $P$ is clamping load, and $d$ is the bolt diameter. Nut factors around 0.15 are typical of lubricated, mid-size, steel nuts and bolts. Non-plated, black finish steel bolts might be expected to have a factor around 0.3, resulting in twice

as much torque required to achieve the same loading. There are equations that allow for more accurate calculation of nut factor and torque but they ultimately depend on accurate knowledge of friction. This is not known well enough in this case to warrant use of these formulas. The variation in torque for different bolt types are given in (86). It states that it is $\pm 35\%$ for unlubricated bolts, and $\pm 25\%$ for lubricated bolts. These large random errors also reduce the importance of accurately predicting bolt loading with more advanced equations.

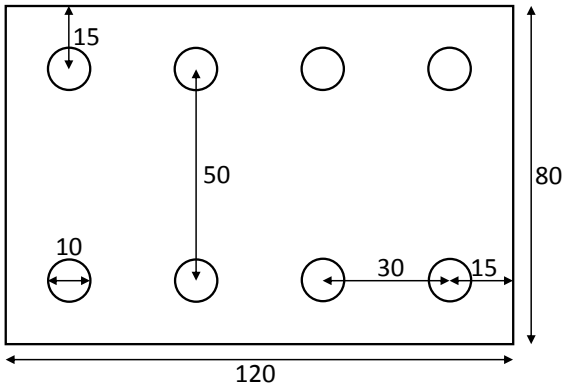


**Figure 3.16:** Dimensions of kissing interface blocks in millimeters. Each block is 30 mm thick.

In order to get even interface loading models were created in Abaqus FEA with a range of dimensions. In the final version the bolts were in two rows on either side of the sample to keep a region along the middle free for the input and output of the ultrasonic beams. This spacing was 50 mm. When using 10 mm bolts this left around 40 mm width of unobstructed sample. The modelling showed that with this bolt spacing the two aluminium plates have to be at least 30 mm thick in order to distribute the bolt loading evenly onto the centre of the interface. At this thickness the sample had to be at least 120 mm long to allow interaction angles up to 145° to be used. The resulting geometry is shown in Figure 3.16. The compressive stress at the interface calculated with the FE model is shown in Figure 3.17.

It can be seen that the load is highest along the outside edge, and that a fairly even load is obtained along the centre of the sample. Many other geometries with different numbers, spacings, and diameters of bolts were tested for comparison, but the results of these tests are not included because they were less optimal. Previous studies had used interface pressures around 2 MPa, (33), so this was set as the target mid-point for this design. The model predicted that with four bolts on each side each bolt would need to apply 3.5 KN of force to load the middle line of the interface to 2 MPa. To achieve 3.5 KN a lubricated 10 mm bolt must be torqued to 5 Nm, a reasonable amount to be applied manually with a torque wrench. This value is good because it is possible to apply an order of magnitude more force if required, and less is also possible, maximising the

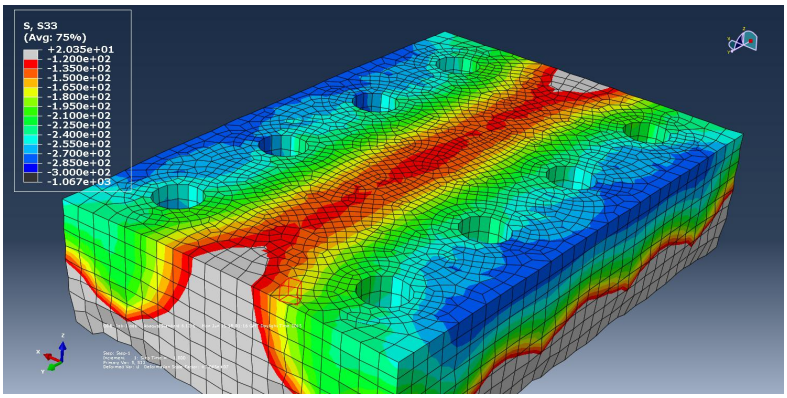


**Figure 3.17:** Distribution of load in the vertical direction due to compressive loading of two plates by bolts. The top block is hidden in this rendering allowing the interface to be observed.

testing options.

With this method of loading it is difficult to know what loading is actually being applied, the torque is the only metric. This is one major negative of this method, but hopefully it will at least provide a way to relatively adjust interface loading and offer repeatability within $\pm 25\%$. An attempt to use pressure sensitive film to determine interface load was made but it was difficult to interpret the results from this and the finite thickness of it likely meant that it was not representative of the loading that the interface would experience without it there, due to surface irregularities. A spring loaded version was also developed to allow smaller interface loads to be investigated. Ultimately this was not used for the final results but it had the benefit of measurable spring compression that indicated loading.

During the testing three different torque wrenches were used in order to cover a wider range of torques than is possible with only one. These were tested against each other to investigate if the calibration of them was accurate. They were all found to agree to within $\pm 5\%$ within their rated ranges. This error is insignificant compared to that of the load to torque relationship described above.

### 3.8.1 Acoustoelastic effect

The loading of the sample causes stresses in the sample which can alter the velocity of waves propagating through it. Using the equations of Hughes and Kelly (53), the effect of this was estimated. The calculation was done for the worst case scenario with 40 Nm bolt torque, loading the aluminium to 16 MPa in the vertical direction. This would result in up to a 0.05% change in velocity for shear waves travelling perpendicular to the loading direction and polarised vertically (this would be the case for an interaction

angle of 180°). If this worst case change in velocity is applied to an intended interaction angle of 120° it would be altered by 0.15%, which is 0.1°. This is negligible in this work.

## 3.9 Linear interface measurements

During the course of testing the interface sample a variety of linear acoustic methods were used to acquire more information about the interface. An attempt was made to measure the pulse-echo signal from each array element in order to monitor the changing transmission properties as load was varied. This was unsuccessful. The interface was highly reflective at all loads so there was little change in the received amplitude. In this the measurements appeared to be more dependent on the array-sample interface quality. This variation is part of the reason the testing in this work is focused on the shape of the fingerprints rather than the absolute amplitudes.

Much better results were achieved by using through transmission measurements of the interface. The input transducers (above the sample) were aimed such that the beam would hit the array (below the sample) for this method. Further details of this testing are given in Chapter 7 where it is used. Also presented in that chapter are the results of a reflection based c-scan of the loaded interface. The focused probe used for this produced much better results than the simple test with the array described above. Again further details are provided where relevant.

## 3.10 Summary

In this chapter the experimental concept, data acquisition, and processing were detailed. It was discussed what experimental factors affect the mixing fingerprints. The fingerprints are dependent on many things such as water temperature and transducer bandwidths. These are detailed so that consistent results can be achieved throughout this work, and future reproduction is possible. The samples that were tested in the following chapters are described, the most complex of which is the contacting interface sample which is used to simulate a kissing bond. There is a discussion of the experimental errors that results from the methods which concludes that good repeatability is achieved, despite the presence of significant absolute interaction angle error. The methods defined in this chapter are used for all the non-collinear results presented this thesis unless otherwise stated.

# Chapter 4

# Modelling Methods

## 4.1 Introduction

There are many ways of modelling the nonlinear mixing of non-collinear acoustic waves. In this work three very different methods are employed to investigate various aspects of the mixing behaviour. In order to understand what signal might be expected to come from a kissing bond it is also necessary to know what signal would be produced by the surrounding medium. Equations for the bulk mixing amplitude were derived in 1963 by Jones and Kobett, (18), but these were only valid at the 'resonant' combinations of interaction angle, $\phi$, and frequency ratio, $a$. More recently these equations have been extended to allow for scattering amplitudes to be calculated for non-resonant conditions. This extended form of the classical equations will be used to predict bulk mixing for a wide range of input beam conditions, the $\phi - a$ (interaction angle-frequency ratio) parameter space.

Another, more subjective, way of viewing the mixing behaviour is to analyse the geometry of the interference pattern of the input beams. This is the second modelling technique employed, and unlike the classical method it has applications in both the bulk and interface mixing cases, particularly for predicting the scattering angle from an interface analytically. The third method is finite element (FE) modelling. Two different FE models are used in this work, one for the prediction of mixing that occurs at the water-solid interface of the sample, Chapter 6, and another for the simulation of two elastically linear bodies forced into contact with each other to simulate a kissing bond, Chapter 7. All four models, classical, geometrical, FE surface, and FE interface, are described in the following sections.

## 4.2 Classical nonlinear solid

Non-collinear mixing caused by classical nonlinearities of the bulk material was modelled analytically in (18) and (41) using equations for the 3rd order elastic energy. These equations can be extended to off-resonance conditions to provide the desired information on bulk mixing over the entire $\phi - a$ parameter space. This extension was done by Jack Potter, a research associate in the UNDT group at Bristol, while the author was mainly involved in the checking and exploration of the model behaviour. The equation for the particle displacements of the scattered longitudinal wave at the sum frequency of the input waves is given by (18) in Equation 4.1.

$$\mathbf{u_s}(\mathbf{r},t) = \frac{(\mathbf{I}\cdot\hat{r})}{4\pi c_l^2 \rho}\int_V \sin\left[\left(\frac{\omega_1+\omega_2}{c_l}\hat{r} - \mathbf{k_1} - \mathbf{k_2}\right)\cdot\mathbf{r}' - (\omega_1+\omega_2)\left(\frac{r}{c_l} - t\right)\right] \mathrm{d}V \quad (4.1)$$

Where $\mathbf{r}$ is the position vector of the observation point relative to the centre of interaction, $\hat{r}$ is a unit vector in the direction of $\mathbf{r}$, $\mathbf{r}'$ is the position vector of an interaction point relative to interaction volume centre (a figure of these vectors is presented in (18)), $t$ is time, $c_l$ is the longitudinal velocity, $\rho$ is the material density, $V$ is the interaction volume, $\mathbf{k_1}$ and $\mathbf{k_2}$ are the input wave vectors, $\omega_1$ and $\omega_2$ are the corresponding angular frequencies, and $\mathbf{I}$ is an interaction parameter given by the following equation.

$$\begin{aligned}
\mathbf{I}\pm = &-\frac{1}{2}(\mu+\frac{1}{4}A)\,[\,(\mathbf{A_0}\cdot\mathbf{B_0})(\mathbf{k_2}\cdot\mathbf{k_2})\mathbf{k_1} \pm (\mathbf{A_0}\cdot\mathbf{B_0})(\mathbf{k_1}\cdot\mathbf{k_1})\mathbf{k_2}\\
&+(\mathbf{B_0}\cdot\mathbf{k_1})(\mathbf{k_2}\cdot\mathbf{k_2})\mathbf{A_0} \pm (\mathbf{A_0}\cdot\mathbf{k_2})(\mathbf{k_1}\cdot\mathbf{k_1})\mathbf{B_0}\\
&+2(\mathbf{A_0}\cdot\mathbf{k_2})(\mathbf{k_1}\cdot\mathbf{k_2})\mathbf{B_0} \pm 2(\mathbf{B_0}\cdot\mathbf{k_1})(\mathbf{k_1}\cdot\mathbf{k_2})\mathbf{A_0}\,]\\
&-\frac{1}{2}(K+\frac{1}{3}\mu+\frac{1}{4}A+B)\,[\,(\mathbf{A_0}\cdot\mathbf{B_0})(\mathbf{k_1}\cdot\mathbf{k_2})\mathbf{k_2} \pm (\mathbf{A_0}\cdot\mathbf{B_0})(\mathbf{k_1}\cdot\mathbf{k_2})\mathbf{k_1}\\
&+(\mathbf{B_0}\cdot\mathbf{k_2})(\mathbf{k_1}\cdot\mathbf{k_2})\mathbf{A_0} \pm (\mathbf{A_0}\cdot\mathbf{k_1})(\mathbf{k_1}\cdot\mathbf{k_2})\mathbf{B_0}\,]\\
&-\frac{1}{2}(\frac{1}{4}A+B)\,[\,(\mathbf{A_0}\cdot\mathbf{k_2})(\mathbf{B_0}\cdot\mathbf{k_2})\mathbf{k_1} \pm (\mathbf{A_0}\cdot\mathbf{k_1})(\mathbf{B_0}\cdot\mathbf{k_1})\mathbf{k_2}\\
&+(\mathbf{A_0}\cdot\mathbf{k_2})(\mathbf{B_0}\cdot\mathbf{k_1})\mathbf{k_2} \pm (\mathbf{A_0}\cdot\mathbf{k_2})(\mathbf{B_0}\cdot\mathbf{k_1})\mathbf{k_1}\,]\\
&-\frac{1}{2}(B+2C)\,[(\mathbf{A_0}\cdot\mathbf{k_1})(\mathbf{B_0}\cdot\mathbf{k_2})\mathbf{k_2} \pm (\mathbf{A_0}\cdot\mathbf{k_1})(\mathbf{B_0}\cdot\mathbf{k_2})\mathbf{k_1}]\\
&-(K-\frac{2}{3}\mu+B)\,[(\mathbf{A_0}\cdot\mathbf{k_1})(\mathbf{k_1}\cdot\mathbf{k_2})\mathbf{B_0} \pm (\mathbf{B_0}\cdot\mathbf{k_2})(\mathbf{k_1}\cdot\mathbf{k_2})\mathbf{A_0}]
\end{aligned} \quad (4.2)$$

Where $K$ and $\mu$ are the compression and shear moduli respectively, $A$, $B$, and $C$ are the third order elastic constants as defined by Landau and Lifshitz (73), and $\mathbf{A_0}$ and $\mathbf{B_0}$ are the input wave amplitudes in the direction of polarisation. For example, $\mathbf{A_0}$ and $\mathbf{k_1}$ are aligned when a longitudinal wave mode is used. The $\pm$ relates to the sum and difference frequency cases, with the plus being used for sum frequency and vice versa.

Simplifying Equation 4.2 for the sum frequency shear wave mixing case (where $\mathbf{A_0}\cdot\mathbf{k_1} = \mathbf{B_0}\cdot\mathbf{k_2} = 0$) gives

$$\begin{aligned}\mathbf{I}+= &-\frac{1}{2}(\mu+\frac{1}{4}A)\,[\,(\mathbf{A_0}\cdot\mathbf{B_0})(k_2^2\mathbf{k_1}+k_1^2\mathbf{k_2})\\ &+(\mathbf{B_0}\cdot\mathbf{k_1})(k_2^2+2\mathbf{k_1}\cdot\mathbf{k_2})\mathbf{A_0}\\ &+(\mathbf{A_0}\cdot\mathbf{k_2})(k_1^2+2\mathbf{k_1}\cdot\mathbf{k_2})\mathbf{B_0}]\\ &-\frac{1}{2}(K+\frac{1}{3}\mu+\frac{1}{4}A+B)(\mathbf{A_0}\cdot\mathbf{B_0})(\mathbf{k_1}\cdot\mathbf{k_2})(\mathbf{k_1}+\mathbf{k_2})\\ &-\frac{1}{2}(\frac{1}{4}A+B)(\mathbf{A_0}\cdot\mathbf{k_2})(\mathbf{B_0}\cdot\mathbf{k_1})(\mathbf{k_1}+\mathbf{k_2})\end{aligned} \tag{4.3}$$

Using the following conventions for the directions of the waves in combination with Equations 4.1 and 4.3

$$\begin{aligned}\mathbf{k_1}=\omega/c_t[0,1] \quad \mathbf{k_2}=\omega/c_t[\sin\phi,\cos\phi]\\ \mathbf{A_0}=X_1[1,0] \quad \mathbf{B_0}=X_2[\cos\phi,-\sin\phi]\end{aligned} \tag{4.4}$$

where $X_1$ and $X_2$ are input wave amplitudes, allows an equation for the scattered wave pattern to be derived. This equation does not include an observation distance term since only the relative amplitude is of interest here, it is accurate in the far-field.

$$X_3(\theta)=\frac{X_1X_2V\omega_1^2\omega_2}{4\pi\rho c_t^3c_l^2}\Delta(\theta)\chi(\theta) \tag{4.5}$$

Where $\theta$ is the observation angle, and $\Delta(\theta)$ and $\chi(\theta)$ are called the nonlinear directional amplitude function and geometric directional amplitude function respectively. They are described below. The geometric function, $\chi(\theta)$, is dependent on the shape of the interaction volume. Multiple different types of volumes were modelled in order to find a balance between speed and accuracy. It is also interesting to observe how the interaction shape affects the scattering. The most simple case was the cubic interaction volume, for this an exact solution can be found for the diffracted wave pattern.

$$\chi(\theta)=\frac{4\sin\left[R\left(\frac{\omega_1+\omega_2}{c_l}\cos\theta-\frac{1}{c_t}(\omega_1+\omega_2\cos\phi)\right)\right]\sin\left[R\left(\frac{\omega_1+\omega_2}{c_l}\sin\theta-\frac{\omega_2}{c_t}\sin\phi\right)\right]}{V\left(\frac{\omega_1+\omega_2}{c_l}\cos\theta-\frac{1}{c_t}(\omega_1+\omega_2\cos\phi)\right)\left(\frac{\omega_1+\omega_2}{c_l}\sin\theta-\frac{\omega_2}{c_t}\sin\phi\right)} \tag{4.6}$$

Where $R$ is half the side length of the square profile, and $V$ is the volume of interaction. The square is defined such that two of the sides are parallel to the reference input beam direction of propagation. This was required to reach a closed form solution.

For a cylindrical interaction volume (with the circular profile in the plane of interaction) a slightly more computationally intensive solution is found.

$$\chi(\theta) = \int_0^{2\pi} \frac{\sin\left[R\left(\frac{\omega_1+\omega_2}{c_l}\cos\theta - \frac{1}{c_t}(\omega_1+\omega_2\cos\phi)\right)\cos\theta_i + R\left(\frac{\omega_1+\omega_2}{c_l}\sin\theta - \frac{\omega_2}{c_t}\sin\phi\right)\sin\theta_i\right]}{\left(\frac{\omega_1+\omega_2}{c_l}\cos\theta - \frac{1}{c_t}(\omega_1+\omega_2\cos\phi)\right)\cos\theta_i + \left(\frac{\omega_1+\omega_2}{c_l}\sin\theta - \frac{\omega_2}{c_t}\sin\phi\right)\sin\theta_i} d\theta_i \quad (4.7)$$

Where $\theta_i$ is the integration angle around the circle.

Thirdly an interaction type was made with the volume defined by the overlap of two cylinders at an arbitrary angle, $\phi$, representing the input beams. This is referred to as 'real' in this work and the geometric function for it is:

$$\chi(\theta) = \iiint_V \cos\left[\left(\frac{(\omega_1+\omega_2)\cos\theta}{c_l} - \frac{\omega_1+\omega_2\cos\phi)}{c_t}\right)y + \left(\frac{(\omega_1+\omega_2)\sin\theta}{c_l} - \frac{\omega_2\sin\phi)}{c_t}\right)x\right] dxdydz \quad (4.8)$$

For each of these volume types the size is defined by a 'radius' parameter. In the cubic case each edge of the square is two times this radius long, for the cylindrical volume the radius is that of the circle, and for the 'real' case it is the radius of the cylindrical input beams.

The final remaining term in Equation 4.5 is the nonlinear spatial amplitude function. As the name suggests, this term accounts for the impact of the TOECs on the scattering behaviour. It is given by

$$\Delta(\theta) = F_c(K,\mu,A,B,a,\phi)\cos\theta + F_s(K,\mu,A,B,a,\phi)\sin\theta \quad (4.9)$$

where $F_c$ and $F_s$ in the shear-shear in-plane polarisation case is

$$\begin{aligned} F_c = &-\frac{1}{2}(\mu+\frac{1}{4}A)(\cos\phi(a+\cos\phi) - \sin^2\phi(1+2a\cos\phi)) \\ &-\frac{1}{2}(K+\frac{1}{3}\mu+\frac{1}{4}A+B)\cos^2\phi(1+a\cos\phi) \\ &+\frac{1}{2}(\frac{1}{4}A+B)\sin^2\phi(1+a\cos\phi) \end{aligned} \quad (4.10)$$

$$\begin{aligned} F_s = &-\frac{1}{2}(\mu+\frac{1}{4}A)(2a\cos^2\phi\sin\phi - a\sin\phi) \\ &-\frac{1}{2}(K+\frac{1}{3}\mu+\frac{1}{4}A+B)a\cos^2\phi\sin\phi \\ &+\frac{1}{2}(\frac{1}{4}A+B)a\sin^3\phi \end{aligned} \tag{4.11}$$

The above equations can be used to calculate the scattered amplitude, $X_3$, for any combination of interaction angle or frequency ratio. In this work the interest is in what the behaviour looks like away from resonance though it is worth briefly describing how the resonant conditions were found by Jones and Kobett in relation to this model. As stated in (18) the terms, which are grouped into the geometric function in this work, give an integrand that oscillates unless $[(\omega_1+\omega_2)/c_l]\hat{\mathbf{r}} - \mathbf{k_1} - \mathbf{k_2} = 0$. This results in a resonance equation for the interaction of two shear waves producing a sum-frequency longitudinal of

$$cos\phi = c^2 + \left(\frac{(c^2-1)(a^2+1)}{2a}\right) \tag{4.12}$$

where $c$ is the velocity ratio between transverse and longitudinal waves $c_t/c_l$, $a$ is the frequency ratio $\omega_1/\omega_2$. This relationship can also be found by requiring that both momentum and energy are conserved in the scattering.

The model described in this section will be used in the following chapter to investigate non-collinear mixing in general, but particularly how the scattered amplitude changes as the input conditions move away from resonance. It was found that the cylindrical interaction volume produced more logical results than the cubic interaction volume, and was much faster than the 'real' volume. The testing that lead to these conclusions is described in Chapter 12, Appendix B. All of the results presented in Chapter 5 use the cylindrical interaction volume unless otherwise stated.

## 4.3 Geometric interpretation

In the section above resonance occurs when both conservation of momentum and summation of frequencies requirements are met. Another way of looking at what conditions might cause mixing to occur is to observe the interference pattern of the input beams. By looking at the nodal pattern formed it is possible to understand why some combinations of interaction angle and frequency ratio allow for the creation of the third beam. Note that the theory presented in this section is not related to the geometric

term in the classical modelling above. That term is about the integral over the interaction volume while the geometry discussed here is that of the overlapping wavefronts for any arbitrary volume.

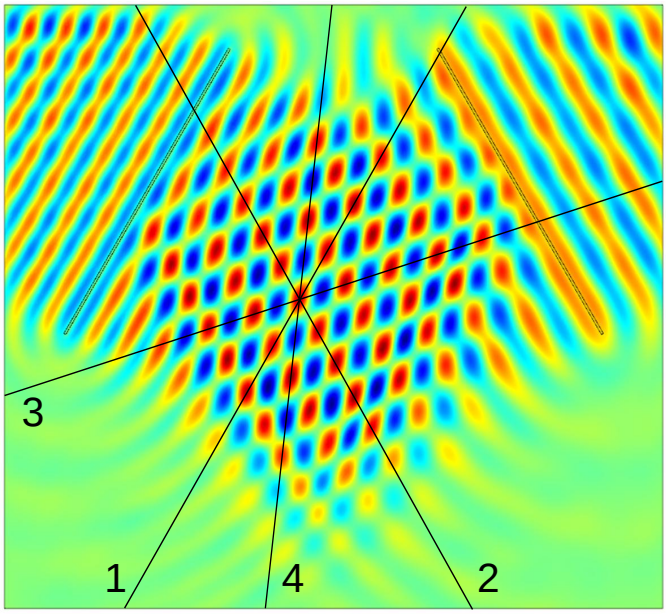


**Figure 4.1:** FE simulation of interference pattern due to two overlapping shear waves. The two sources are in the top half of the frame on either side and the time point is chosen such that the waves have propagated through the interaction area but no further. Lines have been drawn to show the four key axes of the interference pattern; 1 and 2 are at the input beams' wavefront angles, 3 and 4 are the created possible axes for new nonlinear mixing wavefronts. The colour scale represents the stress in the vertical direction with red being positively stressed (compressive) and blue negatively (tensile).

The array of overlap points formed always has four axes in which a pattern of straight lines can be seen, as shown in Figure 4.1. Two of these orientations of lines correspond to the input beams, the other two orientations are the possible orientations in which new beams' wavefronts could be created. If the requirement for the scattered wave to be at the sum or difference frequency of the input waves is applied to this, and the wave velocity for the output mode is known then a scattered wavelength can be calculated. For bulk mixing to occur it is logical that this wavelength must match the nodal spacing in one of the secondary orientations. The spacing and orientation of the nodes and lines can be calculated using trigonometry with frequency ratio and interaction angles as independent variables. The derivation of this geometric formula is as follows.

By approximating the pattern into a series of straight lines representing the wavefronts and the places they overlap being constructive regions of interference it is possible to calculate the geometry of these constructive points, Figure 4.2. The exact application of the geometric model to bulk mixing and interface mixing will be discussed in

the following chapters but a brief explanation is given below in order to explain the significance of the overlapping lines. In the case of bulk mixing it is the constructive interference points that can be thought of as the sources of the mixed wave since they have the highest stresses so are strongly affected by the material nonlinearity. In the case of CAN interface mixing it is actually the regions of destructive interference that are mainly the sources. This is explained in Chapter 7. In either case the geometric model remains the same as the selection of what phase the wavefronts represent is arbitrary and need not be consistent between the two input waves (this allows for selection of constructive or destructive phase points).

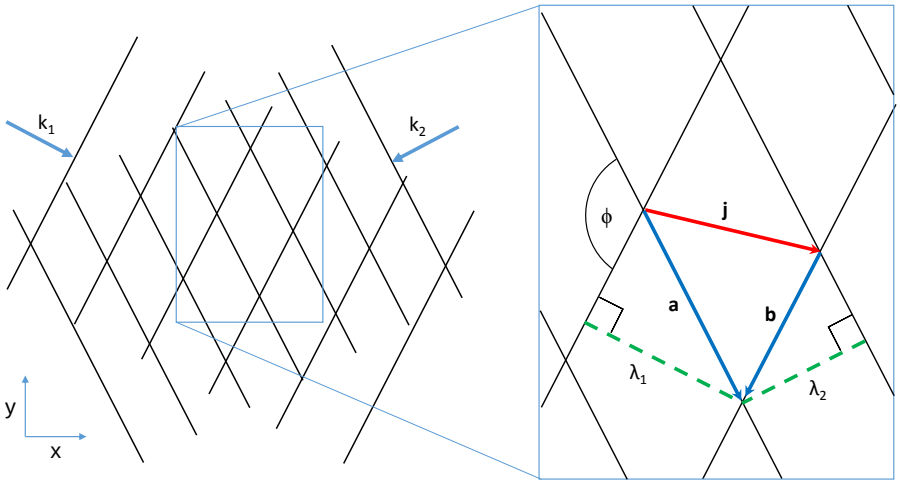


**Figure 4.2:** Approximation of non-collinear mixing with straight lines indicating wavefront of input beams. The expanded section details the interaction angle, $\phi$, input wavelengths, $\lambda_1$ and $\lambda_2$, and the resulting vectors, **a**, **b**, and **j** that link the overlap points.

In Figure 4.2 the wavefronts are depicted for a small section of the interaction volume. The translation from one nodal point to its horizontal neighbour to the right is labeled **j**. This vector is given by $\mathbf{j} = \mathbf{a} - \mathbf{b}$ as defined in the figure. Vectors **a** and **b** can be thought of as the projections of the input beam wavelengths onto the wavefronts of the opposite beam. As such the lengths are given by

$$|\mathbf{a}| = \frac{\lambda_1}{\sin(180-\phi)} = \frac{\lambda_1}{\sin(\phi)} \tag{4.13}$$

$$|\mathbf{b}| = \frac{\lambda_2}{\sin(180-\phi)} = \frac{\lambda_2}{\sin(\phi)} \tag{4.14}$$

Resolving these into $x$ and $y$ directions shown on Figure 4.2 gives

$$\mathbf{a} = |\mathbf{a}|(\cos(\phi/2)\hat{\mathbf{x}} - \sin(\phi/2)\hat{\mathbf{y}}) \tag{4.15}$$

$$\mathbf{b} = |\mathbf{b}|(-\cos(\phi/2)\hat{\mathbf{x}} - \sin(\phi/2)\hat{\mathbf{y}}) \tag{4.16}$$

Therefore, **j** can be expressed as

$$\mathbf{j} = \frac{\lambda_1 + \lambda_2}{\sin(\phi)}\cos(\phi/2)\hat{\mathbf{x}} - \frac{\lambda_1 - \lambda_2}{\sin(\phi)}\sin(\phi/2)\hat{\mathbf{y}} \tag{4.17}$$

With these equations for the spacing of the nodes it is possible to derive further equations that allow for the prediction of angle of scattering and resonance conditions. Examples of the derivations and calculations for bulk mixing are presented in the following section, while work related to interface mixing is presented in Chapters 6, 7, and 8.

### 4.3.1 Bulk mixing prediction

#### Bulk resonance

Above it was mentioned that it is reasonable to assume that mixing will occur when the spacing between lines labelled 3 or 4 in Figure 4.1 is equal to the predicted wavelength of the scattered wave. Mixing in the orientation labelled 4 is not expected in the real world for the sum frequency case due to conservation of momentum limitations, however, this direction is likely relevant to the difference frequency case, but that will not be investigated here.

The spacing between the lines oriented in the 3-direction is given by the vector that relates nodal points that are above each other, in contrast to **j** which was the horizontal relation. This new vector, **l**, is equal to $\mathbf{a} + \mathbf{b}$ which expands to

$$\mathbf{l} = \frac{\lambda_1 - \lambda_2}{\sin(\phi)}\cos(\phi/2)\hat{\mathbf{x}} - \frac{\lambda_1 + \lambda_2}{\sin(\phi)}\sin(\phi/2)\hat{\mathbf{y}} \tag{4.18}$$

Therefore resonance might be predicted to occur when $|\mathbf{l}| = \lambda_3$. This is inaccurate however because the higher order stress terms are proportional to the square of displacement so two peaks occur for every input wavelength. This results in the required length being halved. This can be visualised in Figure 4.1 as the blue and red regions being equivalent in terms of being sources of nonlinear scattering, while **l** relates nodes of the same colour. For the case where $a = 1$ a solution was found.

$$2\lambda_3 = \frac{\lambda_1}{\cos(\phi/2)} \tag{4.19}$$

By expressing $\lambda_3$ in terms of velocity ratio, $c$ (which is $c_t/c_l$) and $\lambda_1$ the resonance case for $a = 1$ is found to be

$$\phi = 2\cos^{-1} c \tag{4.20}$$

Using the properties of aluminium listed in the previous chapter gives a resonant interaction angle of 119.5°. This can be compared with the classical resonance conditions, Equation 4.12, which, when $a = 1$, reduces to

$$\phi = \cos^{-1}(2c^2 - 1) \tag{4.21}$$

Equations 4.20 and 4.21 are trigonometrically identical. This demonstrates that by looking at the interference pattern formed by the overlap of the two beams and the conservation of energy ($\omega_3 = \omega_1 + \omega_2$) it is possible to conclude the interaction angle that will cause optimal mixing. It would be good to prove that the geometric equations can be extended to the arbitrary frequency ratio case, but this is not required here as it does not give any information that cannot be obtained from the classical equations.

**Bulk scattering direction**

The vector **j** calculated earlier gives the orientation of the line labelled 3 in Figure 4.1. It is supposed that scattering will occur in the direction perpendicular to this due to the wavefronts being created in the **j** angle. If this is the case then the angle of scattering can be found from the relative magnitudes of the x and y components of **j**.

$$\theta = \tan^{-1} \frac{j_y}{j_x} \tag{4.22}$$

Where $\theta$ is the angle of scattering, relative to the y-axis. The above gives

$$\theta = \tan^{-1} \frac{1-a}{1+a} \tan(\phi/2) \tag{4.23}$$

which is exactly the same as the solution found classically from the summation of k-vectors. It is good to see that the geometry of the interference pattern leads to the same conclusion as the momentum summation despite taking quite a different route. Although this result does not tell us anything new it gives confidence in the further extensions of this geometric model that will be used in later chapters.

### 4.3.2 Geometric model conclusions

It has been shown that the geometry of the interference is a valid alternative route for the qualitative prediction of bulk mixing behaviour. It lacks objective output so is limited in comparison to the relations derived by Jones and Kobett (18). It also offers little insight into off-resonance behaviour, only suggesting that the scattering angle of bulk mixing might be in the classical momentum conserving direction. The model's real potential is in the prediction of mixing at an interface, such as a kissing bond. It is possible to assess the way the nodes move and overlap with an interface to predict if mixing is possible and at what angle the beam will be output. This angle is not necessarily the same as that given by the classical formula as will be shown in Chapter 6. Concepts explored there are also used and extended further in Chapters 7 and 8.

## 4.4 Finite element modelling

Finite element modelling was used for two different cases; one was to model the fingerprint that would be produced by a contacting interface without the effects of bulk nonlinearity, the other was to investigate some unexpected experimental behaviour when the interaction volume was near the surface of the sample. The former model will be discussed first. FE modelling was used for this work because it does not rely on as many approximations as the previous models, allowing it to model the real world more accurately. This includes the ability to simulate beams of finite width and pulse length. Neither of these features were included in the previous models.

### 4.4.1 Kissing interface model

The model was made by Blanloeuil et al. and is reported in many publications (4; 5; 6; 15; 16; 57; 69). It was run by Blanloeuil for a geometry and parameter space requested by the author. The processing of the particle velocities of the model into the fingerprint was conducted by the author. This ensured that the same processing method was used for both the experimental and modelled data.

The following is a section about the FE model from a paper written by the the author, Blanloeuil, Croxford, and Potter (87).

The nonlinearity of the kissing interface is very different from the classical bulk nonlinearity, as such it is not obvious based upon previously established theory that the interface would cause two incident shear waves to interact to produce a scattered

longitudinal wave. The modelling conducted using this model in Chapter 7 shows that a kissing interface can cause non-collinear mixing, as others have done previously, and it explores the parametric sensitivity of the mixing.

The behaviour of a contacting interface requires a model that can accurately capture three interface states, strongly closed (transferring transverse and normal stresses), slipping (transferring only normal stress), and open. This was achieved using a 2D plane strain FE model. The model is similar to the one reported in (4), with differences in terms of geometry and incident frequencies. The main characteristics of the FE model are detailed below for completeness. This model does not include the higher order elastic terms so classical bulk mixing should not occur.

The two contacting aluminium blocks were 120 $\times$ 30 mm and modelled as homogeneous and isotropic solids, with Young's modulus $E = 69$ GPa, Poisson coefficient $\nu = 0.33$ and density $\rho = 2700$ kg.m$^{-3}$. Clamped boundary conditions were imposed on both left and right faces of the blocks to prevent any body motion, while input excitations were imposed on the top face of the assembly and output displacements were recorded at the bottom face. More precisely, two incident shear waves were generated, to match experiments, from the top face by imposing nodal displacement along the x-axis over 10 mm long segments, and appropriate time-delays were used to generate the waves with the desired angle of incidence. Additionally, the spacing between the excitation sources was always chosen to ensure intersection of the incident beams at the contact interface. The angle between the incident beams was varied from 50° to 110° in 5° steps. The left shear wave had a fixed frequency of 2 MHz, whereas the right shear wave had a frequency between 1.2 MHz and 3 MHz giving frequency ratios between 0.6 and 1.5 in increments of 0.1. A centre frequency of 2 MHz was used in the FE model instead of the 5 MHz used for most of the experimentation to maintain reasonable computation time, since high frequencies impose small element dimensions which require smaller time steps and thus larger computation time. Both incident shear waves were 8-cycle sinusoidal Hann-windowed tone bursts regardless of the excitation frequency. Note that when varying the frequency of the right source, the angle between the incident beams was kept fixed. If CAN is activated, a longitudinal wave is expected to propagate toward the bottom face. Displacements were recorded along the bottom face and post-processed in the same way as experimental signals, as detailed in Chapter 3. Measurements could also have been taken from the top surface but the aim was to mimic the experimental method as closely as possible. Previous work by Blanloeuil et al. showed this modelling technique predicts a backwards propagating scattered wave (4).

The modelling of the contact interface between the two solids must account for CAN. In the FE model, a unilateral contact law with Coulomb's friction was considered between the two solids, with a coefficient of friction $\mu = 0.5$. Thus, three states can be observed simultaneously at different locations along the interface: open interface, frictional sliding contact and closed interface. Moreover, a static compression stress $\sigma_0 = -0.05$ MPa was introduced in the definition of the contact laws to account for external compression of the system. The contact laws are defined in (4) and represent a simplified model of the contact interface that captures the essential contribution of contact dynamics to the scattering response as done previously in (4; 5; 88).

The FE model was obtained from the discretisation of this geometry and the resolution was done using the 2D FE code Plast2 (89; 90). A comparison between Plast2 and Abaqus for large deformation contact problems is presented in (91). In Plast2, the solution is evaluated in the time domain with contact algorithms formulated using the forward Lagrange multipliers method (92) which enables the use of Lagrange multipliers in a time explicit integration. More precisely, the contact equations are respectively satisfied at time $t$ and $t + \Delta t$. To make this possible, the contact equations are solved using a Gauss-Seidel iterative solver. The global method is thus semi-implicit and the time step is subject to the Courant-Friedrichs-Lewy (CFL) stability condition $\Delta t \leq a_{min}/c$, where $a_{min}$ corresponds to the smallest element dimension and $c$ to the longitudinal wave velocity in the medium. The spatial discretisation is essential in the FE method. In order to have an accurate solution, the wavelength of the highest frequency component of interest should be sufficiently discretised. As the frequency of the scattered longitudinal wave is equal to the sum of incident frequency, its maximum value is thus 3.5 MHz and the corresponding wavelength is close to 1.7 mm. Therefore, a regular mesh was constructed with 0.1 mm square elements, thus ensuring a sufficient discretisation of the wavelength for both the incident shear waves and the scattered longitudinal wave. The mesh was made only of fully integrated quadrangle elements of type $Q_1$ (93). To satisfy the CFL stability condition for the current mesh dimensions, the time step was set to $\Delta t = 3$ ns.

The model consisted of 720000 elements, 723002 nodes (each node has 2 degrees of freedom) and took about 11 hours to solve for each parametric point on an average desktop PC. Since 130 different points in the parameter space were investigated over 1000 hours of computation time was required to generate the fingerprint. The code does not currently make use of parallel or GPU computing so it might be possible to reduce the time requirements by these methods in the future. Since the model used for this work is presented in other publications further details will not be shown or discussed here.

The fingerprints that resulted from this model are presented in Chapter 7.

### 4.4.2 Near-surface modelling

In contrast to the model described in the section above, which only included interface nonlinearity, the aim of the near-surface modelling was to include many possible sources of nonlinearity. The reasoning for this is made clearer in Chapter 6 but, in short, scattering of unknown origin was observed experimentally when the interaction volume was near the surface and no literature could be found that explained it. Therefore, a model that replicated many features of the experiment was designed in the hope that it would also show this behaviour and allow the source to be examined in detail.

To create this model COMSOL was selected due to its ability to combine multiple physics types, such as the pressure acoustics of the water and the solid mechanics of the sample. It also included a module that allowed hyperelastic solids to be modelled which was required to simulate bulk mixing, which might have been related to the near-surface mixing. The model was run using LiveLink for MATLAB which allowed the geometry to be generated according to the interaction angle requirements, and fed the nodal displacement information back into MATLAB from the COMSOL server to allow it to be processed as if it were data captured from the experimental array.

The details of this model are described in Chapter 6 and further validation of it is presented in the Appendix.

## 4.5 Summary

This chapter has summarised the many different modelling strategies that were used in this work. They ranged from simple geometry based models, which are used to investigate bulk resonance and scattering angles, to advanced FE models including many different physics elements in an attempt to understand a previously unreported mixing phenomenon. The next chapter will use two of the models detailed above to study the behaviour of bulk mixing, and compare their predictions with experimental measurements.

# Chapter 5

# Bulk material mixing

## 5.1 Introduction

The literature review demonstrated that while work has been done on the behaviour of non-collinear mixing in solid materials and at interfaces there is a lack of understanding about the behaviour away from resonance in both cases. It has been shown that in the case of aluminium for example the bulk mixing should be strongest at an interaction angle of around 120°, and an interface should produce most mixing at 90°. This would allow the two behaviours to be studied in isolation provided they do not occur over a wide range of interaction angles. In this case the bulk mixing signal strength could be used as a baseline indicator of the amplitude of the input waves reaching the interaction volume and could be compared with the strength observed at the optimal CAN mixing conditions, creating a robust measurement of the presence of a kissing interface.

However, if the bulk mixing is produced over a wide range of interaction angles the separation of the two effects becomes more difficult. In order to interpret the $a - \phi$ (frequency ratio - interaction angle) parameter space fingerprint in this case a good understanding of the bulk mixing is required to prevent it from obscuring the signal from the kissing interface.

The first step in improving the knowledge of the bulk mixing behaviour is developing the tools to model it at conditions away from resonance. This was mainly conducted by Jack Potter, using an extended form of the equations present in the seminal works of Jones and Kobett (18). This model allows the parameters which shape the fingerprint to be investigated and it predicts the ranges over which interesting behaviour might be observed. Experimentally it is difficult to measure over a wide range of interaction angles and frequency ratios so the guidance of the modelling is needed when designing the layout of the apparatus.

Experimental testing can then be used to test the validity of the model and to investigate other real world factors that affect the fingerprints. These results should provide the benchmark of a sample with no kissing defects for comparison with later interface work, and will inform whether interference with CAN mixing signals would be expected or not. More detailed analysis of the scattered beam properties is also included in this chapter, such as beam width and scattering direction. This information is useful in determining how the raw data should be processed to produce reliable and informative fingerprints.

The final part of this chapter looks at the possibility of using the technique to detect fatigue, something that has been investigated in terms of amplitude of response at resonance in the past but never by using data gathered over the wider $a - \phi$ parameter

space. It is unknown if more information about the fatigue state may be contained within this parameter space. This work was also partly conducted to test and refine the methodology, as a result of the testing many improvements were made to the experimental procedures. During these tests on thin fatigue samples (14 mm thick) some interesting behaviour was noticed when the input beams overlapped near the surface that led to further investigation being required. That work is presented in Chapter 6.

## 5.2 Classical Nonlinear Solid Modelling

Numerical modelling was undertaken in order to determine the effects of classical nonlinearity on the wave mixing parameter space. This modelling is useful to inform which areas of the $a$-$\phi$ parameter space are likely to be of interest so that the experiment can be designed to include these ranges.

In this section the equations derived in Chapter 4 will be further explored to understand how the various parts impact the fingerprint that would be formed from the mixing of two shear waves in a solid material with nonlinear elasticity. As was stated previously the key equation that defines the expected scattered wave amplitude at a particular observation angle, $\theta$, is

$$X_3(\theta) = \frac{X_1 X_2 V \omega_1^2 \omega_2}{4\pi\rho c_t^3 c_l^2} \Delta(\theta)\chi(\theta) \tag{5.1}$$

where $X_1$, $X_2$, and $X_3$ are the two input wave amplitudes and scattered wave amplitude respectively, $\omega_1$ and $\omega_2$ are the input frequencies, $\Delta(\theta)$ is the nonlinear directional amplitude function, and $\chi(\theta)$ the geometric directional amplitude function (also referred to as geometric weighting term). Both of these directional functions were derived previously. The directions defined in this work are such that an observation angle of zero is in the direction defined by the bisector of the two input beams and is in the direction of forwards propagation.

Knowledge of the experimental geometry, apparatus, and processing techniques is used in the production of modelled results that more accurately relate to the experimental measurements. Many factors such as transducer bandwidth, mode conversion at the water-aluminium interface, and interaction volume have significant impacts on the resulting fingerprints so are included, where stated, in many of the following results.

### 5.2.1 Geometric directional amplitude function

This section seeks to understand the behaviour of $\chi(\theta)$, the geometric directional amplitude function. This will be done by using the equations derived in Chapter 4 to observe its contribution to the beam shape and response to changes in interaction angle, interaction volume, and input frequency.

In Figure 12.3 the effects of interaction radius and frequency are shown for a few examples in the cylindrical volume case. This figure shows the expected angular distribution of the scattered beam over a range of interaction angles. The material properties used for this model were $E = 70$ GPa, $v = 0.33$, $\rho = 2780$ kg.m$^{-3}$, $a = 1$. The reference input frequency, $\omega_1$, and the radius of the interaction cylinder are shown in the figure. Values were chosen to be similar to those used in the experimental investigations shown later in this chapter. It can be seen that the geometric function peaks at $\phi = 120^\circ$ and a scattering angle of $0^\circ$ as would be expected from classical predictions. This is true for all interaction volume sizes and frequencies.

Away from the peak (the resonance) interaction angle the beam splits into two equal amplitude lobes in places. The beam pattern is related to the ratio between the frequency and the inverse of the interaction radius; doubling the frequency while halving the radius results in the same pattern, as shown in Figure 12.3 (a) and (c).

Also included in the right column of Figure 12.3 is a summation over all observation angles. This simulates the extreme case of the experimental method where a scattering amplitude value is taken from the summation over a spatial window. In practice the window size was set much narrower than this, to approximately the width of the central lobe of the beam, because increasing it further added more noise to the summation without a significant gain in signal amplitude. This concept is discussed in more detail in Appendix B. The model did not produce a valid result (due to a division by zero) when $\phi = 108^\circ$ and $\theta = 180^\circ$ so there is a gap in the summation for this case. It can be seen that the summation smooths out the off-resonance lobes in the geometric weighting term but it does not remove them completely.

Further investigation of the geometric weighting term is presented in Appendix B, including analysis of the other interaction volume types, and the amplitude responses they have to changes in frequency and radius. Broadly, they give similar patterns as the cylindrical results presented above, and this is only one minor factor in the fingerprint pattern so the further understanding is not required for interpretation of the rest of this modelling and experimental work.

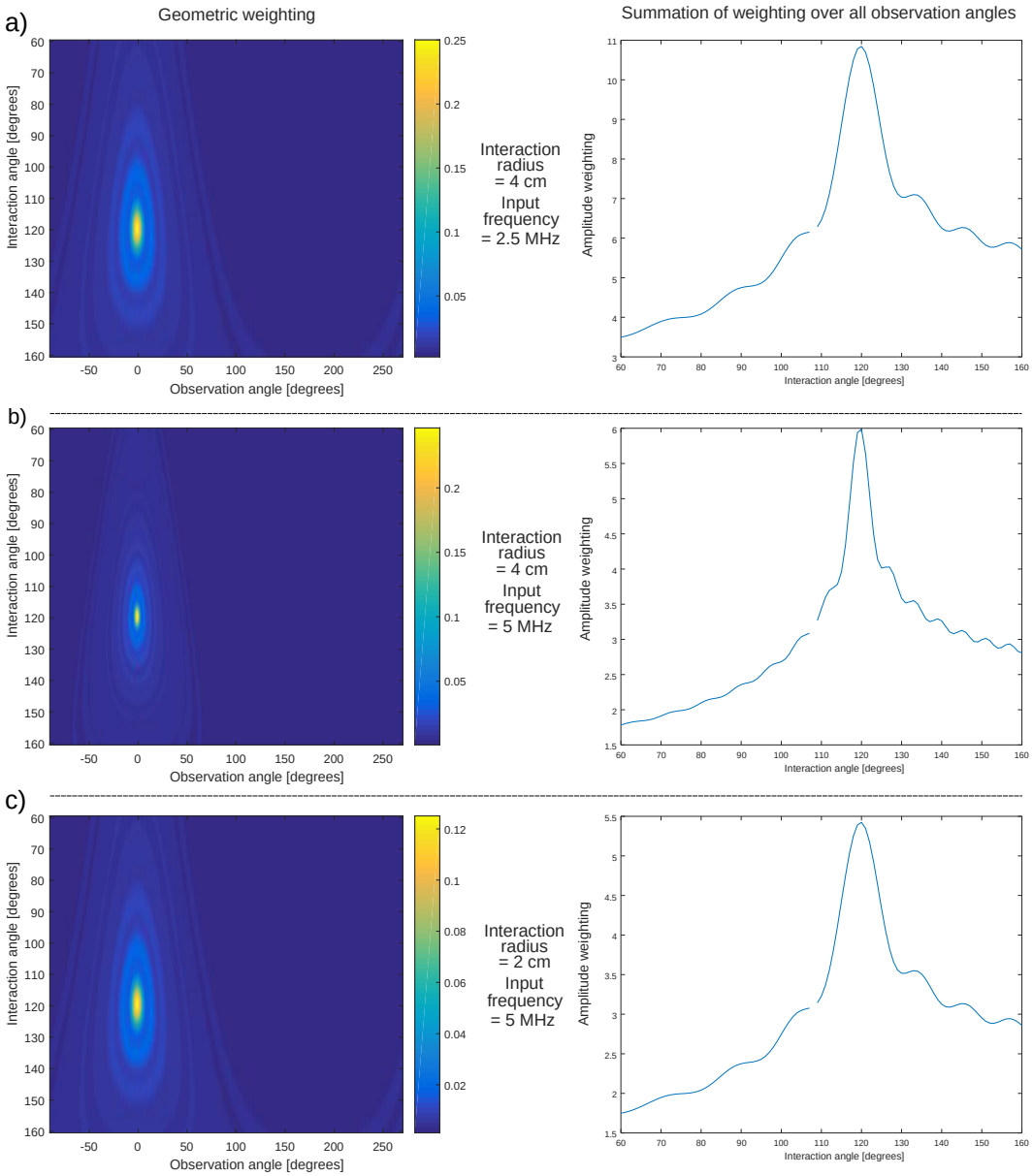


**Figure 5.1:** On the left are similar plots to Figure 12.2 but for a wider range of interaction and observation angles. All of the data is from modelling of the $\chi(\theta)$ term for a cylindrical volume. On the right are the results of summation across all observation angles, $\theta$, for $\chi(\theta)$. a) Is the distribution created with an interaction radius of 4 cm and input frequency of 2.5 MHz. $a = 1$ was used for all these examples. b) 4 cm, $\omega_1 = 5$ MHz. c) 2 cm, $\omega_1 = 5$ MHz.

### 5.2.2 Nonlinear directional amplitude function

The nonlinear angular directivity term, $\Delta(\theta)$, is not a function of interaction volume or frequency, unlike $\chi(\theta)$ and its impact on the fingerprint is quite different. It is given by the following equation that was derived in Chapter 4.

$$\Delta(\theta) = F_c(K,\mu,A,B,a,\phi)\cos\theta + F_s(K,\mu,A,B,a,\phi)\sin\theta \tag{5.2}$$

Where $K$ and $\mu$ are the compression and shear moduli respectively. $A$ and $B$ are third order elastic constants. $F_c$ and $F_s$ are functions defined in the previous chapter. All of the terms are constants when testing a solid block of material except for the interaction angle, frequency ratio, and the observation angle $\theta$. Figure 5.2 shows the resulting distribution using the same material properties as for the geometric weighting above; $E = 70$ GPa, $\nu = 0.33$, $m = -397$ GPa, $n = -403$ GPa, and $\rho = 2780$ kg.m$^{-3}$. Where $A = n$ and $B = m - \frac{n}{2}$. The values of $l$ and $m$ were as measured by Mohrbacker and Salama (94). The frequency ratio was one.

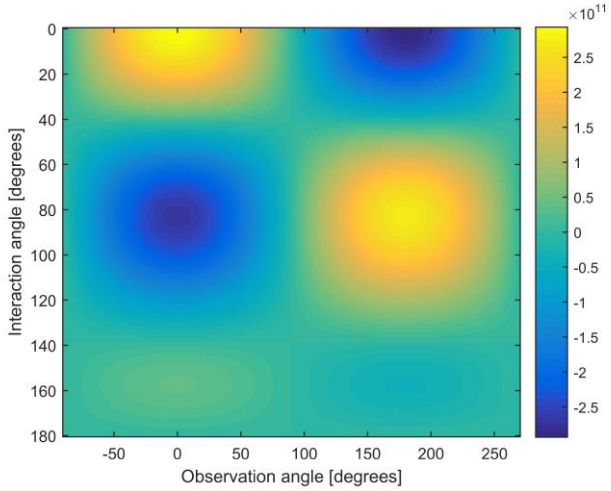


**Figure 5.2:** Modelled prediction of angular distribution of scattering due to nonlinear weighting term for solid aluminium over a range of interaction angles with $a = 1$. The colour scale indicates signal amplitude.

It can be seen in Figure 5.2 that the peak amplitude for $a = 1$ occurred at 0°, the same as the geometric term, but that there is also a peak in the backwards propagating direction, 180°. Unlike the geometric weighting term the interaction angle peaks were much less narrow, smoothly varying from zero at $\phi = 42°$ to a peak at $\phi = 84°$ and back to zero again by $\phi = 137°$. Since we are interested in the relative amplitude of the signal at different points in the parameter space the fact that the sign of the weighting changes does not matter. It might correspond to a change in phase, but the conditions at which it

occurs seem to be cases where no mixing would be expected due to a very low value of the geometric term.

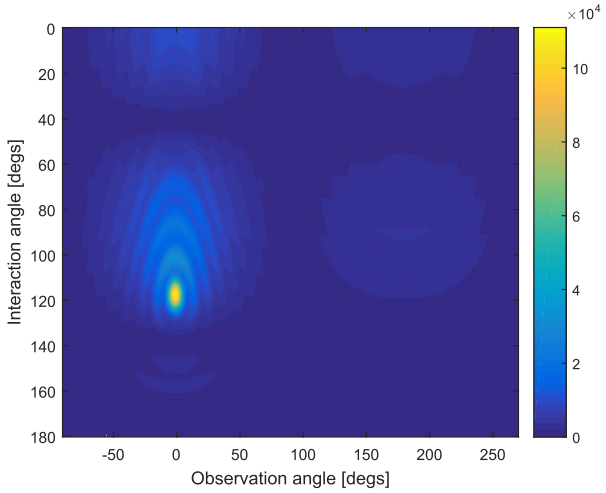


**Figure 5.3:** The combined result of the nonlinear and geometric weightings as shown independently in previous figures for a cylindrical interaction volume. The modulus has been taken of the values.

When the geometric and nonlinear terms are multiplied together the geometric pattern is dominant but has been modified in some key ways by the nonlinear response, see Figure 5.3. The main resonance peak in interaction angle is shifted towards smaller angles in this particular case, and minima are created at 42° and 137°. In the above investigation the frequency ratio has been kept at one for simplicity. Tests were also done at other frequency ratios but all behaviour remained similar, only shifting of the pattern to different observation angles was seen. The peaks in both the nonlinear and geometric weighting patterns shifted to the same observation angles for a given frequency ratio. The relative amplitude behaviour relating to this is discussed in the fingerprint below.

### 5.2.3 Fingerprints

By combining the two terms, described in the sections above, with the rest of the terms in Equation 5.1 the classical scattering amplitude from bulk mixing can be calculated. The maximal value of $X_3(\theta)$ is found for each desired point in the $\phi$-$a$ parameter space, forming the fingerprint. Many factors such as transducer bandwidth, and mode conversion at the water-aluminium interface have significant impacts on the resulting fingerprints when measured experimentally so are factored in to the following results. The bandwidth of the input transducers and detection array was modelled as Gaussian with the values stated in Section 3. Mode conversion at the water-aluminium interface was accounted for with the equations stated in (82), and angular sensitivity of the

experimental array due to the pitch of its elements was calculated using the directivity function, $D$, applied based upon the predicted scattering angle.

$$D(\theta) = \text{sinc}\left(\frac{\pi p \sin\theta}{\lambda}\right) \tag{5.3}$$

Where $\theta$ is the angle to the normal of the array, $p$ the array pitch, and $\lambda$ the wavelength of the scattered wave.

It should be remembered that, as was noted in the Experimental Methods chapter, by keeping one input beam's frequency fixed (the reference beam) when altering frequency ratio there is a coupling with the scattered wave frequency effects into the frequency ratio response. The effects of increased reference frequency on the geometric weightings were discussed above, including the flaws in the accuracy of this model. If Equation 5.1 is written in terms of $\omega_1$ and $a$ it can be seen that

$$X_3 \propto \omega_1^3 a \tag{5.4}$$

if the geometric weighting term's more complicated relation is ignored. This equation demonstrates that the scattering is expected to increase proportionally with $a$ in this fixed reference frequency case.

For this modelling a radius of 17.5 mm was used for the interaction volume because it gave geometric weightings that were similar to experimentally measured behaviour. The properties of the aluminium were; Young's modulus $E = 73.1$ GPa, Poisson coefficient $\nu = 0.33$, density $\rho = 2780$ kg.m$^{-3}$, and Murnaghan coefficients $n = -403$ GPa and $m = -397$ GPa. It was found that the response was insensitive to changes of about a factor of two in the the third order elastic coefficients (TOECs) so although there is significant variation in the literature values (95; 96) of these TOECs a similar fingerprint would be expected of an experimental aluminium sample. The sensitivity to these parameters is discussed in more detail in a section below. The model was run with the frequency of one of the input beams fixed at 5 MHz, results shown in Figure 5.4. Resonant conditions predicted by the equation $\cos\phi = c^2 + \left(\frac{(c^2-1)(a^2+1)}{2a}\right)$ are plotted on most fingerprints in this report for reference.

It can be seen in Figure 5.4 that the strongest mixing response is predicted at 118° and a frequency ratio of 1.06. This is approximately the same angle as the resonance angle given by the equation stated in (41), 120°. This small discrepancy was discussed in the nonlinear direction amplitude function section and can be seen to occur across the range of frequency ratios. There are also two secondary lobes of nonlinear scattering

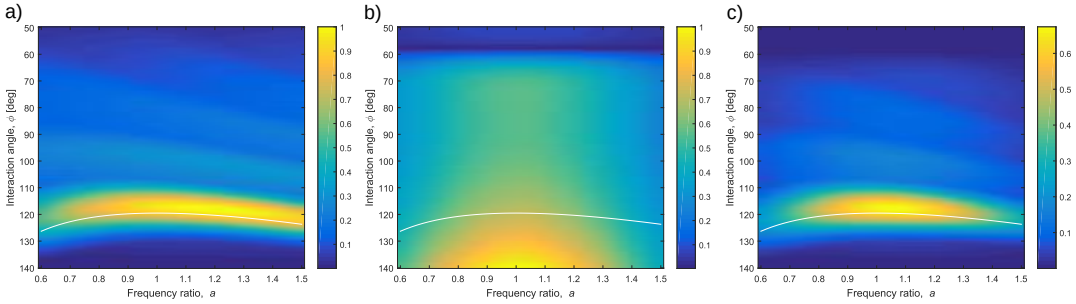


**Figure 5.4:** Analytic modelling of parametric space of mixing in solid aluminium. a) The uncorrected output from the model, b) the experimental correction factors, and c) the adjusted fingerprint to match what would be observed experimentally. Colour scale indicates scattering amplitude. White line indicates the resonant conditions.

that can be seen at smaller interaction angles, peaking at around 100° and 85°. The reduction in amplitude at frequency ratios far from one in Figure 5.4 (c) is due mainly to the bandwidth of the transducers, and the cut off at angles smaller than 60° is caused by very little production of shear waves at the water/aluminium interface below the first critical angle, as seen in Figure 3.6. These results predict that there are multiple features in the fingerprint within the 60° to 140° range that might interfere with the CAN signals of interest presented in Chapter 7.

The smaller peaks might not be expected to be so prominent in the experimental results due to the summation across multiple observation angles, as discussed in the geometric weighting term section and shown in Figure 12.3. Also it was mentioned that the off-resonance behaviour could have less pronounced features due to the smoother variation in beam intensity in the experiment. It is possible to create a more accurate model by using the 'real' type interaction volume integral with a position specific intensity term but this was beyond the scope of this work as the classical model was only intended to provide a rough guide for expected bulk mixing behaviour.

### Impact of material properties on fingerprint

The final question that this work aims to answer using this classical model is: how does the sensitivity to the material properties manifest in the fingerprint? Unless the material properties drastically change the shape of the fingerprint in such a way that might further obscure mixing caused by a kissing bond, which is expected to be at around $\phi = 80°$, this understanding would not be completely necessary for the detection of kissing bonds. However, if the fingerprints provide information about the bulk material then this could be useful for other purposes.

In this section linear elastic coefficients $E$, $\nu$, as well as TOECs $m$, and $n$ are varied.

Also some further examples of the impact of beam radius are presented in order to cover most possible variables that could affect the shape of fingerprints. This testing was conducted at $a = 1$ since features in the $\phi$ dimension of the parameter space appeared to be more information rich than $a$. The presentation of a single frequency ratio is also much easier to interpret visually. A beam radius of 20 mm was used for these tests, and material properties were as used for the previous fingerprints, unless specifically varied. The cylindrical interaction volume was used, as above.

The results were calculated using the peak scattering amplitude, not the sum over a range of observation angles as the decision of what range is somewhat arbitrary and adds complication to the model. Therefore the smaller peaks will be more pronounced in this data than they would be in the experimental case as has been discussed before. Some of the plots have been peak normalised to allow for more accurate shape comparison.

Figures 5.5 (a) and (b) show that increasing Young's modulus results in a small increase in peak amplitude and a stretching of the pattern centred at an interaction angle of about 122°, close to the resonant condition at $a = 1$. This causes the main peak to shift to smaller interaction angles due to the nonlinear weighting term's offset peak. It also caused changes in the relative heights of the peaks, increasing the height of the secondary peak but having negligible effect on the third. The other linear elastic term $\nu$ had a large impact on the pattern so is shown in Figure 5.5 (h) plotted for a smaller fractional variation than the others. As it was increased the pattern reduced in amplitude and shifted to larger interaction angles. The shifting is not constant; increasing $\nu$ by 20% shifted the main peak by 11°, the second peak moved by 12.5°, and the third peak 14.5° so there is clearly some stretching occurring too. As well as the pattern shifting effect of $\nu$ it also alters the shape. Increasing $\nu$ results in an reduced primary to secondary peak ratio.

Initially it appeared that altering the Murnaghan coefficient $m$ scaled the amplitude of scattering equally at all interaction angles, Figure 5.5 (e). Upon normalisation, shown in (f), it can be seen that increasing $m$ very slightly altered the ratio of the main peak to the secondary peak; doubling $m$ reduced the ratio by 6%, from 1:0.2819 to 1:0.2995. This change is quite small compared to the large change in $m$ and might have a different trend if summation over a range of observation angles is used instead. This point should be noted for all the analysis presented here; different trends may occur with different 'scattering amplitude' metrics. The linear coefficients and radius/frequency are likely to have the greatest sensitivity to summation method due to their significant effects on beam divergence. $n$ had no effect on the fingerprint as expected from the literature. $l$ was not included because its does not feature at all in the classical equations for sum-

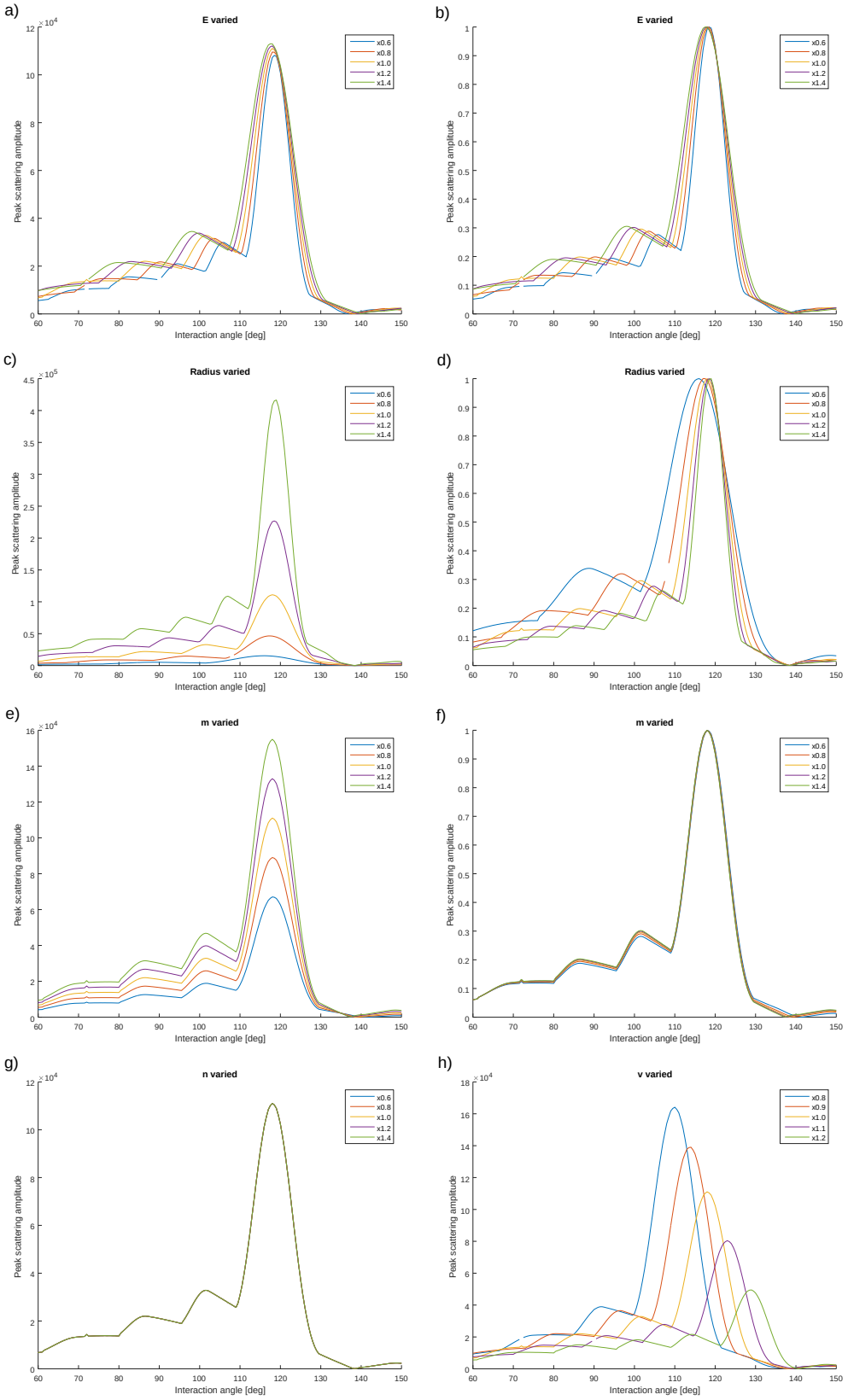


**Figure 5.5:** Predicted parametric response of the bulk mixing of in-plane shear waves for a range of interaction angles. a) and b) show variation of Young's modulus, $E$, radius is shown in c) and d), Murnaghan TOEC $m$ in e) and f), Murnaghan TOEC $n$ in g), and Poisson's ratio, $\nu$, in h). b), d), and f) are peak normalised. Legend indicates multiplier applied to selected parameter.

frequency mixing of two shear waves.

Beam radius appears to act similarly to $E$, Figures 5.5 (c) and (d), although the amount it scales the pattern is more than $E$ for the same amount of stretching. The scaling of amplitude is an absolute measure and can be difficult to measure accurately so analysis here will focus on only the shape component of the fingerprint. Similar to the case of $m$, there appears to be another more subtle change occurring in the main peak to secondary peak ratio. When the radius was reduced by 20% the secondary peak grew from 1:0.296 to 1:0.320, peaking at 97°. To get equivalent stretching $E$ had to be increased by 40% but this did not result in as large a change in peak ratio; going from 1:0.296 to 1:0.305.

It is possible that these subtle differences could result in the ability to extract material properties; for example by using a best fit approximation method that tests possible ranges of properties. In practice there would probably be issues with the coupling of an unknown $E$ resulting in an unknown divergence in the material and thus unknown interaction radius though so some properties may have to be known in advance. The small difference between behaviour of $E$ and radius, and tiny impact of $m$ on the shape would likely result in experimental noise reducing the accuracy of this method below other conventional approaches. It should be remembered that the above is only true for in-plane shear wave mixing, and that other modes have different sensitivities that might yield more extractable information from the fingerprints.

### 5.2.4 Modelling summary

The work presented so far has shown in detail the expected non-collinear mixing behaviour away from the resonant conditions; investigating the various factors of the mixing phenomenon that come together to make the overall fingerprint patterns. It was shown that the geometric and nonlinear weighting functions peak at different interaction angles, creating a combined peak in response away from the classically resonant condition. The importance of how a 'scattering amplitude' value is extracted from the array data has been demonstrated and the sensitivity of the fingerprint to various material and experimental parameters was investigated. These results were based upon a model using uniform intensity waves at single frequencies so there will likely be some differences when compared to experimental measurements. Also testing has shown that there are some problems with the current model requiring further work to improve confidence and accuracy in the solutions.

## 5.3 Experimental fingerprints

As mentioned above there were many approximations in the modelling of bulk mixing behaviour and ultimately only experimental testing can show what results will be produced with the particular experimental method as defined in Chapter 3. An FE model could possibly come close but, as will be shown in the following chapter in Section 6.4, due to the high frequencies involved and the desire to measure a detailed parameter space it would likely take too long to be practical.

The analytic modelling showed that most of the fingerprint features occurred in the range $\phi = 80^\circ - 135^\circ$. So this range will be the focus of most of the work below. A minima was predicted at an angle larger than this but it would be difficult to measure experimentally due to the noise floor. This range should also capture the region where mixing is expected to occur in the kissing bond case, which is vital for comparison. No features of interest were observed in the frequency ratio dimension and experimentally subtle ones might be obscured by the limited bandwidth of the transducers anyway, however some measurements will still be taken to validate this.

In the experimental testing fewer variables are altered compared to the modelling above. This work focuses on measuring the $a - \phi$ parameter space for constant material properties, and beam radius. Measurements are taken at varying depths in the material to tests the fingerprints sensitivity to this. Altering the depth has some effect on the beam radius and is discussed in Section 5.3.3. Testing is conducted with two different reference input frequencies, 5 MHz and 2.25 MHz, to investigate its impact.

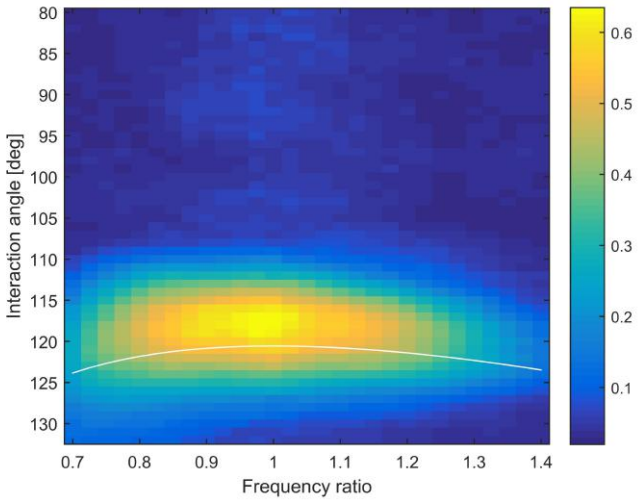


**Figure 5.6:** Experimentally measured parametric response of solid aluminium sample at a depth of 22 mm. 5 MHz used for the reference input pulse. Colour scale indicates scattered amplitude. White line indicates the resonant conditions.

Figure 5.6 shows an experimentally measured fingerprint for a solid block of aluminium, conducted using one input pulse fixed at 5 MHz. The interaction volume was centred 22 mm below the top surface of the 60 mm thick block and the detection array was in contact with the bottom surface. The mixing is strongest with around 118° interaction angle, and 0.95 frequency ratio. The peak in terms of angle differs by about 3° from the resonance condition, this is approximately the same magnitude as the uncertainty in the absolute angular error of the experiment so it is not certain that this disagreement is significant.

Like the modelling suggested, the mixing is not restricted to only the resonant conditions but extends about 10° above and below them in this 5 MHz input case. The curved shape of the resonance conditions is apparent in the shape of the fingerprint. The modelling predicted that there would be bands of signal at smaller interaction angles but these were not observed above the noise level experimentally.

### 5.3.1 2.25 MHz input frequency

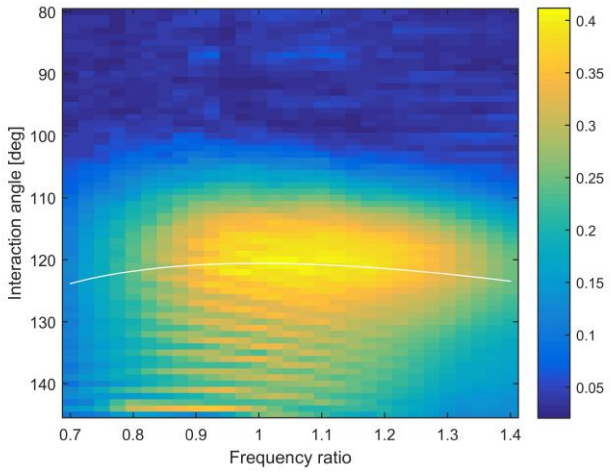


**Figure 5.7:** Experimentally measured parametric response of solid aluminium sample at a depth of 15 mm. 2.25 MHz used for the reference input pulse. Colour scale indicates scattered amplitude. White line indicates the resonant conditions.

For the testing at 2.25 MHz appropriate input transducers and detection array were used for the frequencies involved, as detailed in Chapter 3. The transducers had the same diameter as used for 5 MHz testing so the input beams would be expected to diverge at roughly twice the angle. This should result in a larger interaction volume. The fingerprint is shown in Figure 5.7. Experimentally it is observed that the mixing occurs over a wider range of the parameter space and is strongest at the resonant conditions. Again, no signal can been seen between 80° and 100° unlike the modelling predicted.

Some banding is visible between 125° and 145°, the cause of this is unclear. The bands occurred roughly every 3° and slope downwards as frequency ratio is increased. They may be caused by an interference effect, possibly due to the large interaction volume interfering with itself in a more complex manner than discussed in the theory above. The classical and geometric modelling is based upon the creation of a regular grid of interference points but in reality the wavefronts are not completely flat and the beams diverge as they propagate. These two factors would distort the pattern possibly leading to more complicated interference effects. It might be expected that these effects would be more pronounced at lower frequencies due to the increased divergence and interaction volume.

### 5.3.2 Power scaling

It is stated in Equation 5.1 that the output signal amplitude is the product of the two input amplitudes. To check this and to make sure if this relationship holds at all off-resonance cases three fingerprints were captured at different power levels. The tests were conducted on a 14 mm thick aluminium sample with the volume of interaction at its centre with the reference frequency fixed at 5 MHz. Reference transducer strength measurements were made at each power level by aiming them at the array with the sample removed, these numbers are reported in the form 'left beam amplitude'/'right beam amplitude'. The full power test had reference power levels of 0.297/0.401, middle had 0.151/0.200, and the minimum had 0.125/0.124. The product of the input amplitudes gives expected signal ratios of 1:0.265:0.130 respectively. Figure 5.8 shows the fingerprints, normalised to the peak of the full power test. The signal amplitudes match the predictions well, 1:0.26:0.14. Noise becomes much more noticeable in the lower powered tests, this is likely because the primary source of noise in this case (poor subtraction of input beams) scales linearly with the input transducer amplitude.

It can be seen that the fingerprint pattern remains the same at all power levels, although fainter features are harder to notice among the noise at lower power levels. The feature seen at 105° is due to the small thickness of the sample being tested and is not normal bulk behaviour. This effect is mentioned in the following section on depth variation, section 5.4.1, and discussed in detail in Chapter 6.

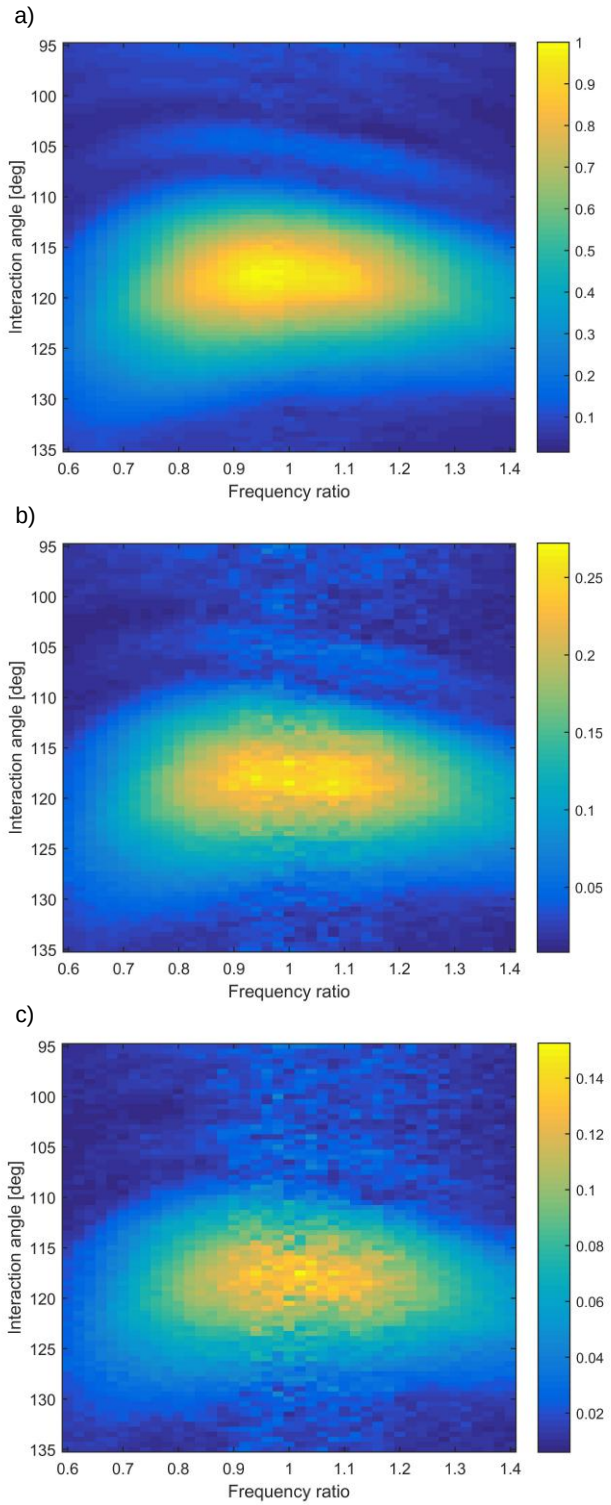


**Figure 5.8:** a) Fingerprint at 7 mm deep in 14 mm thick solid aluminium sample at full power, 5 MHz reference input. b) medium input power, c) low input power. Different colour scales are used for each but the values are consistent between them.

### 5.3.3 Depth variation

Ideally the method for acquiring a 'fingerprint' of the material would produce results that are independent of the depth in the sample at which the measurement is taken, provided the material is homogeneous. This is unlikely to be the case with the experimental method used for the testing in this work as will be explained below.

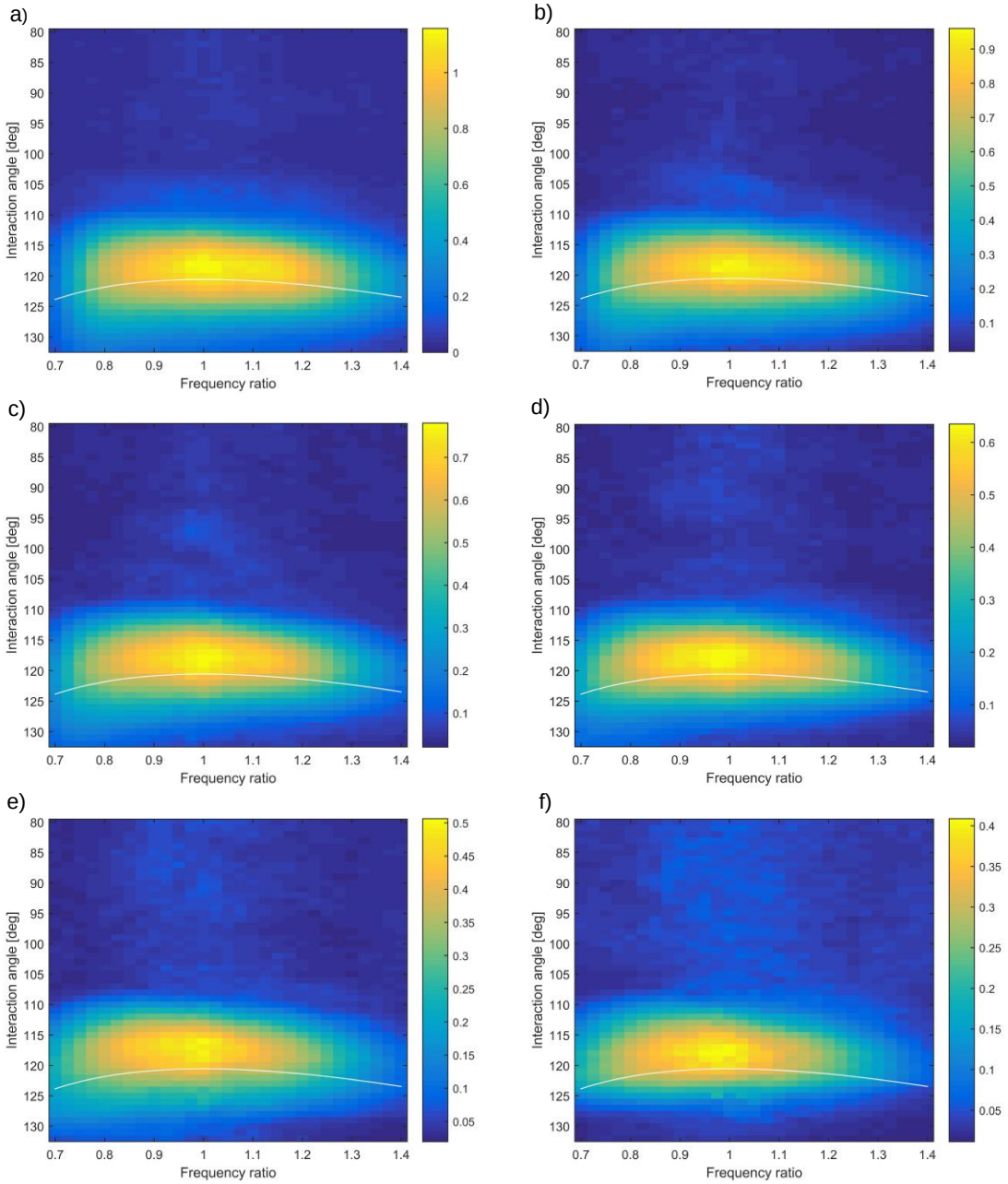


**Figure 5.9:** Fingerprints of 60 mm thick aluminium solid block at the following depths; (a) 10 mm, (b) 14 mm, (c) 18 mm, (d) 22 mm, (e) 26 mm, (f) 30 mm. The resonance conditions are plotted in white.

Measurements of the bulk mixing in solid aluminium were conducted at various depths.

Depth of inspection alters the size of the interaction volume due to beam divergence, this is the main factor that is expected to influence the fingerprint shape. Figure 5.9 shows measurements between 10 mm and 30 mm deep in the 60 mm thick solid aluminium sample. The geometry of the experiment causes the input beams to clip the ends of the sample at large interaction angles. This causes the reduction visible at the bottom of the fingerprints in the deeper measurements. Excluding this limitation the fingerprints look very similar. They all peak at $\phi = 118^\circ$ and $a = 1$. There are some slight differences in response at interaction angles between 100° and 110°. At 14 mm deep for example there is a clear minima at 107° and a second peak at 105°. The fingerprints taken at greater depth don't appear to have this secondary peak, although it is hard to be certain as the mixing strength is reduced at greater depths and the noise is increased. The secondary peak seen at 14 mm is not as strong as predicted by the classical model but may be related, alternatively it might be caused by small amounts of surface mixing as discussed in Chapter 6.

The peak mixing amplitude reduces as depth of inspection is increased, this is mainly due to the divergence of the input beams. The following paragraphs investigate this behaviour.

**Divergence**

Divergence can be estimated by the following equation.

$$\sin(\theta) = \frac{qV}{DF} \tag{5.5}$$

Where $\theta$ is the far-field approximation of the edge to edge beam spread angle, $q$ is a constant related to what drop in intensity is defined as the beam edge, $V$ is the velocity, $D$ is the source diameter, and $F$ the frequency. For a -6 dB beamwidth $q = 51$.

Taking depths of 18 mm and 30 mm as examples the -6 dB widths of the beams at the interaction depths can be calculated to estimate the effect of divergence on mixing strength. In water the divergence angle is 8.7° and in aluminium it is 19° for the shear waves. For an interaction angle of 120° the beams propagate through the water at 24°, this resulted in a path length from transducer to the aluminium of 27 mm, over which length the beams would diverge by 4.1 mm (this is less than the beam width because it is in the near field). The path lengths in the aluminium are 36 mm for the 18 mm deep interaction, and 60 mm for 30 mm deep. The amounts of beam spread over these distances are 12 mm and 20 mm respectively. This gives a beam diameter of 16 mm at

18 mm deep and 24 mm at 30 mm deep. The mixing strength is given by the following equation, which is based on Equation 5.1.

$$X_3 \propto X_1 X_2 V \tag{5.6}$$

Where $X_1$ and $X_2$ are the displacement amplitudes of the input beams, $X_3$ is the scattered amplitude, and $V$ is the interaction volume.

The volume of interaction scales with the cube of beam diameter, and the amplitude of the beams scale with the inverse square of the diameter. This results in the mixing amplitude being inversely proportional to the beam diameters. Therefore the 30 mm deep measurement would be expected to be 33% smaller in amplitude than the 18 mm one. The measured difference is actually approximately 50% smaller, so where does this extra 25% decrease in signal come from? It might just be due to approximations in the divergence calculations, or due to the simplification of the volume interaction being the result of plane waves. Another cause could be the attenuation of the input beams as they propagate through the sample.

**Attenuation**

$$A = A_0 e^{-\alpha z} \tag{5.7}$$

Attenuation is given by the above equation where $A$ is the attenuated amplitude, $A_0$ is the initial amplitude, $\alpha$ is the attenuation coefficient of the material, and $z$ is the distance propagated through the medium. For aluminium at 5 MHz $\alpha$ is 0.07 dB/cm (97). The equation above is for $\alpha$ given in terms of a linear attenuation coefficient with a logarithmic base of $e$, not the base-10 used for decibels. The standard base $e$ unit is the Neper, 1 Np = 8.7 dB. This gives an $\alpha$ of 0.8 Np/m. For the two measurement depths, 18 mm and 30 mm, this results in an extra attenuation due to the 24 mm of added propagation distance of 2%. Since the scattered amplitude is the product of both input beam amplitudes the output signal would be expected to be 4% weaker in the deeper interaction case. However, in the 18 mm depth case the 10 MHz beam has to travel 12 mm further to reach the detection array. Using the value of attenuation at 10 MHz of 3.0 Np/m, (97), it can be seen that this would cause an added attenuation of 3.5%, cancelling out the other effect. Therefore, attenuation is not a significant cause of amplitude decrease as depth of interaction is increased in aluminium.

Since attenuation has been shown to be negligible in terms of its impact on depth related scattering amplitudes it is likely that the simple divergence approximations in

the previous section do not accurately account for the changes in interaction volume size and are responsible for the extra variation.

### 5.3.4 Angle of scattering

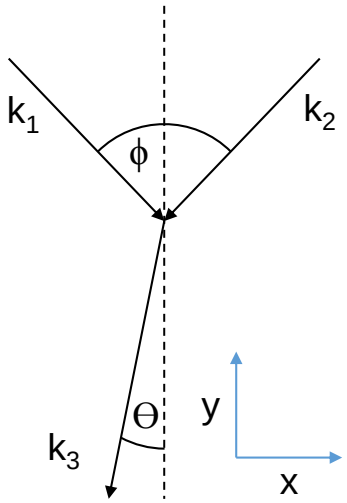


**Figure 5.10:** General interaction geometry of non-collinear mixing, $\phi$ is the interaction angle and $\theta$ is the scattering angle.

In the post-processing of the experimental data a spatial window is applied. This window requires the prediction of where the mixed signal will hit the array, the key factor in this calculation is the scattering angle. The classical prediction of scattering angle is based on the summation of the k-vectors of the input beams, Figure 5.10. Resolving these vectors into x and y components with the symmetric definition of interaction angle used in this work gives

$$\mathbf{k_1} = k_1 \sin(\phi/2)\hat{\mathbf{x}} - k_1 \cos(\phi/2)\hat{\mathbf{y}} \tag{5.8}$$

$$\mathbf{k_2} = -k_2 \sin(\phi/2)\hat{\mathbf{x}} - k_2 \cos(\phi/2)\hat{\mathbf{y}} \tag{5.9}$$

The angle of the resulting scattered beam can then be found from the sum of these components

$$\theta = \tan^{-1}\left(\frac{(k_1 - k_2)\sin(\phi/2)}{(k_1 + k_2)\cos(\phi/2)}\right) \tag{5.10}$$

Since $k_1 = a * k_2$, and $\tan = \sin/\cos$ this gives

$$\theta = \tan^{-1}\left(\frac{1-a}{1+a}\tan(\phi/2)\right) \tag{5.11}$$

Here the scattering angle is defined as the angle between the scattering direction and the bisector of the input beams, although in most literature (18; 9; 34) it is defined instead as the angle between the scattering direction and the reference input beam. Resulting in this alternate form of the equation.

$$\theta = \tan^{-1}\left(\frac{a}{1+a}\tan(\phi)\right) \tag{5.12}$$

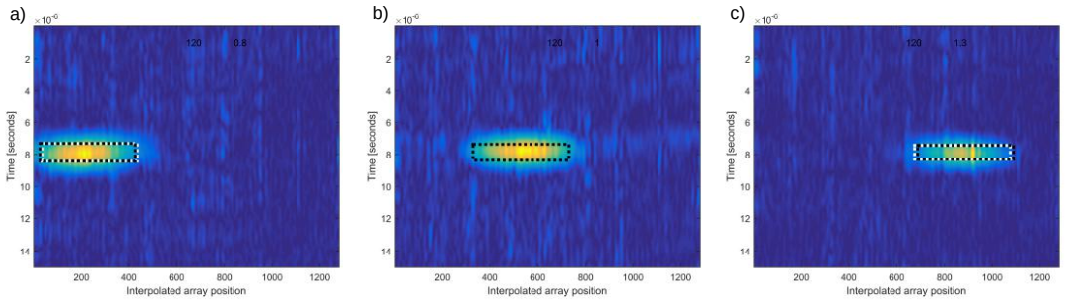


**Figure 5.11:** Post processed time traces of the signal received at $\phi = 120°$, depth $= 14$ mm, thickness $= 60$ mm, and $a = 0.8$, 1.0, and 1.3 for plots a), b), and c) respectively. The boxes drawn on the plots are the space and time windows from which the peak value was taken. There are actually two boxes plotted, one in white using the classical angle prediction and one in black using the interface method as discussed later.

The bisecting definition seems more appropriate in this experimental configuration where symmetry in the input angles relative to the sample is always maintained. It was found that the classical equation predicted the angle well, particularly at resonant conditions, allowing for a small spatial window which reduced the amount of noise included in the focusing summation. The classical angle prediction worked less well at parametric points further away from resonance and is investigated in detail in the following section. Figure 5.11 shows the post processed time traces with an interaction angle of 120° and 14 mm depth of interaction.

The prediction worked well considering the interaction volume is fairly large compared with the distance of propagation from its centre to the array, meaning the assumption that it acts like a point source at the centre of the volume of interaction might not be assumed.

### 5.3.5 Bulk mixing mechanisms at non-resonant conditions

The scattering angle prediction appeared to work well at 5 MHz but during the the 2.25 MHz post processing there were some discrepancies visible at mixing conditions far away from resonance. It is unclear from the classical theory what scattering angle should be expected away from resonance since the equations are only valid at resonance. It is possible that the extended classical theory developed by Potter could allow for some prediction of this behaviour but many real world factors are missing from the model such as beams of spatially varying intensity and a range of frequency components.

The classical theory, which is simply the summation of k-vectors, results in Equation 5.11 for scattering angle. Assuming this is still the case away from resonance, it predicts that as interaction angle is reduced so will the scattering angle and vice versa. One visualisation of mixing at conditions away from resonance that agrees with this scattering angle prediction is the view that due to the finite size of the interaction volume constructive interference between the source points is possible with a range of spacings of the points. The resonant spacing is when they are the scattered wavelength apart but mixing will still be possible with some variation on this. In this case scattering might be expected to occur in the direction perpendicular to the interference lines, which was shown in Chapter 4, Section 4.3 to be an equivalent direction to the summation of k-vectors. Therefore, if this interpretation is correct the classical angle prediction should be applicable away from resonance.

An alternative way of looking at off-resonance mixing is that it is due to the range of components (frequency or angle) that make up the input beams, some of which are at resonant conditions. For example, the input waves can be thought of a summation of plane waves at a range of angles (98). In this view mixing can occur due to the presence of a component at the resonant angle even though the central beam angle is not. In a similar way, the input pulses include a range of frequency components and thus there is a range of frequency ratios present which may allow mixing. With this interpretation the mixing happens at the resonant conditions even when the bulk of the beams are not so the scattering angle would be expected to occur as if the beams were at the resonant conditions. In this case it might be expected that the observed scattering angle is related to a resonant condition that is parametrically close to the imperfect ones used.

In order to test which of these two types of behaviour is more accurate, detailed analysis was conducted on the data collected for the 2.25 MHz fingerprints. The lower frequency produced mixing at a wider range of interaction angles than the 5 MHz tests. The difference between scattering angle predictions is greater further away from the resonant conditions so this should allow for greater certainty in the outcome. There are some

negatives to testing at 2.25 MHz though, the mixing effect is weaker at lower frequencies and the scattered beam is more divergent again lowering the intensity. These factors mean that finding the centre of the output beam is more challenging due to the worse signal to noise ratio.

By summing over a time window and smoothing the resulting spatial profile of the output beam it was possible to acquire a position trend strong enough to be observed above the noise, Figure 5.12. The spatial data from the array was interpolated by a factor of 10 (from 128 elements to 1280) to improve the possible precision. The black line in the plots is the measured peak scattered pulse position on the array. It can be seen that the predictions match quite well in the symmetrical scattering case of $a = 1.0$. There is a shift in position as interaction angle changes, this is due to angular error in the transducers. It was calculated that the errors shown in Figure 3.10 in Chapter 3 result in a rotation of the interaction that causes a gradual 2 mm drift in detection position over the full range of interaction angle measurements. This corresponds to a drift of 7 elements, or 70 interpolated elements as can be seen in Figure 5.12 (b).

In parts (a), (c), and (d) of Figure 5.12 the prediction using the classical equations can be seen to be a poor match for the measured position except at the resonance point (around 120°). The measured position appears to vary much less than predicted, this suggests that the scattering is occurring as if the beams were mixing at the resonance interaction angle. It is difficult to be sure what is going on at larger interaction angles due to the oscillating effect growing large. This pattern can be seen in the fingerprint Figure 5.7. This appears to be caused by an interference effect due to the way the pulse periodically changes shape (position) and amplitude but its source is unknown. The $a = 1.35$ result is interesting because the effect is much smaller producing a measured position that appears to have a much smaller error. In this case the position moves in the opposite direction to the prediction as interaction angle is varied. Shifting in this direction might correspond to mixing effectively occurring at a resonance condition that is smaller in frequency ratio. This does not agree with the concept that mixing occurs at some sort of nearest resonance condition because as the interaction angle increased the nearest resonance cases should shift towards larger interaction angles and larger frequency ratios in this case. Therefore, neither of the rationalisations of off-resonance mixing stated in the paragraphs above completely agree with the results.

Angle predictions made using the CAN suitable method are included in these figures, the explanation of this angle prediction is given in Chapter 6. It relates to the expected scattering angle from a 2D/planar source, in contrast with the classical 3D bulk source that is used in this chapter. The CAN predictions can be ignored for now, they are

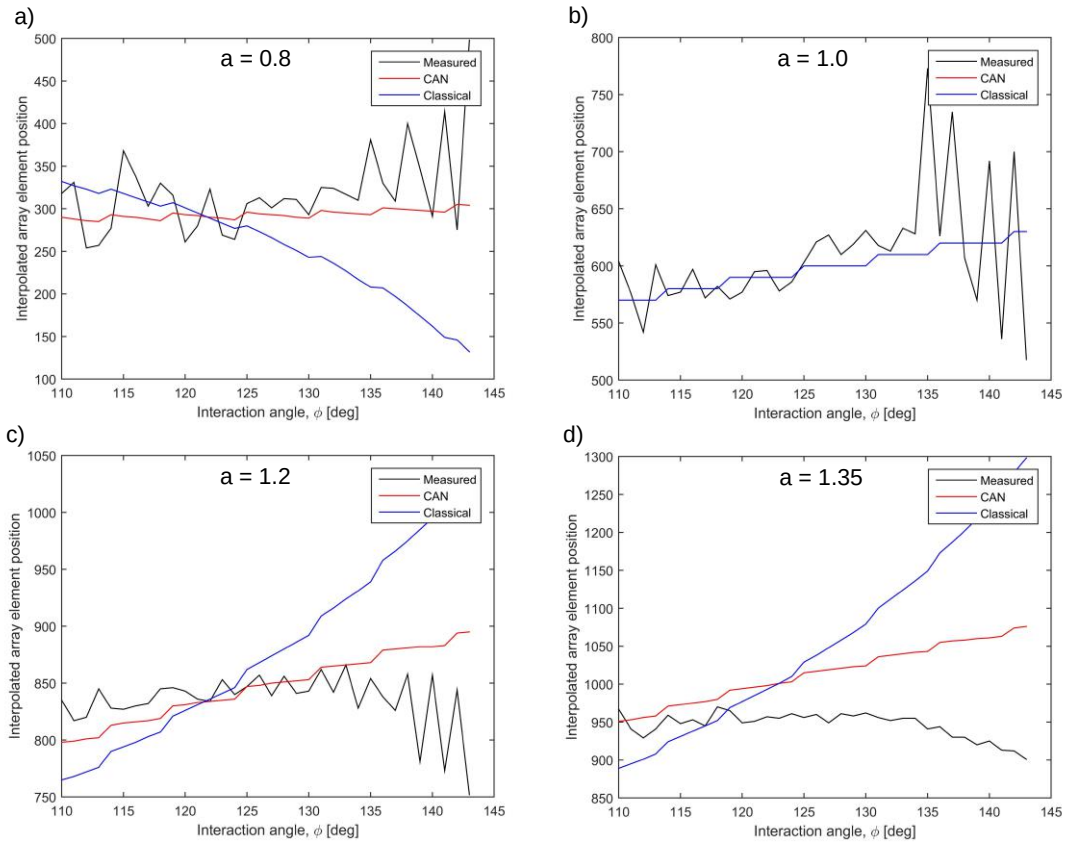


**Figure 5.12:** Position of the centre of the scattered pulse on the array measured and predicted for the interaction angle range 110° to 143°. The position is in terms of the 1:10 interpolated array element number, and the predictions are made using the classical angle of scattering equation and the CAN angle equation (discussed in later chapters). a) is $a = 0.8$, b) $a = 1.0$, c) $a = 1.2$, d) $a = 1.35$. A correction factor has been applied to the predictions to account for angular error in the transducers. This can be seen most clearly in b) where a constant array position would be expected without this error.

provided for later possible interest.

In conclusion, the classical angle prediction methods appears to be highly inaccurate at mixing conditions far away from resonance. There is little change in the angle of scattering as interaction angle is altered suggesting the nearest resonant component view might be correct. But further, more accurate, tests are required to confirm this as there were indications that this theory may not be perfect either.

### 5.3.6 Amplitude-frequency relationship

The classical theory predicts that scattering amplitude should be proportional to the cube of the reference input frequency, Equation 5.4. To check this the scattering amplitudes from the 5 MHz and 2.25 MHz testing can be compared, this is difficult due to the number of differences between the two experimental cases though. Different input transducers and detection arrays were used which have different sensitivities, as well as the changes in input beam width that occur due to keeping the transducer sizes the same while changing frequency. This means that the numbers calculated in this section are rough estimates.

According to the specifications the 10 MHz array has a sensitivity of 318 mV when excited at 70 V in a pulse-echo test. In the same test the 5 MHz array had a sensitivity of 150 mV when excited at 60 V. Since these are pulse-echo tests the sensitivity is factored into the measurement twice, also the larger excitation voltage used for the 10 MHz array must be included. The result is that the 5 MHz array has 74% the sensitivity of the 10 MHz array. In order to find the relative amplitudes from the input transducers measurements taken daily during standard testing of power output stability can be used. For these tests the input transducers were aimed at the array at an angle of 10° from the normal. An example recording of the amplitudes for the 2.25 MHz input case gave a value of 0.67 for the left and 0.39 for the right transducer (these units are arbitrary due to the summation method). This measurement was taken with an array gain of 20 dB. An example from 5 MHz testing had 0.40 left and 0.39 right at 15 dB gain. If this is standardised to a 20 dB gain this gives values of 0.71 left, 0.69 right.

To compare the two amplitude values that were measured above the bandwidth of the arrays must be taken into account since the input beams are not at the centre frequencies of the arrays (they are roughly half). The bandwidth of the 5 MHz array means that it had a -20 dB sensitivity to 2.25 MHz, and the 10 MHz array had a -9 dB sensitivity to 5 MHz. Again these sensitivities are for transmit-receive so the decibel values should be halved, giving a difference of 5.5 dB. Not only was the 10 MHz array more sensitive at

its centre frequency but it had a wider bandwidth resulting in the combined sensitivity of the array in the 2.25 MHz case being only 39% of the 5 MHz case. If you apply this difference in sensitivity to the calibration amplitude of the 5 MHz input test in the paragraph above it gives 0.28 on the left, and 0.27 for the right. Since the scattering is generally the product of the amplitude of the two input beams the left and right readings can be multiplied together to get a single value for each frequency case. 2.25 MHz gives 0.26, and 5 MHz is 0.076 meaning that the product of the 5 MHz input transducer amplitudes is 29% that of the 2.25 MHz transducers.

The relative strength of the input transducers that was calculated above can be combined with the array sensitivities to create a scaling factor for the measured scattering amplitudes. The more sensitive 10 MHz array (135%) with the much lower amplitude 5 MHz transducers' product (29%) results in an overall factor of 39%. Thus the 2.25 MHz scattering amplitude must be multiplied by 0.39 to standardise it with the 5 MHz measurements. It should be noted that this is based on the assumption of scattering amplitude scaling with the product of input amplitudes, which is true in the bulk case but not necessarily in others due to the possible differences in nonlinearity types.

The maximal scattering that occurred in the 2.25 MHz test was 0.4, as can be seen in Figure 5.7. This was measured at a depth of 15 mm with a reception gain of 50 dB. The most similar reading taken at 5 MHz was the one at 14 mm deep, Figure 5.9 (b), which had a peak of 0.95 captured with a gain of 45 dB. If the 2.25 MHz testing is adjusted to account for the difference in gain it would be 0.22. Taking into account the 0.39 factor calculated above this results in a value of 0.088 for the 2.25 MHz case, versus 0.95 at 5 MHz. The ratio of these two values is 11, as would be expected due to the cubic frequency relation, $(5/2.25)^3 \approx 11$. There were many approximations used in the calculation of the relative amplitudes so it is somewhat surprising that it matched so well. It is difficult to quantify the size of the uncertainties involved so this should not be taken as proof that the scattering scaled with frequency cubed but it does not give us any reason to doubt that that is the case.

This method of comparison is used again in the near surface chapter, Section 6.2. Some extra analysis of the flaws and limitations is presented there.

The frequency testing above concludes the investigation into bulk mixing that was vital for later kissing bond tests. Presented below is the examination of the effects of altered TOECs on the fingerprints. It is possible that changes in these coefficients could occur in adhesive layers in a way that predicts failure so this research could be useful for future testing but the primary focus of this thesis is on the detection of kissing bonds by CAN

related mixing.

## 5.4 Experimental fatigue measurement

Having gained an understanding of all the variables some tests were conducted to investigate the method's sensitivity to fatigue state. These tests helped develop the experimental method and improved the understanding of the detectability of bulk material properties.

### 5.4.1 Aluminium fatigue specimens

This testing was conducted to investigate the impact of altered elastic properties (including TOECs) due to high cycle fatigue on measured fingerprints. Previous work has shown that higher order elastic terms are more sensitive to fatigue and could provide an earlier warning than methods that are only sensitive to second order terms (Young's modulus and Poisson's ratio) (11). The previous non-collinear fatigue in aluminium work used a sample subjected to low cycle fatigue, typically failing before 100 cycles. The samples studied here are high cycle so may present a different response due to the different type of fatigue damage.

This testing was conducted before it was identified that interaction volumes near the surface of the sample affected the bulk results. More detail of this is provided in Chapter 6. In that chapter it is shown that the 7 mm depth used for this testing is on the borderline between purely bulk mixing behaviour and near-surface behaviour.

Figure 5.13 shows a fingerprint of the unfatigued 14 mm thick aluminium sample for reference. The testing was conducted at 5 MHz using a standoff below the sample of around 50 mm. This was required due to the small thickness of the sample that resulted in poor spatial separation between the input pulses and the scattered output. The fingerprint shown in the figure was one taken before temperature control of the immersion tank was implemented. This means that the velocity in water was not accurate resulting in angles of refraction, and thus interaction angles, that were not as accurate as stated in the methodology. This test was one of the highest resolution parametric sweeps conducted in the research presented in this thesis, taking over four hours to acquire.

The pattern of the fingerprint is similar to that seen in the bulk measurements apart from the additional bands at 105° and 98°. These bands appear to be similar to the

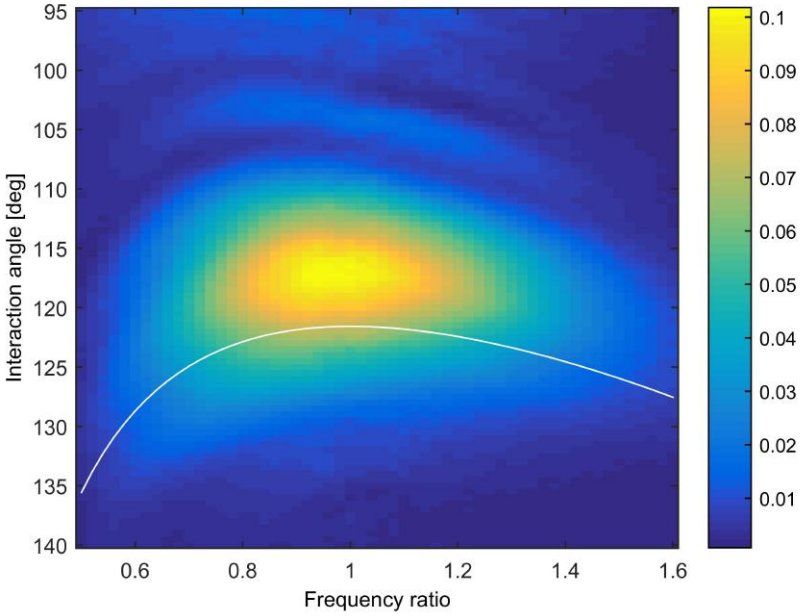


**Figure 5.13:** Experimentally measured parametric response of 14 mm thick unfatigued solid aluminium sample at a depth of 7 mm. 5 MHz used for the reference input pulse. Colour scale indicates scattered amplitude. White line indicates the resonant conditions.

predictions of the classical and geometric models but actually they are more likely due to the interaction volume intersecting with the surface of the sample. This effect is discussed in the following chapter. The fingerprint does not quite match with the near surface results shown there, this may be because the interaction volume overlapped with both the top and bottom surfaces of the sample in this case. In that chapter it is shown that the beams interact at the surface of the material to produce signal at any interaction angle, in this case the bands may be formed by the interference of sources on the top and bottom surfaces of the sample. Much of the following analysis is based on the shape of these bands, this makes the cause of fingerprint shape changes difficult to explain due to the complex interaction of multiple sources.

Wide range fingerprints like that shown in Figure 5.13 were captured for the other fatigue samples but they all appear very similar so they are not displayed here. The differences between the fingerprints are best seen by looking at cross-sections at a single frequency ratio. The full range fingerprints also take a long time to acquire so capturing only one frequency ratio allowed more repeat measurements to be made.

0.84 was selected as a good frequency ratio due to the balance of being near the peak mixing response and being far enough from 1 to allow good frequency filtering. The bandwidth of the Gaussian frequency filter was 1.5 MHz, thus the 9.2 MHz signals produced by a ratio of 0.84 were suitably far from the 10 MHz harmonic of the input

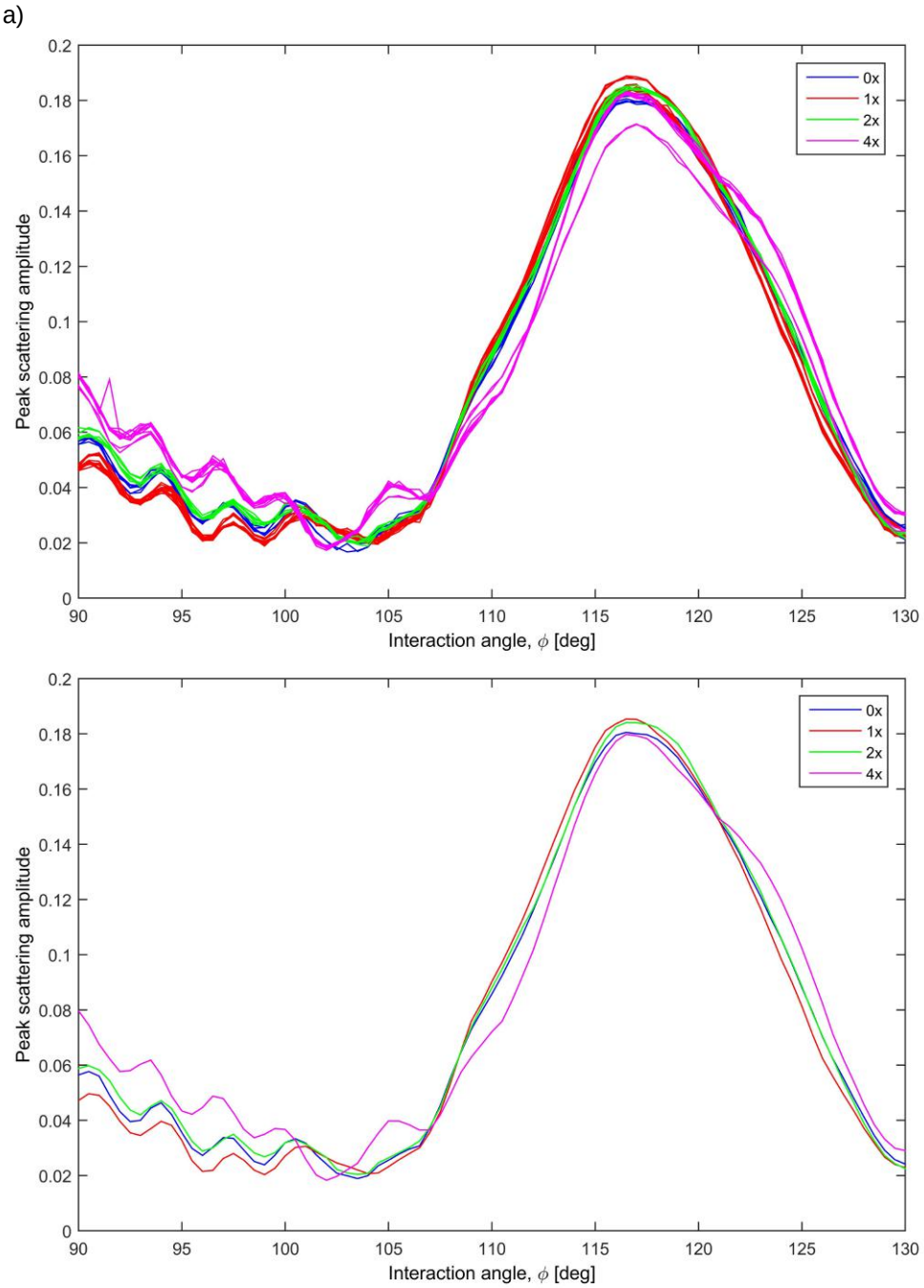


**Figure 5.14:** Experimentally measured parametric responses of 14 mm thick fatigued aluminium samples at a depth of 7 mm and frequency ratio of 0.84. 5 MHz used for the reference input pulse. a) the un-averaged measurements, b) the average for each fatigue level. The fatigue states were: 0x is 0%, 1x is 40%, 2x is 60%, 4x is 80% of their fatigue lives.

beams.

Figure 5.14 shows mixing measurements taken for the fatigued aluminium samples over the 90° to 130° interaction angle range at a frequency ratio of 0.84. There are four different samples tested at various percentages of their fatigue lives; 0x is 0%, 1x is 40%, 2x is 60%, 4x is 80%. Measurements were taken at two different points on the samples both near the centre. The same measurement points were used for all the samples. It can be seen that the repeatability is good in most cases, and where there is variation the trends often form two distinct patterns. In most cases this is due to the two measurement points used and is particularly prominent in the most fatigued sample where there is significant disagreement between 110° and 130°. The 40% sample also displayed this behaviour to a lesser extent.

The results from the unfatigued, 40%, and 60% samples were quite similar, peaking at roughly the same amplitudes and having maxima and minima at similar angles. The 80% sample was notably different, with one measurement position having a lower maximum amplitude, and all measurements having a distinctive shape to their off-resonance peaks. The greater variation in response would be expected for the more fatigued sample as the fatigue damage tends to concentrate in particular areas but leave others unaffected. From the data collected it appears that the shape of the fingerprint is a more robust indicator of fatigue state than the maximum amplitude. There are many shape differences between 4x and the others, which might give a reliable indication of fatigue state but further testing of more samples would be required to validate this.

### 5.4.2 Steel fatigue specimens

Testing was conducted on steel fatigue specimens to further examine how fatigue altered properties affect the fingerprint and to test the technique in a more challenging material; the larger grain size of the 347 stainless steel results in increased attenuation when compared to the aluminium. This required the development of better post processing methods in order to extract reliable information from the fingerprints, something that is likely to be required when testing CFRP samples and poorly transmissive kissing interfaces. These samples were also fatigued in bending so would be expected to have a similar distribution of fatigue damage to the aluminium samples. All of the results presented below were based on analysis of frequency filtered fingerprints to remove some of the noise. 5 MHz was used as the reference input frequency for this testing, like most of the other testing presented in this work. The interaction volume was centered on the middle of the sample in the depth direction and a jig was used to position the samples

**Table 5.1:** Steel fatigue sample numbers, order of testing, number of fatigue cycles, and interaction angle correction factor.

| | | | | | | | | | | |
|---|---|---|---|---|---|---|---|---|---|---|
| Sample No. | 22 | 17 | 24 | 9 | 15 | 7 | 7 | 7 | 7 | 7 |
| Test order | 1 | 2 | 3 | 4 | 5 | 6 | 7 | 8 | 9 | 10 |
| Cycles | 100 | 12000 | 15000 | 6000 | 9000 | 3000 | 3000 | 3000 | 3000 | 3000 |
| Angle correction (°) | 0.02 | 0.06 | 0.18 | 0.06 | -0.06 | -0.02 | -0.02 | -0.02 | 0.04 | 0.04 |

consistently. The order in which the samples were tested, and other information about them is shown in Table 5.1.

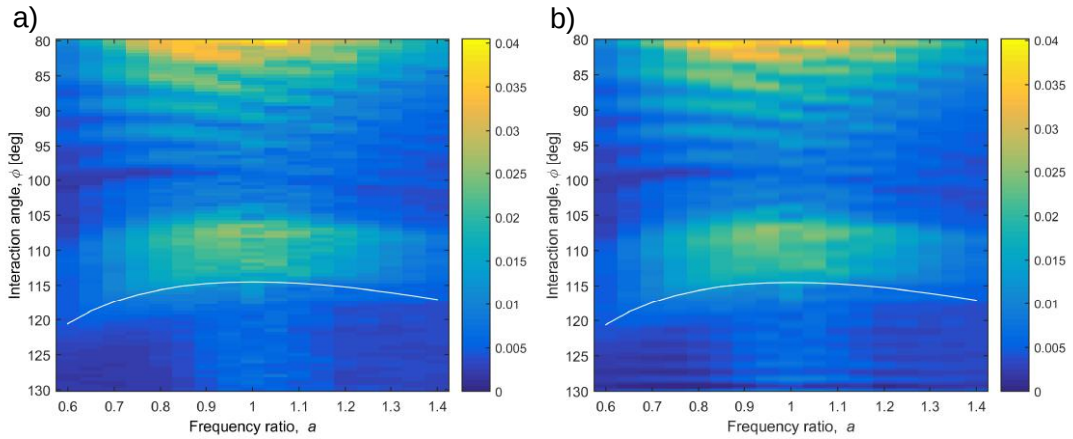


**Figure 5.15:** Fingerprints of the 3000 cycle steel fatigue sample using the mean of the five measurements. b) A Fourier smoothed version of a). White line indicates resonant conditions.

An example fingerprint and filtered counterpart are presented in Figure 5.15. The fingerprint is the result of an average of the five measurements taken of the 3000 cycles sample. The data was formally captured only once for each of the other samples due to time limitations and each fingerprint requiring over an hour to acquire. The signal is much noisier than in the aluminium fatigue samples as expected, but the overall shape is similar; there is a main band that follows the shape of the resonant conditions and there are lower intensity bands at smaller interaction angles. In the steel fingerprints the bands appear to get stronger as interaction angle is decreased, this is similar to the aluminium samples, but the larger parameter space allows us to see that the scattering becomes even more intense than the resonant case at interaction angles smaller than 85°. This behaviour is believed to be due to the near surface mixing effect that is explored in the following chapter. The bands above the main resonant lobe may also be a result of the near surface effect but will be analysed in this chapter anyway.

The fingerprint pattern is offset from the resonant conditions by around 5°. This could be due to the error in the shear wave velocity, meaning that the applied interaction angle was not accurate. The inaccurate prediction of resonance conditions would also add to this error. The longitudinal velocity was measured experimentally and found to be

significantly different from the expected value for 347 steel therefore it is likely that the shear value is also unreliable. An experimental value for the steel could have been measured but the absolute angles were not the focus of this testing so this was not done.

Figure 5.16 presents a cross section of the fingerprints for all the samples at $a = 0.75$. The data includes a measurement of sample 7 (3000 cycles) taken before the others that was excluded from later analysis due to an anomalous response. The cause of the difference is not known, it might be due to poor angle calibration or a problem with one of the amplifiers. The anomalous pattern matches the others in many ways except for a significantly lower amplitude at small interaction angles. It can be seen in this plot that the main peak at around $\phi = 110°$ does not have the smooth rounded shape that is expected. This may also be related to the near surface behaviour investigated in the following chapter. The peak amplitudes and positions are analysed in detail in the sections that follow.

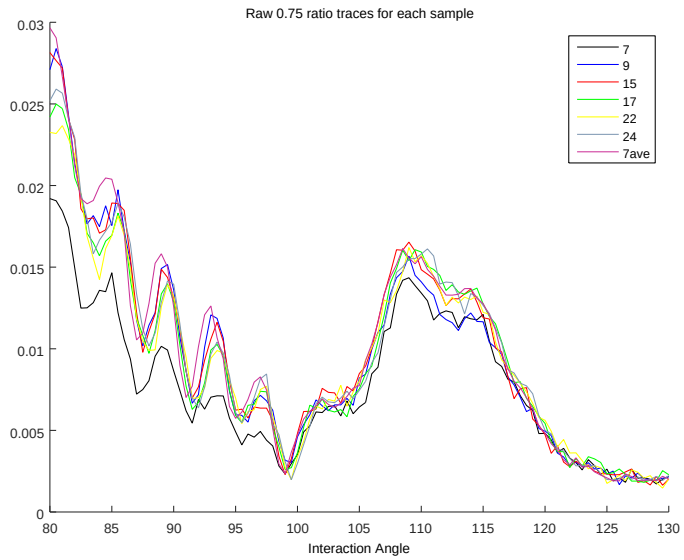


**Figure 5.16:** Mixing response at $a = 0.75$ for a range of interaction angles without Fourier smoothing. Sample numbers are shown in the legend and are in order of testing. The extra test of sample 7 has been included in the plot although it was excluded from later analysis.

### Amplitude trends

In previous studies the amplitude of non-collinear shear wave scattering has been shown to relate to the fatigue state of a material (11), but testing conducted by the author on the aluminium samples showed poor correlation and a general lack of sensitivity to the high cycle fatigue. The shear-shear non-collinear mixing is dependent upon only the $m$ Murnaghan TOEC so this may explain some of the lack of sensitivity, unlike harmonic

generation techniques. The testing of the steel samples also yielded uncertain results, Figure 5.17.

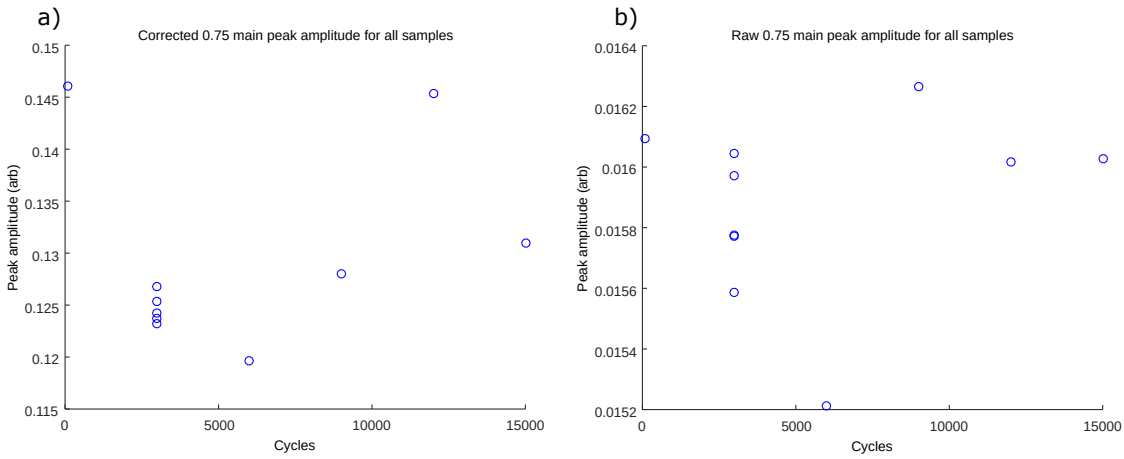


**Figure 5.17:** Peak amplitude of resonant feature against fatigue cycles. a) Corrected using reference input amplitudes, b) uncorrected.

The figure shows the peak amplitude of scattering that was recorded between 100° and 120° (the main resonant peak) for a range of differently fatigued samples at a frequency ratio of 0.75. This frequency ratio was selected for most of the analysis since it provided the best signal to noise ratio. The 100 and 12000 cycle samples produced significantly more signal than the others. However, this data was amplitude corrected based upon a calibration amplitude measurement taken before each sample was tested. If we look at the uncorrected data it can be seen that there is a much smaller variation in scattering amplitude. It was later learnt that the amplifiers can take more than an hour to reach a constant output so it is believed that some of the calibration readings were taken before they had fully stabilised. It took about an hour and a half to collect the fingerprint of each sample so the resonant interaction angle of around 110° was not reached until about half an hour into the scan. This would have given the amplifiers more time to stabilise than when the calibration measurement was taken so the uncorrected readings are probably more accurate than the 'corrected' ones.

Looking at the uncorrected amplitudes the random error can be seen in the 3000 cycles readings, $\pm$ 1.5%. If error bars based on this were applied to the other readings there would be no trends visible above the noise. Therefore it seems that the amplitude of the resonant peak again was a poor indicator of fatigue state.

To further test the fatigue sensitivity measurements were taken at multiple points on the 'fatigued to failure', 15000 cycle, sample. The uncorrected main peak amplitudes are plotted in Figure 5.18. The distance on the x-axis is from the failure point of the dogbone sample. The sample reached its full width approximately 90 mm from

the failure so this distance should have experienced the lowest stresses. It might be expected that this highly fatigued sample would have regions of high and low fatigue due to the way fatigue damage accumulates in certain regions of the sample but the experimental data shows that the amplitude of scattering remained fairly constant across all measurement points. Again the variation between measurement points is on the same order of magnitude as the random error so there is no significant sensitivity. Similar analysis was also conducted on the 100 cycle sample as well, including measurement of the angular position of fingerprint features as described below but neither sample showed significant variation in amplitude or angle response.

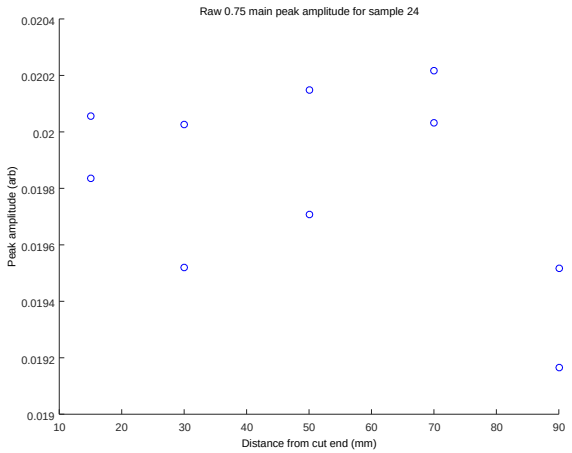


**Figure 5.18:** Peak scattering amplitude of the 15000 cycle steel sample at various points along its length with $a = 0.75$.

### Angle trends

The peak interaction angle of the main resonant lobe was recorded for each sample at a frequency ratio of 0.75. The scattering response was smoothed in the interaction angle dimension and interpolated to improve the accuracy of peak detection. The results presented in Figure 5.19 were adjusted to correct for drift in the input transducer angles. The correction factor applied was the average of the angle errors measured during the calibration procedure, as discussed in experimental methods chapter. It is usually quite reliable to take an average of multiple transducer angles because the errors normally form a consistent pattern. However during the testing of the steel samples the error pattern changed making this correction method less accurate. The order of testing was; 100 cycles, 12000, 15000 (failure), 6000, 9000, and finally five 3000 cycle tests. The pattern changed between the 15000 and 6000 measurements. The repeatability of the angles is therefore better within the two sets of tests separated by this change.

This higher level of repeatability is shown by the variation in the 3000 cycle results, approximately $\pm 0.4^{\circ}$, so a larger variation would be expected between the two sets.

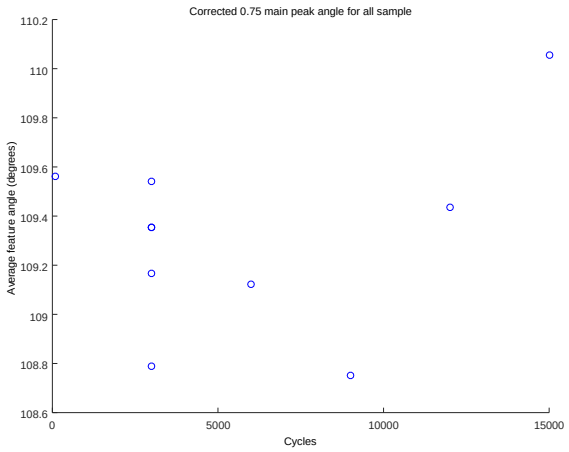


**Figure 5.19:** Resonant peak angle of fingerprints at $a = 0.75$, adjusted by angle calibration measurement.

Due to the size of the uncertainty in the main peak angle compared with the variation between different fatigue levels no trends can be identified. The main peak angle was also unsuccessful in detecting fatigue in the aluminium samples, but the angles of the bands above the main resonance lobe appeared to have some sensitivity. The high level of noise means it is not possible to see the change in angular response like in aluminium samples, Figure 5.14. Instead the position of the three peaks and troughs between $87^{\circ}$ and $103^{\circ}$ were recorded and averaged at a frequency ratio of 0.75 to create a metric of the position of the off-resonance peaks. This is shown in Figure 5.20.

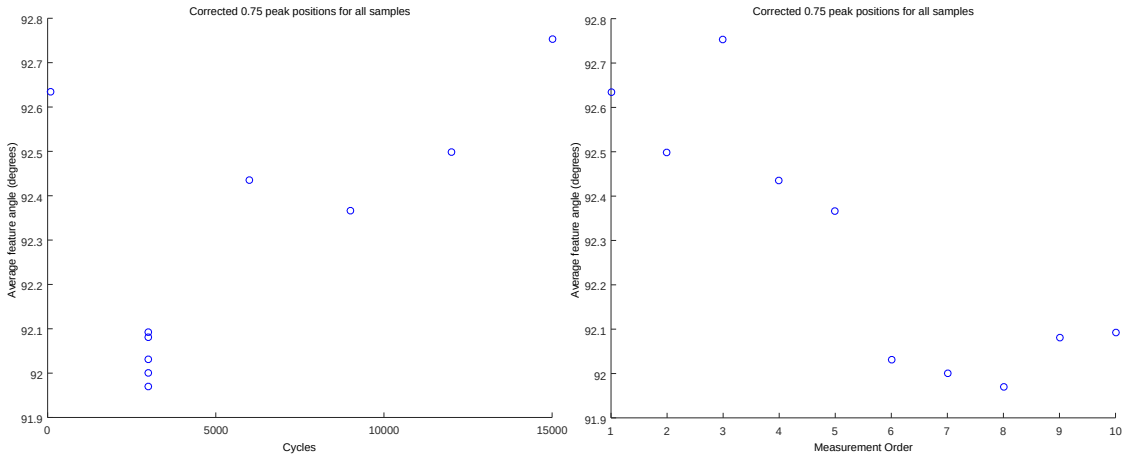


**Figure 5.20:** Averaged angle of secondary fingerprint features at $a = 0.75$, adjusted by angle calibration measurement. a) Plotted in terms of fatigue cycles, b) in order of measurement.

The variation in the 3000 cycle results is much smaller for this metric, probably due to the fact that it is the average of six features. Angular corrections were applied to these

results as stated in Table 5.1. The data for the frequency ratio of 0.85 was also analysed and produced a very similar graph, adding to the confidence in this data. The trend is that initially the increase in fatigue shifts the angular pattern towards smaller interaction angles, but after 3000 cycles increasing fatigue results in a positive shift. The positive shift was also observed in the aluminium fatigue samples.

One weakness of this data is the order in which the results were acquired, which can be seen in the second plot of Figure 5.20. There is a trend of decreasing interaction angle as time went on. There was originally a measurement of the 3000 cycle sample collected first which would have provided a more balanced ordering of the samples but the results were anomalous so were excluded due to experimental error. However, there was consistency in the repeated 3000 cycle measurements so it seems unlikely that there was a general drifting in the results related to the order that they were captured. It is also notable that the transducer angular pattern changed between measurements 3 and 4 but the average feature angle change was in line with the trend observed in part a of the figure. Results 4 to 10 were conducted with consistent input transducer angles and show a clear distinction between the less fatigued (3000 cycle) and the more fatigued (6000 and 9000) samples.

Even in the 3000 vs 6000/9000 cycles case where the probable experimental error is at a minimum, the difference between the results (0.4°) is so small that the results are inconclusive when compared to the possible inaccuracies. Many improvements to the experimental setup were made since this data was collected but an accuracy of 0.5° remains at the limit of its capabilities. The only certain conclusion is that the non-collinear mixing of shear waves in 347 stainless steel fatigued in high cycle, high temperature bending does not produce amplitude variation greater than 7%, or angular shifts in fingerprint features greater than 1°.

## 5.5 Conclusions

A model for the prediction of bulk mixing at arbitrary interaction angles and frequency ratio, created by Potter, was improved and tested. The predicted behaviour matched the experimentally observed behaviour well in many ways but further improvements are required. The model suggested the presence of secondary bands of mixing within the $a$-$\phi$ parameter space but these were not seen in the experimental tests. No features of particular interest were seen in the frequency ratio dimension of the modelled or experimental fingerprints.

Most importantly for the goals of this work, the testing showed that the bulk non-collinear mixing of two shear waves in aluminium occurred only within the $\phi = 110^\circ - 130^\circ$ range with a reference input frequency of 5 MHz. Therefore, bulk mixing should not occur at a similar angle to the predicted $\phi = 90^\circ$ optimum for CAN mixing, allowing it to be measured without interference and possibly giving the opportunity to use the bulk mixing signal strength at classical resonance as a benchmark for the CAN mixing.

Testing at a lower reference input frequency of 2.25 MHz resulted in a fingerprint with a larger region of potential mixing conditions, and a lower peak amplitude of scattering at resonant conditions. The ability to cause mixing at conditions further away from the classically resonant cases allowed for the examination of the angle of the scattered beam. In these cases the scattered beam did not appear to obey the rules of momentum conservation, scattering in a direction different from the sum of the two input wave k-vectors.

The effect of depth of beam interaction in the sample was tested and shown to have only minor effects on the fingerprint pattern. Shallower depths produced stronger signals mainly due to the more concentrated beams. Input beams with adjustable focus would be ideal for maintaining an equal interaction volume at all depths but it is likely possible to create a correction factor for the effects of depth if this cannot be done.

Measurement of the fingerprints of aluminium and steel fatigue samples exhibited banding at interaction angles smaller than the main peak. It is thought that this is due to their reduced thickness compared with the 60 mm thick sample used for the rest of the bulk mixing testing. It was noticed during this testing that moving the interaction volume even closer to the surface produced unexpectedly large signals and may have affected the fatigue data. This behaviour is examined in the following chapter. The interaction angles at which the secondary bands peaked in the aluminium fatigue samples showed weak correlation with fatigue state but no reliable trends were observed in the steel samples, or in the main peak angle for either material.

# Chapter 6

# Near surface mixing

## 6.1 Introduction

During the experimental testing of non-collinear mixing in solid materials it was noticed that mixing was stronger when the interaction volume was near the surface. This chapter is about the investigation of this behaviour, attempting to find the source of it, and what implications it might have on the implementation of non-collinear mixing as an NDT technique.

In some cases the mixing appeared to be very strong in comparison to the normal bulk mixing behaviour, thus it seems likely that this behaviour has been noticed by other researchers before. However, no description of mixing matching with the behaviour observed in this chapter could be found in the literature, possibly because it was referred to using different nomenclature.

In order to begin this investigation further experimental testing was conducted. The results of this are detailed in the first section of this chapter. Next the application of the geometric model to this problem is discussed and tested against the experimental results. Finally, the development of a COMSOL model with the aim of replicating this phenomenon is examined.

## 6.2 Experimental fingerprints

Fingerprints were collected from the 60 mm thick solid 2024 T351 aluminium sample at a range of depths. It was noticed that the patterns gradually transitioned from the bulk behaviour presented in the previous chapter into a very different one as the depth of interaction was reduced to zero. This is illustrated in the 5 MHz testing shown in Figure 6.1.

Testing was also conducted at 2.25 MHz reference input frequency to explore the frequency dependence of the mixing and for easier comparison with the FE modelled results detailed later in this chapter, Figure 6.2. The equipment used for these tests is detailed in Chapter 3. The lower frequency testing was done with much higher resolution parameter spaces (as well as wider ranges), this was purely due to time constraints when conducting each set of experimentation. Each of the 2.25 MHz fingerprints took about two and a half hours to collect.

The 6 mm deep fingerprint at 5 MHz, Figure 6.1 (a), looks most like a normal bulk fingerprint, there is only a faint band at 108° that is unusual. Such bands were seen in the fatigue testing with measurement depths of 7 mm, so this adds to the evidence

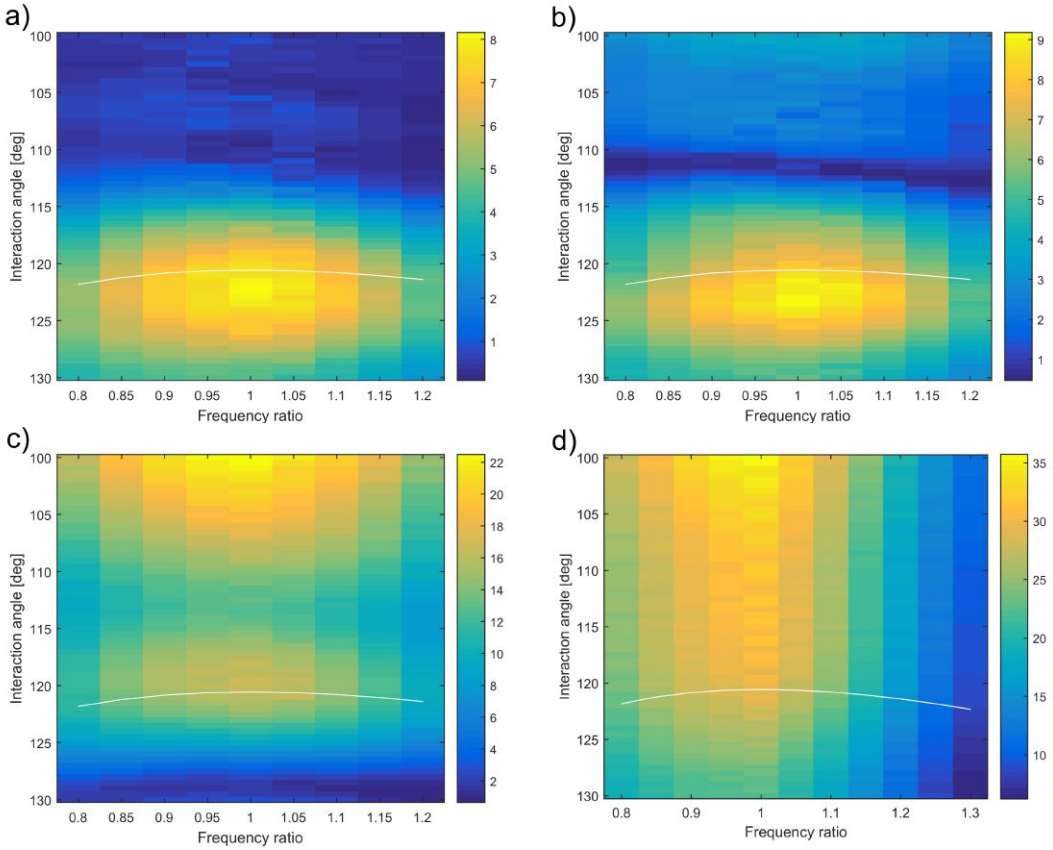


**Figure 6.1:** Experimentally measured parametric response of solid aluminium sample at a range of depths. a) 6 mm deep centre of interaction volume, b) 4 mm, c) 2 mm, d) 0 mm (on the surface). 5 MHz used for the reference input pulse. Colour scale indicates scattered amplitude. White line indicates the resonant conditions.

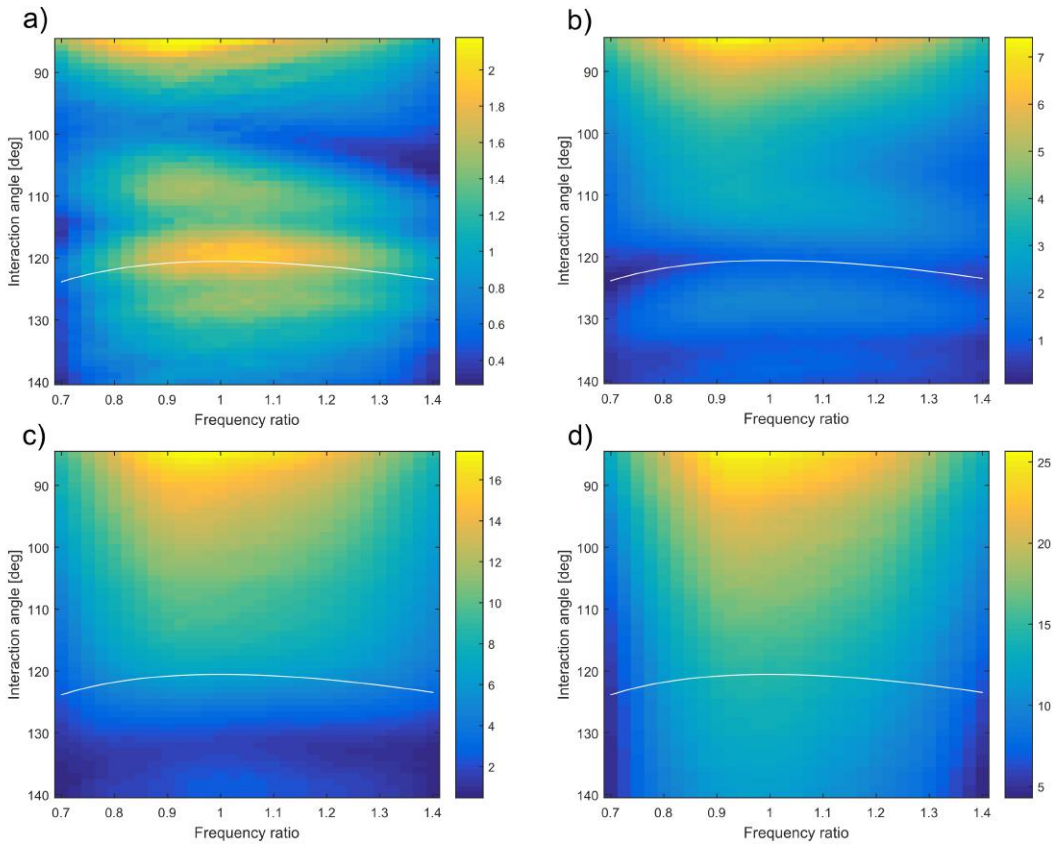


**Figure 6.2:** Experimentally measured parametric response of solid aluminium sample at a range of depths. a) 6 mm deep centre of interaction volume, b) 4 mm, c) 2 mm, d) 0 mm (on the surface). 2.25 MHz used for the reference input pulse. Colour scale indicates scattered amplitude. White line indicates the resonant conditions.

that those features were a result of the interaction volume intersecting with the surface. The peak scattering occurred at an interaction angle of 122°, this is a larger angle than the bulk mixing fingerprints collected at greater depths. This difference is likely due to the poor angular calibration of the 5 MHz near surface testing due to the limited time available and the focus not being on precise angular measurement but rather general near surface behaviour. The 2.25 MHz fingerprint at 6 mm on the other hand did not look normal, the main peak was split into three lobes and a bright region at small interaction angles appeared. It makes sense that the 2.25 MHz fingerprint would show greater abnormalities because the beams are more divergent at the lower frequency (since they have the same transducer size) so a larger fraction of the interaction volume was above the sample.

At this point in the investigation it was not known if the new mixing behaviour was confined to within the sample (either coming from the interaction volume within the solid, or from the surface of the sample), or if it was occurring in the water near the surface. These three cases would be expected to have different mixing behaviours. The following section, 6.3, investigates these critical differences in detail. Before that a few more features of the fingerprints will be discussed.

It can be seen in Figures 6.1 and 6.2 that the peak amplitude of the fingerprints increased greatly as the interaction volume approached the surface. In the 5 MHz case the signal observed when $\phi = 100°$ at 0 mm deep was nearly five times stronger than at classical resonance at 6 mm deep. In the 2.25 MHz testing the signal at $\phi = 85°$ was an order of magnitude greater in amplitude. These very strong signals over a wide range of interaction angles have the potential to cause major implications in the application of non-collinear mixing in NDT. As was discussed in the thesis introduction, previously it has been predicted that kissing bonds would exhibit CAN mixing behaviour with an optimal interaction angle around 90°. Therefore it is likely that this near surface mixing would interfere with kissing bond detection unless the interaction volume can be kept within the sample. Of course, this new type of mixing may contain information that is useful so might not always be a problem.

There is another interesting change in the shape of the fingerprints when taken at about 2 mm deep at 5 MHz and 4 mm deep at 2.25 MHz, the main resonant peak appears to have shifted. In the 5 MHz case it has shifted to a smaller interaction angle and a strong minima has appeared at 128°. At 2.25 MHz the resonant conditions have become a minima with lobes of similar magnitude both above and below it. These patterns are probably due to interference between the surface related mixing and that coming from the bulk. It is interesting that the signal coming from the near surface mixing therefore is

roughly equal in magnitude but completely out of phase from the bulk when $\phi = 120^{\circ}$, depth is 2 mm, and frequency is 2.25 MHz.

Testing was conducted with interaction depths above the surface of the sample, this resulted in a reduced scattering amplitude in all cases when compared with 0 mm interaction depth. This suggests that the mixing is due to the amount of input beam overlap on the water-sample interface, or the volume within the sample. Measurements were also taken with no sample in the beam paths and no signs of mixing could be detected. Non-collinear mixing would not be expected since only the longitudinal mode is possible in fluids thus bulk wavelength matching with another mode is not possible. Therefore, it is highly unlikely that the mixing is occurring in the bulk of the water, but it does not rule out the interaction between the water and the solid at the interface between them being responsible.

## 6.3 Volumetric versus planar mixing

In order to investigate if the mixing was actually coming from the surface, rather than a volume below (or above) it the angular directivity of the scattering was analysed. It would be expected that the direction of scattering and beam width changes could allow confirmation of the mixing source as will be described in the rest of this section.

### 6.3.1 Scattering angle

One way to tell if the non-collinear mixing is happening in a 3D volume or a 2D plane is to analyse the scattering angle. This is because, as will be shown, the two cases lead to different predictions of scattering angle. The geometric model of mixing will be used to calculate this, the fundamentals of which were described in Chapter 4. In that chapter the spacing between the nodal points of the interference pattern was found and the angle at which they formed a line was used in the bulk mixing chapter to predict the angle of propagation of the third beam. The geometric model can be used in the 2D source case as well but a few further factors must be considered.

In the geometric model the interface plane exists as a one dimensional line.For this model it is assumed that when regions of constructive interference of the input beams occur at the interface they become sources. These regions are simplified to points (antinodes) of maximal constructive interference and the timing of these points hitting the plane can be used to predict what angle a scattered beam would be generated at. This

can be thought of as a Huygens model, forming a flat wavefront due to the combination of many point sources. As was discussed in Chapter 4 the definition of which points cause mixing does not matter as the phase between the two beams is arbitrary in the model, the key is really the shape of the phase pattern and how it moves.

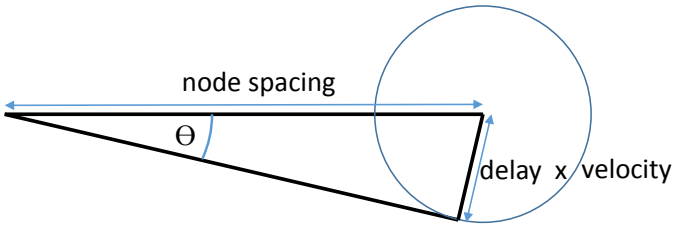


**Figure 6.3:** Geometric relation of the scattering angle $\theta$ with the nodal spacing, delay, and scattered wave velocity terms.

The angle that a beam will be produced at is illustrated by Figure 6.3 in terms of the spacing between neighbouring nodes/antinodes, time delay between them, and the velocity of the scattered wave. This leads to the following equation.

$$\theta = \sin^{-1}\left(\frac{\text{delay} \times \text{velocity}}{\text{spacing}}\right) \tag{6.1}$$

In this chapter the planar source is assumed to be in the $x$-$z$ plane as that is the orientation of the top surface of the sample. In the following chapter on interface mixing this is also the case for all experimental work but in Chapter 8 it has been extended to allow for a 2D source to be rotated around the z-axis in some of the geometric modelling.

In Chapter 4 a vector, **j**, relating the neighbouring points of the interference pattern was found, Equation 4.17. The 'spacing' in the above equation is the $x$ component of **j**. The velocity for the shear-shear sum frequency mixing mode is just the velocity of a longitudinal wave in the medium. The delay is a factor of two parameters; the vertical spacing of neighbouring points and the speed at which the pattern moves downwards (the $y$ direction). The vertical spacing is the $y$ component of **j** but the speed the pattern moves requires further derivation, provided below.

Due to the symmetry of the input beams the interference pattern formed always moves only in the $y$ direction. This can be seen in Figure 6.4 in which a pair of wavefronts at one time are drawn in black, and at a later time in green. The overlap point moves directly downwards even at frequency ratios away from 1 because the waves travel at the same speed. From this geometry it is clear that the speed at which the node travels downward, $v_n$, is given by

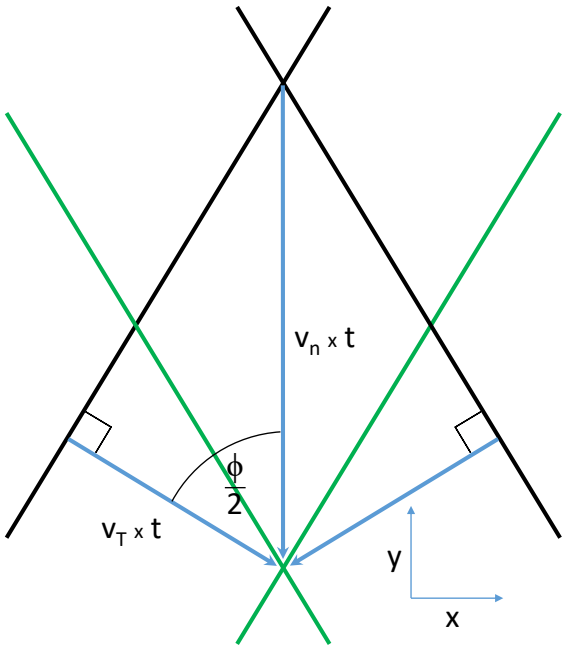


**Figure 6.4:** Diagram of a pair of wavefronts at two points in time, the earlier time in black and time $t$ later in green. This diagram is unaffected by frequency ratio and true for all cases where the vertical axis is defined as the bisector of the interaction angle. $v_T$ is the transverse wave velocity and $v_n$ is the effective overlap point speed.

$$v_n = \frac{v_T}{\cos(\phi/2)} \tag{6.2}$$

where $v_T$ is the transverse wave velocity. With this final unknown in Equation 6.1 defined it is possible to calculate the scattering angle.

$$\text{delay} = \frac{j_y}{\frac{v_T}{\cos(\phi/2)}} \tag{6.3}$$

$$\text{delay} = \frac{\frac{\lambda_1-\lambda_2}{\sin(180-\phi)}\sin(\phi/2)}{\left(\frac{v_T}{\cos(\phi/2)}\right)} = \frac{(\lambda_1-\lambda_2)\cos(\phi/2)\sin(\phi/2)}{v_T\sin(180-\phi)} \tag{6.4}$$

$$\theta = \sin^{-1}\left(\frac{\frac{(\lambda_1-\lambda_2)\cos(\phi/2)\sin(\phi/2)}{v_T\sin(180-\phi)}v_L}{\frac{\lambda_1+\lambda_2}{\sin(180-\phi)}\cos(\phi/2)}\right) = \sin^{-1}\left(\frac{\lambda_1-\lambda_2}{\lambda_1+\lambda_2}\sin(\phi/2)\frac{v_L}{v_T}\right) \tag{6.5}$$

$$\theta = \sin^{-1}\left(\frac{1-a}{1+a}\sin(\phi/2)\frac{v_L}{v_T}\right) \tag{6.6}$$

It is interesting to compare this equation with the classical bulk mixing one in Chapter 5, Equation 5.12. They have quite similar forms except for the additional velocity ratio in

the 2D version and the sine functions instead of tangents. Figure 5.12 in Chapter 5 shows the difference between the angle prediction of the classical formula and this 2D source equation. It is referred to as CAN in the figure. It can be seen that with the parameters for aluminium the CAN/2D prediction gives larger scattering angles than the classical prediction for interaction angles smaller than the resonant angle, and vice versa. The two equations give the same prediction at all resonant conditions.

The two equations are obviously equal when $a = 0$ and thus $\theta = 0^\circ$ in both cases but it is less intuitive that they should also be equal at all resonant conditions. The reason why the equations produce the same scattering angle at classically resonant conditions first requires a reinterpretation of the interface scattering effect. If the nodes of the interface pattern in the third direction are treated as a wave and that wave is refracted by the interface according to Snell's law then it predicts the same scattering angle as Equation 6.6. To do this the effective velocity of the input wave must be found; it is simply the projection of the vertical nodal velocity (given by Equation 6.2) onto the effective direction of propagation. The effective direction of propagation is perpendicular to the vector **j**. This angle was calculated in Section 4.3.1 of Chapter 4. Therefore, the expression for the effective velocity of the interference pattern 'wave' is

$$v_e = v_n \cos\theta_3 \tag{6.7}$$

where

$$\theta_3 = \tan^{-1}\left(\frac{1-a}{1+a}\tan(\phi/2)\right) \tag{6.8}$$

This value of $v_e$ can then be used in Snell's law

$$\frac{v_e}{v_l} = \frac{\sin\theta_3}{\sin\theta_i} \tag{6.9}$$

where $v_l$ is the longitudinal velocity relating to the scattered wave and $\theta_i$ is the scattering angle of that wave from interface. When evaluated Equation 6.9 gave the same results for scattering angle as Equation 6.6 proving the validity of this interpretation of the scattering angle behaviour.

**Experimental peak scattering angle**

To test if the angle of scattering matches with the new interface source equation described above the data from the fingerprints shown at the beginning of this chapter was analysed in more detail. This should indicate whether the signal is coming from the water-aluminium interface or not. The same method was used as in the previous chapter for measuring the scattering angle for off-resonance cases. This involved summing the post processed signal in the time direction within the expected time of arrival window. The position of the peak on the array was then taken from this. The results are shown in terms of position on the detection array rather than angle because there are too many unknowns to infer the angle from the array position. The estimates of array position using the classical and interface (CAN) scattering angle equations use the assumption that the source is at the centre of the interaction depth, something that is not completely accurate when the volume is centred below the surface if the surface is the source. A small error in peak array position prediction may be expected in that case.

Figure 6.5 shows where the centre of the scattered beam hit the array when a reference input beam of 5 MHz was used. It includes results at various frequency ratios at depths from 0 mm to 6 mm. The 0 mm deep test was conducted over a wider range of frequency ratios so a larger frequency ratio of 1.3 was able to be analysed in that case; this better demonstrated the differences in position predictions. The 4 mm low frequency ratio plot was at 0.9 because the 0.8 data gave a large number of results right at the edge of the array, suggesting that the true peak was off the array making the graph less useful.

The results for $a = 1$ are intended to give a reference for the zero scattering angle behaviour of the experiment. Both the classical and the interface equations predict the same scattering angle for this case. In these plots the transducer angle error correction can be clearly seen, creating the steps in the trend. This error was discussed in detail in the previous chapter. The steps were because only whole array element jumps were allowed due to the focusing transform being applied to the raw data before interpolation in order to make it faster. It can be seen that at 2 mm depth the experimental results don't match predictions as well as at 0 mm. Upon analysis of the summed amplitude distribution it was observed that this was because the beam was highly asymmetrical at interaction angles between $100^\circ$ and $110^\circ$ for $a = 1$. An example of this is shown in Figure 6.7. Plotted are results at $\phi = 100$ and $a = 1$ for 0 mm and 2 mm depths. This change in the shape of the output beam can also be seen in the angular distribution results in the next section.

The $a = 1$ plots of Figure 6.5 also show that as the depth increased the variability of the small interaction angle measurements increased due to the lack of signal. This

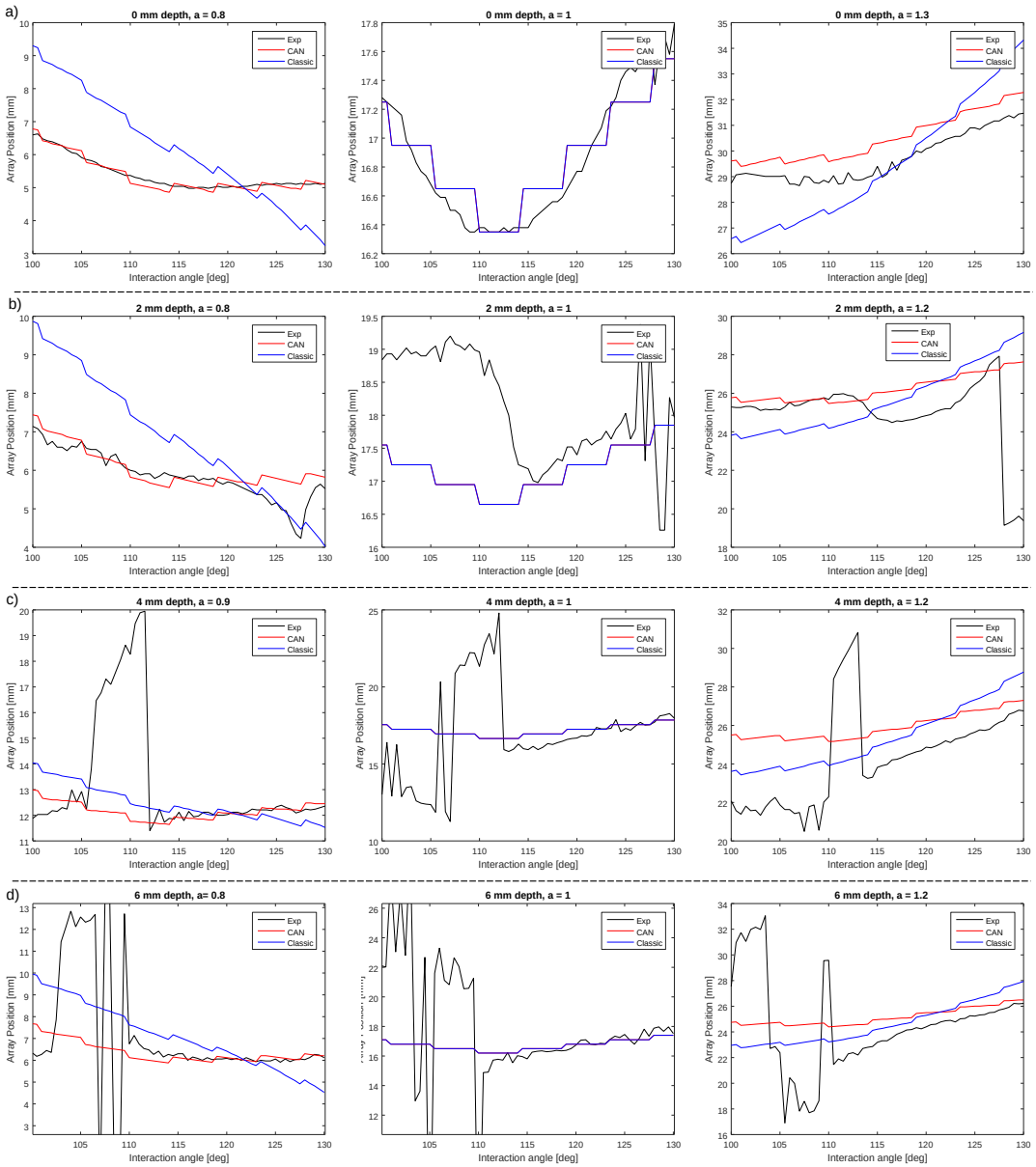


**Figure 6.5:** Position of the centre of the scattered pulse on the array measured and predicted for the interaction angle range 100° to 130°. Testing was conducted with a 5 MHz reference input beam. The 0 mm position is the left edge of the array and is the side of the reference input transducer. The experimentally measured position is shown in black. Predictions are made using the classical angle of scattering equation (shown in blue) and the CAN/interface angle equation (red). a) Results for a depth of interaction of 0 mm (centred on the surface), b) 2 mm deep, c) 4 mm, and d) 6 mm. A variety of frequency ratios are shown as detailed in the title of each. A correction factor has been applied to account for angular error in the transducers. This can be seen most clearly in the central column of plots where a constant array position would be expected without this error.

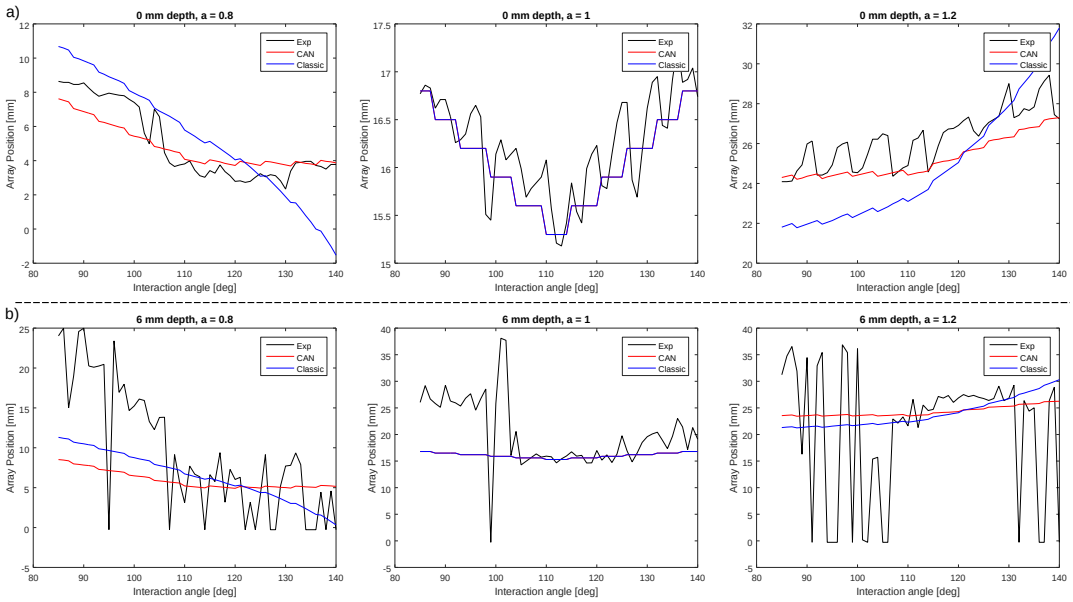


**Figure 6.6:** Position of the centre of the scattered pulse on the array measured and predicted for the interaction angle range 85° to 140°. Testing was conducted with a 2.25 MHz reference input beam. The 0 mm position is the left edge of the array and is the side of the reference input transducer. The experimentally measured position is shown in black. Predictions are made using the classical angle of scattering equation (blue) and the CAN/interface angle equation (red). a) Results for a depth of interaction of 0 mm (centred on the surface) and b) is 6 mm deep. 0.8, 1, and 1.2 frequency ratios are shown for each depth. A correction factor has been applied to account for angular error in the transducers.

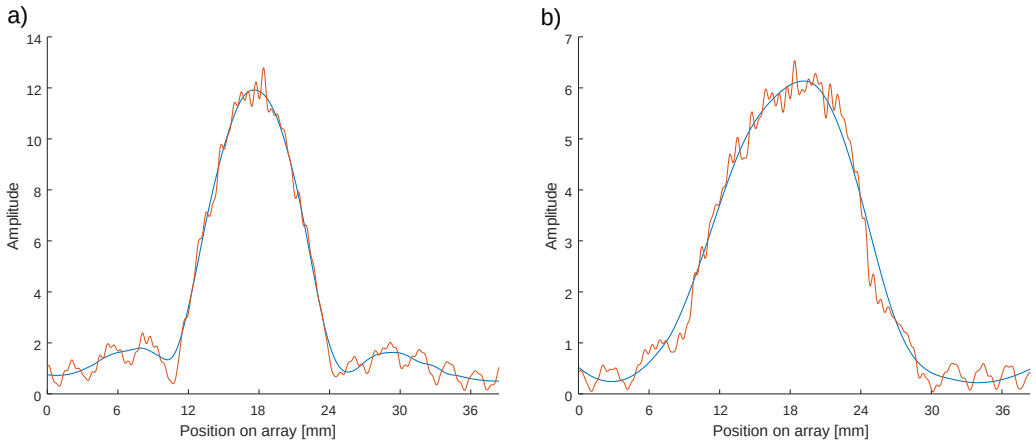


**Figure 6.7:** Summed signal amplitude detected at the array showing the spatial profile of the scattered beam. Both measurements were taken at 5 MHz with $\phi = 100$ and $a = 1$. a) is with an interaction volume centred at the top surface of the sample, b) is 2 mm below the surface. Filtering was applied to each with the result shown in blue. The peak position was taken from this filtered profile.

is additionally partly due to the beam becoming wider and having a less defined peak, suggesting the surface of the sample is the source. This will be discussed in more detail in the following section. The $a = 0.8$ at 0 mm deep plot shows how the interface scattering equation matches the experimental data much better than the classical prediction. It was shown in the previous chapter that even in the bulk mixing case the classical equation does not predict the scattering angle as well as the interface equation at off-resonant conditions. Therefore, the fact that the geometric interface method matches better in this case is not proof alone that the surface of the sample is the scattering source. Interestingly, the $a = 0.8$ case had better agreement with the CAN/interface angle prediction than at $a = 1.2$ in the bulk testing and the near surface testing as well. It is unclear why the equation would be more accurate at $a = 0.8$ and could be coincidence, further testing or modelling is required.

There are some parts of the results in Figure 6.5 that do not fit well with the interface predictions, the dip at $\phi = 127^\circ$ in 2 mm deep, $a = 0.8$ for example. Most of these upon closer analysis appear to be due to deforming of the beam as occurred in Figure 6.7, or a lack of signal though. The offset that occurred in most of the $a = 1.2$ figures did not seem to be related to this asymmetrical beam pattern however.

Analysis of the peak scattering position was also conducted using the 2.25 MHz reference beam data, Figure 6.6. Only the 0 mm and 6 mm depths are shown as the results are quite similar to the 5 MHz testing. In general the position measurement appeared to have more random error in it, probably due to the worse signal to noise ratio and the wider beam spread. Despite the increased error the results clearly matched the interface prediction method better than the classical at 0 mm. The 6 mm deep figures were too noisy for many conclusions to be drawn. The offset in the $a = 1.2$ results can also be seen in the 2.25 MHz data.

### Experimental angular distribution

The peak angle of scattering seemed to fit quite convincingly with the geometric interface model but, as stated above, the data from deeper measurements (as shown in the bulk mixing chapter) also appeared to match this prediction well so more evidence is needed. In this section the angular distribution of the scattered beam will be analysed in more detail, not just looking at the peak position. Changes in this distribution as the interaction depth is altered could provide evidence that either that the mixing is either coming from the surface or the bulk.

In this section the figures are plotted with observation angle on the $x$-axis, as was done in

Chapter 5 for the geometric and nonlinear direction amplitude functions. The conversion of the experimental data into this form is an approximation as was stated in the previous section, but was done in this case since the precise angles are not as important in this section and the intention was to make the figures easier to compare with the modelling figures in the previous chapter. The angle is calculated based upon a source at the surface of the sample for all interaction depths.

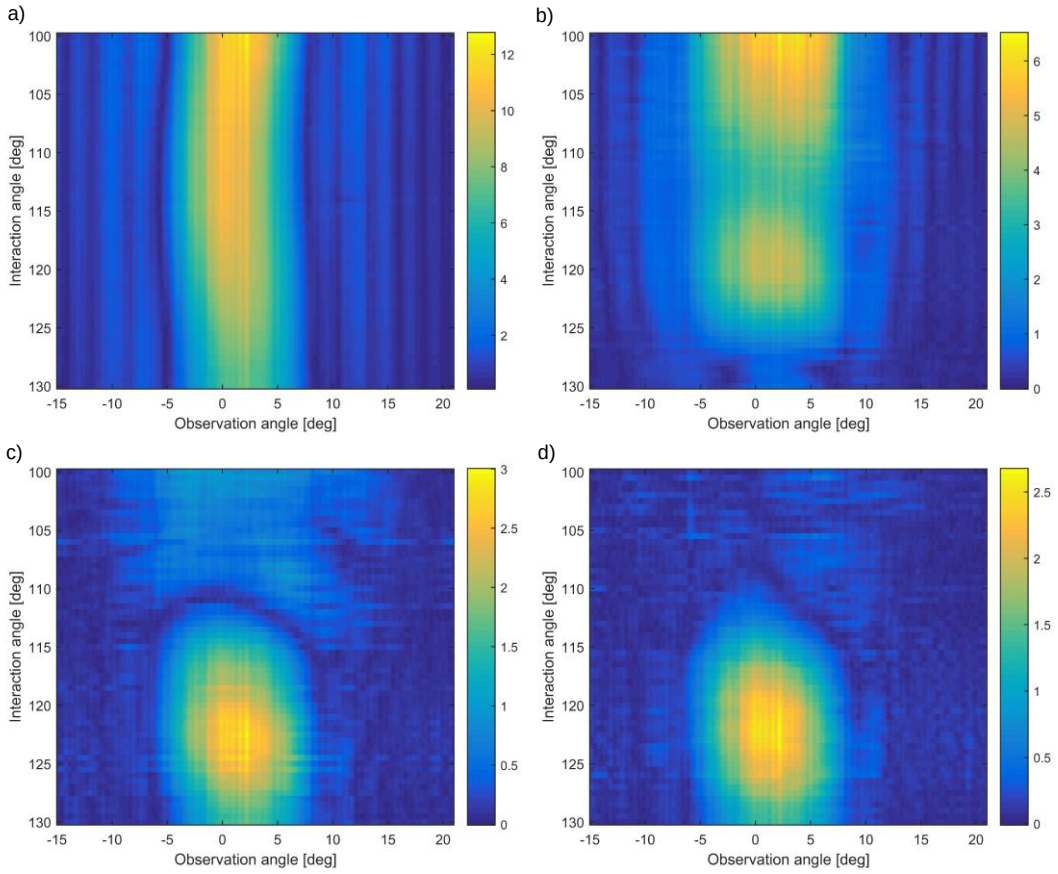


**Figure 6.8:** Experimentally measured angular distribution of scattering for interaction angles ranging from 100° to 130° at interaction depths of a) 0 mm, b) 2 mm, c) 4 mm, and d) 6 mm. Testing was conducted with a 5 MHz reference input beam and a frequency ratio of one. The x-axis angle scale is calculated from an approximation of the volume of interaction being 60 mm away from the detection array (the thickness of the sample).

The directivity at various depths with a 5 MHz reference input beam is shown in Figure 6.8. A frequency ratio of one was used for all this analysis. The 6 mm deep plot looks quite similar to Figure 12.2 (a) in the bulk mixing chapter, but as the depth is reduced a pattern that is more insensitive to interaction angle is produced, as shown by the continuous vertical bands at 0 mm.

When comparing the results at $\phi = 100°$ for 0 mm and 2 mm depths it can be seen that the central lobe is narrower in the 0 mm case (the asymmetry of the scattering, noted earlier, can also be seen in 2 mm plot). This suggests that the source of the mixing

is larger at 0 mm depth. This agrees with the idea that the surface of the sample is the scattering source because the area of the beam overlap would be expected to be at its largest when the interaction volume is centred on the surface. If the source of the scattering were the volume below the surface then there would be little to no change in the horizontal size of the interaction volume as it is moved closer to the surface. This would probably produce a beam that had similar beam widths at a range of depths. The section of the interaction volume that is in the water would create an asymmetry in the interaction volume that might have a complex impact on the scattered beam properties. The data appears to match the more simple solution however so the scattering is probably coming from the surface.

The reasoning above relies upon the assumption that the detection array is in the far field. This assumption might not be correct in this case; at a frequency of 10 MHz and observation distance of 60 mm the source would have to be 12 mm wide or less in order for the observation point to be in the far field. This calculation is quite rough, including many approximations, so it might be possible for sources larger than this to be identified reliably from their intensity profile on the array, but it could not be said with certainty without more accurate modelling.

It should also be noted that the surface source concept agrees with the fact that in the 4 mm depth test the extra scattering does not occur until the interaction angle becomes small which causes the beams to overlap more on the surface, while the 0 mm test shows that the phenomenon can occur over a large range of interaction angles.

The 2.25 MHz data again is less useful due to a worse signal to noise ratio (SNR) but is shown in Figure 6.9 for interest. A lower SNR is expected for the lower frequency mixing if it scales in a similar way to bulk mixing. The wider parameter space allows a couple more features to be identified; the continued increase in scattering at angles smaller than 85° is a notable one. It might be expected that the amplitude of scattering would be maximal at 90° as some of the CAN theory/modelling has suggested, but this is not the case. Also the 85° measurement at 6 mm deep shows that a very wide beam was produced, adding to the small surface source idea. The beam is fairly uniform in profile except for a more intense lobe at about 8°. This may be related to the asymmetry observed in some of the 5 MHz results but has no obvious explanation.

Something that should be remembered during analysis of fingerprints is that the measurement of the scattering amplitudes involves a summation of a spatial window. Therefore the measurements were sensitive to window width when compared to the beam width. The window size was set based upon the beam width of the bulk mixing at resonance. Generally this worked well as can be seen in Figures 6.8 and 6.9 but there

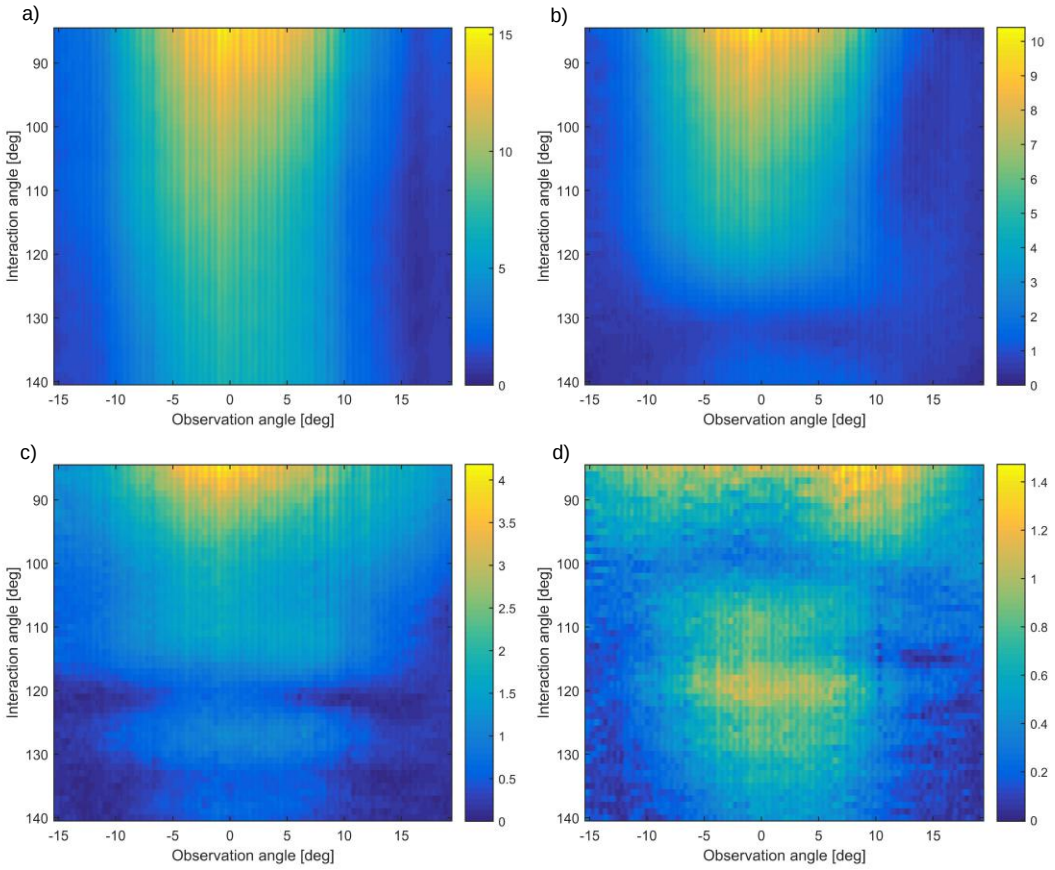


**Figure 6.9:** Experimentally measured angular distribution of scattering for interaction angles ranging from 85° to 140° at interaction depths of a) 0 mm, b) 2 mm, c) 4 mm, and d) 6 mm. Testing was conducted with a 2.25 MHz reference input beam and a frequency ratio of one. The x-axis angle scale is calculated from an approximation of the volume of interaction being 60 mm away from the detection array (the thickness of the sample).

are some interaction cases that produced wider beams than this, $\phi < 110^\circ$ at 4 mm deep and 5 MHz for example. It could therefore be argued that some regions of the fingerprint under represent the true amount of scattering occurring. One solution to this might be to make the window larger but this would increase noise so it was not done for the testing presented in this thesis. Ultimately there is no one fixed way of processing the array information that would be best in all situations, but the directivity of the sources of interest must be kept in mind when selecting spatial window size.

### Amplitude-frequency relationship

The results of the previous section show that it is quite likely that the surface of the sample is the source of the mixing. This section section seeks to investigate another aspect of the near-surface mixing phenomenon to see if it also behaves differently from the bulk mixing.

It would be interesting to know how the surface mixing phenomenon responds to absolute input frequency in terms of scattering amplitude as this might dictate what frequencies would be optimal for near surface non-collinear inspection if it does not scale in the same was as CAN or bulk mixing. The method used in the previous chapter will be applied again here to achieve a rough estimate of this.

The scattering amplitude experimentally measured at 0 mm depth, $a = 1$, $\phi = 100^\circ$, with 2.25 MHz input frequency was 20, while at 5 MHz it was 35. If the results are standardised to the 5 MHz case using the correction factor of 0.39 from Chapter 5 then the 2.25 MHz reading becomes 7.7. The 2.25 MHz test was conducted with an array gain of 65 dB while the 5 MHz tests was only 60 dB. If this extra 5 dB is factored into the 2.25 MHz result it becomes 4.3. Thus the 5 MHz scattering was eight times stronger than the 2.25 MHz scattering with everything standardised. If the scattering were dependent on a cubic relation in terms of frequency it would be expected that the 5 MHz would be 11 times larger. Due to the number of approximations involved in the calculation of the relative amplitudes the measured factor of eight is probably within the margin of error of the predicted value. With this error though it is inconclusive if the cubic relation is a better fit than a squared relation that would predict a factor of 5. In order to measure the relationship more accurately a sweep of frequency could be done with one set of input transducers and array in order to remove many of the steps that contained uncertainty.

## 6.4 Modelling

The experimental testing suggested that there was a nonlinear scattering source at the surface of the sample and that it could cause mixing to occur over a wide range of interaction angles, with smaller angles causing more scattering (within the observed range). It is unclear from this information what the mechanism of this nonlinearity might be and where it is originating from so finite element modelling was conducted to try to understand it better.

A brief introduction to the modelling method that will be used in this section is presented in Chapter 4. It was decided that in order to capture as many of the experimental factors that could possibly cause the surface mixing an advanced and detailed model was required. COMSOL was chosen as the modelling software due to its ability to combine multiple physics elements automatically and had a fairly easy to use graphical user interface. Despite its relative simplicity it contains many modules that allowed advanced modelling, such as that of hyperelastic solids to be performed. Modelling was conducted in the time domain using the same pulses as used experimentally to achieve more realistic results than a single frequency study could provide.

There are many differences between Blanloeuil et al.'s FE model and the COMSOL modelling conducted in this chapter. The key ones are:

- The COMSOL model contains both a pressure acoustics and a solid mechanics domain in order to model the water-aluminium interface.
- The COMSOL model can include higher order elastic terms in both domains which allows for modelling of the bulk nonlinearity and water nonlinearity.
- The COMSOL model does not include the solid-solid contacting interface mechanics which are in Blanloeuil et al.'s.

### 6.4.1 Model validation

#### Bulk mixing

The first stage of the modelling was to test if the bulk mixing behaviour could be replicated in COMSOL. The model was created using the Acoustics, Solid Mechanics, and additional Nonlinear Structural Materials modules. The aim was to replicate as many aspects of the experiment as possible to increase the chances of reproducing the surface mixing effect. The acoustics module allowed the water to be modelled using

the 'Pressure Acoustics, Transient' physics, and the sample was modelled using the 'Solid Mechanics' physics. The interface between the two was automatically handled by COMSOL. The model was created in 2D because 3D would have been too difficult to run on a desktop computer at the desired frequencies. It is expected that most of the behaviour could be captured in 2D anyway due to the symmetry of the interaction.

A simple geometry was used for the initial testing; one large rectangle for the sample, a smaller one above it for the water, and two much smaller rectangles for the input transducers. Rectangles were used for the transducers as they had an angle parameter that allowed them to be rotated more easily in the code. Only one side of each rectangle was an active pressure source. An example of the geometry is shown in Figure 6.10. Each transducer could independently be supplied a pressure waveform, in most of the testing a 20 cycle Hann-windowed pulse was used. In COMSOL it is possible to model a piezoelectric transducer but this would have slowed down the model and was not thought to be relevant to the near surface mixing phenomenon. The use of specified pressure nodes is not ideal since reflected waves or waves from the other transducer will not interact with them accurately. These interactions occur later than the main pulses of interest so the signals from them do not arrive at the detection array early enough to affect the results. In some cases the transducers were closer to the sample than they were experimentally in order to reduce the size of the model. This may reduce the accuracy of the model, but it tended to be used for deep interaction depths (as these required larger transducer separations) where the mixing was in the far field so it would not be expected to have altered the behaviour much.

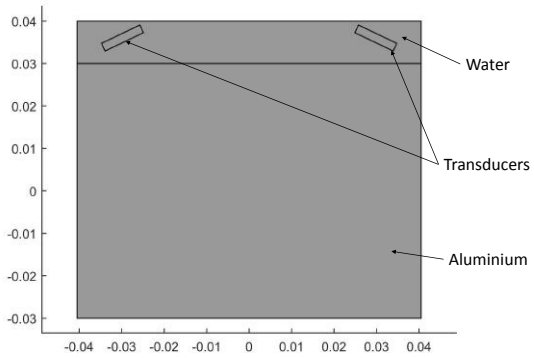


**Figure 6.10:** Example geometry of the model, showing the sample (lower rectangle), water (upper rectangle), and transducers (small slanted rectangles). The units of the axes are meters.

For each interaction angle/frequency ratio combination the model is run three times; once with both transducers active, then twice more with only the left or right active. This is exactly the same as in the laboratory, and allows for subtraction of single beam nonlinearities that might otherwise obscure the non-collinear mixing. MATLAB

LiveLink was used to create the model and extract data from it. Data for a specified set of points was requested from the locally hosted 'COMSOL Server' which interpolated the data set. This was more efficient than extracting the raw data set with uneven spacing and then interpolating that onto a regular grid in MATLAB. In nearly all cases the array of points was specified as the bottom surface of the sample with a spacing between points of the element size.

The solid section of the model had the following properties: $E = 73.1$ GPa, $\nu = 0.33$, $l = -324$ GPa, $m = -397$ GPa, $n = -403$ GPa, and $\rho = 2780$ kg.m$^{-3}$. The TOECs are as measured by Mohrbacker and Salama (94). The water had a density of $\rho = 1000$ kg.m$^{-3}$ and a wave velocity of 1497 m$^{-1}$s. The left and right sides of the sample were set to 'low-reflecting boundaries', and the lower surface was left 'free' in order to get accurate velocity/acceleration results from this edge. Accelerations in the $y$ direction (perpendicular to the bottom of the sample) were used from this boundary as the analogue of the experimental array data. The left and right sides of the water were set to 'cylindrical wave radiation' which is intended to absorb cylindrical waves coming from a particular point. It was found that it absorbed well even though the source point could not be set to match the position of the actual sources accurately. The top surface of the water used the 'plane wave radiation' setting. Perfectly Matched Layers (PMLs) were not available in time dependent model in this version of COMSOL (v5.2). It would be preferable to use PMLs since they can work in the near-field; the boundary conditions used above are intended for far-field absorption and do not offer the same level of reflection suppression as PMLs generally do. Despite this there were no problems due to boundary reflections; the geometry of the model is such that they arrive later than the signals of interest.

The pulse length changes dependent on the frequency, therefore in order to get the peaks of the two pulses to overlap with each other a delay must be added to one of the pulses if their frequencies are not the same. The following equation shows how to calculate the Inter-Probe Delay, IPD $= (\text{cycles}/2)(\frac{1}{f_L} - \frac{1}{f_R})$ where $f_L$ and $f_R$ are the left and right frequencies. The delay is applied to right pulse (beam two) if IPD is positive, and left (beam one) if negative.

Preliminary convergence testing was conducted for a 1 MHz reference input frequency at $\phi = 120^\circ$, and $a = 1.2$. The results of this testing are shown in the appendix. The non-collinearly mixed signal appeared to become artifact free and its amplitude stabilised at an element size of around 0.6 mm. The time step size parameter did not affect the results very much due to the solver used (generalised alpha) which took smaller time steps if it detects that they might be required. More accurate convergence testing was conducted

for the later modelling using fixed time steps.

This rough convergence information was used to model a fingerprint at a 1 MHz reference frequency. An element size of 0.7 mm was used, and the maximum time step was 40 ns. The peak pressure of the input transducers was set to 10 MPa and the interaction depth was 12 mm. The centre of rotation of the transducers was 6 mm above the surface of the sample. $\phi$ between 70° and 138° in 3° steps, and $a$ from 0.6 to 1.5 in 0.1 steps was investigated. It took a total of 55 hours to complete all the solutions.

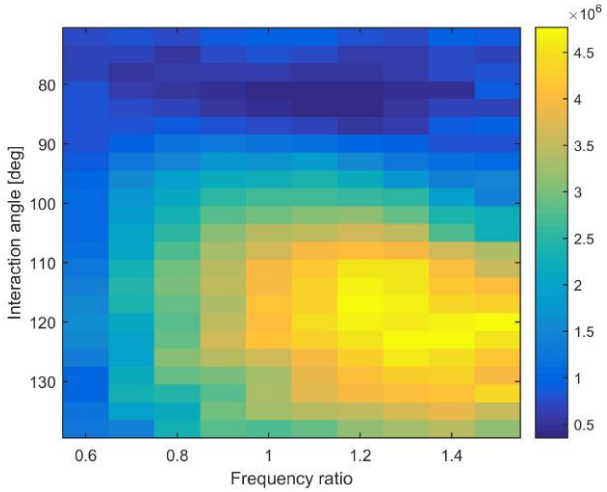


**Figure 6.11:** FE modelled parametric response of solid aluminium sample at a depth of 12 mm. 1 MHz used for the reference input pulse. Colour scale indicates scattered amplitude. No corrections have been applied to the amplitudes so it is not directly comparable to experimental data.

Figure 6.11 shows the resulting fingerprint. It has not been adjusted to include experimental factors such as transducer bandwidth since it is only an approximate test but it is clear that the model has captured many features of the real fingerprints. Mixing over a wider range of angles than seen experimentally is visible in the figure, this was expected due to the lower input frequencies. The interaction angle peaks appear to be close to the classical resonant conditions and the frequency ratio peak also behaves as expected, with signal generally increasing as frequency is increased. This matches with the behaviour of the classical model without the experimental correction factors applied, Figure 5.4 (a).

The above testing showed that the COMSOL model is able to simulate non-collinear mixing but the accuracy of the model is not yet known due to this testing being conducted at frequencies lower than experimentally and with coarse meshes/large time steps. Therefore the next stage was to acquire data to allow for direct comparison with experimental bulk mixing data. The frequency of the modelling was doubled to 2 MHz, which should require element lengths and time steps to be halved. To

satisfy this the maximum element size was set to 0.3 mm and time steps to 20 ns. The frequency was set at 2 MHz rather than 2.25 MHz in order to strike a balance between speeding up the modelling process and getting accurate results. The 2.25 MHz model would take roughly 42% longer to run and the improved accuracy is likely negligible when considering the other limitations in accuracy of them model. The geometry of the experiment was kept the same but the parameter space was slightly reduced and coarsened to allow it to be solved in a reasonable time.

Some examples of time traces from the 2 MHz model are presented side by side with their 2.25 MHz experimental counterparts in Figure 6.12. All of the FE data has been scaled to make the peak amplitude at 120°, $a = 1.3$, equal to the experimental value. Also the correction factors due to transducer bandwidth and array angle sensitivity have been applied to the modelled data. The result is time traces that look very similar to the experimental ones, both in terms of amplitude and shape of the pulses.

Testing was conducted with 20 ns steps, 0.3 mm elements at 2 MHz for $\phi = 88°$ to 138° and $a = 0.55$ to 1.45 to create a fingerprint that could be compared with an experimental one. This took a total of about 220 hours. The data was processed in a similar way to experimental data; subtraction, filtration, focusing, enveloping, windowing, peak value extraction. Correction factors were also calculated in order to make comparison with experimental data easier. Figure 6.13 shows the resulting uncorrected fingerprint, correction factors, and corrected fingerprint.

The 2 MHz FE fingerprint of Figure 6.13 looks similar to the experimental one, Figure 5.7 in Chapter 5. They both drop down to below a tenth of peak intensity at an interaction angle around 100° and peak at the resonant conditions. The experimental measurement had a strange effect at larger interaction angles with frequency ratios between 0.8 and 1.1 that looked liked narrow bands of stronger mixing. It is unclear what caused this but the modelling does not show any sign of this mixing. These bands were not seen at 5 MHz so are probably not a result of bulk mixing in the 2.25 MHz case. Both the FE model and experiment have peaks at frequency ratios larger than one, but the main lobe of the model is further shifted in the positive direction than was measured. These differences are likely due to approximations in the frequency behaviour of the transducers.

Testing was conducted to check if the model reproduced the correct input amplitude scaling behaviour. Increasing the pressure at the input sources by four orders of magnitude increased the scattered output amplitude by eight orders of magnitude as expected but it was noted that the model was generally less stable at higher amplitudes. There was visibly more noise in the full field data at higher amplitudes, if this noise became too large the model became unsolvable.

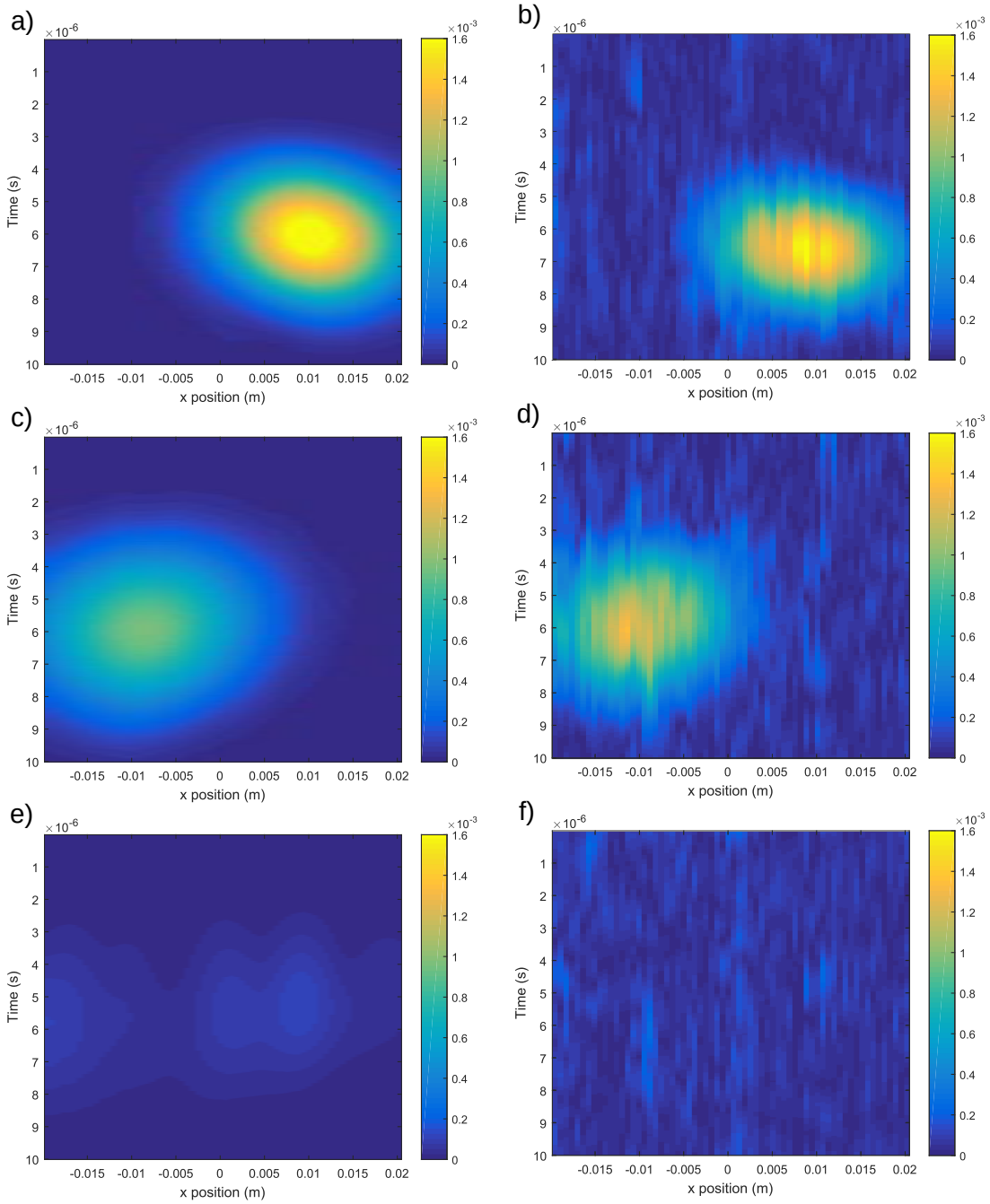


**Figure 6.12:** Time traces of FE and experimental data. The modelling was conducted with a reference frequency of 2 MHz, while the experiment was 2.25 MHz. In the model a time step size of 20 ns and element size of 0.3 mm was used. The experimental data was captured for a depth of interaction of 15 mm so the model was set to this as well for these side-by-side comparisons. a) is the FE result at $\phi = 120°$ and $a = 1.3$, c) is at $\phi = 115°$ and $a = 0.8$, e) is at $\phi = 90°$ and $a = 0.8$, and b), d) and f) are the experimental equivalents. Correction factors have been applied to the modelled data and the amplitude is standardised to the $\phi = 120°$, $a = 1.3$ level.

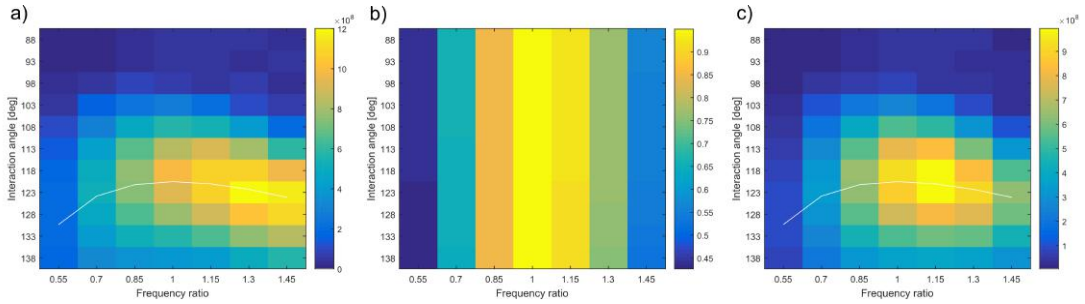


**Figure 6.13:** FE modelled parametric response of solid aluminium sample at a depth of 12 mm. 2 MHz used for the reference input pulse. Colour scale indicates scattered amplitude. a) The result of normal experimental post-processing but with no correction factors applied. b) Correction factors to include the effects of transducer bandwidth, and array directivity differences that are not captured by the model. c) Fingerprint with correction factors applied. White lines indicate the resonant conditions.

The above results have shown that the COMSOL model does a good job replicating the bulk mixing behaviour when the interaction volume is below the surface, it matched the experimental behaviour in every way that would be expected. This allowed the investigation to continue by moving the interaction volume closer to the surface.

### Near surface

The next stage of testing was to compare the signal produced when the interaction volume was below the surface to the case when the volume was centred on the surface. Experimentally these two situations had the greatest difference in fingerprint. This testing was conducted at 1 MHz since the model runs roughly eight times faster than at 2 MHz and it was thought that there would not be much loss of sensitivity operating at a lower frequency. The geometry was a bit different for this testing due to the overlapping of the beams on the surface which required the transducers to be further away from the surface. 20 mm wide transducers were used in order to have the same divergence characteristics as the 10 mm 2 MHz testing, although this would not be expected to have a significant impact on the results. The transducers were 33 mm away from the surface of the sample and the water layer was 40 mm thick. Time steps of 50 ns, and mesh elements of 0.7 mm were used, and the frequency ratio was 0.8. Results were captured at depths of 0 mm and 20 mm and at interaction angles of 80° and 120°, Figure 6.14.

When comparing the 120° results of plots (a) and (b) in Figure 6.14 it can be seen that the 0 mm deep test had a peak intensity roughly a third less than at 20 mm. If only bulk mixing is occurring it might be expected that by halving the interaction volume the scattered amplitude should also halve. It is likely that the signal did not reduce by this amount because the beam widths at the two depths are different, as discussed in

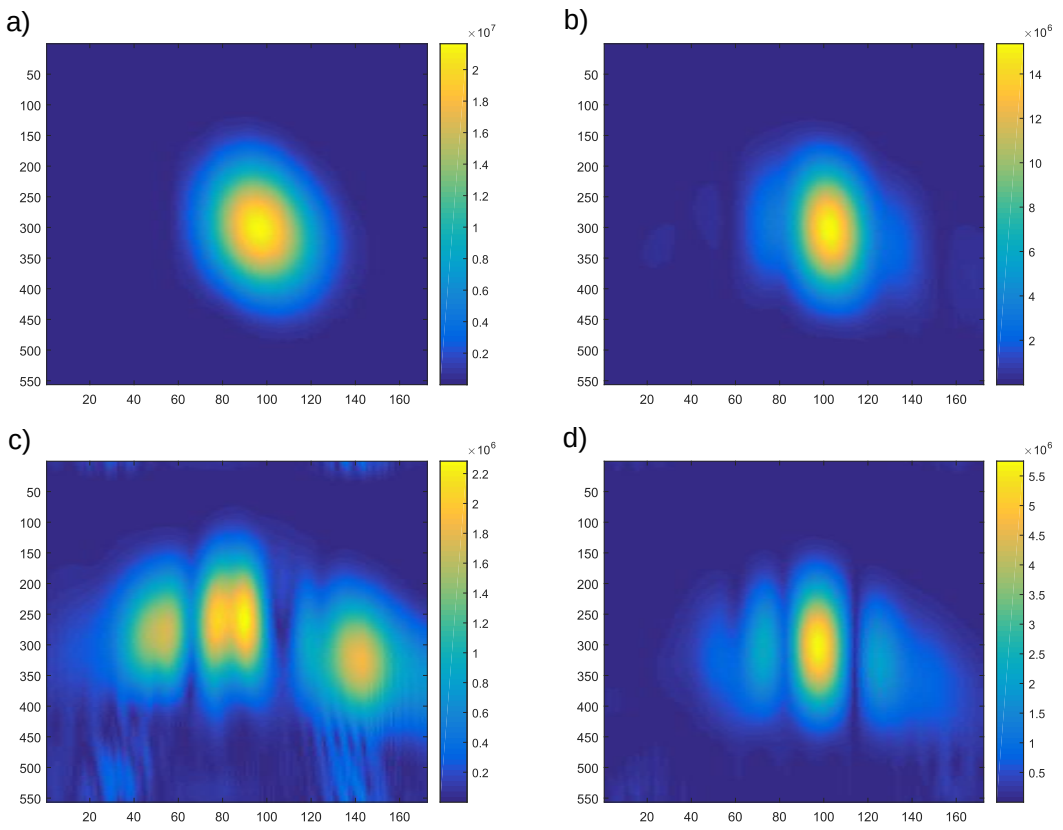


**Figure 6.14:** Processed time traces of the scattered pulse at $a = 0.8$ with a 2 MHz reference frequency. The x-axis is the element number where each element is 0.7 mm long, and y-axis is time step number where each step is 50 ns. a) is at $\phi = 120^\circ$ and a depth of 20 mm, b) is $\phi = 120^\circ$ and 0 mm, c) $\phi = 80^\circ$ and 20 mm, d) $\phi = 80^\circ$ and 0 mm.

Chapter 5, therefore there is no indication that extra scattering from another mechanism is occurring. Experimentally at $\phi = 120^\circ$ the signal generated with the volume centred on the surface was about an order of magnitude larger than when it was in the bulk, the FE modelling definitely is not showing anything on this scale. In these plots it can also be seen that the pulse is distorted when the interaction is at the surface, this would be expected due to the change in shape of the interaction volume.

At $\phi = 80^\circ$ the signal is an order of magnitude smaller in the 20 mm deep case than at $\phi = 120^\circ$ but in the 0 mm case it only dropped by a factor of three. Despite having a smaller interaction volume the scattering at $\phi = 80^\circ$ was nearly three times stronger at 0 mm than at 20 mm. There is clearly some intriguing behaviour here but it is not on the scale that is observed experimentally. The surface mixing signal of the model is only 3% of what was seen in the experimental data. The beam shape of the scattered pulse at $\phi = 80^\circ$, 0 mm deep, has a narrow main lobe with pronounced side lobes. Experimentally the beam width at 0 mm was similar to bulk mixing at greater depths so the pattern observed in the FE is surprising. The fact that the amplitude is so different and the beam shape does not match implies that the model is not capturing the near surface mixing effect properly.

Even though the model at this stage does not accurately simulate the experimentally observed near surface mixing effects it might still be of future interest to investigate why the model produced any increase in signal since no explanation is obvious to the author. It is possible that another unknown mixing phenomenon is occurring although its significance may be limited by its small amplitude in comparison to the primary near surface mixing mechanism that is yet to be identified.

### Nonlinear water

It was difficult to decide how to improve the model so that it might be able to produce more accurate behaviour since the near-surface mixing phenomenon is not presented in the literature. One concept that was discussed was adding nonlinear behaviour to the water. Initially the author believed that this would only add harmonics to the input beams which would not cause any new surface related behaviour. Upon implementation, however, the impact was seen to be far greater than this.

COMSOL provides an example of how to model the nonlinear propagation of an acoustic pressure wave on its website (99). In it the $2^{nd}$ order Westervelt equation is used which is a higher order form of the acoustic wave equation that is normally solved for. This equation can be found in many different forms, (100; 101), but the one most

relevant to this model is the following

$$\frac{1}{\rho c^2}\frac{\partial^2 p}{\partial t^2} - \nabla \cdot (-\frac{1}{\rho}(\nabla p + \frac{\delta}{\rho c^2}\frac{\partial(\nabla p)}{\partial t}))) = \frac{\beta}{\rho^2 c^4}\frac{\partial^2 p^2}{\partial t^2} \tag{6.10}$$

where $p$ is the acoustic pressure, $\beta$ is the nonlinear coefficient, $\rho$ is density, $c$ is the speed of sound, and $\delta$ is the acoustic diffusivity. The diffusivity is set to zero in this work, this results in an equation that only differs from the standard wave equation by the $p^2$ term. COMSOL uses a wave equation of the following form

$$\frac{1}{\rho c^2}\frac{\partial^2 p}{\partial t^2} + \nabla \cdot (-\frac{1}{\rho}(\nabla p - \mathbf{q_d}))) = Q_m \tag{6.11}$$

where $\mathbf{q_d}$, and $Q_m$ are referred to as 'dipole source' and 'monopole source' respectively. In order to make this equation match the simplified Westervelt equation the monopole source term must be set to

$$Q_m = \frac{\beta}{\rho^2 c^4}\frac{\partial^2 p^2}{\partial t^2} \tag{6.12}$$

which, for reference, in COMSOL is written as `(beta/(actd.rho^2*actd.c^4))*d(d(p*p,TIME),TIME)`.

The document by COMSOL, (99), provides useful information on which element types and solvers are best suited to this problem. It suggests at least 2$^{\text{nd}}$ order (quadratic) elements and the BDF time stepping method. It was attempted to use completely fixed time steps in the model by using the manual Generalized Alpha setting, because previous testing with the nonlinear solid mechanics had shown that it was better to prevent instabilities by keeping the time step small at all times, rather than reactively reducing the step size which appeared to happen too late in some cases. The fixed time steps were successful for modelling waves propagating in a nonlinear fluid but in the later testing with a fluid-solid interface it was not possible to complete the simulation due to instabilities, even when using extremely small time steps. Perhaps even smaller steps may have fixed this but the model was already running so slowly that this was not practical. Thus the BDF method with its variable time steps was chosen for the later combined fluid-solid model work.

A 2D rectangular model of nonlinear water was created to test the extension of the example's 1D form into 2D. The rectangle measured 0.2 m by 0.1 m. One of the short sides was made a pressure source and supplied a 10 cycle 1 MHz

Hann-windowed waveform. Some experimentation with different meshing methods (e.g. structured/Delaunay, rectangular/triangular) was carried out but no significant improvements were found so Delaunay tessellated, triangular meshing was kept. The long sides of the model had plane wave absorbing boundaries, and the remaining short side was left free to allow measurements to be taken from its nodes. The properties of the water were the same as in the linear model except for the new $\beta$ parameter. The definition of $\beta$, the coefficient of nonlinearity, is not consistent in the literature, some state that it is defined in the same way as discussed in the literature review as Equation 2.1. The value of this is given in the work by Pantea et al. (102) as $3.5 \pm 0.1$. Others refer to a parameter of nonlinearity as $\frac{A_2}{A_1}$, although they tend not to use the term $\beta$ for this; giving a value of 5.2 (103). One further variant is presented in Blackstock's book (104), $\beta = 1 + \frac{A_2}{2A_1}$. For this research the value was left at the default value in the example provided by COMSOL of 10. Future work should use a more accurate value.

In order to resolve the second harmonic component to within 5% of the asymptotic amplitude value a element size of 0.6 mm and a time step of 67 ns was required. Compared to the fundamental wavelength in water this element length is about a third of it, and compared to the period the time step is about a fifteenth. The element size is therefore surprisingly large considering it must support the oscillation of a wave at double that frequency. Due to the meshing method the actual average element size is significantly smaller than the maximal (approximately 30% less), this combined with the quadratic discretisation allows such waveforms to be approximated.

The nonlinear fluid was then tested in a configuration more like the experimental case, with two sources producing beams that overlapped. An example of the pressure field and frequency components generated by the model are presented in Figure 6.15. In this test the two transducers are fired at 2 MHz in a fluid only model. A region in the path of the input beams was created to allow it to be meshed more finely than the surrounding water in order to reduce the solution time. This region is the large irregular hexagon in plots (a) and (b). The transition between the two meshing densities was gradual and no reflections from the boundary were observed. The bottom edge of the model was set to plane wave absorbing and the fixed time stepping method (generalised alpha) was used for the results shown in Figure 6.15.

Figures 6.15 (a) and (b) were taken at the same time point with the fluid nonlinearity off and on respectively. The time point was chosen such that the beams have propagated from the top of the model to the bottom and the main peak of the pulse has just reached what would be the water-aluminium interface in later models. An input pressure of 2 MPa, and $\beta$ of 10 was used. It can been seen that with these parameters the nonlinear

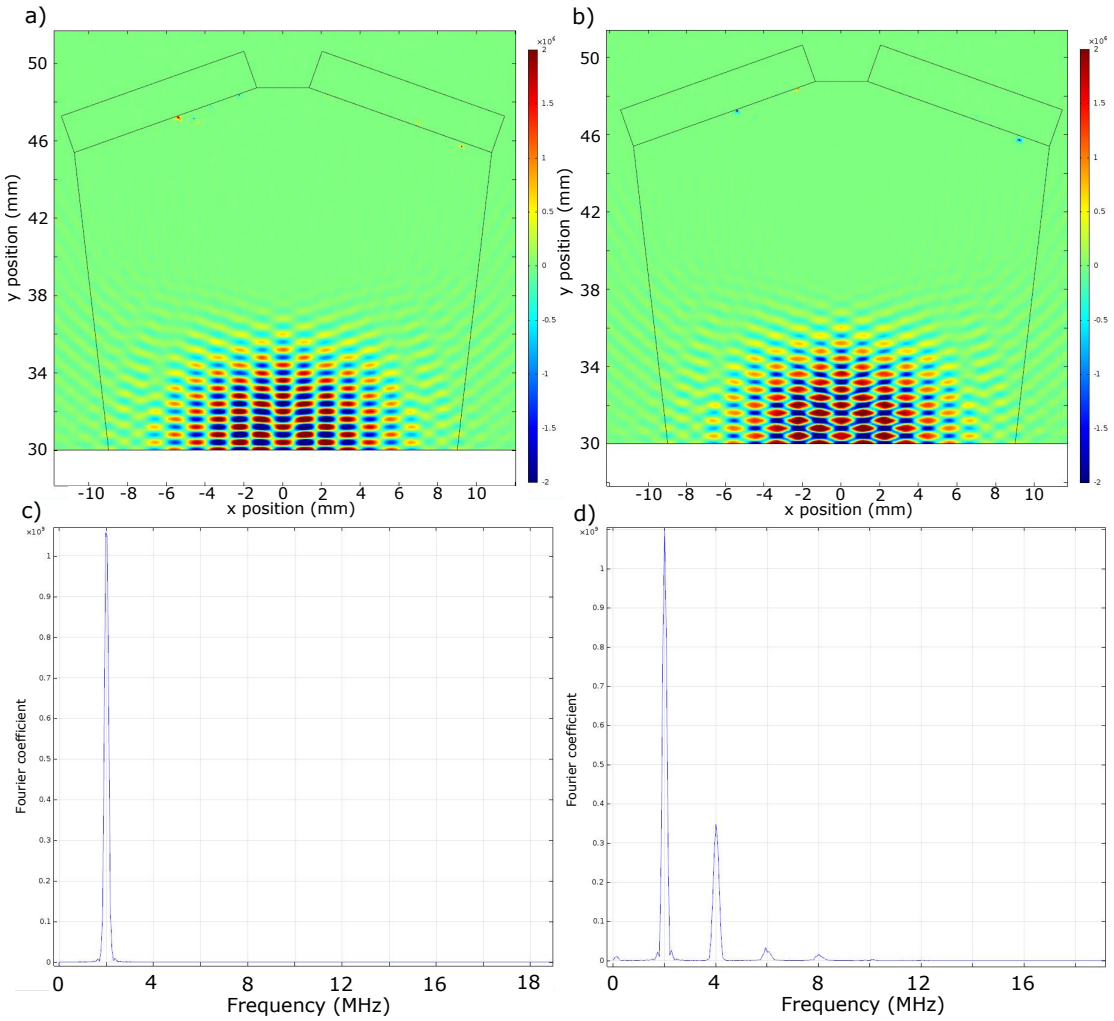


**Figure 6.15:** FE model of experimental water geometry with 2 MHz input pulses. a) Pressure field at a time when the peak of the pulses has reached the bottom of the water with linear water, b) with nonlinear water, $\beta = 10$. These plots show an example geometry of the model, with the water (large rectangle), transducers (slanted rectangles), and region of finer mesh (irregular hexagon) in the path of propagation in water. c) and d) are FFTs of the pressure at a node, horizontally in the centre, near the bottom surface. c) is with the nonlinear source term set to zero, and d) is as defined for nonlinear water. Input pressures of 2 MPa were used. This was at the limit of the model, causing significant errors to form at some points.

behaviour is easily visible. The Fourier transforms shown in (c) and (d) taken at the point with coordinates (0,0.03) demonstrate that with the nonlinearity turned on higher harmonics are produced as the beams travel through the fluid. This behaviour is a good indicator that the nonlinearity of the pressure acoustics is being modelled but it is thought that these harmonics alone would not cause extra mixing at the surface so further changes to the model might be required to capture the nonlinear physics behind it.

The pressure errors present in Figure 6.15 (seen as dots, mainly near the transducers) were fixed in later modelling by switching to the BDF time stepping method and generally using smaller time steps. In the COMSOL example quartic elements were used so testing was conducted to find what performed best in this model. It was found that quadratic elements gave approximately similar performance to quartic elements that were twice the size, but since the quartic elements have more degrees of freedom both models took roughly the same length of time to run. Therefore quadratic elements were kept as they had been used for the previous modelling.

It was also noted during this testing that smaller elements required smaller time steps in order to get stable solutions due to their ability to support higher frequency components, unlike in previous linear convergence testing where the use of a very fine mesh did not appear to affect the time steps required. Therefore it is more critical in this nonlinear model not to use a finer mesh than required as it will force smaller time steps and increase solution time even further.

### 6.4.2 Combined Model Results

The knowledge from the above section was used to adjust the previous complete experimental model; a region of finer meshing was added in the water beam path area, the source term was configured as above, and time step/element sizes were set to 30 ns and 0.3 mm (for the fine water section) respectively. An example of the final geometry is shown in Figure 6.16.

There were many issues with these settings despite the previous work showing that individually all the elements should function. The main problem was instabilities that formed on the water-aluminium interface. Testing was conducted using both fixed time stepping and BDF methods, neither worked until the time steps were reduced to a $64^{th}$ of the expected value. The fixed step method was still unable to create a stable model at this point with 0.5 ns steps. The scattered waveforms produced at classically resonant conditions and at interaction depths greater than 10 mm looked good and were similar

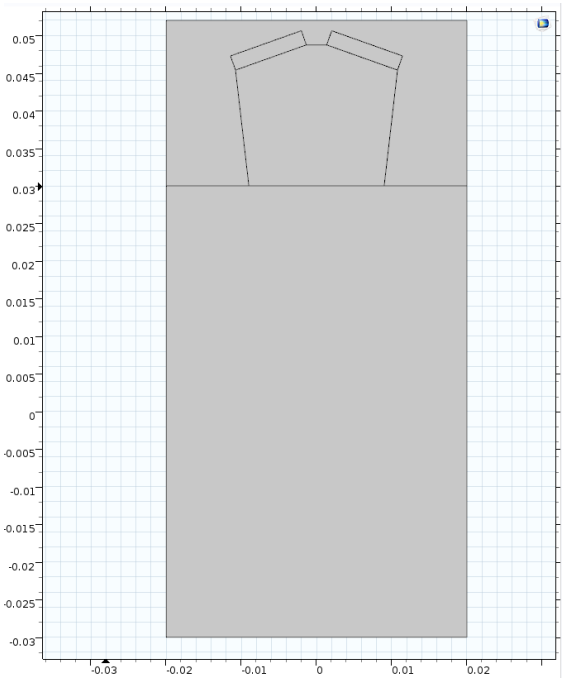


**Figure 6.16:** Example geometry of the model, showing the sample (bottom rectangle), water (upper large rectangle), transducers (slanted rectangles), and region of finer mesh in the path of propagation in water.

to the previous bulk nonlinear modelling. The results when the beams overlapped at the surface were very interesting however, they showed greatly increased amplitudes but the time traces contained many small lobes rather than one single beam as was seen experimentally. This increase in mixing intensity was promising but it was clear that further convergence testing was required to see if this signal was due to inaccuracies in the model or if it would more closely resemble the experimental data with finer meshing/time steps.

The appendix includes the detailed results of the convergence testing. A more relaxed, 10%, convergence requirement was used for this set of modelling due to the limitations in computing power. The time required to compute at higher resolutions would have prohibited the testing of as many interaction angles and depths, making comparison with experimental data less informative. This 10% level resulted in a maximal element size in water of 0.15 mm, and in the solid and lower resolution areas of the water 0.3 mm was used. Step size was 0.55 ns. This is approximately a thousandth of the period of the fundamental input frequency, a surprisingly small time step. For comparison Blanloeuil et al.'s work that is presented in the following chapter, which was also conducted with a reference frequency of 2 MHz, used a time step of 3 ns for a 0.1 mm square element mesh. This model was tested at frequency ratios up to 1.5, producing an output wave at 3.5 MHz, hence the finer mesh. Despite the smaller element size much longer time

steps were used than were required than in the COMSOL modelling.

The final COMSOL models had the same sample thickness of 60 mm and transducer width of 10 mm as previously. The transducers were positioned 18 mm above the surface, in a 22 mm thick water layer. The width of the model was varied in order to reduce modelling time where possible. The largest of the models ($\phi = 120^\circ$ at 10 mm deep) required about 5 GB of memory. Transducer peak pressure was reduced down to 1 MPa to make the model more stable. Water and aluminium properties were as described in previous sections. The input waveforms were the same as the experimental ones, 20 cycle Hann-windowed pulses defined at a resolution of 20 points per cycle. A frequency ratio of one was used as subtraction was very effective in the model so the extra frequency filtering of interaction ratios away from one was not required. The pulses were at 2 MHz, slightly less than the 2.25 MHz used experimentally. This decision was made because modelling at 2.25 MHz would have taken 42% longer and the behaviour is expected to be very similar. The boundaries were configured as before, cylindrical absorbing boundaries were used on the left and right water sides and a plane wave absorbing boundary on top. The left and right sides of the solid were set as 'low-reflecting boundaries'.

With these settings the model took about a day to run each simulation, so roughly three days were required to acquire the both, left, and right signals needed for each combination of interaction angle and interaction depth that was investigated. The frequency ratio behaviour was not tested since the experimental trends did not conclusively show any distinguishing features between the bulk mixing and surface mixing. Tests were conducted to check that the width of the model had negligible impact on the scattering results and this was confirmed. The greater width allowed more of the beam profile to be observed so the model was not reduced below 30 mm wide as it would limit this analysis.

The time traces in Figure 6.17 clearly demonstrate the surface mixing effect and match well with the theories developed from the experimental data. When the beams were fully overlapped on the surface maximal signal was produced at both interaction angles. Increasing the depth of interaction saw a greater reduction in $\phi = 120^\circ$ signal than at $90^\circ$ due to the a smaller fraction of beam overlap as expected. At 10 mm deep plots (e) and (f) show the modelling behaving very similarly to the model without the nonlinear water, dropping in amplitude by an order of magnitude between the resonant $\phi = 120^\circ$ and far from resonant $\phi = 90^\circ$ cases. At 4 mm deep and $\phi = 90^\circ$ a wider beam is produced due to the small source area on the surface, again confirming the surface as the source of this mixing.

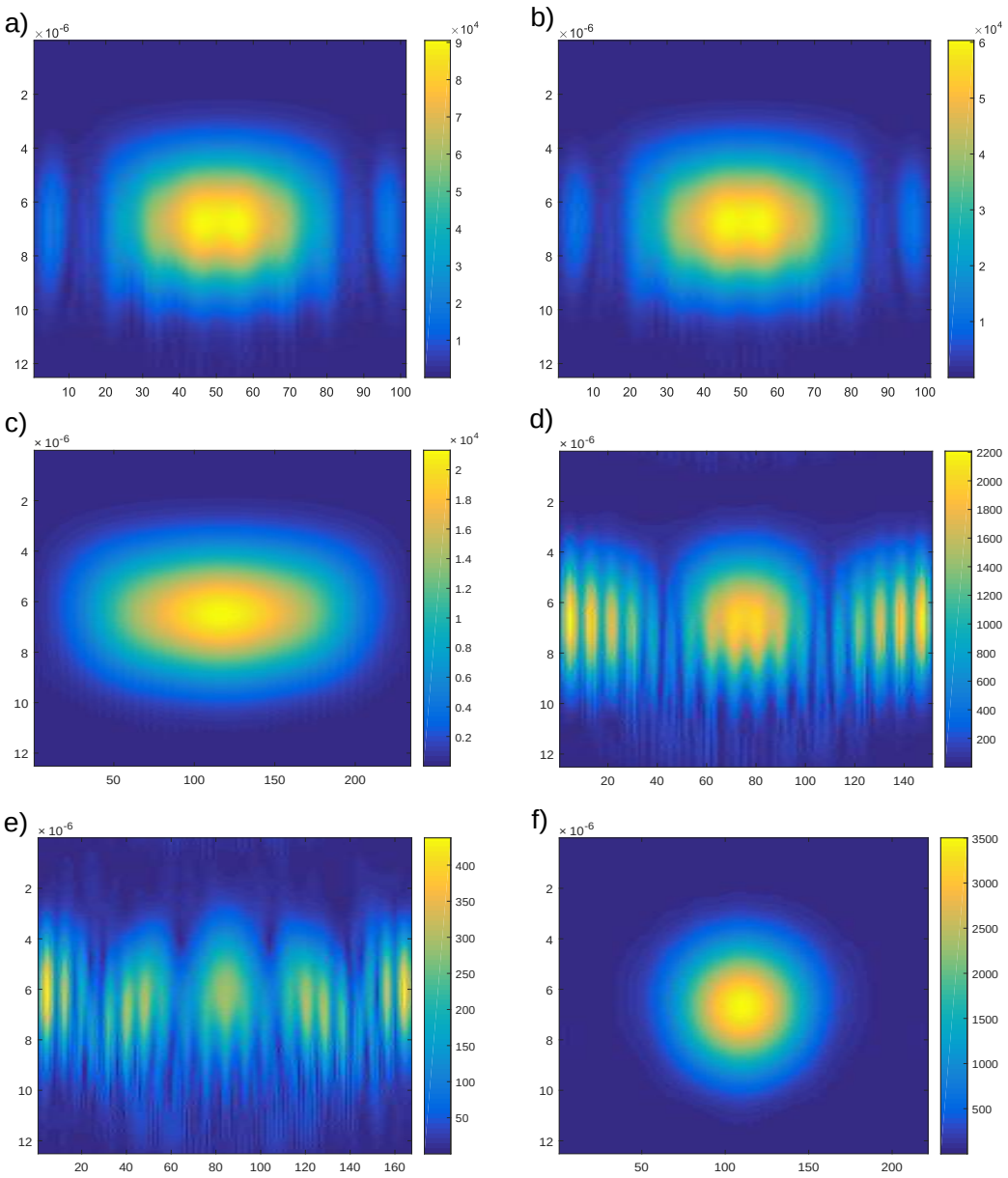


**Figure 6.17:** Processed time traces of the scattered pulse at $a = 1$ with a 2 MHz reference frequency at a range of interaction depths and angles. The x-axis is the element number where each element is 0.3 mm long (note that the range varies), and y-axis is time in seconds. The left column of plots, a), c), and e), are at $\phi = 90°$, and the right column are at the classically resonant $\phi = 120°$. The top row, a) and b), are with the interaction volume centred on the surface, c) and d) are at 4 mm deep, and e) and f) are 10 mm deep.

**Table 6.1:** Comparison of scattered wave amplitude after post-processing at various interaction conditions for COMSOL FE model and experimental measurements. Modelling was conducted at 2 MHz while the experiment used 2.25 MHz. Amplitudes are normalised to 0 mm deep, $\phi = 90^\circ$ values.

| Depth | Exp 90° | FE 90° | Exp 120° | FE 120° |
|---|---|---|---|---|
| 0 mm | 1 | 1 | 0.644 | 0.666 |
| 4 mm | 0.235 | 0.235 | 0.057 | 0.024 |
| 6 mm | 0.089 | - | 0.084 | - |
| 10 mm | - | 0.005 | - | 0.039 |

It is notable that scattered signal at $\phi = 120^\circ$ was lower when the interaction depth was 4 mm than at 10 mm. This might be surprising since some surface overlap is expected at 4 mm but this matched with experimental results that indicated an interference effect may be occurring between the two phenomenon with these parameters. It is encouraging to observe this behaviour in the model, despite the artifacts in the time trace which are likely a sign that the model is not fine enough to quite capture this response fully.

This subjective analysis shows a much improved performance of this model due to the inclusion of the nonlinear wave equation in the fluid domain but how well does it compare objectively with the experimental data? Table 6.1 contains the scattering amplitude measurements for a range of interaction cases for the experimental and FE model. The modelling investigated a depth of 10 mm rather than 6 mm as the aim was to get a measurement of bulk mixing to use as a reference for comparison. Experimental testing showed that at 6 mm with 2.25 MHz input beams the interaction volume was a little too close to the surface to escape surface effects at smaller interaction angles. Unfortunately data was not captured experimentally at 10 mm within the same set of testing so accurate comparison of signal amplitude is not possible.

Table 6.1 shows that the model produced relative signal amplitudes that were quite similar to the experimentally measured ones. Good performance was observed at the key depths of 0 mm and 4 mm. There was some discrepancy in the $\phi = 120^\circ$, 4 mm deep case, but this is understandable from the discussion of Figure 6.17 above that suggested the model was not quite detailed enough to capture the interference of bulk and surface mixing. It is also possible that the difference between 2 MHz and 2.25 MHz is significant in this scenario. The 10 mm deep measurements, which represent only bulk mixing, could not be compared with equivalent experimental data but the results appear to fit the trends of a reduction in signal as the interaction volume is moved fully below the surface.

Overall, these results show that the COMSOL model is quite accurate at capturing this near surface mixing. The six FE results presented in the table took over a month to

acquire, this slow pace limits the usefulness of the model in generating fingerprints but has shown what modelling elements are required to capture the physics behind this previously unknown near surface mixing behaviour. In order to try to understand the phenomenon better a few more tests were run with various small changes but ultimately the model's efficiency needs to be improved in future work before much more information can be extracted from it.

### 6.4.3 Further model investigation

The model was also run at 74° for 0 mm and 4 mm depths. This gave amplitudes of 1.46 and 0.609 respectively relative to the 90° 0 mm reference. This shows that the model predict an increase in surface mixing as interaction angle is reduced from 90°, as was seen in the experimental data, Figure 6.2. Experimental measurements were not able to be taken at quite this small an interaction angle and depth for direct comparison though. The 4 mm deep result is notable because it is an order of magnitude larger than at 90°, highlighting the very large impact surface mixing has at small interaction angles even if the interaction depth is intended to be significantly below the surface.

A test was run with the elastic modulus of the solid set to 120 GPa. The idea behind this was to adjust the velocities of the shear and longitudinal waves in the solid so that they do not match with multiples of the velocity in water in order to rule out the possibility that this surface mixing effect only occurred when the wavelengths matched. E = 120 GPa gives velocities for shear and longitudinal waves of approximately 4000 $ms^{-1}$ and 8000 $ms^{-1}$, neither are a multiple of the water velocity, 1500 $ms^{-1}$. The resulting scattered pulse had a peak intensity 19% higher than at 73 GPa, and the beam width was 30% wider. The wider beam makes sense because if the beam divergence is calculated using Equation 5.5 then the 27% increase in longitudinal velocity would be expected to give a 27% wider beam (using small angle approximations, which are probably not very accurate at these divergence levels).

The increase in peak signal amplitude is likely due to the fact that in order to create an interaction angle of 90° the input beam angle was altered to account for the new velocity. Previously the incident angles were 19.4° but for 120 GPa this was reduced to 15.1°. This meant that the test was more similar in a way to the 74° test which had an incident angle of 16.4°. The combination of a 19% increase amplitude and 30% increased width results in a beam that contains roughly 55% more signal when summed over a range of array elements. That increase is similar in scale to the 46% observed at 74° relative to 90°, suggesting that the summed surface mixing magnitude is mainly a

factor of the incident angles and not of the elastic modulus of the solid or the interaction angle within the solid. Further investigation would be required to prove this as more data points are needed. Experimental testing of the impact of material properties might be possible if the attenuation of the materials are known accurately enough. Some surface mixing testing was conducted on the steel fatigue samples, showing very strong signal in some cases, but comparison of scattering amplitudes with aluminium samples would be too inaccurate to draw conclusions using the available data.

One further finding that is of great interest is that in tests where the model was run with hyperelasticity disabled in the solid domain there was a negligible reduction in scattered signal when the interaction depth was 0 mm. The comparison of scattered pulses with various combinations of nonlinearity types is shown in Figure 6.18.

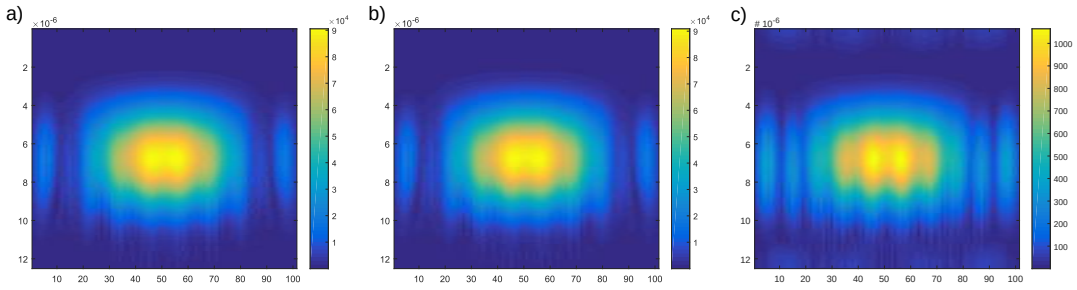


**Figure 6.18:** Processed time traces of the scattered pulse at $\phi = 90°$, $a = 1$, 0 mm depth with a 2 MHz reference frequency. The x-axis is the element number where each element is 0.3 mm long, and y-axis is time in seconds. a) is the result when both water and solid nonlinearity is on, b) is when only the water nonlinearity is included, and c) is only the bulk nonlinearity.

The results of Figure 6.18 show that the surface mixing effect is not dependent on the bulk nonlinear properties of the solid sample. It appears that in COMSOL the equations that govern the behaviour of the interface are able to capture the surface mixing effect with only the inclusion of the nonlinear wave equation in the fluid domain. The idea behind using COMSOL rather than a closer to first principles modelling method was to reduce the amount of depth the author was required to go into to create a functioning model but it also has the result that it is somewhat of a blackbox and that a true understanding of the workings of the model is not always obtained. This has made it difficult to gain a fundamental understanding of the physics causing the mixing at the interface in the model. It was hoped that the model might indicate the mixing source was coming from a more easily understandable part of the physics but it seems that is beyond the scope of the author's investigation and that a deeper theoretical investigation may be required to truly explain the mixing.

A test was run with the beam overlap completely in the water, with a thinner section of aluminium after the overlap region, but otherwise very similar geometry to the 90°

0 mm tests to make the results comparable. This was done to be certain that the mixing was not occurring in the water. Full field analysis of this showed something that looked a bit like mixing happened on a very small scale in the water. This might be due to computation limitations or the mesh being too coarse. The signal produced was an order of magnitude smaller than was seen in the 0 mm interaction depth case but was not negligible. It is likely that the water caused more signal in this case because it had a propagation path that was twice as long as it usually would in the water and this allowed the numerical errors to build up. Despite this the result shows that mixing in the water is not the primary source of mixing in the model under normal conditions, but it does reiterate that improvements could be made to the model accuracy in the future.

One final thing that should be noted from the full field analysis is that there was no scattered signal produced in the direction back out into the water domain. Other researchers have shown that CAN causes non-collinear scattering to occur in both directions from the interface so it is interesting to note that this does not appear to occur in the fluid-solid interface case.

## 6.5 Conclusions

The investigation into the near surface mixing behaviour was fairly successful. Further experimental testing produced results that clearly detailed how the phenomenon affects fingerprints captured near the surface of solid aluminium samples. Detailed analysis of data from this testing, combined with development of the geometric model for a 2D/planar source, suggested that the scattering angle of the mixed beam indicated that input beam overlap on the water-aluminium interface was the source of the mixing. Examination of scattered beam width also agreed with this conclusion. This information was useful but it did not provide an answer for the mechanism of mixing and there was still a possibility that the fluid-solid interface might not be the scattering source. The experimental data showed that it was better to use the newly derived interface scattering angle equation in all cases, including for bulk mixing. This is particularly useful to know for processing data that includes both bulk and interface mixing as will be the case in the following chapter.

In order to understand the mixing behaviour better a time-domain FE model was created using COMSOL. This model was shown to correctly predict bulk mixing behaviour but when the interaction volume was moved close to the surface it did not respond properly. The addition of the nonlinear wave equation to the fluid region of the model resulted in scattering behaviour that matched well with the experimental measurements

but was very slow to run. The slowness limited the use of the model for simulating large parameters spaces but useful information was still obtained from the limited run of tests with carefully chosen parameters. It was shown that the signal due to the surface mixing effect was largely unaffected by the elastic modulus of the solid and also occurred when the solid was modelled as a linearly elastic material. Although an observational understanding of the phenomenon has been greatly developed by the research presented in this chapter further theoretical investigation will likely be required to fully understand the mechanism behind the mixing behaviour.

It is currently unclear if the surface mixing contains useful information about the sample, irrespective of this it is likely that inspection of bonded interfaces would benefit from avoiding the production of mixing at the surface of the sample. To achieve this the interaction volume must therefore not intersect with the surface of the sample when centred on the interface of interest. Experimental testing showed that measurements should be taken at least 10 mm below the surface to avoid surface mixing with the 10 mm diameter 5 MHz transducers used in this work. Therefore, samples at least 20 mm thick are required. This condition is safely satisfied in the testing of kissing bond samples in the following chapter, they have a thickness of 60 mm. In order to measure the response of thinner samples narrower input beams are required, potentially using focused transducers.

# Chapter 7

# Interface mixing

## 7.1 Introduction

In this chapter the non-collinear mixing response of kissing interfaces is investigated, first using an FE model, developed and run by Blanloeuil et al. (4) and later through experimental measurements conducted by the author. A key strength of the modelling results is that the simulation did not include the physics that allows for bulk mixing so any scattered signal is due to wave interactions with the interface. The same cannot be said for the experimental measurements but the previous chapters have worked on understanding the other forms of mixing that could affect the results so it should be possible to identify which features in the fingerprints are due to the presence of an interface.

Both the model and experimental work use the compressively loaded aluminium blocks to produce a 'kissing' interface. The aim was not to produce an interface that could not be detected using conventional ultrasonic methods but to make one that could be varied to create different levels of contact between the surfaces and allow for inspection at a wide range of interaction angles. The details of the sample design are discussed in Chapter 3. The static loading applied to the interface is varied experimentally and changes two key interface parameters; the contact area, and the loading at which that area is under. Both of these factors are key to the understanding of kissing bond detection. These cannot be controlled independently so another degree of control was investigated by using interfaces of different surface roughness. With a combination of loading and surface roughness responses a deeper understanding of the non-collinear method's sensitivities is explored.

## 7.2 CAN finite element model

The details of this model are presented in Chapter 4. It is an FE model using a very similar geometry to the experimental work. It simulates the CAN by catagorising the interface elements between the two blocks into one of three states, open, sliding, and closed. The state controls which stresses can be transferred across the interface. The fundamentals of the model have been used for many other studies published by Blanloeuil et al. which present aspects of non-collinear mixing such as the effects of a finite crack length or a rotated crack. Tests have been run over a range of interaction angles but in this work frequency ratio was also included in the parameter space, forming the fingerprint that is discussed below. Adjustment factors have been applied to the fingerprint to make it more equivalent to the experimentally measured ones that are

presented later in this chapter.

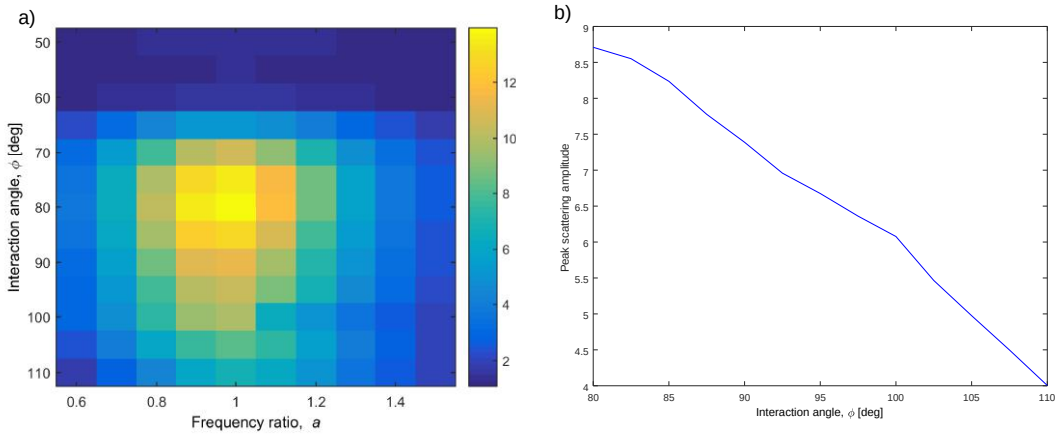


**Figure 7.1:** a) FE modelling of parametric mixing response of aluminium-aluminium kissing interface. Adjusted to include experimental factors. Arbitrary colour scale indicates scattering amplitude. b) A more detailed inspection of the parameter space at $a = 1$.

The fingerprint, shown in Figure 7.1 (a), is different in many ways from that observed in the bulk experimental or modelled work. The response peaks at approximately $\phi = 78°$, much smaller than the bulk mixing in aluminium, and extends over a wide range of interaction angles. Because of this wide range it is likely that experimental measurements of the parameter space will include interference between the bulk and interface mixing. It is unknown from the modelling how the two mixing sources will interfere with each other, it may be possible to subtract the bulk mixing from an experimental fingerprint to leave only the interface signature if the two act constructively. The lack of signal at $\phi \leq 60°$ is mainly due to the experimental adjustment factors related to critical angle of mode conversion at the top surface.

The experimental testing of solid aluminium showed no significant scattering below $\phi = 105°$, Figure 5.6. Therefore, it should be possible to measure interface mixing without bulk interference at angles smaller than this. This method has been used in work by other authors as described in the literature review. It was suggested that measurement of the bulk mixing at around $\phi = 120°$ could be used as a reference for the interface mixing but this is unlikely to work if the FE prediction of a broad mixing response is correct. Instead such a reference may be better obtained by moving the interaction to a part of the sample that produces no mixing at around $\phi = 80°$, indicating solid material. This modelling suggests that fingerprints over the range $70°$ to $130°$ be captured to include the primary features associated with each type of mixing.

Figure 7.1 (b) shows the results of a set of models run at $a = 1$ with smaller interaction angle steps, $2.5°$. This test was conducted to see if there were features in the fingerprint smaller than the $5°$ step size used for the main parameter space. In Figure 7.1 (a) a slight

minima can be seen at $\phi = 100^{\circ}$ but this was likely due to flaws in the post processing method since no features could be seen in the more detailed tests.

The fingerprints captured with the interaction volume at a water-aluminium interface looks similar to that predicted by the FE interface model. This is likely because both are created by mixing on a 2D plane and have no strict resonance requirements. The experimental measurements of the surface mixing were limited in interaction angle range due to the geometry of the apparatus. It would be interesting to see if the response would peak at an interaction similar to that of the kissing interface. This might indicate that the surface mixing is also related to the component of stress normal to the interface as discussed later in this chapter in the section titled 'Absolute interface load'.

## 7.3 Preliminary interface testing

Early on in the project, after confirming the technique could acquire fingerprints from solid aluminium, some preliminary testing was conducted on a kissing interface sample. This sample was constructed as described in Chapter 3, with finely polished surfaces, but there was uncertainty over the alloy of aluminium so the bulk mixing behaviour might not be expected to match exactly with the 2024 T351 aluminium samples used for bulk testing. The behaviour of the interface would likely be the same with the different types of aluminium so it was a useful test of kissing bond behaviour. The results presented later in Sections 7.4 and 7.5 used 2024 T351 aluminium to make them consistent with the bulk work.

When using the bolt loading method it was unknown if the contact between the two faces would be at too high loading to allow the acoustic waves to part them, or if the contact would be so poor as to get very low transmission across the interface. This early work confirmed that the compressive loading of two blocks using bolts created an interface within the desired range and that it was possible to get reliable fingerprints from it. Many improvements to the experimental method were made after or as a result of this testing (including temperature control of the water and adjusting experimental geometry to allow desired interaction angles and depths), as such the accuracy of these results is limited. They have been included here because the lack of precision does not limit the ability to observe the different behaviour of this interface when compared to later samples. Its response helps build a more complete picture of possible interface behaviour.

### 7.3.1 Interface fingerprints

Testing was conducted with a reference input frequency of 5 MHz on a 60 mm thick aluminium sample with the interaction centred on the interface at the middle of the sample. Figure 7.2 (a) shows the result of the high resolution inspection of the $a - \phi$ parameter space, taking 16 hours to complete. This fingerprint is similar in many ways to the FE modelled prediction, Figure 7.1. The dominant feature is the broad, rounded peak at around $\phi = 83^\circ$ and $a = 1.15$. A comparison between the absolute position of this peak and the FE model will not be made here as the precision of the experiment was limited at this time. Later testing will include such comparisons.

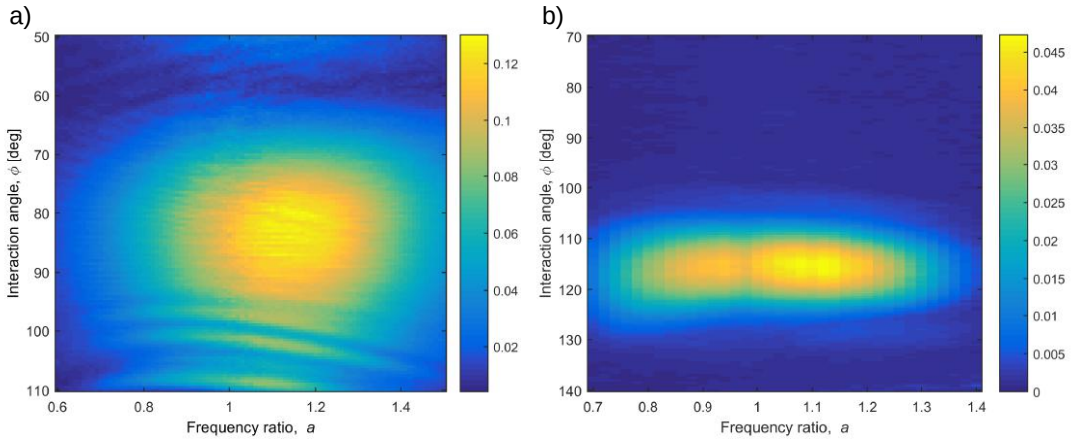


**Figure 7.2:** Fingerprints of preliminary interface sample, a) loaded with 2 Nm bolts and measured at 30 mm deep, b) loaded with 8 Nm and measured at 15 mm deep.

The other notable feature is the multiple bands at large interaction angles. These were not seen in the FE results, Figure 7.1, and it is unclear if their source is related to the CAN mixing or a mechanism similar to that which caused the banding in the solid samples. In the case of the solid samples it was determined that beam overlap at the water-aluminium interface created a mixing effect, perhaps the aluminium-air-aluminium interface can cause something similar.

For comparison, a measurement was taken at a depth of 15 mm in the sample, in the centre of the top block, Figure 7.2 (b). As expected this showed a response similar to that seen in the bulk mixing chapter. The signal produced within the bulk in this case propagated through the interface. Since such a strong signal was received, as indicated by the good signal to noise ratio, this suggests that the interface had good contact between the two aluminium faces. As the frequency ratio was altered the beam would be scattered onto a different part of the interface so the fingerprint presented here is influenced by the spatial variation in transmission of the interface. An attempt to measure the fingerprint of a volume below the interface was made but the geometry

of the experiment meant that the interaction angles were too small to detect the bulk mixing.

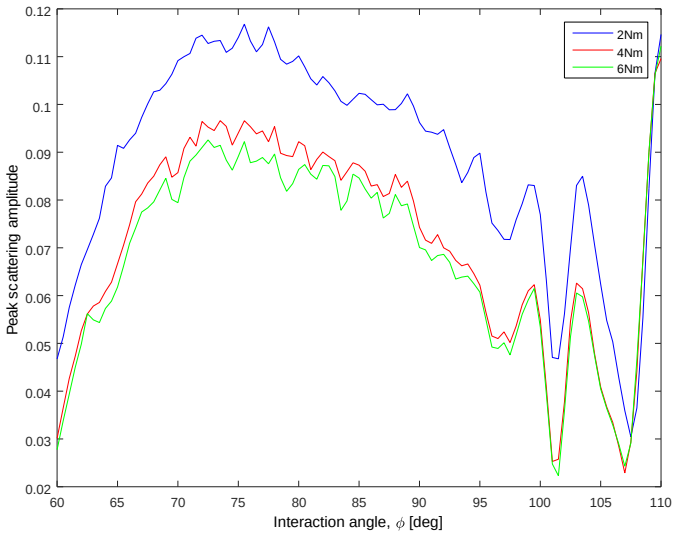


**Figure 7.3:** Scattering amplitudes at $a = 1.2$ for the preliminary aluminium interface sample loaded by bolts at 2 Nm, 4 Nm, and 6 Nm. The results are an average of four measurements each.

Next, testing was conducted with a range of torques on the sample's bolts to investigate which ranges would be useful for later tests. Figure 7.3 shows the response at $a = 1.2$ using a small torque wrench in the 2 Nm $-$ 6 Nm range. It was observed that the scattering reduced in amplitude at all interaction angles (except for perhaps the extreme $\phi = 110^\circ$ case) as torque was increased. This suggests that this range of loading was in the regime where the response was dominated by the behaviour of increased loading making it more difficult for the acoustic waves to open the interface. It would be interesting to observe the other regime where the dominant effect is the increase in signal with loading due to a greater fraction of the surfaces being brought into contact. Thus, plans to produce a lower loading force were devised involving the use of spring force rather than bolting force. This method was not used, however, because later samples appeared to spread the loading differently and did not require it.

There was very little change between the 4 Nm and 6 Nm tests, this is somewhat surprising as it might be expected that by increasing load the signal would keep dropping until none is produced. Instead it appears to be plateauing at a measurable level. To further test this a larger torque wrench was used to apply between 5 Nm and 25 Nm of torque, Figure 7.4. It can be seen that anomalously the 10 Nm test produced less signal than the 15 Nm, but generally the amplitude reduced to a constant level as loading increased. The irregularity may be due to the way bolts load the interface, perhaps one

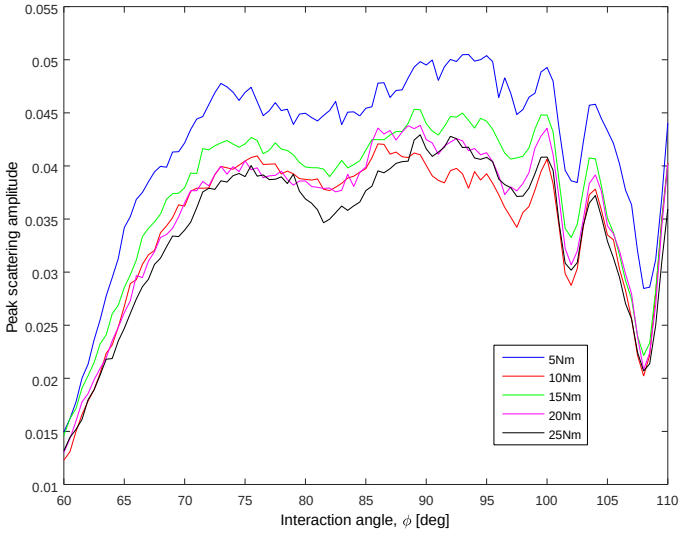


**Figure 7.4:** Scattering amplitudes at $a = 1.2$ for the preliminary aluminium interface sample loaded by bolts at 5 Nm, 10 Nm, 15 Nm, 20 Nm and 25 Nm.

of the bolts increased in loading more than another (when going from 10 Nm to 15 Nm) creating and imbalance and distorting the contact at the interface. It is also possible that the interfaces moved with respect to each other. In later testing great care was taken to load the bolts in an order that minimises imbalances and not to push on the plates unevenly while torque is being applied. Changes in exactly how the interfaces are positioned with respect to each other are likely to be the cause of the many different fingerprint shapes seen throughout this section of preliminary testing.

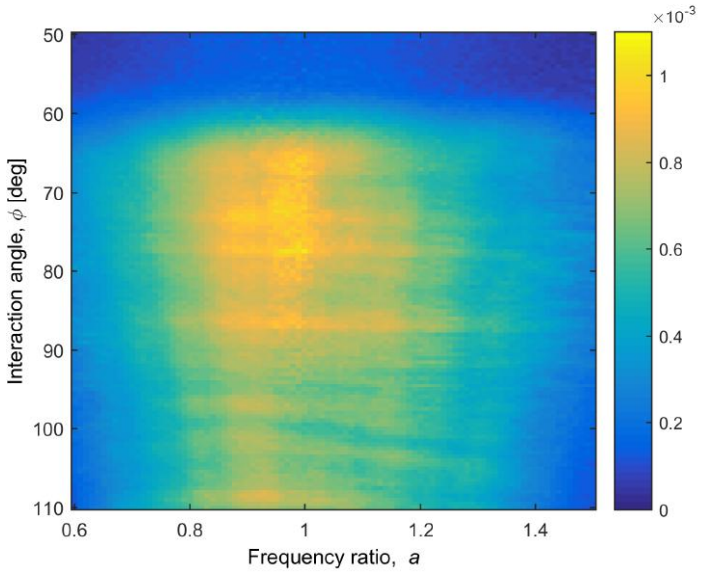


**Figure 7.5:** Parametric mixing response of aluminium-aluminium kissing interface, bolts at 5 Nm, with water ingress. Colour scale indicates scattering amplitude.

In one of the tests water entered the interface due to incomplete sealing of the sample. This resulted in the fingerprint shown in Figure 7.5. It appears that the water shifted the peak frequency ratio and allowed for mixing of a similar amplitude across a wider range of interaction angles. The dynamics of the aluminium-water-aluminium interface are complex and are outside the scope of this work. This fingerprint is significantly different from the dry interface case so might allow for detection of the two different states with further validation.

### 7.3.2 Repeatability

Having seen the sensitivity to conditions it is important to look at measurement variation. The following measurements were made to assess the variability of the fingerprint. In the results presented in Figure 7.6 (a) the sample was left in place between the sweeps of interaction angle. 20 sweeps were made in a row, each one taking 10 minutes. It can be seen that there is a variation in amplitude of approximately $\pm 4\%$ at all interaction angles. This error is much smaller than the features discussed above. Figure 7.6 (b) tests the day to day repeatability of the experimental method. The sample was removed from the set-up between each run so this also tests the effect of sample positioning variation on the order of a millimetre (the approximate accuracy achieved by the sample holder jig). The variation between these measurements was not significantly different from the results shown in (a).

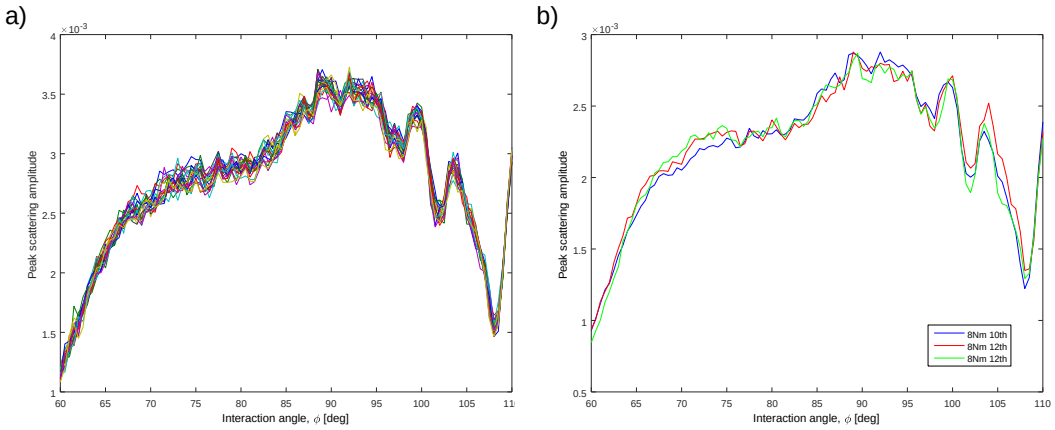


**Figure 7.6:** Scattering amplitudes at $a = 1.2$ for the preliminary aluminium interface sample loaded by bolts at 8 Nm. a) 20 successive measurement sweeps through interaction angle without movement of the sample. b) Three measurements taken on two different days with sample removed and replaced in between. The date is indicated in the legend.

The above results show that the method can achieve reliable measurements of non-collinear scattering from an interface and that the torque on the bolts can be used as

a means to control the interface loading. It was seen that scattering occurred across a wide range of interaction angles and frequency ratios. It was unclear if CAN related mixing extended to interaction angles larger than 110° because these tests were not conducted over a wide enough range and better control of the amplitude is required to make relative comparison with bulk fingerprints. The work below seeks to do this.

One of the major improvements made after this early testing was the prediction of angle of scattering that allowed the post processor to reliably capture the signal of interest. The near surface testing, Chapter 6, showed that a 2D scattering source would produce a wave at a different angle from that predicted by momentum summation of the input waves. In Chapter 8 the new interface/CAN prediction equation is tested on experimental scattering from a kissing interface, and the predictions will be extended to an interface at an arbitrary angle. In general, it was found that the planar source equations gave a better estimate of scattering position on the array so were used for the data presented below.

## 7.4 Rough kissing interface

A new interface sample using the same aluminium alloy as used in the bulk material testing was machined. Initially the blocks were polished in a similar way to the preliminary sample but it was found that very little signal was produced by the interface. This was because of poor contact between the faces, with very little of the input beams propagating through. The reason for this was likely that there was a macroscopic unevenness to the surfaces possibly due to a curvature in one of the grinding or polishing disks. To fix this the surfaces were ground flat by hand on sheets of abrasive paper, the last and finest of which was P1000 grit (18 micron average particle size). This is much coarser than the diamond suspensions, as small as 1 micron, used for the preliminary and later polished sample work. While the sample was in this rough state the opportunity was taken to investigate the response of a rougher interface. This also served to check if the surfaces had been made flat by the sanding.

Figure 7.7 (a) shows a fingerprint of the compression loaded interface sample, with the volume of interaction centred on the interface. The reduction in signal seen at 125° and greater is due to the geometric limitation mentioned in Chapter 5, Section 5.3.3. A peak in mixing behaviour is observed at around 75° and a frequency ratio of 0.9 in this case. There is a much smaller peak at around 100°, and a very slight peak at frequency ratios around 0.85 at 120°. The maximum scattering amplitude from the interface was an order of magnitude larger than that from the solid sample at the same depth, shown

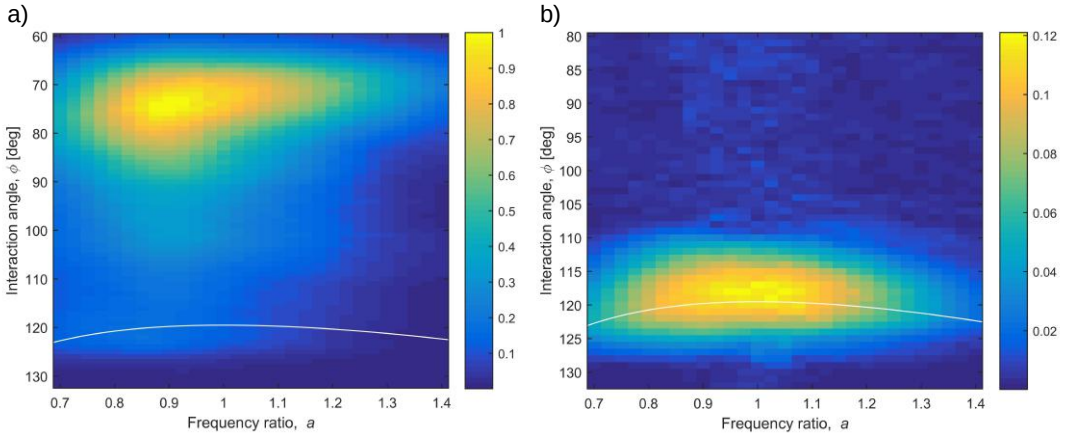


**Figure 7.7:** 5 MHz experimentally measured parametric response of, a) aluminium kissing rough interface sample at a depth of 30 mm, the middle of the block. Bolt torque at 40 Nm. b) solid reference block, also at 30 mm, as seen in Chapter 5. The scattering amplitudes of the two plots have been standardised and normalised to the peak value which occurred in the interface case. White line indicates the resonant conditions.

in Figure 7.7 (b). Both these fingerprints were normalised to the maximal scattering amplitude recorded from the interface mixing case, allowing for relative comparison of the bulk and interface mixing.

FE modelling predicted a peak at 78° compared with the observed 75°. The experiment has an absolute error of ±3° and the modelling only had a resolution of 5° so these values are within error bounds. The optimum frequency ratio of the model was 1.0 but after applying the experimental centre frequency correction it was shifted to around 0.95. This compares with the experimental peak frequency ratio of 0.90, again showing good agreement. The slight peak in Figure 7.7 (a) at 120° is expected as the bulk mixing peaks here, as seen in (b). The peak at 100° was predicted by the classical model but not seen in the solid experimental measurement, thus it is unlikely that this peak is due to bulk nonlinear mixing. The CAN FE modelling also suggested that interface mixing was not the source of this peak, making the origin of this peak unclear. Later in this section fingerprints are captured at different interface loadings, some exhibit no secondary peaking so perhaps the model would also produce secondary peaks given particular interface conditions.

### 7.4.1 Rough interface loading response

The only notable trends in the fingerprints appear to occur in the interaction angle dimension therefore further testing was conducted at a single frequency ratio, 0.9. This was selected as it was near the peak response points of both solid and interface samples

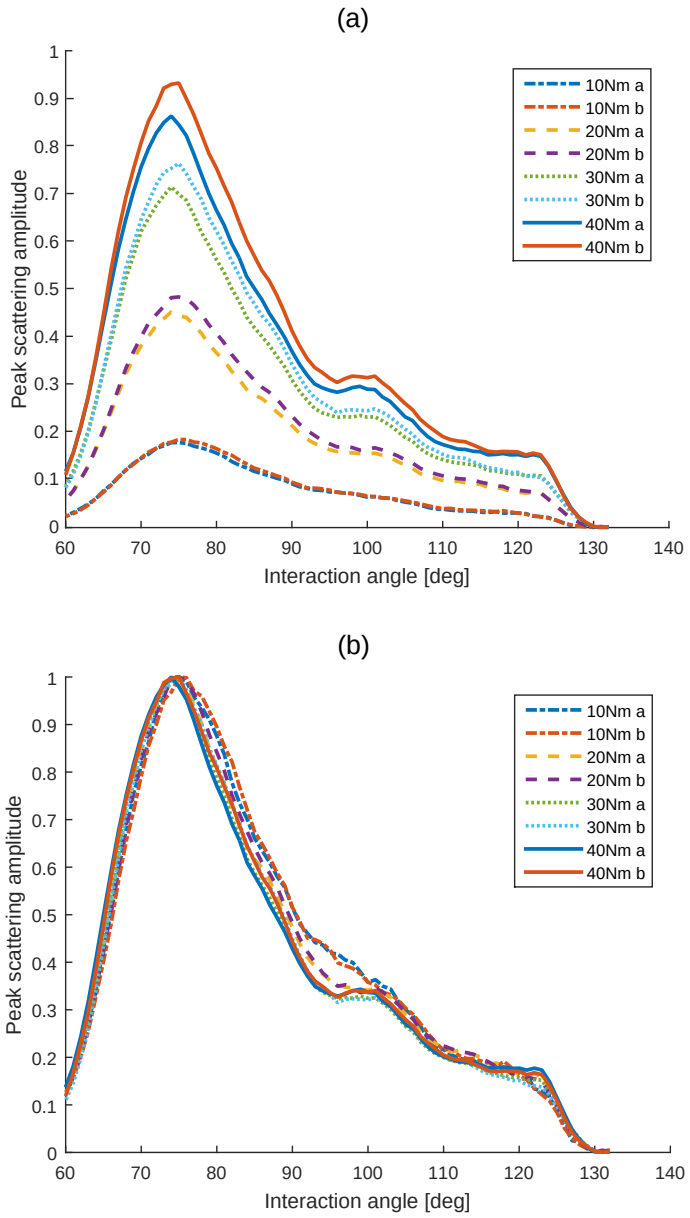


**Figure 7.8:** (a) Scattering amplitudes from aluminium compression loaded rough interface sample at a frequency ratio of 0.9 with bolt torques ranging from 10 to 40 Nm. The first loading cycle is labeled 'a', and the second 'b'. The peak scattering amplitude is an arbitrary unit relative to the maximum scattering observed in Figure 7.7. (b) This plot contains the same data as (a) except it has been peak normalised for each loading point.

and far enough away from 1.0 that it had reduced noise due to the frequency filtering.

Values for the peak scattering amplitude are presented in two ways in the following sections. In part (a) of the subsequent figures the values have been normalised by the peak value obtained in the kissing interface fingerprint, Figure 7.7. In part (b) the data is normalised by the peak scattering of each parametric sweep. The former is to allow for absolute amplitude trends to be compared and the latter for comparison of fingerprint shapes.

Figure 7.8 (a) shows the scattering response of the interface region at a frequency ratio of 0.9 with bolts torqued between 10 Nm and 40 Nm. This range was used because very little signal was observable with the torque below 10 Nm, and 40 Nm was as much as could be applied to the sample with the torque wrench. Since it is very difficult to know accurately the interface pressure with this experimental method bolt torque will be referred to as the controlled variable. Interface pressure and bolt torque are predicted to be proportional and further discussion of the likely interface pressure occurs in Section 7.5. The sample was preloaded to 40 Nm before the two full loading cycles, 'a' and 'b', were tested. For the cycles the bolts were torqued to 10 Nm initially then increased in steps of 10 Nm up to 40 Nm.

As the loading was increased the amount of mixing increased. When 10 Nm was applied the main CAN related peak is seen at around 76°, this shifted approximately 2° towards smaller interaction angles as the load increased. This plot also shows that there was an overall trend of increased scattering with each loading cycle. This can be explained by the fact that the interface was never fully unloaded during these cycles, each bolt was unloaded from 40 Nm and re-tightened to 10 Nm in turn, keeping the faces in constant contact. This method was intended to stop the faces moving relative to each other between each cycle, keeping the same parts of the interface in contact. Due to this it is expected that the surface asperities will gradually deform to match each other, increasing the contact between the two faces and thus the transmission.

Despite the many differences in the parameter space at various loads it is notable how similar the trends are when peak normalised, as shown in Figure 7.8 (b). The shape produced is very different from the solid sample response demonstrating the potential of this technique to identify the presence of kissing bonds at a range of loads. There are also many subtle trends visible in this normalised data; firstly, as torque is increased from 10 Nm to 30 Nm the 100° feature becomes more pronounced, but it is unchanged when further increased to 40 Nm. Secondly, there is a notable lack of change in the relative amplitudes of scattering seen at 76° and 120°. It might be expected that these areas should respond differently to increased interface load if the former is due to CAN

and the latter classical bulk nonlinearities. If it is assumed that half the interaction volume is above the interface and half below an equation for the expected bulk signal as a fraction of the solid sample's can be formed. The signal produced above the interface is reduced by a factor of $T_o$, the transmission coefficient at the output frequency, and the signal created below the interface would be reduced by $T_i^2$ due to the reduction of both input beams by the interface, thus

$$S_i = 0.5 \times (T_i^2 + T_o) \times S_s \tag{7.1}$$

where $S_i$ is the predicted classical signal amplitude from the interface sample, and $S_s$ is the signal from a solid sample. As loading is increased both the transmission coefficients would be expected to increase resulting in a monotonic relationship between loading and $S_i$. There is not a direct relationship predicted between transmission coefficient and CAN mixing amplitude so it would be likely to scale differently. The assumption that the signal seen at 120° is due to bulk nonlinearities is likely to be false though, as can be seen upon further analysis of Figure 7.8. The scattering amplitude of the interface sample is 0.17 arbitrary units at 120° and frequency ratio of 0.9. This compares with 0.11 in the solid block in Figure 7.7 (b) at the same frequency ratio and angle. Therefore, even if the interface were perfectly transmissive (which it is not) the scattering due to bulk nonlinearities could only account for 64% of the overall scattering produced. Therefore the interface must be responsible for a significant amount of the scattering observed at 120°. This concept is investigated in greater detail in relation to the polished interface in Section 7.5.

### 7.4.2 Input amplitude scaling

For CAN to occur it is critical that the acoustic waves create enough tensile force at the interface to allow the interface to open (or slide). The behaviour of the interface would be expected to be related to the ratio of the acoustic force to the static mechanical loading. The sample was tested above by varying the mechanical load but in this section the ratio is altered by changing the acoustic stresses. This was done by varying the output voltage of the arbitrary waveform generators from 1 V down to 0.1 V. The results are presented differently in this section, focusing on only the amplitude of the scattered signal. Figure 7.9 shows the peak scattered signal amplitude produced at $a = 0.9$ and $\phi = 75°$ with bolts at 40 Nm. There is a strong linear correlation between the product of the input amplitudes and the scattered amplitude, with only a slight offset due to noise. The strength of the input beams was measured without the sample in the rig in order

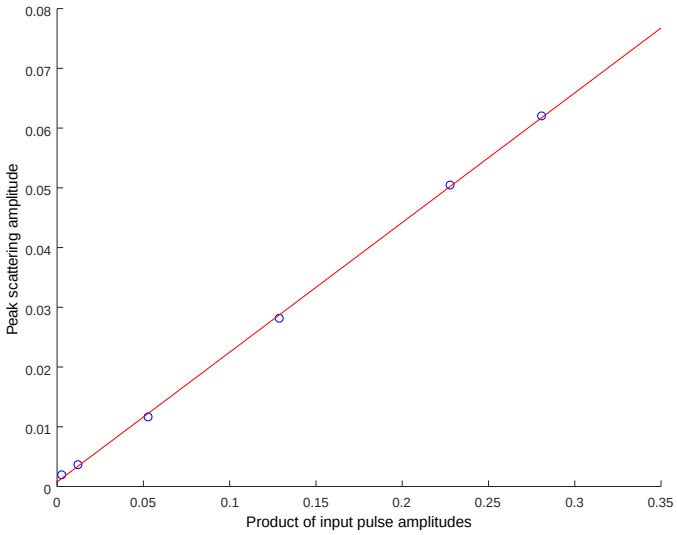


**Figure 7.9:** Scattering amplitudes at $a = 0.9$ and $\phi = 75°$ for rough aluminium interface loaded by bolts at 40 Nm. Tests were conducted with six different input signal amplitudes.

to calibrate the results because the output voltage setting from the arbitrary waveform generators is not accurate enough on its own.

This directly proportional relationship might be expected since bulk mixing showed a similar response. The precision of the applied acoustic stresses was much better than that of the bolt torque method allowing for certainty in the load-scattered amplitude relationship. As was mentioned during discussion of the static load results it would be interesting to conduct tests on an interface in a different static:acoustic loading regime. The intention of conducting this test at maximal loading was to see if the reduction in acoustic stress would reduce it to levels unable to open the interface. This did not occur, likely due to the microscopic variation in surface contact that had a large range of contact loadings present. It would also be interesting to conduct this test on a polished interface as the range of microscopic loading should be much less, however due to time constraints this was not possible in this work.

### 7.4.3 Repeatability

To demonstrate the repeatability of the method a plot of measurements taken at 40 Nm torque is shown in Figure 7.10. It contains a parametric sweep taken after the plates were first loaded to 40 Nm (the pretest measurement), another taken after the load was released and then reapplied on each bolt in turn ‘a’, and two after a second load cycle ‘b’. The sample was removed from the immersion tank and replaced between

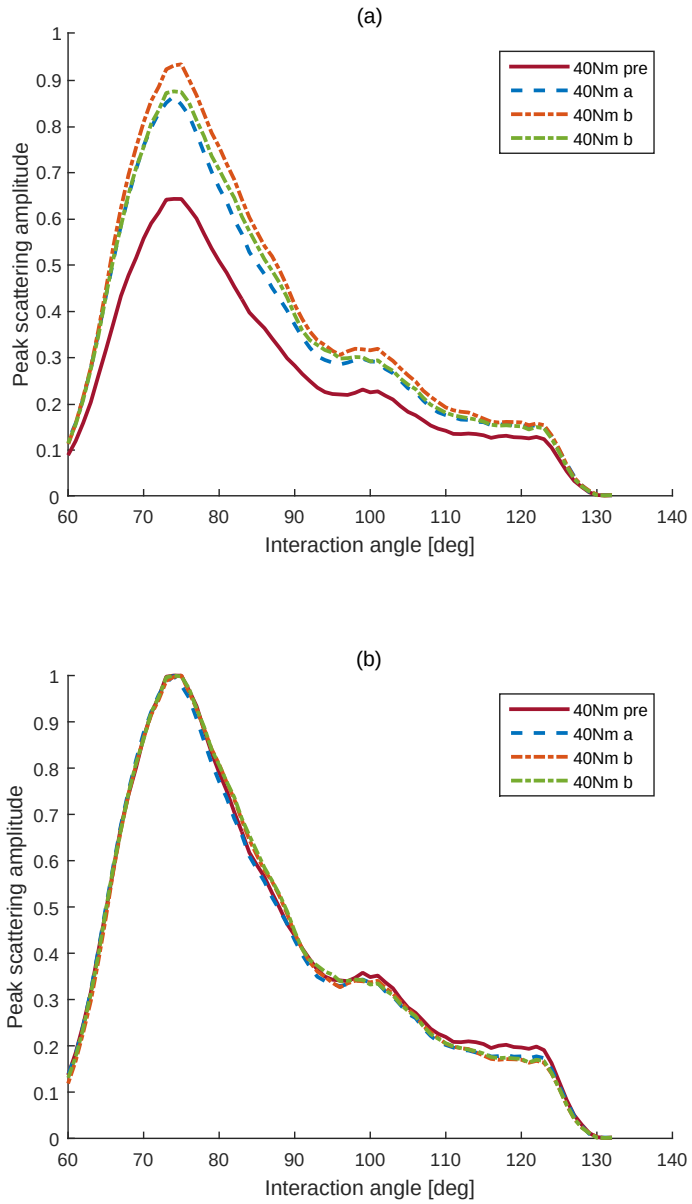


**Figure 7.10:** Scattering amplitudes at a frequency ratio of 0.9 for the rough interface sample. (a) The measurements at 40 Nm torque are shown from the pretest cycle, cycle 'a', and two cycle 'b' tests. The peak scattering amplitude is an arbitrary unit relative to the maximum scattering observed in Figure 7.7 (a). (b) This plot contains the same data as (a) except it has been peak normalised for each loading point.

the two ‘b’ tests. It can be seen in Figure 7.10 (a) that the pretest measurement had amplitudes 25% smaller than the cycles that followed, and that there was about a 10% variation in amplitudes of cycles a and b. The variation in amplitude with cycle number is expected as surface asperities are altered by each successive cycle, although most of the deformation occurs during the first, as shown in Drinkwater et al.’s study (105). Initially the surfaces only contact where they are locally raised. Due to the small area in contact this area is under high load and unable to be overcome by the acoustic stress. The remaining troughs are not in contact so transmit no signal. The combination of these factors leads to small CAN signals when the plates are first brought together but cause the signal to increase as the surfaces conform to each other. This process is expected to be more dominant in a roughly ground interface case than for a polished interface because the asperities of the polished interface should be much smaller and form a better match initially.

The normalised data in Figure 7.10 (b) displays very good agreement between the measurements, only the pretest response significantly differed from the others, having a smaller 120° to main peak ratio. Some difference would be expected due to the changing interface condition discussed above. This data gives an indication of the repeatability of the measurement, showing that peak normalisation results in consistent parametric trends when the sample is unaltered. Measurements taken consecutively without the removal of the sample were conducted, these showed even smaller variation than seen above, leading to the conclusion that positioning of the sample is the primary cause of the slight variation observed in ‘40Nm b’ trends in Figure 7.10. The impact of positioning is explored in the following section.

### 7.4.4 Position sensitivity

There is certainly variation, to some degree, in the average surface height of the blocks between points a few millimeters apart due to the limitations of the production method used, therefore it is expected that some macroscopic regions of the interface will be under greater average load than others despite efforts to design a geometry that minimises loading variability. Due to this it might be expected that testing a different region of the interface could yield a fingerprint that resembles another taken at a different torque setting. To investigate this the interface sample had scattering measurements taken at various points along the central axis of the sample, specifically at 0, 2, 4, and 5 mm from the centre. In Figure 7.11 (a) the unadjusted scattering amplitudes can be seen. The bolt torque was 40 Nm for this testing. The reduction in signal observed at above 120° for increasing displacements is related to the input beam clipping issue

mentioned previously.

At all measured loads the parametric response peaked at around $74 \pm 2^{\circ}$, clearly identifying the presence of a kissing interface. There is some variation between measurements taken at nominally the same position, but when peak normalised the four different positions show clearly distinct trends. This demonstrates that the method was sensitive to position changes on the order of 1 mm. Therefore some of the error between measurements at the same intended position is likely due to positioning inaccuracies which were approximately $\pm 0.5$ mm.

The largest difference between measurement points in Figure 7.11 (a) was the drop in amplitude when displacing from the central position. Moving only 2 mm caused a 25% drop in signal. The diameter of the interaction area on the interface at the -3dB limits is estimated to be 21 mm by beam divergence calculations (-3dB was selected rather than -6dB due to the scattering being a product of the square of the input amplitude). In the 2 mm translation roughly 12% of the initial surface area moved outside of the new overlap area. It is possible that a highly CAN active area of the interface was moved outside the interaction region and that the new area was not very active, but the disproportionately large change of 25% means this is unlikely. Another possible explanation is proposed at the end of this section.

Figure 7.11 (b) also contains some interesting trends. The width of the main peak is much larger at 4 mm displacement and it has a rounded peak. The peak response interaction angle varies by about $4^{\circ}$ between the tests and the smaller peak at $100^{\circ}$ does not exist other than at 0 mm. Some of these trends are similar to those observed as load was varied in Figure 7.8, such as peak shifting, but others are quite different, e.g. the large peak width changes. This implies that the shape of the response must be related to more than just average interface loading within the interaction area, indicating that there are other factor(s) causing the variation despite the surfaces being uniformly rough.

The combination of the rapidly changing amplitudes and shapes of the parametric trend therefore probably have a more complex cause than has been discussed above. One explanation is that the overlapping input shear waves constructively produce lines of positive and negative tensile stress on the interface with regions of destructive interference in between. It is these lines where the waves cancel each other that create transmission at the interface when otherwise it might be open due to the tensile forces of the individual beams, thus these lines are the sources of the non-collinearly mixed signal. The lines have a spacing of approximately 1 mm (dependent on interaction angle and frequency ratio) and are at fixed places on the interface when the frequency ratio is one. At other ratios these sampling lines sweep across the interface, sweeping faster

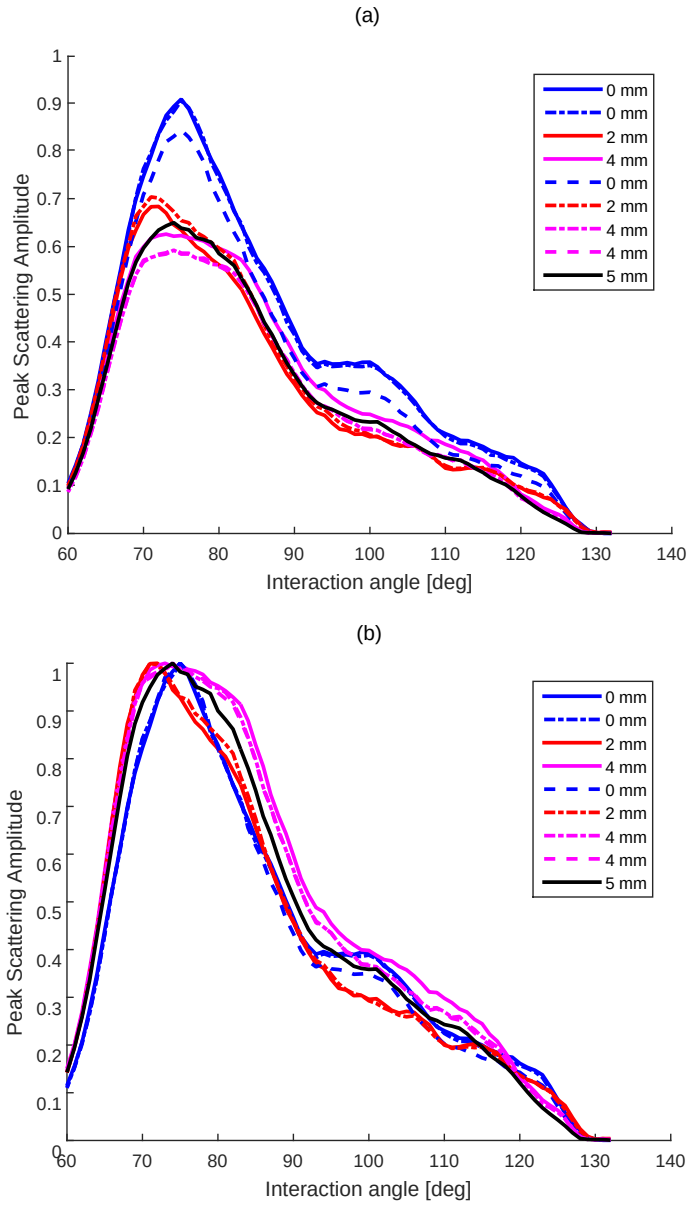


**Figure 7.11:** Scattering amplitudes at 0.9 frequency ratio of rough aluminium interface loaded by bolts at 40 Nm. Tests were conducted with the sample in four different positions, with 0 mm displacement being the same position as used for the other rough interface tests. The legend indicates the order in which the measurements were taken. The peak scattering amplitude is an arbitrary unit relative to the maximum scattering observed in Figure 7.7. (b) This plot contains the same data as (a) except it has been peak normalised for each position point.

the further ratio is away from one. For the case of a 0.9 ratio, as used in this study, the sampling lines will shift back to the starting pattern over the course of 10 cycles of the reference input beam (at 5 MHz in this research). Therefore, the experiment's sensitivity is biased towards the lines of the interface that are sampled when the input pulses are near their maxima due to the peak scattering amplitude being used as the measurement metric. Movement of the sample or change in the interaction angle causes the position of the sampling lines to be altered resulting in the complex parametric-space response that was observed.

The theory presented above explains why a small movement, on the order of 1 mm, could result in a different set of subsections of the interface being probed. The combination of the movement of the interaction volume with the movements of the sampling lines as interaction angle is changed therefore results in a complicated response dependent on the interface conditions at all points within the regions being sampled, rather than any averaged parameters. This behaviour is examined further in Section 7.6 in relation to the adjustment of the timing of one input pulse in relation to the other.

## 7.5 Polished kissing interface

After the rough interface had been tested another attempt was made to produce a polished interface, finishing with the 1 micron diamond suspension on the rotary cloth disk. Pictures of the surfaces are shown in Figure 7.12. It can be seen that the surfaces were optically highly reflective but there were a few distortions visible in the reflections around the bolt holes.

Everything else was kept the same between the rough and polished rounds of testing. It is expected that the loading response of the polished sample should differ from the rough one since lower loading is required to deform the smaller surface asperities resulting in greater contact area at the same load. This larger contact area should spread the load, reducing the average pressure of the contacting regions and result in an interface that behaves more like the perfectly flat simulated interface of the FE modelling.

### 7.5.1 Linear interface properties

A c-scan of the kissing bond interface was taken with the bolts torqued to 20 Nm to get a better basic understanding of the interface properties, Figure 7.13. A 25 mm diameter

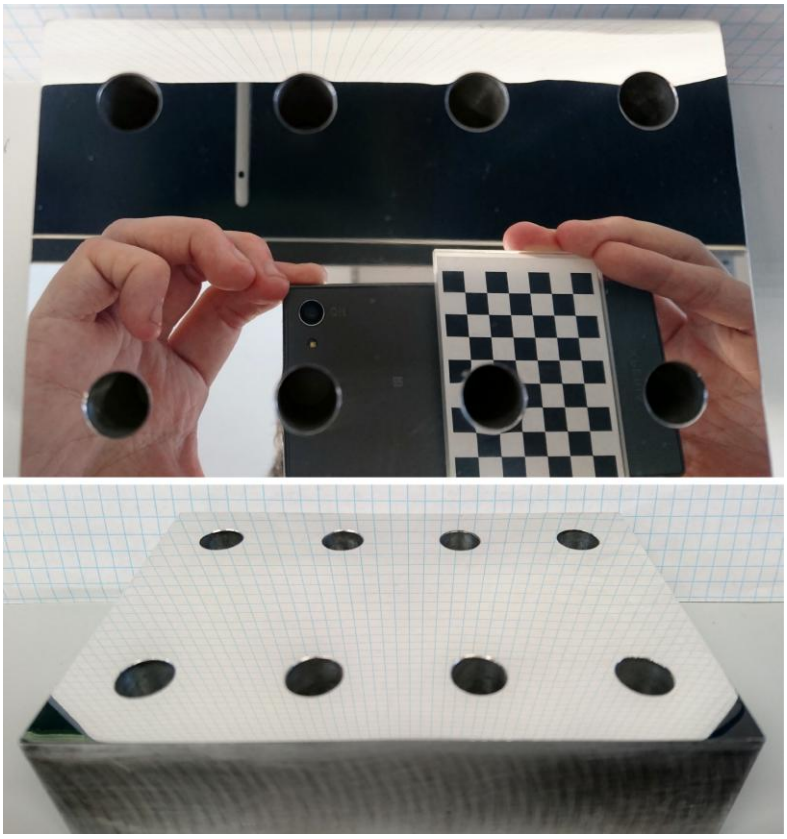

**Figure 7.12:** Photos of the interface surfaces after final polishing. Regular grids shown to assess surface flatness.

10 MHz transducer with a 203 mm focal length in water was used. The colour scale indicates the relative amplitude of the reflection coming from the interface depth. The figure shows that there is a ring of low reflecting interface about 20 mm from the centre of the sample. This region of the interface probably has better transmission because the surfaces are raised causing them to be under greater load than the rest of the interface. The highest amplitude reflection came from a region near the edge of the interface, but the centre of the interface was only 10% less reflective than this region. These features indicate that the polishing or grinding did not create a perfectly flat surface, instead removing too much material from the edges and centre of the plates. This profile was probably created by the use of a rotary machine that was too small in diameter for the sample or perhaps had an uneven surface. The rotary machine was only used for the polished sample. The rougher sample was sanded by hand on a static flat sheet of wet and dry paper so would not be expected to have this uneven profile.

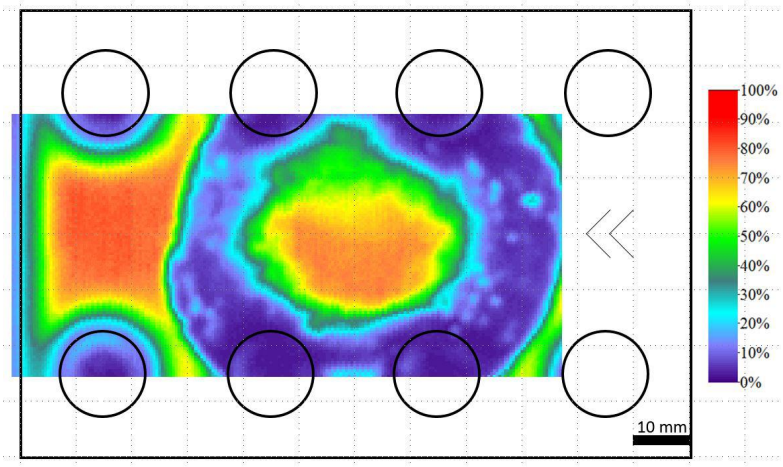


**Figure 7.13:** C-scan of reflection from polished interface. Taken at 20 Nm bolt torque with 10 MHz, 25 mm diameter, focused transducer. A 10 mm grid is shown for scale. Arbitrary reflection amplitude scale shown by colour.

To complement the c-scan information, through-thickness transmission measurements were taken at various points along the long axis of the sample. The solid aluminium sample was used as a reference for 100% interface transmission, Figure 7.14. This testing was conducted with bolts torqued to 25 Nm with 5 MHz, 10 mm diameter, unfocused transducers, with a 12° angle of incidence at the interface. The transmission coefficient had a minimum of 2.3%, this occurred at -1 mm from the centre, and a maximum of 71% at -23 mm. The negative distance is towards the end of the sample marked '<<' on the c-scan, Figure 7.13. There is a good agreement between the trends observed in the c-scan and the transmission testing.

Clearly this interface is not ideal for testing. The geometry of the experiment is such

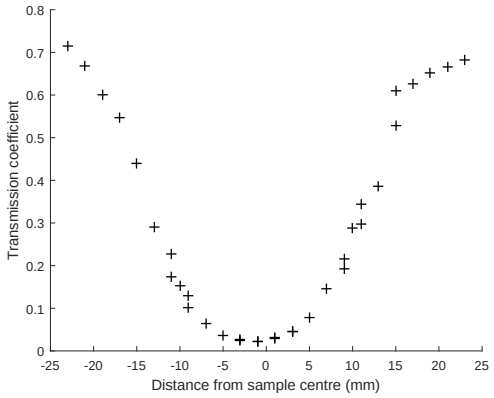


**Figure 7.14:** Polished interface transmission tested at 25 Nm bolt torque. Negative distances are towards chevron marked end of sample.

that the interaction angle range becomes more limited the further away the interaction volume is from the centre of the sample so it cannot simply be moved off to the sides where contact is better. In the future the use of a longer sample would allow more flexibility in regards to this.

According to the divergence calculations in Section 7.4.4 using the -3dB beam width the diameter of the interaction area at a depth of 30 mm and $\phi = 80^\circ$ is around 21 mm. This large interaction area will therefore extend into regions of the interface where the transmission coefficient is 20% so it should be possible to get results despite the poor contact at the centre. A small offset of 2 mm was used to put the interaction area closer to the region of the interface with better contact with limited effect on the possible interaction angles. The zero distance in Figure 7.14 corresponds to this 2 mm offset position.

### 7.5.2 Nonlinear response

Positioning the interaction volume slightly off-centre as described above allowed a fingerprint to be captured that had a reasonable signal to noise ratio. This was done at a low resolution as earlier work had shown that the single frequency ratio tests were a better use of scanning time. Bolts were torqued to 25 Nm, and the usual 5 MHz reference frequency was used. The fingerprint, shown in Figure 7.15, indicated that scattering was strongest at around $\phi = 75^\circ$, as was seen in the preliminary and rough tests, and at $a = 0.9$, in agreement with the rough interface results. The main difference in the fingerprint was the increase in prominence of the secondary peak at $\phi = 106^\circ$. This compared with only a minor peak at around $\phi = 100^\circ$ for the rough interface. In the discussion of those results it was suggested that this peak may be an artifact of the

sampling lines, meaning that the exact angle of occurrence is not significant.

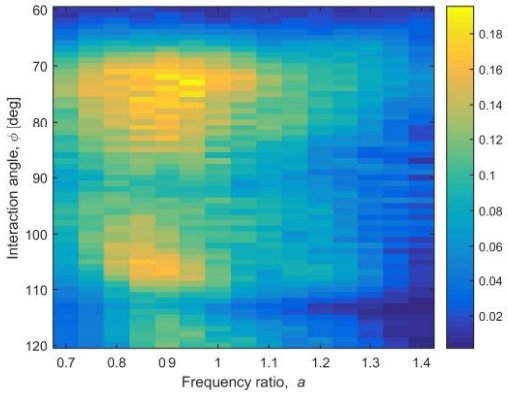


**Figure 7.15:** 5 MHz experimentally measured parametric response of aluminium polished kissing interface sample at a depth of 30 mm, the middle of the block. Bolt torque at 25 Nm. The colour scale indicates the scattering amplitude.

This test suggested that again $a = 0.9$ would be optimal for further testing and that enough signal was received to allow for investigation into loading response and other behaviours.

The polished interface sample was tested with a range of applied loads in the same way as the rough surface sample in Section 7.4. The data displayed in Figure 7.16 was collected over the course of two loading cycles; the sample's bolts were initially torqued to 40 Nm before being individually unloaded and reloaded to 10 Nm to start the main test cycles. This process aimed to reduce the effect of the surface asperities changing during the following load cycles. It was noted that a strong mixing signal could be seen at the 10 Nm torque case so for the second cycle a lower torque, 5 Nm, was investigated. To inspect this lower torque a different torque wrench had to be used that could only go up to 25 Nm. The smallest increments of load tested were 5 Nm as this was the lowest change achievable with the method. A solid reference block made from the same aluminium as the interface sample was also tested and is shown in Figure 7.16 (a).

The results seen in Figure 7.16 are very different from those of the rough interface sample, Figure 7.8. They both have a main peak at around 70-80°, but the trends in relation to applied torque are almost opposites, with the exception of the 5 Nm load case. 10 Nm produced the largest mixing signal, and as load increased to around 25 Nm the signal dropped down to a plateau at about a third of the 10 Nm amplitude. There was some significant variation visible between the two load cycles but overall trends remained similar. The main variation was between 20 Nm measurements, with cycle 'a' producing half the signal of cycle 'b'. This may be due to the inaccuracies of the loading method, or perhaps the changing surface asperities. In cycle 'b' the reduction

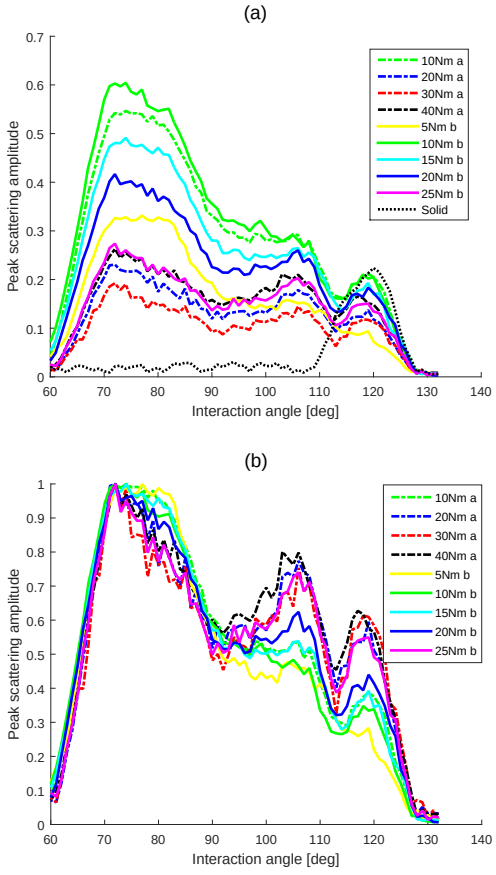


**Figure 7.16:** (a) Scattering amplitudes from polished aluminium interface sample at a frequency ratio of 0.9 with bolt torques ranging from 5 to 40 Nm. The first loading cycle is labeled ‘a’, and the second ‘b’. (b) Is the same data but peak normalised.

in scattering happened gradually over the 10 - 25 Nm range, eventually reaching the low scattering state seen in the 20 - 40 Nm measurements of cycle ‘a’. The particularly interesting load case was the lowest one, with bolt torque at 5 Nm. This produced less signal at all interaction angles than both the 10 Nm tests. These trends are shown with greater clarity in Figure 7.17. This behaviour is expected due to the poorer contact between the surfaces at lower load leading to low transmission across the interface, and was probably the dominant mechanism behind the trend observed in the rough interface sample. The polished sample data is interesting because it captures the transition from the poor contact regime into the overloaded regime where the acoustic pressure is not enough to open the interface.

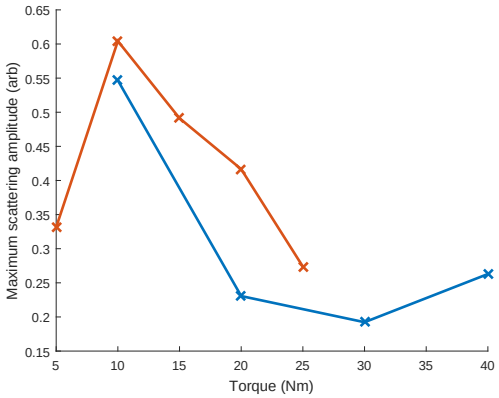


**Figure 7.17:** Maximum scattering amplitudes from polished aluminium interface sample at a frequency ratio of 0.9 with bolt torque ranging from 5 to 40 Nm. The first loading cycle is shown in blue, and the second in orange.

A couple more load dependent trends are apparent in the peak normalised Figure 7.16 (b). Higher load causes the main peak to narrow and increases the relative amplitude of local maxima at 108° and 118°. The narrowing of the main peak happens from one side shifting it towards smaller interaction angles, this trend is similar to that of the rough interface. The reason for this shift of the peak to smaller interaction angles as load is increased is not known. These trends were shown most clearly in cycle ‘b’, gradually transitioning from one shape to another while cycle ‘a’ changed more between 10 and 20 Nm but very little after then. This was the same as was observed in the amplitude trends of part (a) of the figure.

In order to understand whether the differences between the rough and polished data are due to a change in the macro surface profile (i.e. the creation of the raised circle, seen in Figure 7.13) or if the roughness was the primary contributor the following argument is presented: The surface profile of the rough sample is unknown but due to its production method (linear sanding on a flat sheet of wet and dry paper) it is likely flatter than the polished sample on a macroscopic level. This means that the interaction area in

the middle of the rough sample would have been under greater average load than the polished sample at the same torque level (due to the raised ring transferring most of the force in the polished case). Despite this the rough sample showed no signs of entering the overloaded regime, therefore the surface roughness is the primary contributor to the loading trends observed.

### Absolute Interface load

In the section above a peak in scattering from the interface was observed in terms of bolt loading. In Blanloeuil et al.'s work (4) FE modelling predicted that the maximal mixing response occurs when the interface load is 25% of the peak combined acoustic loading. By knowing the acoustic loading that was applied to the experimental interface it is possible to estimate what static load it was under. Predictions of interface loading from the applied torque were made but the raised ring of the surfaces means that this calculation is likely inaccurate for the central region.

To measure the acoustic load a laser vibrometer was used, Polytec OFV 2700. For this test one of the interface sample blocks (30 mm thick) was placed with the polished interface surface above the waterline and the rest of it below. One of the 5 MHz transducers was submerged in the water and aimed at normal incidence to the underside of the block. The spacing between the transducer and the block was similar to that used in typical fingerprint measurements. The laser vibrometer was then used to measure the displacement of the surface above the water. It detected a displacement of $2\text{x}10^{-10}$ m. Using the equations below this can be converted into a pressure that would be observed at the interface.

$$\delta = \frac{P}{\omega Z} \tag{7.2}$$

Where $\delta$ is the displacement, $P$ is the pressure, $\omega$ is the angular frequency, and $Z$ is the impedance. Impedance is given by $Z = \rho c$ where $c$ is the wave velocity. Rearranging this gives an equation for pressure of

$$P = \delta \rho c \omega \tag{7.3}$$

Because the measured displacement is at the boundary between materials with vastly different impedances (aluminium-air) the surface of the solid will be displaced twice the usual distance due to most of the wave reflecting off the interface, imparting extra force on the solid. Therefore, in the bulk of the material (or in a perfect kissing interface)

the displacement would be $10^{-10}$ m. This gives a pressure of 50 kNmm$^{-2}$. This was the estimated pressure caused by a longitudinal wave in the bulk material but in the experiment shear waves are used. Looking at the mode conversion plot in Chapter 3, Figure 3.6 it can be seen that at normal incidence (as was used for the interferometer measurement) the pressure of the longitudinal wave is similar to that of a shear wave produced by an incident angle of 15° to 25°. This range produces interaction angles from 65° to 125° so is fairly accurate for most of the experimental range. As discussed in Blanloeuil et al.'s work, (5), at 45° to the interface a shear wave produces no tangential stress in the interface, only normal stress. Thus, at an interaction angle of 90° the two shear waves combine to exert up to double the stress calculated above, totaling 100 kNmm$^{-2}$ = 0.1 MPa.

The experimental acoustic loading therefore suggests that a maximum in scattering will occur when the static load on the interface is 0.025 MPa. Since the polished interface produced a peak in scattering with a torque of 10 Nm this implies that 0.025 MPa was applied in the centre of the interface in this case, not the 5 MPa predicted for a perfectly flat surface. See Section 3.8 for the relation between torque and interface load.

The rough sample is believed to have had a more even load distribution across the interface, so the prediction of 5 MPa in the interaction area is more likely. In this case the loading is much higher than peak value of 0.025 MPa suggested above, yet as load was increased the scattering did not decline. This is further proof that the rough interface is not represented well by Blanloeuil et al.'s FE model, probably due to the large distribution of contact stresses between the two faces.

### 7.5.3 Bulk mixing impact on interface fingerprints

The solid sample gives a baseline mixing response for the bulk nonlinearity. Figure 7.16 (a) shows that at 120° it produces slightly more signal than the polished interface at any load. Equation 7.1, derived in the rough interface section, can be used to predict the bulk nonlinear signal contribution to the overall measured signal by using the solid sample measurement amplitude with the measured transmission coefficients of the interface. The transmission was only measured at 5 MHz so this value will be used for the 10 MHz factor as well. Generally higher frequencies would have a lower transmission coefficient so the predicted bulk signal from the interface will likely be an overestimate.

It is difficult to estimate an accurate averaged transmission coefficient due to the non-uniform beam intensity profiles; the centre of the beams contribute more to the mixing than the edges. This is somewhat factored into the reduced -3 dB beam width as used

earlier in this work. Taking a rough mean of the transmission coefficients over the 21 mm beam diameter gives a factor of about 8%. Using this value in Equation 7.1 predicts that the interface would reduce the bulk mixing signal amplitude by 96%. Figure 7.16 (a) shows the solid sample produced a peak scattering amplitude of 0.22 (as normalised to the largest amplitude produced by interface mixing). This would be reduced to 0.01 in this case, which is more than an order of magnitude smaller than the signal detected at around $\phi = 120^\circ$ in the loaded interface samples. Therefore, this work confirms that the majority of signal produced in this region of the parameter space in the polished interface sample was not due bulk mixing.

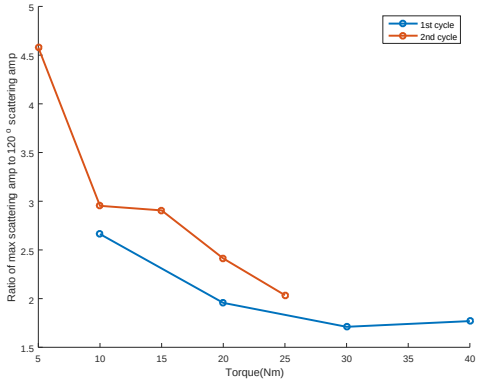


**Figure 7.18:** Ratio of overall maximum to $\phi = 120^\circ$ scattering amplitude for polished aluminium interface sample at a frequency ratio of 0.9 with bolt torque ranging from 5 to 40 Nm. The first loading cycle is shown in blue, and the second in orange.

A piece of evidence that could be thought of as conflicting with the above conclusion is the ratio between the amplitude of scattering at the 'CAN' peak around $\phi = 76^\circ$ and $\phi = 120^\circ$, shown in Figure 7.18. It shows that increasing torque reduced the ratio, this happened because it lowered the 'CAN' peak amplitude much more than the mixing at $\phi = 120^\circ$. One reason why the mixing at $120^\circ$ was not reduced as much could be that a considerable component of it is due to bulk mixing, which would be increasing with load, offsetting some of the reduction in CAN mixing. However, the loading tests have shown that the relative strength of scattering at different interaction angles can change even when at interaction angles outside of those that cause bulk mixing (e.g. the $\phi = 100^\circ$ feature in the rough sample). It seems more likely that something similar is occurring in this case, perhaps due to a different subset of areas of the interface being sampled at $\phi = 120^\circ$ than at $\phi = 70^\circ - 80^\circ$, and these areas were responding differently to the loading conditions.

It would have been useful to observe how the shape of the fingerprints changed with position for the polished interface. It might have shown that the mixing at larger interaction angles was position sensitive and therefore likely related to the sampling

lines concept. Attempts were made to run the test with this polished interface but problems with a lack of transmission in some regions meant that the results from this were of little value. The results from the rough interface were highly informative in regards to the potential for position sensitivity in the fingerprints, but further investigation into smoother interfaces is required before firmer conclusions can be drawn.

## 7.6 Inter-probe delay

As part of the calibration of the equipment before testing the delay between the two input pulses was altered in order to ensure that the peaks of the pulses overlapped. This was done simply by varying the delay on one of the pulses and observing the amplitude of nonlinear scattering. If no peak in response was observed delay would be applied to the other pulse instead. It is assumed that the delay that produces maximal scattering corresponds to when the pulses are perfectly in sync. When testing solid materials a smooth trend was observed in terms of delay, but when the interaction volume was centred on a kissing interface a different behaviour occurred.

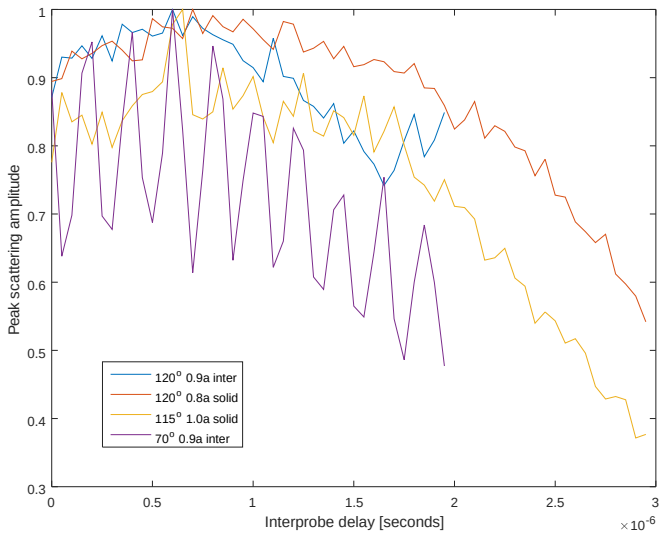


**Figure 7.19:** Peak scattering amplitude as the delay between the input pulses was varied. The results include tests on a solid sample and the interface sample, and were taken with a variety of interaction parameters as indicated in the legend. The scattering amplitudes are normalised for each test.

Figure 7.19 shows an example of the results from these calibration procedures. The plot includes two tests of a solid sample with the interaction volume within the solid at interaction conditions near enough to resonance to get a strong mixing response.

These measurements are indicated by the lines marked 'solid' in the legend. Different frequency ratios were used to show that the smooth behaviour is independent of it. Fourier analysis of these solid results showed no significant higher frequency terms. In contrast, the $\phi = 70°$, $a = 0.9$, interface sample test showed a very strong higher frequency component, corresponding to a delay period of $2.0\times10^{-6}$ seconds. The measurement of this sample at the classically resonant case, however, did not. Results from the polished interface sample are shown in the figure, with bolts torqued to 25 Nm. The solid samples were checked many times at multiple frequency ratios and interaction angles, but the periodic feature was never observed.

The explanation for the pattern seen in the interface sample at $\phi = 70°$ is related to the discussion in Section 7.4.4 about position sensitivity in the rough interface. The concept developed there was that the non-collinear method samples the interface at an array of lines. As the delay between the pulses is altered these lines are shifted across the interface. Delaying one of the beams by $2.0\times10^{-6}$ s when the pulse is at 5 MHz shifts the pulse a complete wavelength and results in approximately the same lines of the interface being sampled, hence the observed periodicity. It is unclear why the testing of interface samples at larger interaction angles did not also present this behaviour though. Perhaps this is because the mixing occurring at $\phi = 120°$ in the interface sample is mainly due to the bulk nonlinearities. This contradicts the conclusion reached from analysis of the amplitude of the bulk signal and transmission coefficients in the previous section, 7.5.3.

In order to collect fingerprints that are representative of an area of the interface a method of sampling it more uniformly is required. This could be achieved in multiple ways; the inter-probe delay could be swept by one period and the results from each increment averaged, or longer input pulses could be used in combination with frequency ratios away from one as these naturally sweep the interface over the course of the pulse. The longer pulses method may be preferable because it does not require multiple measurements to be made. Perhaps in this case it would be possible to see fluctuations in the time domain of the scattered signal amplitude coming from the interface as the probing lines sweep across it. Simply taking the peak from the signal (as is currently done) may not be a good metric of the average interface properties in this case, as that peak would relate only to the parts of the interface that create the most mixing, but says nothing about the other parts of the interface. The measurement of the fluctuations as the sampling lines sweep the interface may also be useful in understanding the variation in properties of the interface that might relate to different types of defects.

On an unrelated note; during the inter-probe delay testing it was observed that the

position of the scattered pulse on the array changed as the delay was altered. The arrival time also changed, as would be expected, by half of the delay amount due to an averaging effect between the overlap of the two beams. A delay of $2.0\times10^{-6}$ seconds caused the signal to move by about 4 mm on the array, analysis showed that this was likely due to the fact that by changing the delay the overlap point of the peaks of the input waves is moved spatially. Therefore, it is important when doing non-collinear testing that the delay is properly calibrated, not only for the maximisation of scattered signal, but also to avoid an offset effective interaction point which can reduce the quality of the focusing on reception.

## 7.7 Conclusions

The non-collinear interaction of two shear waves in dry, aluminium, compression loaded interfaces has been studied over a wide range of interaction angles and frequency ratios in the shear-shear mixing case at around 5 MHz, forming 'fingerprints' of the interface. This sample is intended to simulate an acoustically simple case of a kissing bond to allow the fundamentals of a non-collinear approach to detecting more realistic kissing bonds to be developed. The kissing interface samples displayed nonlinear scattering fingerprints very different from the reference solid sample, producing signal at interaction angles between 60° and 120°. At all points in the loading range investigated a characteristic shape was produced, peaking at around 75°. This fingerprint was similar to that predicted by Blanloeuil's FE modelling (4) except for the secondary peaks in the 100° to 120° region in some cases. Frequency ratio was not studied in detail in this work as the initial fingerprints had few apparent features in this dimension.

The rough and polished interfaces displayed different loading related behaviour; the rough interface produced increasing amplitudes of scattering at all interaction angles as the torque on the bolts was increased, the polished interface was more complex, rising then falling within the loading range. These differences are likely due to the way the surfaces contact each other; in the rough case increasing the loading brings more surface area into contact increasing the CAN signal, but in the polished case a higher fraction of the interface is in contact at a lower load and increasing the load further results in much of the interface being under too much pressure to be acoustically separated, thus reducing CAN signal. The results were complicated by the presence of a raised ring on the polished surfaces, reducing the loading transferred to the central part of the interface. Some preliminary results for a polished interface were included for comparison as this test did not appear to have the same problem. In that case the scattering amplitude

always reduced as loading increased, even when testing with a very low torque of 2 Nm.

It might be expected that for a smooth interface the load could be increased to the point where the acoustic forces were not large enough to open it and cause CAN. The optically smooth polished surface of both the preliminary and later tests however did not appear to be reducing to a state of no scattering, instead plateauing in response as the load increased above a certain level.

As well as changes in overall amplitude the shape of the fingerprints were altered by the loading. Both interface types had smoother fingerprints at lower loads (less prominent secondary peaks) and the interaction angle of the main peak shifted to smaller angles as load increased. This showed that there is the possibility of measuring multiple fingerprint features that relate to one interface/material parameter (in this case loading) in order to improve the robustness of measurement of that parameter. From the testing it was unclear what was causing many of these fingerprint features and the FE model did not predict secondary peaks. The situation was complicated further when significantly different fingerprints were measured for overlapping areas (around 20 mm in diameter) of the rough interface, moved by only a couple of millimetres. It was shown that the changes in the fingerprints did not correspond to the loading related behaviours observed previously and that something else is likely the cause. Further testing of this behaviour was attempted for the polished interface but problems with the interface quality prevented meaningful analysis.

It is hypothesised that the position sensitivity and the secondary peaks could be due to the non-collinear method having regions of greatly enhanced sensitivity where the component of stress normal to the interface of the input beams cancel, forming an array of sampling lines. These lines are spaced approximately one wavelength of the input reference beam apart, with a sinusoidal transition from complete cancellation of normal stresses to constructive interference and back again over that spacing, giving some degree of width to the lines of high sensitivity. Therefore, this hypothesis suggests that unevenness on the length scale less than a wavelength but greater than about a tenth of a wavelength could cause the observed position sensitivity, about $0.1 - 1$ mm at 5 MHz. Accurate measurement of the surface roughness on this length scale combined with modelling is required to understand what the variation in loading would be in order to confirm if this is a likely cause. The polished sample visually appeared to be smooth on this length scale in the centre but the raised ring profile created gradients in contact pressure around them and the large interaction area of the beams meant that it was not possible to sample regions of uniform pressure.

Investigation of the impact of the delay between the two input beams added further

evidence for the concept of sampling lines. It showed that with a solid sample a smooth variation in scattering amplitude was seen, with a single significant peak when the pulses overlapped temporally and spatially. The $\phi \approx 80^\circ$ tests on the kissing interfaces had this overall shape but superimposed on that an amplitude feature that oscillated with a period corresponding to delaying one of the input beams by a wavelength. This was shown to relate to sweeping the interference pattern across the interface by one step, approximately back to its starting position. Tests conducted on interfaces at an interaction angle of $120^\circ$ however did not demonstrate this behaviour. This suggests that the mixing at that angle was not due to the interface but to the bulk nonlinearities. This conflicted with other evidence presented during the chapter that showed that the contribution of bulk mixing to the fingerprints, even at classically resonant conditions, was minor for the interfaces tested.

The loading method of adjusting bolt torque allowed for great flexibility in investigation of the interface causing very little obstruction to measurement. This enabled multiple parts of the interface to be tested and the sample to be moved under load to be c-scanned and transmission tested, this would not be possible with a conventional universal testing machine method. The main negative of the technique was the random error in loading magnitude due to the unreliable frictional behaviour of the nuts/bolts and the systematic error due to the difficulty in directly measuring the applied load. Calculating the interface pressure was complicated further by the unevenness of the interface.

There are many more tests to be conducted to achieve a better understanding of the non-collinear mixing at kissing interfaces. Testing on the polished interface was cut short due to problems with its quality; it would be desirable to investigate the position sensitivity of fingerprint features for a better contacting interface, as well as behaviour at reduced acoustic loading. The effect of altering the reference input frequency was also not explored, this could be of importance if scattering amplitude does not scale cubicly like bulk mixing.

In the future use of focusing on input beams would allow interaction regions with far fewer overlapping wavefronts to be made. This would probe the interface in greater detail and might aid in the confirmation of interface properties varying on a wavelength scale causing the position sensitivity trends and occurrence of features in the fingerprint at large interaction angles. If using unfocused beams, sweeping the interaction nodes along the interface, perhaps by altering the phase of the beams, and summing the responses together might be a route to measuring a more averaged scattering value for the interaction area. Alternatively, frequency ratios further from one with longer pulses could achieve a similar level of sampling coverage. This could be useful if a faster

measurement is required than scanning a focus across the whole area and would also ensure that no parts of the interface are unsampled.

In this work there was only one interface at a known depth, in this case a non-collinear c-scan could have been conducted by moving the input transducers and array along the sample. If the defect is at an unknown depth the technique could be easily extended to 3D by sweeping the depth of the interaction volume. The fingerprint at each location might then be analysed to identify the properties of the sample within the interaction volume, allowing 3D positional detection of kissing bonds.

The following chapter studies the angle of scattering of the interface mixing in an attempt to test the predictions of the geometric model that were developed in the previous chapter. This model is then use to extend the mixing situations beyond what was possible with the experimental configuration used for the above testing; with smaller interaction angles, and arbitrary interface angles to the input beams. This leads to predictions of alternative mixing modes.

# Chapter 8

# Further interface theory

# 8.1 Introduction

In this chapter the theory behind non-collinear mixing at an interface will be studied in more detail by using the geometric model developed in previous chapters. In the near surface mixing chapter the model was used to predict the angle of scattering that would be caused by a planar source, and compared with experimental data. This will also be done here with the data collected from kissing interface scattering with the goal of confirming if the scattering from an interface agrees with the model or the classical momentum conservation equation.

Later the model is extended to cases not tested experimentally such as for an interface at an arbitrary angle, and the possibility of mixing in other directions due to other features of the interference pattern. It is hoped that in the future these predictions could be validated either experimentally or with a more powerful model, such as Blanloeuil et al.'s FE model. The amplitude of the scattering at an interface is not predicted by the geometric model so that will not be discussed, rather, the model indicates what types of mixing might be possible and what angles beams would be produced at.

# 8.2 Scattering angle from interface

In this section the angle prediction for a two-dimensional source that was derived in Chapter 6 is applied to the experimental interface data to investigate if its predictions are correct and the concept is also extended to include inclination of the source plane to allow for the prediction of the scattering angle from oblique cracks/interfaces. The previously derived equation for scattering angle, $\theta$, is shown in terms of frequency ratio, $a$, interaction angle, $\phi$, and wave velocities, $v_L$ and $v_T$ below.

$$\theta = \sin^{-1}\left(\frac{1-a}{1+a}\sin(\phi/2)\frac{v_L}{v_T}\right) \tag{8.1}$$

This equation is only applicable to the scattering of a sum frequency longitudinal wave from two input shear waves. $\theta$ is defined relative to the bisector of the input waves.

## 8.2.1 Comparison with experimental measurements

In order to compare the predictions of the classical and geometric models with the experimental results the point of highest scattering intensity on the array is plotted in

Figure 8.1 as well as the predictions for a range of frequency ratios. The data shown is from the rough contacting interface. As explained in Chapter 6, the scattering angle is not plotted directly for a variety of reasons but is related to the position. Plots at a range of frequency ratios are shown, with (c) $a = 1$ being a useful reference of symmetrical scattering. In this case the predictions of the classical scattering angle, Equation 2.3, and the new geometric prediction agree. The geometric prediction is labelled 'CAN' in the plots due to its expected relevance to CAN scattering. A correction for the drift in position due to experimental errors has been included in the predictions.

It can be seen that at $a = 0.7, 0.8, 1.1$ the 'CAN' prediction fits the experimental data much better than the classical. However at $a = 1.2$ and $1.3$ it might be thought that the classical prediction fits better. The results from the near surface mixing showed worse agreement at positive frequency ratios as well, suggesting something wrong with either the model or the experiment. In future work the derivation should be checked, paying close attention to the $a$ terms.

Generally the results here are inconclusive due to the small difference between the predictions of the two models compared with the errors inherent in the experiments. The differences are smaller here than in Chapter 6 because the interaction volume is half the distance from the array. The mixing is also weaker in this case reducing the signal to noise ratio. It was mentioned in that chapter that at some points where the experimental data appeared to disagree with the CAN prediction it was actually due to an asymmetric beam being produced. This also is sometimes the case here, an example of $a = 1.2$, $\phi = 86^\circ$ is shown in Figure 8.2. The peak position used in Figure 8.1 is based upon the smoothed data, plotted in blue in Figure 8.2.

Further work, either experimental or FE modelling, is required to validate the scattering angle prediction of the geometric model. This is necessary to allow for accurate calculation of scattered beam propagation direction which is important for industrial use of non-collinear mixing techniques.

Although the kissing interface results were inconclusive the surface mixing ones suggested that this model does a better job of predicting scattering angle from a 2D source than the classical equation. Therefore, it is likely that the model is suitable for modelling scattering from kissing bonds and is worthwhile developing the model further in sections below.

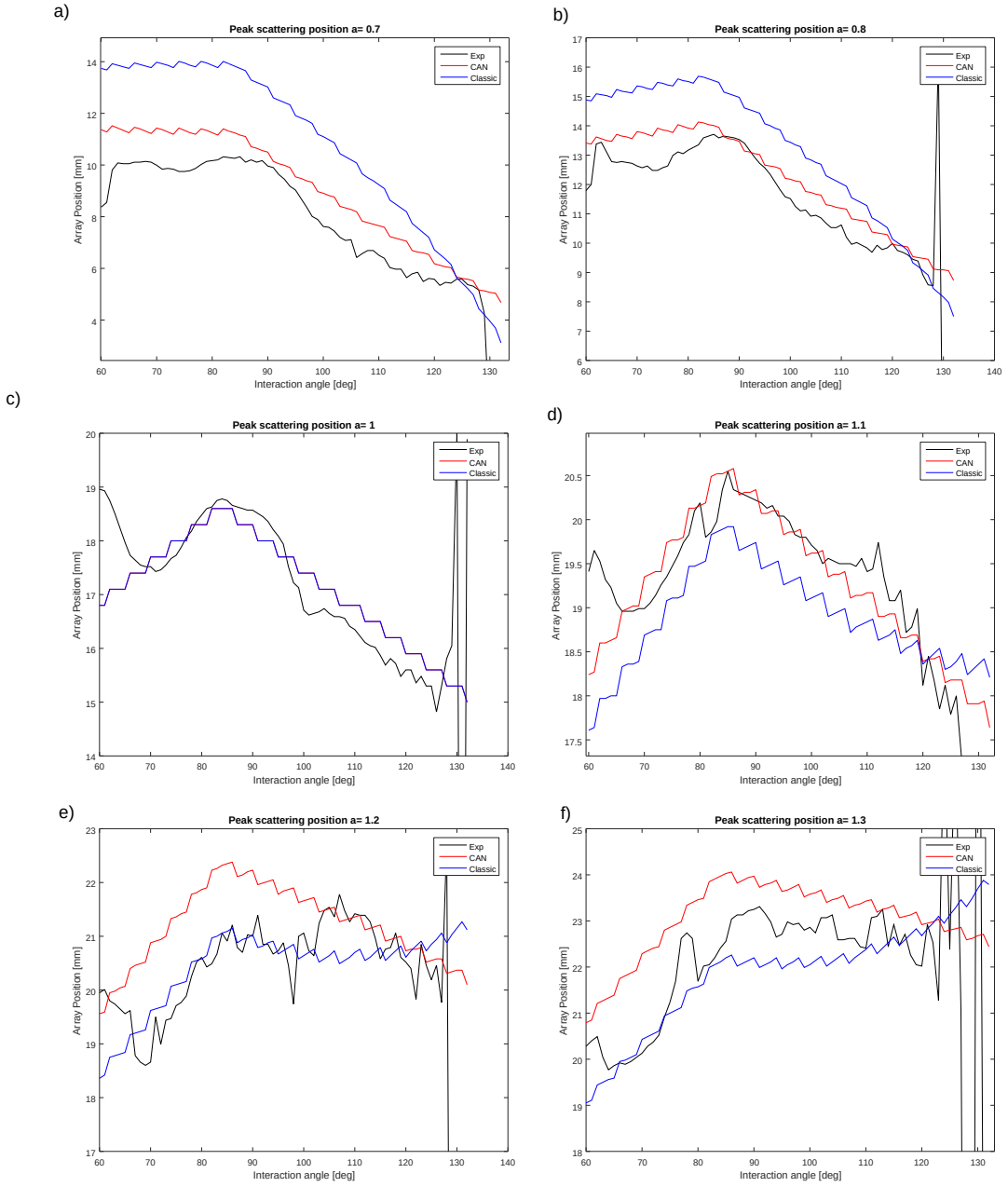


**Figure 8.1:** Position of peak signal on the array produced by mixing at a rough interface. A range of frequency ratios are shown: a) 0.7, b) 0.8, c) 1, d) 1.2, and e) 1.3. The measured position is plotted in black, the classical prediction in blue and the 2D source prediction in red.

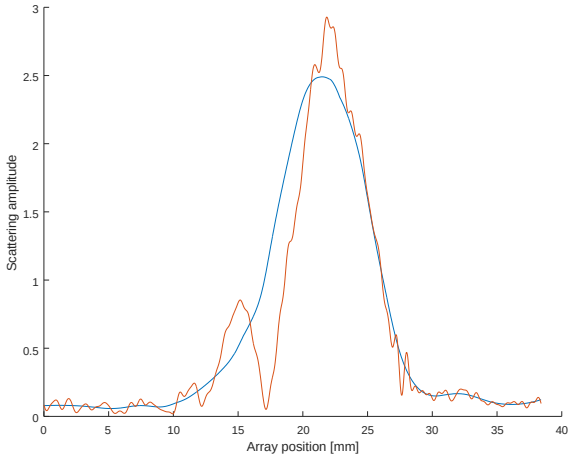


**Figure 8.2:** Beam profile of scattered beam at $a = 1.2$, $\phi = 86°$ from a rough kissing interface. The measured signal is shown in orange and the fitted peak is in blue.

### Rotated interface

In the section above the input beams were symmetrical in relation to the interface they were mixing at. In the real world cracks or bond lines could be at any angle thus a more general form of the equations are needed to predict the scattering angle for these cases. The extension of the geometric model to an interface at an arbitrary angle is quite simple, it uses the same basic equation as the normal case. The angle of scattering, $\theta$, is dictated by spacing between where the interference pattern nodes hit the interface, and the time delay between them.

$$\theta = \sin^{-1}\left(\frac{\text{delay} * \text{velocity}}{\text{spacing}}\right) \tag{8.2}$$

The difference is that the delay term must be modified to include the added time delay for the downwards moving nodes to reach the interface due to its slant. Also the spacing must be modified to account for the increased distance between the points where the nodes hit the interface. Both of these adjustments can be seen in Figure 8.3.

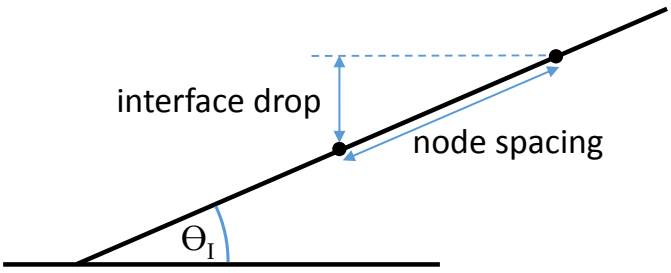


**Figure 8.3:** Schematic of modifiers geometric model due to an interface at an arbitrary angle $\theta$.

With these adjustments the delay term then becomes

$$\text{delay} = \frac{\mathbf{j_y} + \text{interface drop}}{v_n} \tag{8.3}$$

where the change in the interface's vertical position is given by

$$\text{interface drop} = \tan(\theta_I)\mathbf{j_x} = \tan(\theta_I)\left(\frac{(\lambda_1+\lambda_2)\cos(\phi/2)}{\sin(180-\phi)}\right) \tag{8.4}$$

$$\text{delay} = \frac{\frac{(\lambda_1-\lambda_2)\sin(\phi/2)}{\sin(180-\phi)} + \tan(\theta_I)\left(\frac{(\lambda_1+\lambda_2)\cos(\phi/2)}{\sin(180-\phi)}\right)}{v_T/\cos(\phi/2)} \tag{8.5}$$

$$\text{delay} = \frac{[(\lambda_1-\lambda_2)\sin(\phi/2)\cos(\phi/2)] + [\tan(\theta_I)(\lambda_1+\lambda_2)\cos^2(\phi/2)]}{v_T\sin(180-\phi)} \tag{8.6}$$

The spacing between the nodes was previously given by the horizontal component of $\mathbf{j}$. Therefore, the distance between nodes for an arbitrary angle interface is $\mathbf{j_x}\cos(\theta_I)$. Using these terms in Equation 8.2 gives

$$\theta = -\sin^{-1}\left(\frac{v_L\frac{[(\lambda_1-\lambda_2)\sin(\phi/2)\cos(\phi/2)]+[\tan(\theta_I)(\lambda_1+\lambda_2)\cos^2(\phi/2)]}{v_T\sin(180-\phi)}}{\frac{(\lambda_1+\lambda_2)\cos(\phi/2)}{\sin(180-\phi)\cos(\theta_I)}}\right) \tag{8.7}$$

$$\theta = -\sin^{-1}\left(\frac{v_L}{v_T}\cos\theta_I\left[\tan\theta_I\cos(\phi/2) + \frac{\lambda_1-\lambda_2}{\lambda_1+\lambda_2}\sin(\phi/2)\right]\right) \tag{8.8}$$

$$\theta = -\sin^{-1}\left(\frac{v_L}{v_T}\cos\theta_I\left[\tan\theta_I\cos(\phi/2) + \frac{1-a}{1+a}\sin(\phi/2)\right]\right) \tag{8.9}$$

It should be noted that these equations calculate the scattering angle from the interface, but since the interface can now be rotated this rotation must be added to the above result to obtain the scattering angle in terms of from the y-axis direction, $\theta_y$.

$$\theta_y = \theta_I - \sin^{-1}\left(\frac{v_L}{v_T}\cos\theta_I\left[\tan\theta_I\cos(\phi/2) + \frac{1-a}{1+a}\sin(\phi/2)\right]\right) \tag{8.10}$$

The sign convention is such that rotation of the interface is positive in the clockwise direction, and deflection of the scattered beam is also positive in the clockwise direction. The left input beam is defined as the reference for frequency ratio. Putting some example values into this equation of $v_L = 6374$, $v_T = 3160$, $a = 1$, $\phi = 100^\circ$, and $\theta_I = 20^\circ$ gives

a scattering angle relative to the y-axis, $\theta_y$, of $-6^\circ$. Showing that positive rotation of the interface causes the wave to scatter at a negative angle in this case. This cannot be assumed for all cases though; at much larger interaction angles the scattering angle becomes positive with positive interface rotation.

Comparing Equation 8.10 to its fixed interface angle equivalent, Equation 8.1, shows three main differences, firstly the rotation of the scattering by the interface angle due to the $\theta_I$ term at the start. Next is the $\cos\theta_I$ term which can be thought of as due to the modification of the nodal spacing when projected onto the angled interface, and finally $\tan\theta_I\cos(\phi/2)$ which is due to the modified time delay between successive node-interface overlaps because of the inclined plane.

There is very little data available to verify if the above equation is correct. One example is in a modelling paper by Blanloeuil et al. (4), reproduced in Figure 8.4, which suggests that the classical, momentum conserving, prediction is not correct. In the bottom right quadrant of the figure the scattered wave is slightly off to the side of the predicted blue arrow. The parameters of the model were $v_L = 6153$, $v_T = 3100$, $a = 1$, $\phi = 100^\circ$, and $\theta_I = -20^\circ$. If these are put into the 2D source scattering angle equation, Equation 8.10, it gives $6^\circ$, matching the observed scattered beam.

If proved to be correct the above equation would be very useful for quickly calculating scattering angles for a wide range of mixing cases without the need to simulate the mixing in a more detailed way, such as using FE.

## 8.3 Scattering in alternative directions

### 8.3.1 Fourth direction scattering

This model can be extended further to include mixing in the fourth direction as identified in Figure 4.1. In the bulk case this direction is not allowed due to momentum conservation rules, but these do not apply in the same way to a 2D interface. The vector **j** was defined as the relative position between two horizontally neighbouring nodal points, but for scattering in the fourth direction it is the relation between vertical neighbours that would be of interest. This vector, **l**, was derived in the modelling methods chapter as

$$\mathbf{l} = \frac{\lambda_1 - \lambda_2}{\sin(\phi)}\cos(\phi/2)\hat{\mathbf{x}} - \frac{\lambda_1 + \lambda_2}{\sin(\phi)}\sin(\phi/2)\hat{\mathbf{y}} \tag{8.11}$$

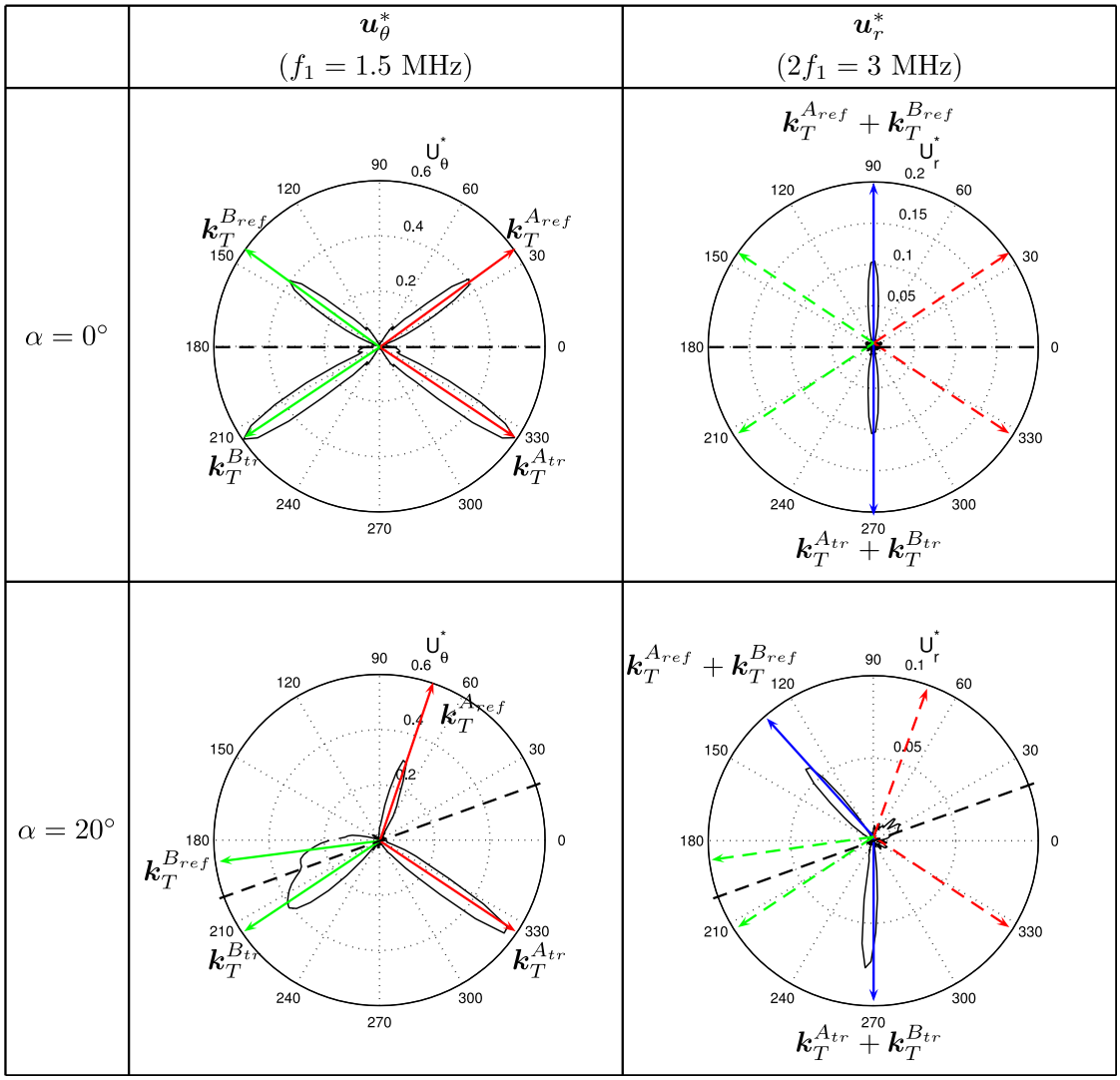


**Figure 8.4:** From Blanloeuil et al.'s work (4). Directivity patterns for two incident shear waves, for crack angle $\alpha = 0°$ and $20°$. Tangential displacements, $\mathbf{u}_\theta^*$, for the fundamental frequency and radial displacements, $\mathbf{u}_\mathbf{r}^*$, for double frequency are plotted. The direction of propagation of the reflected ($\mathbf{k}_\mathbf{T}^{\mathbf{A_{ref}}}$ and $\mathbf{k}_\mathbf{T}^{\mathbf{B_{ref}}}$) and transmitted ($\mathbf{k}_\mathbf{T}^{\mathbf{A_{tr}}}$ and $\mathbf{k}_\mathbf{T}^{\mathbf{B_{tr}}}$) shear waves predicted by the Snell-Descartes law are represented. Longitudinal waves are scattered in two directions collinear to $\mathbf{k}_\mathbf{T}^{\mathbf{A_{ref}}} + \mathbf{k}_\mathbf{T}^{\mathbf{B_{ref}}}$ and $\mathbf{k}_\mathbf{T}^{\mathbf{A_{tr}}} + \mathbf{k}_\mathbf{T}^{\mathbf{B_{tr}}}$. The crack is represented by the dashed line.

Following the same steps as used above for scattering in the third direction results in the following equation.

$$\theta_y = \theta_I - \sin^{-1}\left(\frac{v_L}{v_T}\cos\theta_I\left[\tan\theta_I\cos(\phi/2) + \frac{1+a}{1-a}\sin(\phi/2)\right]\right) \tag{8.12}$$

The only difference between this and Equation 8.10 is the inversion of the frequency ratio term. This results in a division by zero when $a = 1$. It also does not produce a real solution with any of the values of $a$ and $\phi$ experimentally tested in this work. Instead it requires quite extreme conditions to produce a result. In the case where the interface is horizontal an equation can be derived for how small an interaction is required to produce a scattered wave in the 4th direction for a given frequency ratio and velocity ratio.

$$\phi < 2\sin^{-1}\left(\frac{v_T}{v_L}\frac{1-a}{1+a}\right) \tag{8.13}$$

For $v_L = 6153$, $v_T = 3100$, $a = 0.5$ this gives $\phi < 19^\circ$ for example. With these values and an interaction angle of $\phi = 16^\circ$ equation 8.12 predicts a beam would be produced at $-57^\circ$. This compares with $-5^\circ$ predicted by interference nodes in the 3-direction which was discussed in the sections above, and $-3^\circ$ given by the classical momentum summation. The classical equation essentially calculates the angle of lines formed in the interference pattern. Although classical mixing is not allowed in the fourth direction an equation for the angle at which the interference lines are formed in that direction is.

$$\theta = \tan^{-1}\left(\frac{1+a}{1-a}\tan(\phi/2)\right) \tag{8.14}$$

This was derived in the same way as the bulk mixing angle Equation 5.11 from geometric principles. The value from this equation can be useful for visualising how the interference pattern will interact with interfaces at varying angles. The fourth direction CAN scattering equation only gives solutions when the interface is at angles close to the fourth direction interference pattern angle.

When the mismatch between the two angles is too large it results in the signal from one node-interface overlap point arriving at the next node-interface overlap point before the interference pattern has translated towards the interface enough for the overlap to occur. This problem can also occur in the normal third direction CAN scattering case, but with the parametric ranges investigated here a steep interface angle is required. For $v_L = 6153$, $v_T = 3100$, $a = 1.0$, and $\phi = 80^\circ$ the cutoff interface angle is $\pm 40^\circ$. This makes sense because it is the angle of directions one and two, the input beam angles.

Since $a = 1.0$ there is no forth direction so both third and fourth direction equations for scattering prediction do not work for interfaces rotated more than this angle in this case.

The fact that neither the third or fourth direction equations for scattering angle produce results with some input conditions does not necessarily mean that interface mixing will not occur. It is possible that in these cases the scattering angle would instead be defined by the delay between nodal overlaps from successive cycles. To factor this in the equations would need to include an integer term corresponding to the time delay, and position change of the nodes corresponding to the following, or earlier, cycles. This extension of the theory was not done here as the basic equations have not been proven correct yet.

Despite the author's hesitation to further develop the theory for the third and fourth direction scattering it was felt that scattering due to the first and second directions patterns warranted examination. But again, this should not be approached as fact due to a lack of experimental validation.

### 8.3.2 First and second direction scattering

The first and second directions are simply those relating to the wavefronts of the input waves. In the bulk case mixing caused by constructive nodes in these orientations would be expected to produce scattering in the same directions as the input waves. It is unclear if this form of mixing is possible and it might be difficult to differentiate it from the harmonics of the input beams on their own. This topic might be worth investigating further in the future but for now the focus is on the behaviour of mixing at interfaces instead.

Due to the way the interference pattern moves it is possible that interface mixing may occur in a direction dictated by the first and second lines of the pattern if the interface is rotated such that it is in a similar orientation. This beam would not simply propagate in the same direction as one of the input beams (unless the interface was at the same angle as the input beam wavefront) due to the time delay between nodal-interface overlaps. Following a similar method to that used for scattering from third and forth directions an equation can be derived for the scattering angles that would be expected in this new case.

$$\theta_y = \theta_I - \sin^{-1}\left(\frac{v_L}{v_T}\cos\theta_I\left[\tan\theta_I\cos(\phi/2) \pm \sin(\phi/2)\right]\right) \tag{8.15}$$

Where $\pm$ is positive for the first direction case, and negative for the second, as defined

by the sign convention described earlier. This equation is similar to the previous one except it is not dependent on frequency ratio. This is because the orientation of the nodes in the first and second directions is only due to the input wave angles, not their relative frequencies.

## 8.4 Snell's law

Another way of approaching this problem is to consider the interference pattern directions as beam wavefronts that are refracted by the interface according to Snell's law. This method was approached with skepticism by the author as these are not real waves, only existing in the interference pattern. If the input beam is treated as though it is traveling in the direction perpendicular to the 'wavefronts' that define it and the velocity of it is calculated as the component of the node velocity, Equation 6.2, in the effective direction of motion of the wavefronts, $v_e = v_n \cos\theta_{input}$, then this interpretation produces the same results as the equations derived above. It works for all of the directions discussed previously and provides a more visual way to understand the scattering behaviour at an interface.

## 8.5 Conclusions

The geometric model offers great potential for prediction of scattering angles for a variety of interface mixing cases. Currently it is difficult to validate the predictions but in Chapter 6 it was shown that a planar mixing source appeared to behave more similarly to the geometric equations than the classical ones, and in this chapter some further validation was provided, although the errors in the process prevented a conclusive result.

Mixing at an interface does not appear to be limited by any 'resonant conditions', as was seen in the previous chapter where mixing occurred over a wide range of interaction angles. In this chapter it was suggested that many other mixing cases may also exist due to the other lines formed in the interference pattern, although these would not have occurred within the parametric ranges investigated experimentally. These other interface interaction cases appear to become possible when the interface is rotated to an angle similar to the wavefronts of one of the input beams, Figure 8.5 (a), or when a narrow interaction angle is used, (b).

In the example of Figure 8.5 (a) a frequency ratio of 2.5 was used. This results in the orientation of the fourth nodal direction becoming close to that of the interface

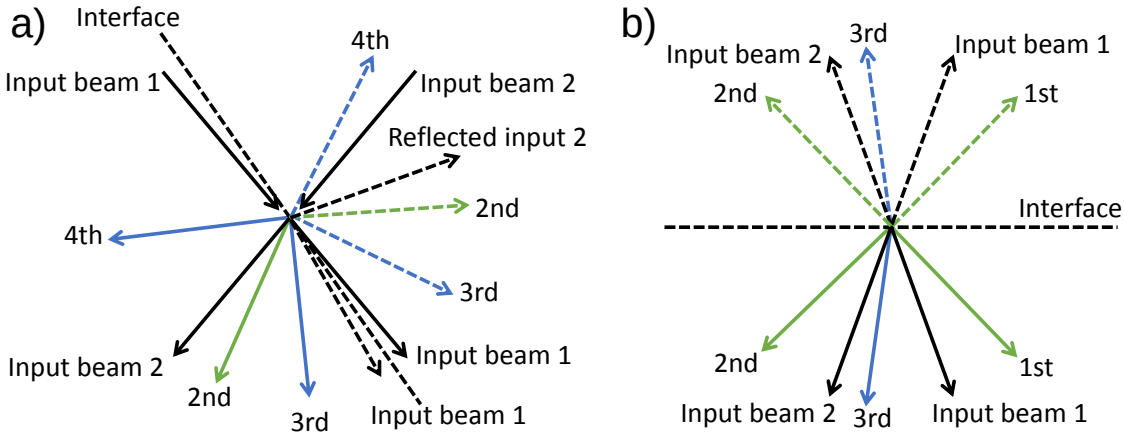


**Figure 8.5:** Examples of the direction of propagation of all possible beams. a) For the $\phi = 80°$, $a = 2.5$, $\theta_I = 55°$ case. b) $\phi = 40°$, $a = 1.5$, $\theta_I = 0°$. Transmitted beams are shown as solid lines and dashed lines are reflected although this concept is not rigidly applicable when beams enter the interface from opposite sides.

angle, giving valid solutions for the production of a fourth directional beam. The cases shown in the examples suggests that interface mixing could produce scattering in three directions at once (or six if scattering in the reflection direction is included). Further testing should be done to confirm if these beams are actually produced and what their relative amplitudes are. If these first, second, and fourth directional beams are real understanding them will be vital to interpretation of future non-collinear mixing results and may provide improved sensitivity by the collection of more information.

# Chapter 9

# Composites

## 9.1 Introduction

This chapter discusses how the work presented in previous chapters relates to the application of non-collinear mixing in composite materials, such as CFRP. It also includes some further test results that inform how the technique might be used for inspection on composites in the future.

## 9.2 Complexities of composite testing

The original goal of this research was to develop a method of detecting kissing bonds in the adhesive bond lines of CFRP structures. Early on in the research testing was conducted on 4.4 mm thick co-bonded CFRP samples. The samples had a range of concentrations of release agent applied to the half that was cured first. The fingerprints measured from these samples had many more features than those of the solid metal samples and no correlation between release agent concentration and fingerprint features could be found. An example fingerprint is shown in Figure 9.1.

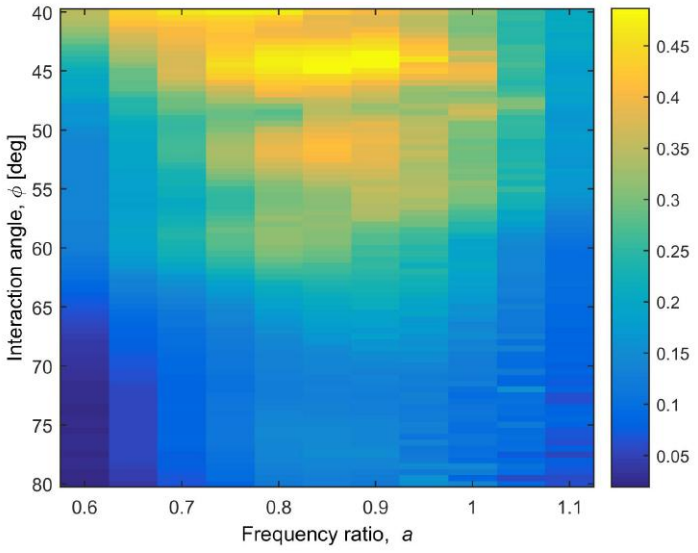


**Figure 9.1:** An example fingerprint of a thin co-bonded CFRP sample measured with a reference input frequency of 5 MHz.

Interpretation of the result from the CFRP sample is made more difficult by the lack of understanding of bulk mixing in such materials. Calculation of the bulk resonant conditions is dependent upon the ratio of the longitudinal and transverse wave velocities. The resonant interaction angle can easily be found for isotropic media because they have fixed velocities, but it is much more challenging in anisotropic composites. The

measured velocities are an average of the true velocities experienced by the waves as they travel through the constituents of the composite. It is possible that bulk mixing would occur based upon the true velocities, with distinct resonances for both the epoxy and carbon components in CFRP. Mixing in epoxy is discussed in Section 9.3 in this chapter.

If it is assumed that bulk mixing occurs based upon the averaged velocities then a rough estimate of the resonant interaction angle can be made. Highly approximated values for the averaged velocities (3000 $ms^{-1}$ longitudinal and 1800 $ms^{-1}$ transverse) give a velocity ratio of 0.6 which would result in a resonant interaction angle of 106°. This angle is likely larger than would experimentally yield results because of the high attenuation of the input beams at such angles. Interaction angles larger than 80° were not included in the fingerprint of Figure 9.1 due to this lack of signal.

It was realised that more work was needed on the fundamentals of non-collinear mixing to better understand what factors affected the fingerprints. A detailed analysis of bulk mixing in isotropic media was conducted, the results of which were presented in Chapter 5. These tests showed that consistent fingerprints could be achieved in samples thicker than the interaction volume diameter, but if this volume intersected with the surface of the sample the fingerprint became more complicated. This was investigated in detail in Chapter 6. This work showed that mixing occurred at the interface between water and solid and was large in amplitude, potentially interfering with or obscuring other sources of mixing that occur within the sample.

The surface mixing likely prevented useful fingerprints of the CFRP samples being measured. Out of curiosity a test was done to mimic the thin CFRP samples in terms of thickness, but in aluminium to remove the uncertainty due to the lack of knowledge of bulk and interface mixing in CFRP. This test showed that an interesting repeating pattern was formed across a wide range of the parameter space, Figure 9.2.

Fingerprints from these thin samples show that the surface mixing can produce complex patterns and should be avoided unless it can be understood well enough to allow for subtraction of the signal, or useful information to be extracted. This posed an issue to further investigation of CFRP since the immediate solution was to test samples thicker than the beamwidth but the attenuation of the ultrasound meant that these samples were unlikely to transmit enough signal to get good results. Therefore, aluminium samples were used for the remainder of the work because of their much lower attenuation, with a focus on mixing at a kissing interface.

There are many other challenges, besides attenuation, in inspecting CFRP with non-collinear methods that make it difficult to obtain fingerprints that would reliably

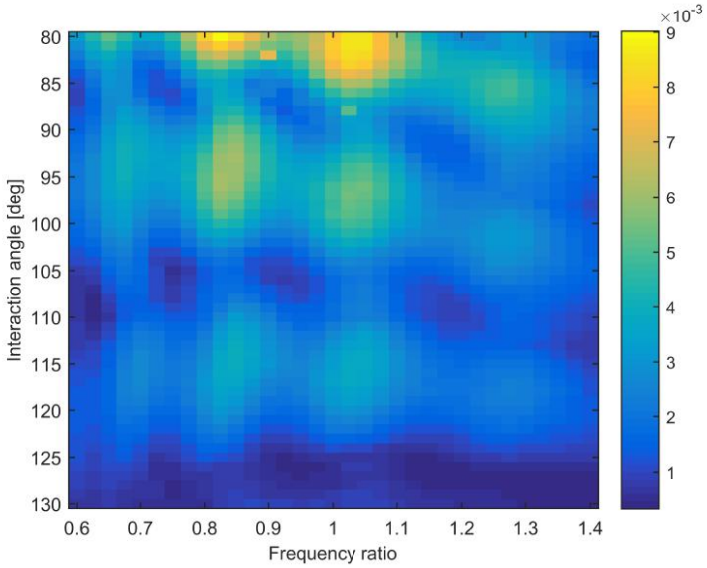


**Figure 9.2:** Fingerprint of a 3 mm thick aluminium plate measured with a reference input frequency of 5 MHz.

represent the state of the bonded interface. The direction dependent wave velocity discussed earlier complicates many of the calculations related to the interaction angle, and the situation becomes even more involved if the velocity is analysed on a ply by ply basis, with different ply orientations resulting in different velocities, causing refraction and creating multiple interaction angles and resonant conditions on the microscopic scale.

The boundaries between the plies cause reflection due to the mismatching acoustic impedances. If the spacing of the plies is at a critical length enhanced reflection can occur due to the thin-film interference effect. This occurs when the repeating structure is on a similar length scale to the wavelength. When using 5 MHz the wavelength is around 0.6 mm which is similar to the ply thickness. Depending upon what metric of the fingerprint is being measured this interference could completely obstruct the acquisition of a useful measurement.

Related to the interference caused by repeating plies is the adhesive bond line between two parts of the composite structure. The following section investigates this in isolation by studying the bond between two aluminium plates.

## 9.3 Adhesive interface

Previously in this thesis the fingerprints from the interface samples have been compared with a solid reference sample. This comparison is similar to the case of diffusion bonds which can effectively become continuous material if done correctly but it is not representative of the comparison that would occur in an adhesive bond case. The result presented in this section is a step towards that by measuring the fingerprint of a 'perfect' adhesive bond. It is likely that the fingerprint of a kissing adhesive bond will be some combination of the response of the good adhesive interface and the contacting aluminium surfaces observed in Chapter 7.

In order to avoid thin-film interference effects it is preferable to construct an adhesive layer that is on a different length scale from the ultrasonic wavelengths being used. In epoxy resin a 5 MHz shear wave has a wavelength around 0.16 mm, as does the 10 MHz longitudinal wave that will be produced by the mixing. Maximal reflection occurs when the thickness is a quarter of the wavelength, 0.04 mm, and also at half wavelength intervals larger than that, i.e. 0.12 mm, 0.2 mm and so on. Yan's research into the topic experimentally showed that in order to reduce this periodic variation in transmission coefficient below a factor of two the adhesive layer should be greater than four wavelengths thick (33). This would be 0.64 mm in the 5 MHz case.

Since it was not practical to produce an adhesive interface thinner than 0.04 mm it was decided to use a thick adhesive layer. For this test the same 30 mm thick plates were used from the CAN testing, bonded with 3M Scotch-weld Epoxy DP490. Spacers were used to create a bond that was 0.86 mm thick. The interface was conventionally inspected using a 10 MHz array. Imaging the interface using the Total Focusing Method (TFM) did not indicate any flaws in the bond line.

Figure 9.3 shows the resulting fingerprint of the adhesively bonded aluminium sample. It is quite similar to the interface fingerprints in Chapter 7 in terms of overall distribution. However, it has many more features such as two lines of increased scattering at $a = 0.82$ and $a = 0.96$, and a clear band of mixing about $5^\circ$ above the resonance line. The features in the frequency ratio dimension are likely due to thin-film interference effects as similar behaviour was observed in the thin aluminium plate test. The band at around $\phi = 118^\circ$ may be due to bulk mixing though it does not match with the expected behaviour of the aluminium. Epoxy resin has a velocity ratio, $c$, of 0.53, compared with 0.50 of the aluminium, this results in a resonant interaction angle at $a = 1$ of $116^\circ$. This matches well with the fingerprint showing that this band is likely due to bulk mixing in the epoxy resin.

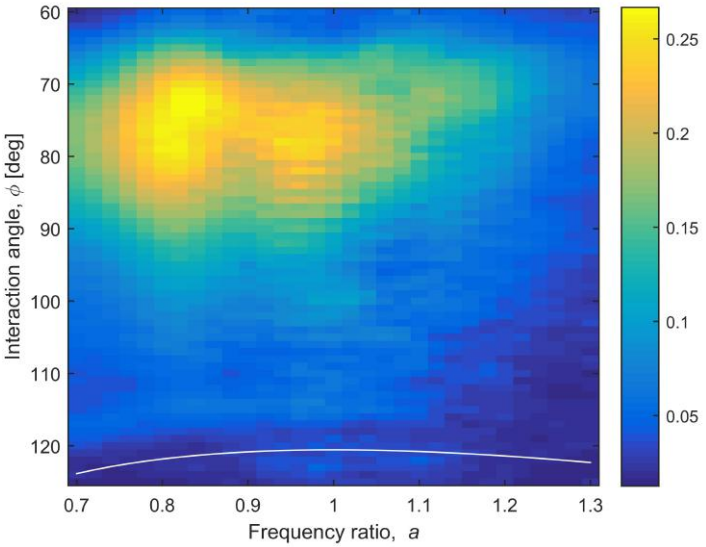


**Figure 9.3:** Fingerprint of a good adhesively bonded interface measured with a reference input frequency of 5 MHz. White line indicates the resonant conditions of bulk mixing in aluminium.

It is interesting that the overall pattern is similar to that of the previously observed kissing interfaces. This could make differentiation between good adhesive interfaces and poor ones difficult. Further testing of kissing bonds in adhesive interfaces would be required to confirm this. There is other information contained within the fingerprint though that could be valuable, the spacing between the $a = 0.82$ and $a = 0.96$ lines is likely an indicator of interface thickness, and the band at $\phi = 118^\circ$ relates to the mechanical properties of the adhesive. In this case it appears as though the bulk mixing might be a useful amplitude reference for the interface mixing at smaller interaction angles, which could be key to reliable detection of a small increase in scattering at around $\phi = 80^\circ$ if a kissing bond were present.

### 9.3.1 Inter-probe delay

During the testing of the adhesively bonded sample it was noticed that it inter-probe delay behaviour was notably different from the kissing interface sample. The delay was investigated in Chapter 7 where it was mentioned that the kissing interface sample gave a different response from the solid block. The solid block produced no fluctuations, while the interface sample oscillated greatly at $\phi = 70^\circ$, $a = 0.9$. The results for the adhesively bonded sample are shown for comparison in Figure 9.4.

It can be seen that at $\phi = 70^\circ$, $a = 0.9$ some small oscillations occur, and at $a = 1.0$ they are larger. This makes sense because at $a = 1.0$ the interference points occur at

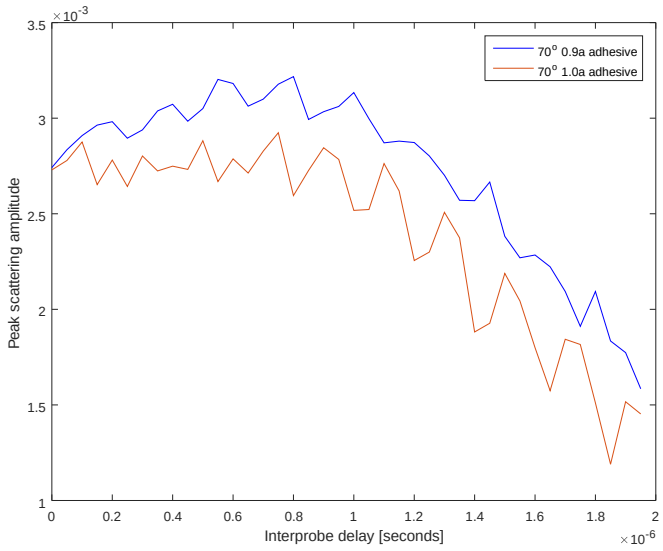


**Figure 9.4:** Peak scattering amplitude as the delay between the input pulses was varied for the adhesive sample. Both tests were done with $\phi = 70°$, but one was at $a = 0.9$ and the other $a = 1.0$.

the same position on the interface throughout the pulse duration, enhancing the position sensitivity. The fact that these oscillation are smaller than those of the kissing interface suggests that the adhesive interface has more uniform properties than the kissing one, as would be expected. If kissing defects in adhesive bond lines are uneven on a 0.1-1 mm length scale then a method based upon these oscillations could potentially detect the difference between a good bond and a kissing bond.

## 9.4 Possible solutions

Many difficulties for the application of non-collinear mixing for the detection of kissing bonds in composites have been discussed above. The thickness of the samples was the first major obstacle that was identified, with the conclusion that the interaction volume must fit within the sample to avoid surface mixing effects. This could be solved in future experimental tests by using focused input waves that result in much smaller interaction volumes. Either focused probes or arrays would allow this. The use of smaller interaction volumes could be beneficial to kissing bond detection in general due to the scaling effects in comparison with bulk mixing. Bulk mixing is proportional to the cube of the interaction radius because it is a volumetric effect, while it is believed that the CAN mixing is proportional to the square of the radius. Testing is required to confirm this behaviour.

The increased amplitude that would result from focused beams may also be useful in overcoming problems with attenuation in composites. Another way to counter the attenuation is to use lower frequencies. Tests were done for the bulk mixing and surface mixing that showed cubic frequency relationships with scattering amplitudes, but these tests were not done for CAN mixing. If the CAN mixing amplitude also has a cubic relationship with frequency this could be a problem but is worth future investigation.

Use of different frequencies, particularly lower ones might also be useful for reducing the thin-film interference effects due to adhesive bond lines because it would mean that it is possible to make the adhesive layer much smaller than the wavelength. It also might be possible to model the interference effect and create a method for removing its impact on the fingerprint if the bond line thickness is known, or perhaps measure the bond thickness from the fingerprint pattern.

Alternatively it could be that the detection of kissing bonds is best done not by analysis of the fingerprint but rather by detection of interface roughness as demonstrated through the inter-probe delay testing. This might produce a method that is robust to amplitude changes across the parameter space by only requiring measurement at one combination of input parameters. Testing in Chapter 7 suggested that there might be some interaction cases that produce a greater sensitivity to this variation than others. It could be that the particular conditions that create the largest signal variation may differ according to the defect type. Much more investigation into this behaviour is required.

In summary, none of the difficulties appear to be insurmountable, and a better understanding of a few key areas as detailed above might provide a route for the method's implementation in CFRP bond line inspection.

# Chapter 10

# Conclusions

The goal of this work was to develop an NDT method for detection of kissing bonds in composite structures. Nonlinear ultrasonics was identified as a promising way to achieve this but it was found that there was much more to be understood before it could be used to reliably detect kissing bonds. In recent years non-collinear mixing has received attention for its potential in detection of closed cracks with contributions from Zhang, Demchenko, and Blanloeuil et al. with much of the work being focused on the modelling and very little on exploring the interaction angle and frequency ratio parameter space. Therefore, this research set out to fill in the gaps in our understanding, and resulted in the following areas of improvement.

## 10.1 Key achievements

- Experimental measurement of bulk mixing over a wide range of interaction angles and frequency ratios, greatly improving the knowledge of mixing at non-resonant conditions.
- Discovery of a new type of non-collinear mixing due to the interface between a nonlinear fluid and a solid, studied both experimentally and numerically.
- Experimental measurement of mixing at a kissing interface over a large parameter space, confirming the modelled predictions of other authors and demonstrating that the response of real contacting surfaces is far more complicated than suggested by those models.

Within each of these areas many insights were made which will briefly be discussed now. In regards to bulk mixing it was found that the model developed by Potter predicted secondary peaks in the fingerprints but these were not observed experimentally when the interaction volume was fully contained within the solid. The method showed little sensitivity to fatigue levels in aluminium and steel, the only feature of the fingerprint which appeared to correlate were the interaction angles of the secondary peaks. Since these secondary peaks were found to be due to surface effects, which are discussed in the next paragraph, it is likely that the shear-shear bulk mixing is not responsive, in terms of changes to the fingerprint pattern, to the type of fatigue tested. There may be some overall amplitude relationship but this is not a reliable metric for industrial use so was not focused on in this work. It should be remembered that only one interaction case was investigated in this research and that others are dependent upon other TOECs.

The mixing from the water-solid boundary was a vital discovery in this work. It explained why the early measurements of thin CFRP samples were not informative

and guided the research that followed towards thicker samples. This type of mixing has not been reported in the literature. Experimental testing showed that the scattered signal from the interface was produced at a different angle from the classical momentum conserving predictions and an analytic model was developed to better predict this angle, referred to in this work as the geometric model. An FE model was made, using COMSOL, that could replicate the mixing behaviour. It showed that for this effect to occur the water must be considered as nonlinear, using the Westervelt acoustic wave equation. Inclusion of nonlinear solid mechanics did not alter the surface mixing behaviour so it could be turned off to increase the modelling speed. Therefore, the fatigue related behaviour discussed earlier is not directly due to changes in surface mixing. It is more likely that changes in the fingerprint patterns were due to changes in linear elastic behaviour (e.g. velocity alteration).

Improvement of interface mixing understanding was the focus of this research but the previous topics occupied a larger fraction of the thesis due to the important foundation they provide. Interface mixing was observed to occur over a large range of interaction angles, obstructing the use of bulk mixing as a constant reference for the CAN mixing. This concept had potential for improving the robustness of kissing bond detection. It might still be possible though if a reference can be taken at a region of the structure with no defects present but this has more variables than being able to take a reference from the fingerprint of the bond line itself. The parametric behaviour matched well with Blanloeuils modelling in terms of the main feature. It was observed that some of the fingerprints contained secondary peaks not accounted for by bulk mixing, and the shape of these features was altered by the changing of interface loading. This combined with the variety of patterns observed at different inspection points on the interface indicated that the mixing behaviour is more complex than just a loading dependency.

As a results of the observed complexity a hypothesis was developed to explain how the secondary features in the fingerprints could be formed when they are not predicted by current theory. It was suggested that it is due to the interference pattern of the input beams on the interface only being destructive at fixed lines when a frequency ratio close to one is used. These lines are where the majority of mixing signal generation occurs and their position is altered as interaction angle and frequency ratio are changed. Thus, at each point in a fingerprint different subsections of the interface are being probed so it is not truly representative of the entire interaction area. If shown to be correct this hypothesis has major impacts in the methodology that would be involved in reliably capturing interface measurements.

The testing of different interface surface finishes was negatively impacted by problems

in the manufacture of surfaces. Despite this many conclusions could be drawn from the highly contrasting behaviour of the rough and polished interfaces. The rougher interface produced fingerprints with much less prominent secondary features, perhaps this could be used in a method to detect the roughness of a kissing bond. The loading responses of the two interfaces also differed substantially. The scattering from the polished interface initially increased in amplitude as load was increased but then dropped. The rough interface was probably loaded to higher levels than the polished interface due to the manufacturing issues however the amplitude of scattering from it always increased with increasing bolt torque. This behaviour is different from the modelling predictions of other authors which can only model perfectly flat surfaces in the kissing bonds. It is reasonable to assume that at some loading level the rough interface sample would have reduced in scattered amplitude but this must occur at a significantly higher load than predicted for completely smooth surfaces. Both interfaces displayed increased secondary features as loading was increased. This behaviour might be useful for detecting kissing bond loading, though the many other factors involved could make this unreliable.

Measurement of the adhesively bonded aluminium blocks showed that a good bond produces a fingerprint that is similar to that of a kissing bond. This could make differentiation between the two cases difficult. A possible solution to this could be the exploitation of the sampling line effect, with a good bond having more uniform properties than a kissing bond.

The previous chapter detailed the challenges involved in the application of non-collinear mixing to composites. It is certainly more difficult than the case of kissing bonds in diffusion bonded or welded metals, but none of the challenges appeared to be impossible to overcome. Many potential solutions were suggested there, most of which relate to the future work that is proposed below.

## 10.2 Future work

During the course of this research many avenues of further exploration have become apparent. Generally these were noted in the relevant chapters but a summary is provided below.

A rigorous investigation into the frequency ratio sensitivity of the various mixing types could be insightful. This might be achieved by adjusting both input frequencies while keeping the output frequency constant, combined with measurement of the frequency

response of the input transducers. Related to this, the overall frequency sensitivity should also be tested (i.e. by alteration of the output frequency). Tests involving many approximations were conducted in this work but by using carefully calibrated transducers more certain results could be obtained. In particular the frequency response of the interface mixing should be measured as it is currently not reported.

A simple improvement to the experimental setup could be to change one of the input transducers to a narrow band one with higher output power (since most mixing scales with the product of the input beam amplitudes), although the effect this asymmetry of beam amplitude will have on interface mixing is not yet known. Another concept to investigate is the production of further scattered beams from the kissing interface that was predicted by the geometric modelling. This could be as easy as using a small interaction angle and positioning the detection array off to the side (see Figure 8.5 (b)). FE modelling could also be used for this testing. Initial further testing of scattering from a kissing interface would likely best be done using an improved set of test blocks with flatter surfaces to avoid the difficulties experienced in this work. This improved sample would be useful for validation of the behaviours presented in this thesis.

The above suggestions were fairly basic in nature, the following ones involve greater changes in terms of the applications of the experiment but only minor changes to the apparatus. Testing of other interaction modes would certainly be useful. This refers to both bulk mixing modes, which might improve sensitivity to fatigue for example, and to interface mixing cases. The interface mixing investigated in this work was related to stresses normal to interface producing a longitudinal wave, but the production of shear waves may also be possible. Understanding the many modes would be useful for inspection in cases where it is not possible to avoid multiple beam types overlapping.

Testing of imperfect diffusion welded bonds is of interest since they can be harder to detect with conventional methods (than the crude compressively loaded blocks used in this work), demonstrating the potential of this NDT method in a more realistic scenario. Also measurements of bulk mixing in solid CFRP samples would be useful for future development of non-collinear mixing in composites. This testing would likely require the use of focused input transducers to reduce the interaction volume size and allow thin samples to be inspected without the obstruction of surface effects. Testing of adhesively bonded aluminium suggested that bulk mixing was occurring in the adhesive layer, perhaps two resonant bands will occur in CFRP due to the presence of two different materials. Related to this is the measurement of scattering in the reflection direction from a CFRP sample with a kissing interface. This might allow the bulk mixing signal to be separated from the interface signal making interpretation of the fingerprints easier.

In the future non-collinear mixing could be enhanced with the use of arrays for the input beams. Currently the hardware to achieve this is very expensive since it requires arbitrary pulse generation combined with variable delays for each channel. This technology would allow for the input beams to be focused at any depth within the sample which might be key for industrial application of this NDT method. The electronic steering of the beams also allows for more precise and faster changes in interaction angle. The improved precision might allow for detection of subtle changes in peak mixing conditions which were identified in this work as possible indicators of interface loading level. Modelling of bulk mixing suggested the potential for inversion of the fingerprint shape into the material's linear and higher order elastic properties if the experimental precision is good enough. The used of arrays also lends itself to the investigation of the interface sampling lines hypothesis because the interaction area can be accurately adjusted in terms of size, position, and relative phase of the input beams.

Finally, there are a couple of areas of theory that could be developed to improve the overall understanding of non-collinear mixing. The first is the surface mixing effect. This work identified its existence and some of its properties but could say little about the fundamental mechanism of the nonlinearity. The other is the improvement of the bulk mixing analytic model. Adding non-uniform beam intensity would likely improve accuracy of predictions. By combining this with the real-type volume even more accurate predictions could be made of bulk mixing for the interaction angle-frequency ratio parameter space.

To conclude, there is still much research to be done on non-collinear mixing in general, and its use as a method of detecting kissing bonds. However, the author feels that the desired understanding is well within reach, not requiring any great leaps in methodology or technology. Many of the points mentioned above are only applications of the current technique to new situations. It appears quite possible that an experimental arrangement involving the use of focused input beams, detecting the reflected scattered wave could be a practical solution for achieving detection of kissing bonds in composites in the near term.

# Chapter 11

# Appendix A

## 11.1 Convergence testing of near-surface model

The results present here are to accompany the work presented in Chapter 6 on the FE modelling of non-collinear mixing near the surface of a solid.

### 11.1.1 Bulk mixing

Testing of the COMSOL FE model with standard pressure acoustics for the water domain and hyperelasticity for the solid was conducted for a 1 MHz reference input frequency at $\phi = 120°$, and $a = 1.2$. Plots of the processed time traces at various mesh sizes and time step lengths are shown in Figures 11.1 and 11.2.

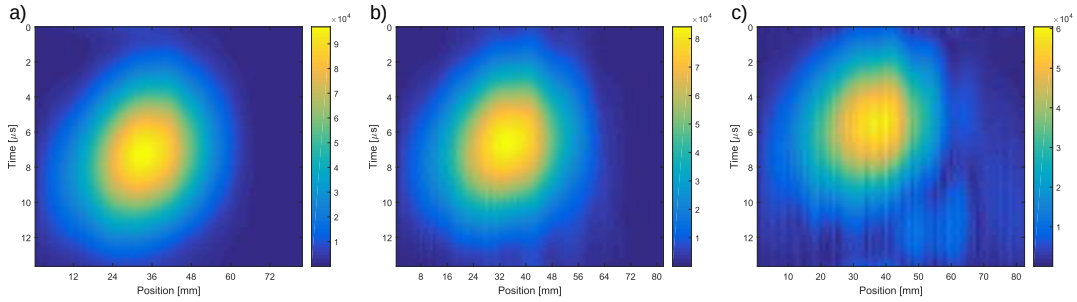


**Figure 11.1:** 1 MHz FE processed time traces, all with a time step of 20 ns. a) Mesh size of 0.6 mm, b) 0.8 mm, c) 1.0 mm. The x-axis is the position on the bottom edge of the sample where the readings were taken (82 mm wide in total) and the y-axis is a time window centred on the expected arrival time, the zero is not a true zero.

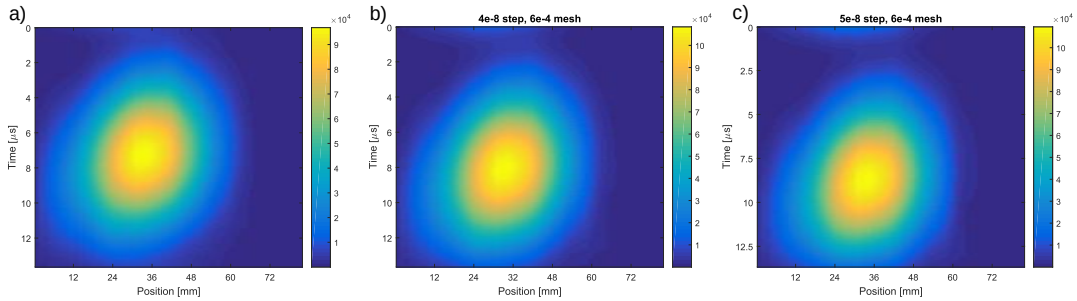


**Figure 11.2:** 1 MHz FE processed time traces, all had a mesh size of 0.6 mm. a) Time step size of 20 ns, b) 40 ns, c) 50 ns.

The 0.6 mm mesh resulted in a clean mixing response in Figure 11.1 part a. This does not necessarily mean that it is fully converged but was a good enough indication for preliminary testing. More rigorous testing is conducted for the 2 MHz modelling and these results helped guide the requirements for the more detailed testing at 2 MHz.

Figure 11.2 shows that altering the time step did not affect the amplitude much but it did change the arrival time. The lack of impact is partly due to the solver used (generalised

alpha) which takes smaller time steps if it detects that they might be required. The time step specified in this case becomes the maximum size that can be used. In later testing this setting was changed from 'strict' to 'manual' which uses completely fixed time steps. It is difficult to say from this data what time step size is optimal, more accurate convergence testing is conducted for the later modelling using fixed time steps.

### 11.1.2 Near surface mixing

Presented here are the convergence testing results for the propagation a wave through a 20 mm length of nonlinear water. More detail on the configuration of this test is in Section 6.4.1 of Chapter 6. Table 11.1 shows the resulting frequency components extracted from the motion of the central node on the short side opposite the source.

**Table 11.1:** Modelled frequency components of a 1 MHz pulse after 0.2 m of propagation through water. The time step length and mesh size of the model are shown as well as the time taken to run. $L_E$ is the maximum element length, $F_1$, $F_2$, $F_3$, and $F_4$ are the magnitudes of each harmonic, $F_1$ being the fundamental, 1 MHz.

| Step (ns) | $L_E$ (mm) | Time taken (mins) | $F_1(10^8)$ | $F_2(10^7)$ | $F_3(10^6)$ | $F_4(10^5)$ |
|---|---|---|---|---|---|---|
| 17 | 0.12 | 42 | 1.65 | 1.24 | 1.53 | 2.15 |
| 34 | 0.24 | 10 | 1.65 | 1.24 | 1.53 | 2.15 |
| 67 | 0.48 | 4 | 1.65 | 1.24 | 1.20 | 5.50 |
| 133 | 0.96 | 1.5 | 1.63 | 0.60 | - | - |
| 83 | 0.63 | 2.5 | 1.63 | 1.12 | 0.48 | - |
| 33 | 0.60 | 2.5 | 1.64 | 1.21 | 1.12 | - |
| 20 | 0.60 | 2.5 | 1.64 | 1.22 | 1.15 | - |

It can be seen from the data in Table 11.1 that if the aim is to resolve the second harmonic accurately a mesh size of around 0.6 mm or less, and step size of 67 ns or less is required. In the above testing the step size was not critical due to the solver automatically adjusting to smaller steps when required. If the maximum step size (the one defined in the table) were not small enough though instabilities were more likely. These either crashed the solver or resulted in increased solution times.

### 11.1.3 Final model

The results of convergence testing of the complete nonlinear water and solid model are shown in Figure 11.3. In this plot a 'mesh and step factor' of 1 indicates the values that were used for the final results collection, presented at the end of Chapter 6, and corresponds to values of 0.15 mm maximal element size in the high resolution

water region and 0.3 mm in the solid and lower resolution areas of the water, and a minimum time step of 0.55 ns. The fixed ratio of mesh sizes was selected based upon the relative wavelengths of the longitudinal waves in water and the shear waves and sum frequency longitudinal wave in the solid. The time step length was selected to be just small enough to achieve stability. The fixed ratio between the element lengths and time steps maintained stability for all resolutions tested.

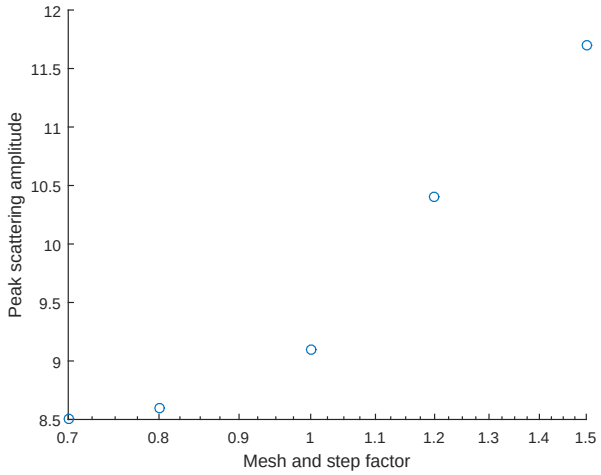


**Figure 11.3:** Amplitude of the nonlinear scattered wave with an interaction depth of 0 mm at $\phi = 90^\circ$ using the combined nonlinear water and nonlinear solid domains. The time steps and element lengths were kept at a fixed ratio and a value of 1 on the x-axis relates to 0.15 mm element lengths in the water, 0.3 mm in the solid, and time steps of 0.55 ns. A logarithmic scale has been used on the x-axis to make it representative of the fractional relation between measurement points.

The testing was conducted at 0 mm interaction depth and 90° to replicate conditions that experimentally produced a strong surface mixing response. Figure 11.3 was plotted with a logarithmic x-axis in order to present the measurement points in a fractionally relative way. The 12.5% reduction in element lengths and time steps in going from the 0.8 to 0.7 factor resulted in 1.2% decrease in signal amplitude indicated a plateauing of the trend. Further inspection of the convergence behaviour to even finer resolutions was not possible as the 0.7 test already required nine days of computation. The factor 1 test appears to be about 10% larger than the asymptote and was selected as the resolution that strikes a balance between accuracy and computation time.

# Chapter 12

# Appendix B

## 12.1 3rd order elastic energy model interaction volume type selection

In Chapter 4 the various interaction volume types used by Jack Potter in the analytic bulk mixing model were introduced. In this appendix some further investigation into the differences in behaviour between the volumes is presented, including analysis of the amplitude responses that result from changes in frequency and interaction volume size.

The cubic and cylindrical cases in the model differ from the 'real' case because they are only evaluated in 2D, i.e. they are just integrals of a square and a circle respectively. To apply them to 3D the integrals should be multiplied by a depth factor but this was not done in the following results due to an oversight. This difference should be remembered when comparing with results from the real-type interaction volume. For each of these volume types the size is defined by a 'radius' parameter. In the cubic case each edge of the square is two times this radius long, for the cylindrical volume the radius is that of the circle, and for the 'real' case it is the radius of the cylindrical input beams.

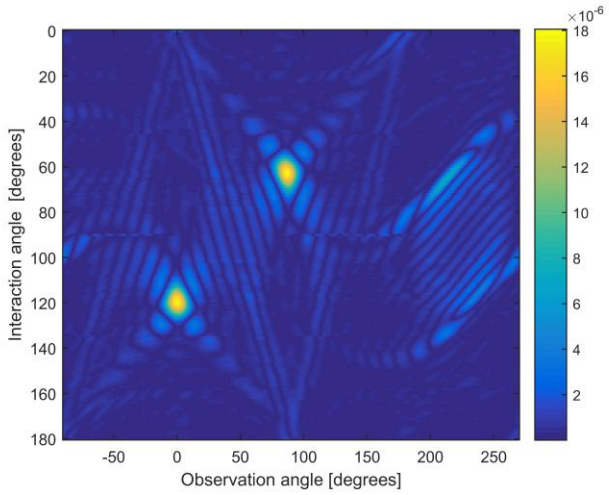


**Figure 12.1:** Geometric directional amplitude term for solid aluminium at a frequency ratio, $a$, of 1 with the 'real' type volume.

As discussed in the modelling methods chapter, different interaction volume approximations lead to different geometric directional amplitude functions. The cubic approximation gives an analytic form resulting in it being the quickest volume type to calculate. The cylindrical approximation requires numerical integration over one dimension and the 'real' approximation requires summation over three dimensions resulting in much longer calculation times than the other two methods. An example of $\chi(\theta)$ over the complete range of interaction and observation angles is shown in Figure 12.1. In this example the 'real' volume integral was used and it results in quite

a complex pattern compared with the other volume types, these will be shown later. There is a region of mixing at the expected classical resonant case $\phi = 120°$ but there is also another at $\phi = 60°$. This produces a signal perpendicular to the expected scattering direction but can be rationalised as the scattering that would be caused if one of the beams were traveling in the opposite direction. Therefore this is not a mixing case that would be expected experimentally due to momentum conservation. In order to select which volume to use for the rest of the modelling the $\chi(\theta)$ terms have been calculated for each volume type for a particular set of input parameters, this can then be compared with an experimental example.

The parameters used for the calculation of $\chi(\theta)$ in Figure 12.2 were $E = 70$ GPa, $v = 0.33$, $\rho = 2780$ kg.m$^{-3}$, $a = 1$, $\omega_1 = 5$ MHz, and a 'radius' term of 20 mm. Also shown is similar experimentally measured data for an interaction 14 mm deep in the solid 60 mm thick aluminium sample with the same $a$ and $\omega_1$. The experimental value is the result of the combination of both the geometric directional term, the nonlinear weighting term, and other experimental factors such as variable array angle sensitivity. The nonlinear term, as shown in Chapter 5 in Figure 5.2, varies gradually over the interaction angle and observation angle range being studied here so it will not have a major effect on the features visible within Figure 12.2. The experimental factors are also quite limited in their impact. The effect of these factors as interaction angle is varied is discussed in Section 5.2.3 in Figure 5.4 (b). The experimental values were created using an average over the predicted time of arrival window of each measurement in order to the improve signal to noise ratio.

It can be seen in Figure 12.2 that the cubic and 'real' volume types produce quite similar results, creating a diamond shaped central lobe with further lobes produced along the diagonals. The cylindrical volume however created a rounder set of features. The cubic pattern is asymmetric because the interaction volume is not symmetric about the direction of scattering axis (except for when the interaction angle is 90°). It is difficult to tell from the experimental data which matches more closely. There is some shifting of the distribution towards more positive observation angles as the interaction angle is increased. This is probably due to errors in the input angle of the transducers as discussed in Chapter 3 and in Section 5.3.4 of Chapter 5 in regards to scattering angle at non-resonant conditions. With this in mind the central lobe in the experimental data is actually quite circular, more like the real or cylindrical volumes. One secondary lobe is possibly visible at around $\phi = 105°$, observation angle $= 5°$. This appears in a diagonal position but is not really enough information to match it to a particular approximate volume type. It would be expected that the experimental side lobes would be weaker than in the model since the intensity profile of the input beam in the model is uniform

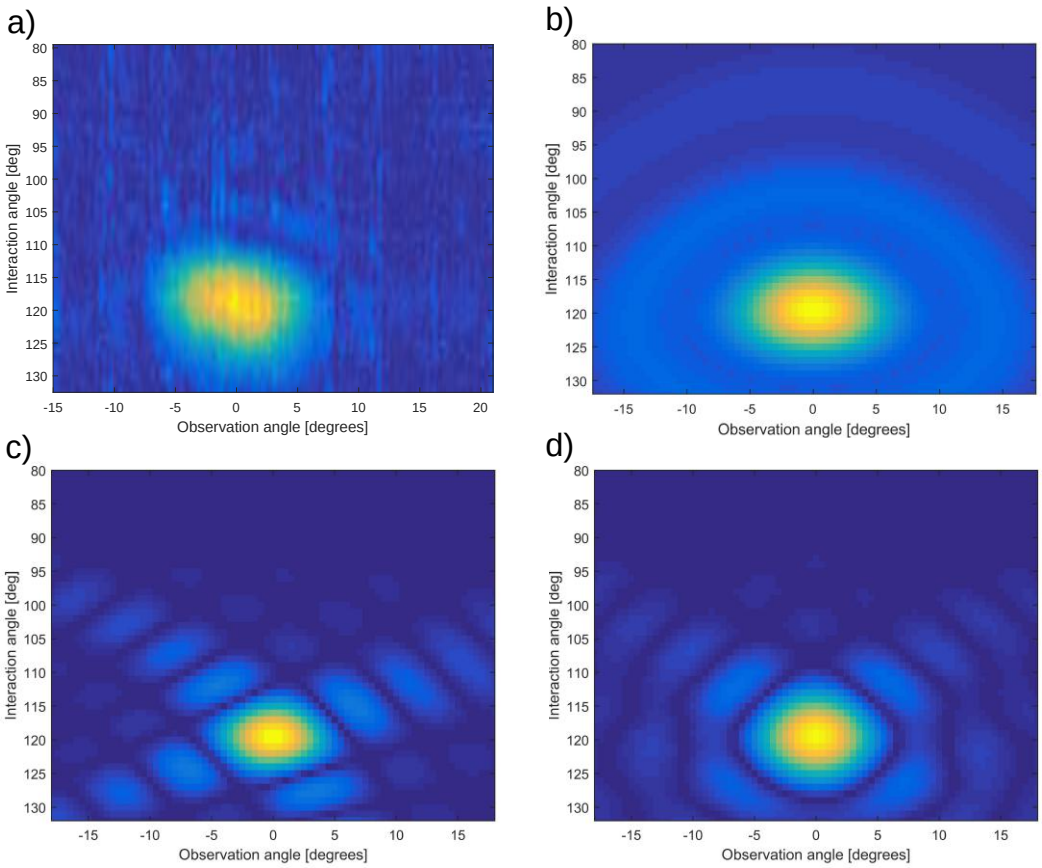


**Figure 12.2:** Angular distribution of scattering in solid aluminium for a range of interaction angles with $a = 1$. a) is an experimentally measured example without any correction for experimental factors. b), c), and d) are only the geometrical term, $\chi(\theta)$, in the classical mixing model. b) is the cylindrical interaction volume type, c) is cubic, and d) is the 'real' type.

but in the experiment they would be more Gaussian, resulting in smaller side bands in the Fourier transform of the spatial distribution.

The above comparison was inconclusive, but to some extent the difference between the patterns produced will have only a small impact on the resulting fingerprint formed from them. This is because the value used for the fingerprint is a summation across a range of observation angles, typically set wide enough to capture the entire main lobe. The way that a value is extracted from the raw data is explained in more detail in Chapter 3. Some slight differences in how the window captures the secondary mixing lobes at conditions away from resonance would be expected but the summation reduces the sensitivity to the exact angular distribution pattern. An example of the smoothing effect of summation is shown in Figure 12.3. Other methods for acquiring a 'scattering amplitude' metric for the fingerprint could result in more or less sensitivity to the angular scattering distribution. Future research should consider if this sensitivity is desirable or not for the selected use case. In the following modelled fingerprints a simple maximal amplitude value is taken without any summation.

### 12.1.1 Impact of input beam width and reference frequency

The analysis so far has used a fixed input beam width, and reference beam frequency. Experimentally these factors will not be constant so it is useful to understand how the geometric weighting term responds to them. The experimental work mainly focuses on the shape of the fingerprints produced but in some cases amplitude is of interest, such as when comparing the overall signal level of fingerprints at different reference input frequencies. Therefore, this section will include amplitude analysis as well as shape.

In Figure 12.3 the effects of interaction radius and frequency are shown for a few examples in the cylindrical volume case. Also included in the right column of this figure is a summation over all observation angles. This relates to the discussion at the end of the previous section about the significance of the size of aperture used to average over for the purposes of extracting a scattering value. The model did not produce a valid result (division by zero) when $\phi = 108^\circ$ and $\theta = 180^\circ$ so there is a gap in the summation for this case. It can be seen that the summation smooths out the off-resonance lobes in the geometric weighting term but it does not remove them completely. This figure was shown previously in Chapter 5 but is also shown here for further discussion.

Figure 12.3 shows that doubling the frequency while halving the interaction radius results in the same angular distribution being formed, as might be expected. The peak amplitude of the geometric weighting is insensitive to variation of frequency, but the

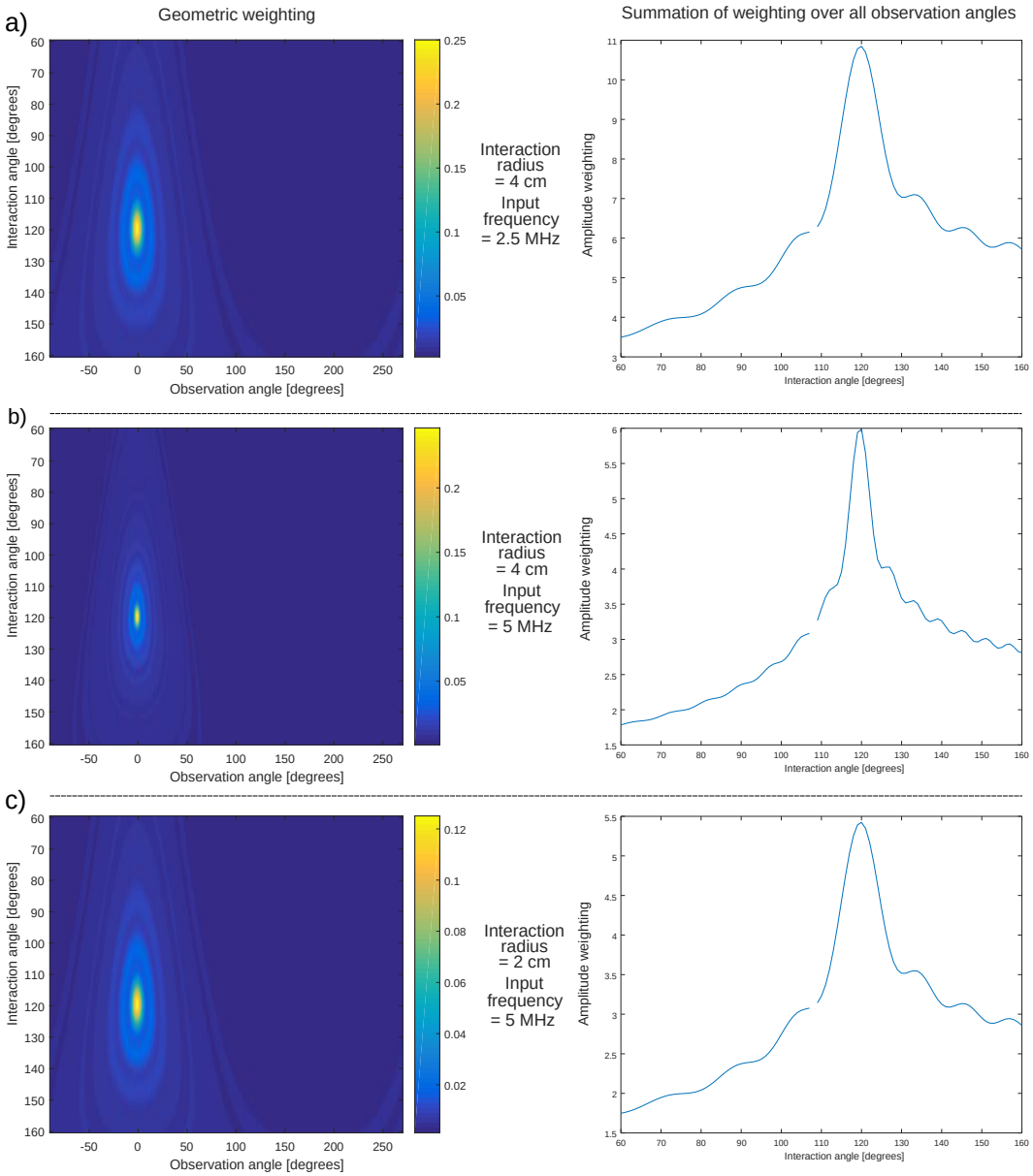


**Figure 12.3:** On the left are similar plots to Figure 12.2 but for a wider range of interaction and observation angles. All of the data is from modelling of the $\chi(\theta)$ term for a cylindrical volume. On the right are the results of summation across all observation angles, $\theta$, for $\chi(\theta)$. a) Is the distribution created with an interaction radius of 4 cm and input frequency of 2.5 MHz. $a = 1$ was used for all these examples. b) 4 cm, $\omega_1 = 5$ MHz. c) 2 cm, $\omega_1 = 5$ MHz.

summation plots showed that overall less scattering was predicted when frequency was increased. On the other hand, the radius was directly proportional to the peak scattering amplitude, but had very little affect on the result after summation. It makes sense that increasing the radius of interaction causes the directivity of the output beam to increase, thus increasing the peak value but not altering the total amount of scattering. The frequency related behaviour is less intuitive, particularly the overall reduction in amplitude as frequency is increased. These tests were repeated for the other volume types for comparison. It was noted that the frequency related behaviour of the cylindrical volume was the same as the cubic interaction volume but in the 'real' volume case frequency was independent of both the peak amplitude and the summed amplitude.

In terms of the radius parameter the cubic and 'real' volumes also presented different amplitude behaviours. The cubic form gives a peak amplitude that is directly proportional to the square of the radius, and a sum that is linearly related. The 'real' volume gave relationships of radius cubed, and radius squared respectively. The 'real' volume has this extra power of radius due to the volume integral being evaluated over a finite depth, compared with the other two volume types where only a 2D interaction area is considered. Neither of these relationships agree with the author's expectation that the summed amplitude (total scattering amount) of the geometric weighting should not change with interaction volume size, but would be expected to alter directivity and thus peak amplitude. This suggests there is a mistake in at least two of the volume types in relation to the radius terms and that the cylindrical form is most likely to be correct.

Originally the model, written by Potter, was intended to model bulk non-collinear mixing away from the resonance conditions, producing fingerprints, and to observe how they responded to different linear and third order elastic terms. The frequency and interaction radius related behaviour was not of high importance to this work so were not checked. Many corrections were made by the author to the model but as can be seen from the multiple flaws discussed above there is more work to be done to make all the different interaction volume types accurate. Since the results of this model are not critical to the ultimate aim of kissing bond detection further improvement of this model was beyond the scope of this work. Below is summarised the problems and what implications they have on the results. This information should be helpful for future researchers attempting to fix the model if results that are accurate in terms of radius and frequency are required.

1. Frequency response differs between cubic/cylindrical and 'real' volume types. It is unclear which of the two responses would be expected; it might appear logical that increasing frequency should only increase directivity and thus peak

amplitude, and not affect summed scattering amplitude. None of the volume types matched this behaviour exactly so it is unclear if they are all incorrect or the expectations are wrong. In light of this the frequency related trends from the model are currently not reliable for any volume type.

2. All three interaction volumes gave different radius related behaviour. The cylindrical one matched with expectations; higher peak amplitude with larger volume but no change in summed amplitude so this volume type is probably the most likely to be correct in relation to the radius term.

Overall the cylindrical volume appeared to perform closest to the author's expectations so it was used in the modelling presented in the main body of work. It also had a good balance of accuracy and speed, running considerably faster than the 'real' volume type.

# References


[1] R. Adams, P. Cawley, A review of defect types and nondestructive testing techniques for composites and bonded joints, NDT international 21 (4) (1988) 208–222.

[2] C. Brotherhood, B. Drinkwater, S. Dixon, The detectability of kissing bonds in adhesive joints using ultrasonic techniques, Ultrasonics 41 (7) (2003) 521–529.

[3] K.-A. Van Den Abeele, P. A. Johnson, A. Sutin, Nonlinear elastic wave spectroscopy (news) techniques to discern material damage, part i: nonlinear wave modulation spectroscopy (nwms), Journal of Research in Nondestructive Evaluation 12 (1) (2000) 17–30.

[4] P. Blanloeuil, A. Meziane, C. Bacon, 2d finite element modeling of the non-collinear mixing method for detection and characterization of closed cracks, NDT & E International 76 (2015) 43–51.

[5] P. Blanloeuil, A. Meziane, C. Bacon, Numerical study of nonlinear interaction between a crack and elastic waves under an oblique incidence, Wave Motion 51 (3) (2014) 425–437.

[6] P. Blanloeuil, L. Rose, J. Guinto, M. Veidt, C. Wang, Closed crack imaging using time reversal method based on fundamental and second harmonic scattering, Wave Motion 66 (2016) 156–176.

[7] M. Dunn, A. Carcione, P. Blanloeuil, M. Veidt, Critical aspects of experimental damage detection methodologies using nonlinear vibro-ultrasonics, Procedia Engineering 188 (2017) 133–140.

[8] F. R. Rollins Jr, L. H. Taylor, P. H. Todd Jr, Ultrasonic study of three-phonon interactions. ii. experimental results, Physical Review 136 (3A) (1964) A597.

[9] V. Korneev, A. Demčenko, Possible second-order nonlinear interactions of plane waves in an elastic solid, The Journal of the Acoustical Society of America 135 (2) (2014) 591–598.

[10] Z. Zhang, P. B. Nagy, W. Hassan, Numerical study of material nonlinearity assessment based on non-collinear ultrasonic wave mixing, in: AIP Conference Proceedings, Vol. 1650, AIP, 2015, pp. 1599–1608.

[11] A. J. Croxford, P. D. Wilcox, B. W. Drinkwater, P. B. Nagy, The use of non-collinear mixing for nonlinear ultrasonic detection of plasticity and fatigue, The Journal of the Acoustical Society of America 126 (5) (2009) EL117–EL122.

[12] M. McGovern, W. Buttlar, H. Reis, Field estimation of oxidative ageing in asphalt concrete pavements using non-collinear wave mixing, Insight-Non-Destructive Testing and Condition Monitoring 57 (11) (2015) 625–634.

[13] F. R. Rollins Jr, Interaction of ultrasonic waves in solid media, Applied Physics Letters 2 (8) (1963) 147–148.

[14] Z. Zhang, P. B. Nagy, W. Hassan, Analytical and numerical modeling of non-collinear shear wave mixing at an imperfect interface, Ultrasonics 65 (2016) 165–176.

[15] P. Blanloeuil, A. Croxford, A. Meziane, Application of the noncollinear mixing method to an interface of contact, in: AIP Conference Proceedings, Vol. 1581, AIP, 2014, pp. 623–630.

[16] P. Blanloeuil, A. Meziane, A. Norris, C. Bacon, Analytical extension of finite element solution for computing the nonlinear far field of ultrasonic waves scattered by a closed crack, Wave Motion 66 (2016) 132–146.

[17] R. Ellwood, The effect of microstructure and fatigue on the acoustoelastic response of aerospace materials, Ph.D. thesis, University of Nottingham (2012).

[18] G. L. Jones, D. R. Kobett, Interaction of elastic waves in an isotropic solid, The Journal of the Acoustical society of America 35 (1) (1963) 5–10.

[19] I. Y. Solodov, Ultrasonics of non-linear contacts: propagation, reflection and nde-applications, Ultrasonics 36 (1-5) (1998) 383–390.

[20] G. Shui, Y.-s. Wang, P. Huang, J. Qu, Nonlinear ultrasonic evaluation of the fatigue damage of adhesive joints, NDT & E International 70 (2015) 9–15.

[21] P. B. Nagy, Ultrasonic detection of kissing bonds at adhesive interfaces, Journal of Adhesion Science and Technology 5 (8) (1991) 619–630.

[22] D. Yan, S. A. Neild, B. W. Drinkwater, Modelling and measurement of the nonlinear behaviour of kissing bonds in adhesive joints, NDT & E International 47 (2012) 18–25.

[23] R. C. Tighe, J. M. Dulieu-Barton, S. Quinn, Identification of kissing defects in adhesive bonds using infrared thermography, International Journal of Adhesion and Adhesives 64 (2016) 168–178.

[24] D. Jiao, J. L. Rose, An ultrasonic interface layer model for bond evaluation, Journal of Adhesion Science and Technology 5 (8) (1991) 631–646.

[25] P. B. Nagy, Ultrasonic classification of imperfect interfaces, Journal of Nondestructive evaluation 11 (3-4) (1992) 127–139.

[26] Y. Ohara, K. Takahashi, Y. Ino, K. Yamanaka, T. Tsuji, T. Mihara, High-selectivity imaging of closed cracks in a coarse-grained stainless steel by nonlinear ultrasonic phased array, NDT & E International 91 (2017) 139–147.

[27] C. Brotherhood, B. Drinkwater, F. Guild, The effect of compressive loading on the ultrasonic detectability of kissing bonds in adhesive joints, Journal of Nondestructive evaluation 21 (3) (2002) 95–104.

[28] G. Scarselli, F. Ciampa, F. Nicassio, M. Meo, Non-linear methods based on ultrasonic waves to analyse disbonds in single lap joints, Proceedings of the Institution of Mechanical Engineers, Part C: Journal of Mechanical Engineering Science 231 (16) (2017) 3066–3076.

[29] S. Delrue, M. Tabatabaeipour, J. Hettler, K. Van Den Abeele, Applying a nonlinear, pitch-catch, ultrasonic technique for the detection of kissing bonds in friction stir welds, Ultrasonics 68 (2016) 71–79.

[30] A. Demčenko, L. Mainini, V. Korneev, A study of the noncollinear ultrasonic-wave-mixing technique under imperfect resonance conditions, Ultrasonics 57 (2015) 179–189.

[31] M. Rahammer, W. Adebahr, R. Sachse, S. Gröninger, M. Kreutzbruck, Crack growth monitoring at cfrp bond lines, in: AIP Conference Proceedings, Vol. 1706, AIP Publishing, 2016, p. 120018.

[32] E. laboratories Inc, Electreleasetm (2018).
URL `http://www.eiclabs.com/ERhome.htm`

[33] D. Yan, The detectability of kissing bonds in adhesive joints using non-linear ultrasonic techniques, Ph.D. thesis, University of Bristol (2010).

[34] E. Escobar-Ruiz, A. Ruiz, W. Hassan, D. C. Wright, I. J. Collison, P. Cawley, P. B. Nagy, Non-linear ultrasonic nde of titanium diffusion bonds, Journal of Nondestructive Evaluation 33 (2) (2014) 187–195.

[35] Z. Zhang, P. B. Nagy, W. Hassan, Enhanced nonlinear inspection of diffusion bonded interfaces using reflected non-collinear ultrasonic wave mixing, in: AIP Conference Proceedings, Vol. 1706, AIP Publishing, 2016, p. 020023.

[36] K. Kawashima, R. Omote, T. Ito, H. Fujita, T. Shima, Nonlinear acoustic response through minute surface cracks: Fem simulation and experimentation, Ultrasonics 40 (1-8) (2002) 611–615.

[37] R. Parkins, P. Singh, Stress corrosion crack coalescence, Corrosion 46 (6) (1990) 485–499.

[38] J. L. Rose, Ultrasonic waves in solid media (2000).

[39] J. Potter, A. Croxford, P. Wilcox, Nonlinear ultrasonic phased array imaging, Physical review letters 113 (14) (2014) 144301.

[40] S. Haupert, G. Renaud, A. Schumm, Ultrasonic imaging of nonlinear scatterers buried in a medium, NDT & E International 87 (2017) 1–6.

[41] L. H. Taylor, F. R. Rollins Jr, Ultrasonic study of three-phonon interactions. i. theory, Physical Review 136 (3A) (1964) A591.

[42] K. Vine, P. Cawley, A. Kinloch, The correlation of non-destructive measurements and toughness changes in adhesive joints during environmental attack, The Journal of Adhesion 77 (2) (2001) 125–161.

[43] A. Pilarski, J. Rose, Ultrasonic oblique incidence for improved sensitivity in interface weakness determination, NDT international 21 (4) (1988) 241–246.

[44] P. N. Marty, N. Desai, J. Andersson, Ndt of kissing bond in aeronautical structures, in: 16th World Conference on NDT, 2004.

[45] E. Glushkov, N. Glushkova, M. Golub, A. Boström, Natural resonance frequencies, wave blocking, and energy localization in an elastic half-space and waveguide with a crack, The Journal of the Acoustical Society of America 119 (6) (2006) 3589–3598.

[46] B. De Ketelaere, P. Coucke, J. De Baerdemaeker, Eggshell crack detection based on acoustic resonance frequency analysis, Journal of Agricultural Engineering Research 76 (2) (2000) 157–163.

[47] J. M. Richardson, Harmonic generation at an unbonded interface-i. planar interface between semi-infinite elastic media, International Journal of Engineering Science 17 (1) (1979) 73–85.

[48] D. Broda, W. Staszewski, A. Martowicz, T. Uhl, V. Silberschmidt, Modelling of nonlinear crack–wave interactions for damage detection based on ultrasound-a review, Journal of Sound and Vibration 333 (4) (2014) 1097–1118.

[49] A. Moussatov, V. Gusev, B. Castagnede, Self-induced hysteresis for nonlinear acoustic waves in cracked material, Physical review letters 90 (12) (2003) 124301.

[50] M. A. Averkiou, D. N. Roundhill, J. E. Powers, A new imaging technique based on the nonlinear properties of tissues, in: Ultrasonics Symposium, 1997. Proceedings., 1997 IEEE, Vol. 2, IEEE, 1997, pp. 1561–1566.

[51] R. Minihold, R. Wagner, Measuring the nonlinearities of rf- amplifiers using signal generators and a spectrum analyzer application note (2014).
URL
https://cdn.rohde-schwarz.com/pws/dl_downloads/dl_application/application_notes/1ma71/1MA71_2e_amplifier_nonlin_meas.pdf

[52] C.-P. Liang, J.-h. Jong, W. E. Stark, J. R. East, Nonlinear amplifier effects in communications systems, IEEE Transactions on Microwave Theory and Techniques 47 (8) (1999) 1461–1466.

[53] D. S. Hughes, J. Kelly, Second-order elastic deformation of solids, Physical review 92 (5) (1953) 1145.

[54] O. Buck, W. Morris, J. M. Richardson, Acoustic harmonic generation at unbonded interfaces and fatigue cracks, Applied Physics Letters 33 (5) (1978) 371–373.

[55] S. Biwa, S. Nakajima, N. Ohno, On the acoustic nonlinearity of solid-solid contact with pressure-dependent interface stiffness, Journal of applied mechanics 71 (4) (2004) 508–515.

[56] S. Biwa, S. Yamaji, E. Matsumoto, Quantitative evaluation of harmonic generation at contacting interface, in: AIP Conference Proceedings, Vol. 1022, AIP, 2008, pp. 505–508.

[57] P. Blanloeuil, A. Meziane, A. N. Norris, M. Renier, M. Veidt, Numerical computation of the nonlinear far field of ultrasonic waves scattered by closed cracks of various orientations, in: EWSHM-7th European Workshop on Structural Health Monitoring, 2014.

[58] X. Gong, D. Zhang, J. Liu, H. Wang, Y. Yan, X. Xu, Study of acoustic nonlinearity parameter imaging methods in reflection mode for biological tissues, The Journal of the Acoustical Society of America 116 (3) (2004) 1819–1825.

[59] D. R. Daum, K. Hynynen, A 256-element ultrasonic phased array system for the treatment of large volumes of deep seated tissue, IEEE transactions on ultrasonics, ferroelectrics, and frequency control 46 (5) (1999) 1254–1268.

[60] J.-L. Thomas, M. A. Fink, Ultrasonic beam focusing through tissue inhomogeneities with a time reversal mirror: application to transskull therapy, IEEE Transactions on Ultrasonics, Ferroelectrics, and Frequency Control 43 (6) (1996) 1122–1129.

[61] J. Potter, P. Wilcox, A. Croxford, Diffuse field full matrix capture for near surface ultrasonic imaging, Ultrasonics 82 (2018) 44–48.

[62] P. A. Johnson, B. Zinszner, P. N. Rasolofosaon, Resonance and elastic nonlinear phenomena in rock, Journal of Geophysical Research: Solid Earth 101 (B5) (1996) 11553–11564.

[63] P. Johnson, A. Sutin, K. Van Den Abeele, Application of nonlinear wave modulation spectroscopy to discern material damage, Tech. rep., Los Alamos National Lab., NM (United States) (1999).

[64] M. Meo, U. Polimeno, G. Zumpano, Detecting damage in composite material using nonlinear elastic wave spectroscopy methods, Applied composite materials 15 (3) (2008) 115–126.

[65] A. Sutin, P. Johnson, Nonlinear elastic wave nde ii. nonlinear wave modulation spectroscopy and nonlinear time reversed acoustics, in: AIP Conference Proceedings, Vol. 760, AIP, 2005, pp. 385–392.

[66] G. Zumpano, M. Meo, Damage localization using transient non-linear elastic wave spectroscopy on composite structures, International Journal of Non-Linear Mechanics 43 (3) (2008) 217–230.

[67] S. Mezil, N. Chigarev, V. Tournat, V. Gusev, Evaluation of crack parameters by a nonlinear frequency-mixing laser ultrasonics method, Ultrasonics 69 (2016) 225–235.

[68] A. Cai, J.-a. Sun, G. Wade, Imaging the acoustic nonlinear parameter with diffraction tomography, IEEE transactions on ultrasonics, ferroelectrics, and frequency control 39 (6) (1992) 708–715.

[69] P. Blanloeuil, L. Rose, C. Wang, M. Veidt, Efficient simulations of the nonlinear wave modulation induced by a closed crack using local contact modelling, Procedia Engineering 188 (2017) 201–208.

[70] L. Zarembo, V. Krasil'Nikov, Nonlinear phenomena in the propagation of elastic waves in solids, Soviet Physics Uspekhi 13 (6) (1971) 778.

[71] V. Korneev, K. Nihei, L. Myer, Nonlinear interaction of plane elastic waves, Tech. rep., Lawrence Berkeley National Lab., CA (United States) (1998).

[72] F. D. Murnaghan, Finite deformations of an elastic solid, American Journal of Mathematics 59 (2) (1937) 235–260.

[73] L. D. Landau, E. M. Lifshitz, Course of Theoretical Physics Vol 7: Theory and Elasticity, Pergamon Press, 1959.

[74] M. McGovern, W. Buttlar, H. Reis, Characterisation of oxidative ageing in asphalt concrete using a non-collinear ultrasonic wave mixing approach, Insight-Non-Destructive Testing and Condition Monitoring 56 (7) (2014) 367–374.

[75] P. A. Johnson, T. J. Shankland, R. J. O'connell, J. N. Albright, Nonlinear generation of elastic waves in crystalline rock, Journal of Geophysical Research: Solid Earth 92 (B5) (1987) 3597–3602.

[76] M. McGovern, W. Buttlar, H. Reis, Estimation of oxidative ageing in asphalt concrete pavements using non-collinear wave mixing of critically-refracted longitudinal waves, Insight-Non-Destructive Testing and Condition Monitoring 57 (1) (2015) 25–34.

[77] A. Demčenko, V. Koissin, V. Korneev, Noncollinear wave mixing for measurement of dynamic processes in polymers: Physical ageing in thermoplastics and epoxy cure, Ultrasonics 54 (2) (2014) 684–693.

[78] A. Demčenko, R. Akkerman, P. Nagy, R. Loendersloot, Non-collinear wave mixing for non-linear ultrasonic detection of physical ageing in pvc, NDT & E International 49 (2012) 34–39.

[79] J. Harman, S. Howard, T. Shacham, A. Wheeler-Booth, Enhanced parameter investigation for robust non collinear inspection, 2013.

[80] J.-Y. Kim, L. J. Jacobs, J. Qu, J. W. Littles, Experimental characterization of fatigue damage in a nickel-base superalloy using nonlinear ultrasonic waves, The Journal of the Acoustical Society of America 120 (3) (2006) 1266–1273.

[81] G. Tang, M. Liu, L. J. Jacobs, J. Qu, Detecting localized plastic strain by a scanning collinear wave mixing method, Journal of Nondestructive Evaluation 33 (2) (2014) 196–204.

[82] J. Krautkrämer, H. Krautkrämer, Ultrasonic Testing of Materials, Springer, 1990.

[83] M. Bauccio, et al., ASM metals reference book, ASM international, 1993.

[84] P. D. Harvey, Engineering properties of steel, Asm Intl, 1982.

[85] A. B. Coppens, Simple equations for the speed of sound in neptunian waters, The Journal of the Acoustical Society of America 69 (3) (1981) 862–863.

[86] K. H. Brown, C. W. Morrow, S. Durbin, A. Baca, Guideline for bolted joint design and analysis: version 1.0., Tech. rep., Sandia National Laboratories (2008).

[87] J. Alston, A. Croxford, J. Potter, P. Blanloeuil, Nonlinear non-collinear ultrasonic detection and characterisation of kissing bonds, NDT & E International.

[88] S. Hirose, 2-d scattering by a crack with contact-boundary conditions, Wave Motion 19 (1) (1994) 37–49.

[89] L. Baillet, T. Sassi, Mixed finite element formulation in large deformation frictional contact problem, Revue Européenne des Eléments 14 (2-3) (2005) 287–304.

[90] L. Baillet, T. Sassi, Mixed finite element methods for the signorini problem with friction, Numerical Methods for Partial Differential Equations 22 (6) (2006) 1489–1508.

[91] L. Baillet, T. Sassi, Simulations numériques de différentes méthodes d'éléments finis pour les problèmes de contact avec frottement, Comptes Rendus Mécanique 331 (11) (2003) 789–796.

[92] N. J. Carpenter, R. L. Taylor, M. G. Katona, Lagrange constraints for transient finite element surface contact, International journal for numerical methods in engineering 32 (1) (1991) 103–128.

[93] P. G. Ciarlet, The finite element method for elliptic problems, Elsevier, 1978.

[94] H. Mohrbacher, K. Salama, The temperature dependence of third-order elastic constants in metal-matrix composites, in: Review of Progress in Quantitative Nondestructive Evaluation, Springer, 1993, pp. 2091–2097.

[95] W. Wasserbäch, Third-order constants of a cubic quasi-isotropic solid, physica status solidi (b) 159 (2) (1990) 689–697.

[96] V. A. Lubarda, New estimates of the third-order elastic constants for isotropic aggregates of cubic crystals, Journal of the Mechanics and Physics of Solids 45 (4) (1997) 471–490.

[97] L. Mordfin, Handbook of reference data for nondestructive testing, ASTM, 2002.

[98] O. Yilmaz, M. T. Taner, Discrete plane-wave decomposition by least-mean-square-error method, Geophysics 59 (6) (1994) 973–982.

[99] C. Inc., Nonlinear acoustics modeling of the 1d westervelt equation (2018).
URL `https://goo.gl/UckGts`

[100] M. Solovchuk, T. W. Sheu, M. Thiriet, Simulation of nonlinear westervelt equation for the investigation of acoustic streaming and nonlinear propagation effects, The Journal of the Acoustical Society of America 134 (5) (2013) 3931–3942.

[101] M. F. Hamilton, D. T. Blackstock, et al., Nonlinear acoustics, Vol. 1, Academic press San Diego, 1998.

[102] C. Pantea, C. F. Osterhoudt, D. N. Sinha, Determination of acoustical nonlinear parameter $\beta$ of water using the finite amplitude method, Ultrasonics 53 (5) (2013) 1012–1019.

[103] P. N. Wells, Ultrasonic imaging of the human body, Reports on progress in physics 62 (5) (1999) 671.

[104] D. T. Blackstock, Fundamentals of physical acoustics, John Wiley & Sons, 2000.

[105] B. Drinkwater, R. Dwyer-Joyce, P. Cawley, A study of the interaction between ultrasound and a partially contacting solid–solid interface, in: Proceedings of the Royal Society of London A: Mathematical, Physical and Engineering Sciences, Vol. 452, The Royal Society, 1996, pp. 2613–2628.